Effect of pre-straining on the dynamic behaviour of titanium



Kwan Lok Wong

Exeter College

University of Oxford

A thesis submitted for the degree of

Doctor of Philosophy

Trinity 2025

Abstract

Titanium and its alloys are widely used in aerospace engineering due to their high strength-to-weight ratios. In particular, they are used to construct turbine engine components such as fan blades and casings, which are susceptible to impact loading from bird or ice. The mechanical properties of titanium are strongly correlated to its microstructure due to the inherent anisotropy. Pre-straining from manufacturing processes often induces microscopic defects and changes the overall texture, influencing its mechanical behaviour. Despite decades of research, the high strain-rate behaviour of pre-strained titanium remains obscure. In this thesis, pure titanium (CP-Ti, grade 2) is studied as the microstructure is less complex than alloys, thus minimising variables in the specimens. The effect of pre-straining on pure titanium is investigated experimentally, with a strong focus on the microstructure evolutions under high strain-rate deformation. Key microstructure features are identified and their correlations with the respective bulk behaviour are evaluated with statistical modelling.

The first experimental campaign explores the role of strain-path in pure titanium, with the specimens undergoing two stages of compression, first quasistatic (QS) then high-rate (HR). At the first stage, specimens are compressed to various levels to generate different pre-strained microstructures. High-rate testing is then conducted using a modified compression split-Hopkinson pressure bars (SHPB), equipped with a newly-implemented momentum trap to interrupt deformations. Electron backscatter diffraction (EBSD) is then employed to examine the microstructures of recovered specimens. Large areas are examined to obtain statistical features. The results show that the twin activation sequence under HR in titanium with a prismatic/pyramidal texture is identified as: $\{10\bar{1}2\} \rightarrow \{11\bar{2}1\} \rightarrow \{11\bar{2}2\} \rightarrow \{10\bar{1}1\}$. The results also reveal that twin boundaries generated from the first QS compression act as a key strengthening mechanism for the second HR loading. This mechanism has rarely been considered in literature, and conventional microstructure-aware models also do not incorporate this mechanism.

From the first campaign, several questions are raised, including the effect of barrelling from the first QS compression on the second HR compression, and the strain-rate effect on the early-stage and incipient failure mechanisms. The second campaign begins with designing a novel approach to generate pre-strained specimens, which involves compressing large cylinders and machining small specimens from regions of uniform strain. Two different pre-strained levels are generated, and their microstructure evolution under QS and HR loading are investigated. The results show that the QS deformation is determined by slip systems, and pre-straining does not influence the mechanisms beyond texture changes. Under HR loading, deformation

is dictated by twinning activities and dislocation structures. Evidence suggests that for the prismatic/pyramidal-textured titanium, growth of $\{10\bar{1}2\}$ twin is favoured, and the twin boundaries sweep through the parent grains. As twin boundaries are sources of dislocation generation, the internal stress in twinned regions is high. Coupled with the geometrically-favoured low critical resolved shear stress (CRSS) Prismatic<a> slip, the hardening rate is high. In contrast, titanium with a strong basal texture favours nucleation of $\{11\bar{2}2\}$ twin, leading to high twin boundary fractions but small changes in the texture. The high low-angle grain boundary (LAGB) density implies that they are the primary strain-accommodation mechanism. By allowing partial transmission of slip and their ability to carry plasticity through boundary migration result in a lower hardening rate. At the incipient failure stage, the two pre-strained titanium result in surprisingly similar microstructures, with features exhibiting dynamic recrystallisation and low geometric-likelihood of the easily-activated Prismatic <a> slip.

To explore the correlations between microstructures and bulk behaviour, a statistical modelling approach is employed, since the small dataset in this study would be insufficient to derive phenomenological or physical laws. This approach aims to minimise human interpretation which often leads to biases in feature identification. To study the underlying correlations and patterns, key microstructure features are first extracted using Principal Component Analysis. Their correlations with the respective bulk yield or flow stresses are then examined using machine learning models: neural network and Gaussian Process. The results re-emphasis the correlation between twin boundaries and bulk stresses, and identify grain shapes and LAGB densities as important features. Additionally, features that are not extracted due to low variance, such as grain sizes, can infer that targeted experiments are required for these features. The data generated and the novel approaches developed improve the current understanding of microscopic deformation mechanisms in titanium, which in turn aid the development of microstructure modelling.

Prior to the development of a robust physically-based model, an alternative approach is to use machine learning models as surrogate models. However, they require very large training datasets. Given the expensive and time-consuming nature of experiments, the final body of work evaluates the use of generative machine learning models for data augmentation. In particular, the Generative Adversarial Network successfully recreates realistic non-parametric microstructure features. This approach demonstrates a strong potential for synthetic microstructure generation, paving ways to data-driven materials design and modelling.

Presentations

- *Application of Machine Learning in Data Augmentation*, **Doctoral Symposium**, 1st July 2025
- *Dynamic behaviour of pre-strained titanium*, **Mechanical & Design Excellence Doctoral Conference**, 22nd April 2024
- *Effects of Pre-Straining on the Dynamic Behaviour of Titanium*, **2023 CornerStone Prosperity Partnership & Doctoral Training Conference**, 26th April 2023
- *Effects of Changing Plastic Work on Macroscopic Properties*, **2022 CornerStone Prosperity Partnership & Doctoral Training Conference**, 21st June 2022

Papers

- **K. L. Wong**, D. J. Chapman, D. E. Eakins. *Deformation mechanisms of commercially-pure titanium under strain path changes with quasistatic and high strain-rate compression.* **In preparation**
- **K. L. Wong**, D. J. Chapman, D. E. Eakins. *Effect of pre-straining on the deformation mechanisms onset of yielding and incipient failure of commercially-pure titanium.* **In preparation**
- H. Soyama, **K. L. Wong**, D. E. Eakins, A. M. Korsunsky. *The effects of submerged laser peening, cavitation peening, and shot peening on the improvement of the torsional fatigue strength of powder bed fused Ti6Al4V produced through laser sintering.* **International Journal of Fatigue**, 185, 108348 (2024). https://doi.org/10.1016/j.ijfatigue.2024.108348

Acknowledgments

Throughout my DPhil journey, I have been incredibly fortunate to be supported by many individuals. First and foremost, I would like to thank my supervisors, Prof Daniel Eakins and Dr David Chapman, who entrusted me with this project and allowed me to pursue a doctorate with them. They have offered me invaluable advice and suggestions, generously shared their research experience and vision, and transformed me into an independent researcher. I would also like to thank Drs David Sory and Lukasz Farbaniec for providing guidance on experiment designs at the beginning of my DPhil journey.

To my colleagues at the Impact and Shock Mechanics Laboratory: David, Jasper, Jan, Ed, Kin, James, Thomas, Liam and Indrajeet - thank you for bringing joy into my DPhil journey, Begbroke would feel so isolated without you all.

To Karen Bamford - thank you for handling all of the administrative tasks with efficiently and professionalism.

To the Begbroke Workshop staff: Stuart Carter, Derek Robinson, Jeffrey Fullerton and Peter Tantrum - thank you for fulfilling the manufacturing requests I submitted with your exceptional skills and precision.

To Dr Phani Karamched at DCCEM, Oxford - thank you for training me to use the SEM/EBSD system, and providing support in collecting high-quality data throughout the journey.

To my parents - thank you for your love and care.
To my sister - thank you for your support and encouragement.

Institutional

I would like to thank EPSRC and Rolls-Royce plc. for financially supporting this study under the CASE-conversion doctoral training studentship. I acknowledge use of characterisation facilities within the David Cockayne Centre for Electron Microscopy, Department of Materials, University of Oxford, alongside financial support provided by the Henry Royce Institute (Grant ref EP/R010145/1).

Declaration

I hereby declare that this thesis is wholly my own work, unless otherwise stated. No part of this thesis or the research herein has been accepted or submitted for another degree, diploma, certificate or other qualification at any other universities, educational or research institutions. Any external sources of information or data used have been properly acknowledged and references.

Kwan Lok Wong

Trinity 2025

Contents

Abstract **i**

List of Figures **ix**

List of Tables **xxi**

1 Introduction **1**

1.1 Research motivations 1

1.2 Literature review 2

1.2.1 Titanium crystallographic structure 2

1.2.2 Effect of alloying elements 4

1.3 Deformation and strengthening mechanisms 4

1.3.1 Dislocation slip 5

1.3.2 Deformation twinning 7

1.4 Mechanical processing of titanium 9

1.5 Micro-mechanical studies of titanium 15

1.5.1 Deformation slip characterisation 15

1.5.2 Twinning characterisation 17

1.6 Summary 22

1.7 Objectives 23

1.8 Thesis overview 24

2 Experimental Methodology **25**

2.1 General Workflow 25

2.2 Quasistatic testing 26

2.3 High-rate testing 28

2.3.1 Deformation under dynamic loading 29

2.4 Split-Hopkinson pressure bars (SHPB) 30

2.4.1 Theoretical principles 30
2.4.2 Practical considerations 35
2.4.3 In-house SHPB systems at Oxford 42
2.5 Microscopy 44
2.5.1 Electron microscopy 44
2.5.2 Electron backscatter diffraction (EBSD) 46
2.5.2.1 Modern EBSD setup 47
2.5.2.2 Sample preparation 49
2.6 Conclusion on Experimental Methodology 52

3 Effect of strain-path changes on the deformation mechanisms of pure titanium 53
3.1 Primary objectives 53
3.2 Experimental procedures 54
3.2.1 Mechanical testing 54
3.2.2 Microstructure characterisation 57
3.3 Results 59
3.3.1 Mechanical behaviour 59
3.3.2 Microstructure evolution 60
3.4 Discussions 63
3.4.1 Quasistatic deformation 63
3.4.2 High-rate deformation 65
3.4.3 Distributions of twin types 68
3.4.4 Dislocations and Schmid Factors 71
3.4.5 Changes in yield stress 73
3.5 Conclusions on strain-path changes 76

4 Effect of pre-existing defects on the strain-rate dependent deformation mechanisms of pure titanium 79
4.1 Primary objectives 80
4.2 Experimental procedures 80
4.2.1 Novel pre-straining method 81

4.2.2 Mechanical testing . . . 89
4.3 Results . . . 92
4.3.1 High-rate interrupted testing . . . 92
4.3.2 Strain-rate dependent mechanical behaviour . . . 96
4.3.3 Microstructures . . . 99
4.4 Discussion 1 - Feature extractions from microstructures . . . 104
4.4.1 Novel twin identification - Kernel Density Estimation . . . 106
4.4.2 Grain orientations - Gaussian Mixture . . . 109
4.5 Discussion 2 - Microstructure evolutions . . . 115
4.5.1 Early-stage deformation . . . 115
4.5.2 Incipient failure . . . 123
4.6 Statistical analyses of microstructures . . . 135
4.6.1 Motivations . . . 135
4.6.2 Feature correlations . . . 136
4.6.3 PCA on Microstructure Features . . . 139
4.6.4 Microstructure and bulk behaviour correlations . . . 142
4.6.4.1 Overview of Neural Network . . . 144
4.6.4.2 Overview of Gaussian Process . . . 151
4.6.4.3 Neural Network vs Gaussian Process . . . 154
4.7 Summary and conclusions . . . 162

5 Application of generative machine learning on data augmentation of microstructural data 166

5.1 Introduction . . . 166
5.1.1 Objectives . . . 168
5.2 Models overview . . . 169
5.2.1 Overview of Diffusion models . . . 169
5.2.2 Overview of Generative Adversarial Networks (GAN) . . . 172
5.2.3 Overview of Recurrent Neural Network . . . 176
5.3 Methodology . . . 179
5.3.1 Pre-processing of misorientation distributions . . . 179

5.3.2 Diffusion model . . . 183
5.3.3 WGAN-GP . . . 185
5.3.4 RNN with GRU . . . 188
5.4 Results and discussions . . . 188
5.4.1 Accuracy of generative models . . . 190
5.5 Conclusions . . . 196

6 Conclusions **198**
6.1 Summary and key contributions . . . 198
6.2 Future works . . . 203
6.2.1 Limitations and potential improvements . . . 203
6.2.2 Future implications on materials discovery . . . 205

Bibliography **207**

List of Figures

1.1 The two solid phases of pure titanium. The α phase has a hexagonal close-packed (HCP) structure and the β phase has a body-centred cubic (BCC) structure. 3

1.2 The Burgers orientation relationship, adopted from [2]. 3

1.3 Slip systems in HCP titanium. Prismatic slips are favoured due to the c/a ratio of titanium being lower than the ideal c/a of 1.633. Basal and pyramidal slips are less favoured but are still active. 7

1.4 Schematic illustrating the process of deformation twinning. 8

1.5 The Schmid Factor of a slip system. 12

2.1 The general experimental workflow, including pre-straining to generate defects, mechanical testing of pre-strained specimens and microscopy. 26

2.2 Schematic of a typical universal testing machine (UMT). 27

2.3 An example of the compliance testing, specimen testing uncorrected and corrected for machine compliance. 28

2.4 Basic components of a simple compression SHPB system. 31

2.5 Stress wave propagation in the striker and input bars upon impact. . 32

2.6 Bar velocities and stress waves at the specimen interface, adopted from [82], where $\dot{u}_1$ and $\dot{u}_2$ are the input and output bar end velocities, l_s is the initial specimen length, σ_i, σ_r and σ_t are the incident, reflected and transmitted waves. 34

2.7 The idealised stress wave at the centre of the rod and typical experimental stress wave measured on the rod surface. Note that both waves are artificially generated to represent the two cases. These are not experimental results. 36

2.8 An example of laser alignment on the SHPB. (a) A schematic of the alignment components. (b) The actual setup used for the alignment, consisting of off-the-shelf optical components. (c) A laser coherent diffraction pattern at the far end (muzzle) of the barrel. 38
2.9 The tandem momentum trap design from Prot and Cloete [88]: (a) the conceptual design consisting to two tubes, (b) the actual design with the second tube being wrapped around the inner tube. 40
2.10 The two compression SHPB systems used in this thesis, all bars are made of Ti-6Al-4V: (a) the SHPB with a tandem momentum trap used in Chapter 3, with all bars being 12.7 mm in diameter, and (b) the long SHPB system used Chapter 4, with the input and output bars being 16 mm in diameter and the striker bar being 20 mm in diameter. 43
2.11 Two common electron microscope: (a) a scanning electron microscope (SEM), and (b) a transmission electron microscope (TEM). 45
2.12 The phenomenon of electron scattering: (a) the incident electron beam enters the specimen, and electrons interact with the atoms near the surface. Some electrons backscatter and escape the surface, forming diffraction patterns. (b) Bragg's law that causes electron diffraction to be unique to the lattice structure and orientation. . . . 47
2.13 The EBSD setup in a SEM: (a) the real setup, (b) a schematic showcasing the components, and (c) an example of Kikuchi patterns. . . . 49
2.14 Example of SEM specimens: (a) specimens hot-mounted in acrylic (clear) and conductive Bakelite (black), and (b) unmounted specimens bonded to stubs after mechanical polishing. 50
2.15 A schematic of the ion polisher: the specimen is placed on a rotating stage, with two ion guns mounted at an angle, emitting broad argon ion beams to polish the specimen surface. 52

3.1 The work flow of the first experimental campaign. 54

3.2 An example of the strain gauge signals from the input and output bars with the momentum trapping device. 57
3.3 Both the 1- and 3-wave analyses are showing similar engineering stress-strain responses. The different phases of waves in the 3-wave analysis overlapped with the longitudinal wave, causing oscillations around the stress-strain behaviour. Therefore, the 1-wave analysis was applied as it produces a cleaner result. 58
3.4 The forces at the specimen-bar interface at the input and output bar ends show slight differences, possibly due to adiabatic heating and inertial effects of the specimen. 58
3.5 As-received CP-Ti Grade 2 used in this study. The cross-section EBSD map is obtained from the plane normal to the Z-direction (loading direction) of the cylinder. 59
3.6 Engineering stress-strain curves at the quasistatic stage and the subsequent high strain-rate loading. The high-rate curves are shifted to their respective QS-strained levels. HRLS and HRHS refer to high-rate low strain and high-rate high strain respectively. The arrows indicate deviations in late-stage hardening from the flow stress projection. 61
3.7 EBSD maps of the recovered specimens at different loading stages. The scanned regions were $(1.117 \times 0.838)\,\mathrm{mm}^2$ at the centre of the cross-section planes, with step sizes of approximately 1.117 µm for QS and 0.931 µm for HRLS and HRHS. 64
3.8 Evolution of (0001) pole figures from the cross-section planes of the specimens, obtained from large area $(1.117 \times 0.838)\,\mathrm{mm}^2$ EBSD scans. 65
3.9 Twin boundary fractions (a) and twin volume fractions (b) of $\{11\bar{2}1\}$ ET, $\{10\bar{1}1\}$ CT, $\{11\bar{2}2\}$ CT and $\{10\bar{1}2\}$ ET twinning systems. 69
3.10 The average grain sizes in equivalent diameters of the pre-strained specimens at different loading stages. Total strain was measured *post-mortem*. The error bars indicate the interquartile range (middle 50%) of the grain sizes. 71

3.11 Area fractions of grains with high Schmid Factors (SF = 0.4 to 0.5) for each slip system at different loading stages. 72
3.12 The average GND densities (solid lines) and average LAGB densities (dotted lines) of the specimens at different loading stages. 72
3.13 Flow stresses at 1% engineering strain against different starting GND densities. Experimental data is shown as the blue dots and the linear regression is shown as the red dotted line. 74
3.14 Linear regression of the yield stress obtained from experiments, the prediction using the modified Hall-Petch model and the Taylor dislocation hardening model. The x-axis indicates the level of strain at the initial QS stage, from no QS-strain (0%), to 5%, 8% and 20% QS-strain. 77
3.15 Twin boundary and volume fractions against yield stress (taken as flow stress at 1% engineering strain) under high-rate compression. The straight dotted lines show the linear regression of the data points. 77

4.1 The Abaqus FEA model for determining the strain distribution of a CP-Ti (grade 2) cylinder of 60 mm diameter by 120 mm height. The top and bottom "anvils" were analytical rigid with friction added to the interfaces. The bottom anvil was fixed while the top anvil displaced downwards. 82
4.2 Examples of tensile and compressive plastic strain distributions: (a) PE11 for tensile strain, and (b) PE22 for compressive strain. 83
4.3 The centre region to be studied for the strain variations, with a width of 0.25 D and height of 0.2 L: (a) This ring section of material (assuming radial symmetry about the centre axis) was selected to maximise the number of test specimens that could be machined from one large cylinder, and (b) elements selected (highlighted in red) to calculate the strain distributions. 84
4.4 The tensile and compressive strain distributions at 5% strain, with different coefficient of friction (F_c) at the interfaces. 85

4.5 The tensile and compressive strain distributions at 20% strain, with different coefficient of friction (F_c) at the interfaces. 86
4.6 The as-received large cylinder was sliced into 5 pieces. The top and bottom sections (Slices 1 and 5) were discarded to ensure good parallelism of Bars 2 and 4, which were subsequently compressed to generate pre-strained specimens, labelled "PS 5" and "PS 20" respectively. Slice 3 was reserved for microscopy of the as-received material. 87
4.7 The Instron hydraulic machine (model SATEC 3500 kN), located at Imperial College London, was used to compress the large CP-Ti cylinders. 88
4.8 The displacement-force curves from the Intron hydraulic machine for the compression loading on the two cylinders of CP-Ti. 88
4.9 (a) The large (60 mm diameter × 120 mm length) cylinders of CP-Ti grade 2 used to generate pre-strained specimens: (left) an undeformed bar, not used in this study, (middle) PS 5 - ∼5% strain and (right) PS 20 - ∼20% strain. The strain levels were characterised by the height reduction, and (b) the cross-section of the PS 20 cylinder. Test specimens were extracted from the ring section of the cylinder, which was identified to have similar strain distributions. 89
4.10 An example of the long SHPB data: (a) the raw strain gauge data from the long SHPB with three sets of strain gauges, and (b) the reconstructed waves using the data analysis from [90]. Waves were shifted to the specimen-bar interfaces at time = 0. 90
4.11 Engineering stress-strain curves (smoothed) of the PS 5 (∼ 5% pre-strained) and PS 20 (∼ 20% pre-strained) specimens. The red "X" symbols indicate failure occurring at $\varepsilon_{\text{eng.}} > 40\%$ and $\varepsilon_{\text{eng.}} > 30\%$ for PS 5 and PS 20 respectively. The other curves were from the interrupted testing. Results from the early stages cannot be validated due to stress not being in equilibrium. 93

4.12 A tilted input bar (exaggerated) can cause contact with one side of the stop ring to transmit the incident wave into the output bar before deformation of the specimen occurs. 95
4.13 The engineering stress-strain curves of QS and HR compressions on PS 5 and PS 20. Note that the HR curves were the same as those from Fig. 4.11. It is clear that the flow stresses increased with strain-rate. 98
4.14 Stress-strain curves of the QS and HR compressions on PS 5 and PS 20, with Young's modulus plotted on each curve. For each curve, a linear regression was fitted to the plastic deformation region. 98
4.15 The as-received large cylinder of CP-Ti (grade 2) for this study. All the EBSD maps were scanned from the circular face, X-Y plane, and the loading was applied in the Z direction (out-of-plane). 100
4.16 The EBSD maps, texture plots and MO distributions of recovered specimens from mechanical testing on PS 5 ($\sim$ 5% pre-strained). Peaks identified in PS 5 and PS 5 QS 10 are likely not twins - possibly due to the sensitivity in peak detections. 101
4.17 The EBSD maps, texture plots and MO distributions of recovered specimens from mechanical testing on PS 20 ($\sim$ 20% pre-strained). In PS 20 HR 25, a peak was identified between 40° and 50°, however it does not correlate to any twin systems from literature. 102
4.18 An example of the grain size distribution - it has the form of a skewed normal (Gaussian) distribution. As only one peak was identified, the mean value (the average grain size) was considered. 106
4.19 Examples of KDE with a fixed (1.6) bandwidth and a dynamic bandwidth using Scott's Rule. 108

4.20 The twin system identification method: (1) the grain boundary MO angles are plotted as a histogram with 256 bins and normalised to a probability density, (2) a KDE (Kernel Density Estimation) is fitted to the data and plotted against the histogram, (3) peaks are identified from the KDE - a smoother transition than the histogram heights, and finally (4) data around the peaks are highlighted, and counted as the twin boundary fraction of the specific twin system. 109
4.21 Grain orientation expressed as Euler angles (φ_1, ϕ, φ_2). The reference grain with Euler angles (0, 0, 0) is shown against the EBSD map (global) coordinates. 110
4.22 Examples of Euler angles (φ_1, ϕ, φ_2) distributions for the PS 5 HR specimens. Only ϕ shows quantifiable differences and was therefore considered as the metric for grain orientation evolution. 111
4.23 Extracting statistical features from the distributions of Euler angle Phi (ϕ): (1) plot a histogram, normalised to the probability density, (2) fit a Gaussian Mixture (GM) model with 2 components on each histogram to extract two underlying Gaussian distributions, (3) for each component, GM1 and GM2, extract the means, standard deviations and weights - which represents the ratio of each component. . . 113
4.24 The evolution of ϕ distributions, with a two-component Gaussian Mixture model fitted to each histogram. The histograms are normalised to the probability density (PD). 114
4.25 Evolution of the average grain sizes and grain shapes in their aspect ratios during QS and HR compression of PS 5 and PS 20. 127
4.26 The average values of the long and short radii, labelled “a” and “b” respectively, of the equivalent ellipses fitted to each grain from the EBSD maps. 128
4.27 The evolution of (a) the total low-angle grain boundary (LAGB) densities, taken as: $\mathrm{LAGB_{total}/Area_{total}}$ (b) LAGB densities per grain (μ_{LAGB}/N, where N is number of grains) , and (c) maximum grain orientation spread (GOS). 129

4.28 The area fractions of grains with the highest SF for each slip systems in α-phase (HCP) titanium. Here only four slip systems are considered: Basal <a>, Prismatic <a>, Pyramidal <a> and Pyramidal <c+a>. 130
4.29 The evolution of the KDE curves fitted to the MO distributions of PS 5 and PS 20, QS and HR loading. 131
4.30 The evolution of the Gaussian Mixture (GM) curves fitted to the Phi (ϕ) distributions of PS 5 and PS 20, QS and HR loading. 132
4.31 Evolutions of twin boundary fractions of each twin systems, except the $\{11\bar{2}4\}$ twin ($\sim$77°) as it was not detected. 133
4.32 Evolution of the total twin boundary (TB) fractions of PS 5 and PS 20, QS and HR loading. 133
4.33 The changes in means, standard deviations and weights (relative ratios) of GM1 and GM2 in the Gaussian Mixtures fitted to the ϕ distributions. 134
4.34 Absolute loadings of features from PC1, PC2, PC3 and PC4. The top three features with the highest loadings are highlighted. 142
4.35 A visual illustration of a single neuron in a neural network: an input x is passed onto the first half of the neuron, which is a linear function $z = wx + b$, the z value is then passed onto the second half which is a non-linear function that generates an output a (or $\hat{y}$ for the final output). 146
4.36 Two commonly used activation functions in a neural network, the sigmoid function for classification tasks and ReLU function for regression tasks. 146
4.37 A visual illustration of a typical neural network consisting of multiple layers of neurons. The output of neurons of layer (l) are passed onto the neurons in the next layer ($l+1$). The number of neurons in each layer is denoted as n. 147

4.38 An example of different learning rates for the gradient descent optimisation after 5 epochs. The black curves are the true loss against different weight w. When the learning rate is too small (left) or too large (right), the parameter w cannot quickly converge and more epochs are required to compute to the optimised value. When the learning rate is at its optimal (middle), the parameter w quickly converges to give the lowest loss. 149
4.39 An example of a linear regression model with uncertainty shown as a Gaussian distribution (in red). 151
4.40 The losses of neural networks during training. All models quickly converged at around 300 epochs with the high learning rate, and were trained further to fine-tune the learning parameters. Each line represents a model trained using LOOCV. 158
4.41 An example of normal fitting against over-fitting. When the dataset is too small or NN model is too complex, it can often lead to over-fitting. 160
4.42 Predictions of yield and flow stresses using neural network (NN) and Gaussian process (GP) regressor, with (a), (b): initial 11 features, (c), (d): PCA-reduced dataset and (e), (f): manually selected features. The mean-squared percentage error (MAPE) values are shown for each model and dataset. 163

5.1 The forward and reverse processes of a diffusion model. The U-Net is trained to predict noise, which is gradually removed to obtain a clean input. 170
5.2 Schematic of a Diffusion model, which consists of a (fixed, untrained) noise scheduler, a U-Net for noise prediction, and a fixed DDPM (Denoising Diffusion Probabilistic Model). 170
5.3 Schematic of a GAN model, which consists of a generator model and a discriminator (or critic) model. The typical labels for real and fake are “1” and “0” respectively. 174

5.4 The computation of a single unit in a RNN: the input vector at the current timestep t (x_t) is multiplied by a weight matrix W_x, and the output (or the hidden state) from the previous timestep y_{t-1} is multiplied by W_y, and a bias b is added. This is then passed onto an activation function, usually a hyperbolic tangent, generating an output of this current timestep. This process is then repeated to generate a desired sequence. 177
5.5 A standard RNN architecture with the output from the previous computation unit passing onto the current unit. 177
5.6 Schematic of a GRU used to resolve the issue with long-term memory loss in a traditional RNN unit, while being faster and lighter weight than LSTM. 179
5.7 An example of pre-processing of the non-parametric KDE for the MO distribution. 181
5.8 Synthetic MO distributions generated by combined Gaussian distributions, as shown in Fig. 5.7. 182
5.9 To generate more training data points, each 24 original EBSD map (from Chapters 3 and 4) was cropped to 16 smaller EBSD maps with no overlapping. From each set of 16 EBSD maps, only 12 (80%) were chosen for training. 183
5.10 The diffusion model with time embedding and prompt encoding for conditional generation of output features. This model failed to learn to generate desirable features, which could be attributed to the model's complexity relative to the dataset. 185
5.11 Architecture of the WGAN-GP used to convert the combined Gaussian to a realistic MO distribution. The generator essentially added the baseline "noise" to the input, and the critic helped the generator learn the appropriate noise. 187
5.12 Training losses of the generator and critic of the WGAN-GP used. . . 187

5.13 Architecture of the RNN with 2-layer GRU used as a sequential generation model, using the peak statistics as prompt to convert an input sequence of combined Gaussian to a realistic MO distribution. 189
5.14 Training losses of the RNN with 2-layer GRU, using a prompt as the initial hidden state. 189
5.15 Synthetic MO distributions generated by diffusion. 191
5.16 Synthetic MO distributions generated by WGAN-GP. 192
5.17 Synthetic MO distributions generated by GRU. 193
5.18 The mean squared errors (MSE) between the synthetic and real MO distributions. The specimen labels (1 to 24) are as defined previous figures (*e.g.* Fig. 5.16). 194
5.19 Predictions (middle figures) using interpolated twin peak statistics from real specimens (left and right figures). The arrows indicate the underlying features generated from the trained WGAN-GP model. . . 195

List of Tables

1.1 Extension (ET's) and contraction (CT's) twin systems in α-Ti [24]. . 8

3.1 Chemical composition in weight percentage (Wt. %) of the commercially-pure titanium (grade 2) used in Chapter 3, with oxygen being the primary strengthening element. 57

3.2 The original length (OL) and engineering strain-rates under high-rate loading of the recovered specimens. 61

3.3 Evolution of low-angle grain boundary density (μ_{LAGB}), average GND density (μ_{GND}), twin volume and twin boundary fractions (TV and TB frac.), and average grain size in equivalent diameter of the specimens. 64

3.4 Twinning systems, types (ET: extension twins, CT: contraction twins), twin boundary misorientation angles [22] and shear strains in pure titanium [1, 2, 21]. 66

4.1 The material properties and standard Johnson-Cook plasticity model parameters of CP-Ti (grade 2) [120] used in the model. The parameter **A** is the reference yield stress, **B** and **n** are strain-hardening constants. 82

4.2 The percentage differences of the maximum and minimum values of absolute tensile (PE11) and compressive (PE22) strain distributions. Displacements of 6 mm and 24 mm correspond to $\varepsilon_{\mathrm{eng.}}$ =5% and 20% respectively. 84

4.3 Chemical composition in weight(Wt. %) of the large bar of commercially-pure titanium (grade 2) used in Chapter 4. 87

4.4 Geometries of pre-strained specimens before and after the mechanical testing: OD and OL are the original diameter and length, and L_{test} is the length post-test. The specimen labelling convention is: PS 5/20 (pre-strained ∼5% or ∼20%), QS/HR indicates the strain-rate, followed by the strain levels. For example, PS 5 QS 10 refers to the ∼5% pre-strained specimen which was quasistatically-compressed to ∼10% strain. 91

4.5 Failure engineering stresses ($\sigma_{eng.}$) and strains ($\varepsilon_{eng.}$) of HR compression on PS 5 and PS 20, shown in Fig. 4.11. The true stress strain values (σ_{true} and ε_{true}) were computed using the standard analytical conversions. 92

4.6 Parameters of linear regression of plastic flow stresses in Fig. 4.14. . . 97

4.7 The maximum engineering stresses and strains ($\sigma_{eng.}$, $\varepsilon_{eng.}$), and the analytically-converted true stresses and strains (σ_{true}, ε_{true}) of the recovered specimens as shown in Fig. 4.14. 99

4.8 Twin boundary fractions of individual twin systems. Note that the $\{11\bar{2}4\}$ (∼77°) system was not detected statistically from any of the specimens in this study. 108

4.9 Mean, standard deviation (Std. Dev.) and weight of the components, GM1 and GM2, of the Gaussian Mixture fitted to each ϕ distributions. 114

4.10 The CRSS values (in MPa) of titanium obtained from literature. . . . 119

4.11 The average grain sizes (Fig. 4.25a) , grain shapes in aspect ratios AR (Fig. 4.25b), and the average long and short radii, labelled a and b respectively, of an equivalent ellipse, shown in Fig. 4.26. 126

4.12 The LAGB densities of the entire EBSD maps (μ_{LAGB}, total), the per-grain average (μ_{LAGB}, per grain), and the maximum grain orientation spread (GOS) in degrees. These values are plotted on Fig. 4.27. 126

4.13 Area fraction of grains with the highest Schmid Factor (SF) among all four slip systems considered in this study, as shown in Fig. 4.28. . 127

4.14 Architecture of the simple neural network used to correlate microstructure features and strain-rates to their respective yield and flow stresses. The input dimension is denoted as n. 157

5.1 The generator architecture in the WGAN-GP used in this study, where n is the number of input features: the number of MO histogram bins. The Leaky ReLU had a negative slope of 0.2 and the drop out probability of 0.5. The total number of learnable parameters in this generator model was 2624768. 186

5.2 The critic architecture in the WGAN-GP used in this study. The Leaky ReLU activation functions all had a negative slope of 0.1. The total number of learnable parameters in this critic was 2560513. . . . 186

Chapter 1

Introduction

This chapter begins with an overview of the thesis and the research motivation. It is followed by a literature review, which covers the relevant previous studies on the deformation mechanisms in titanium, and identifies the gaps in existing literature. Finally, the goals and objectives of the thesis are outlined in the last section.

1.1 Research motivations

Titanium and its alloys are widely used in many applications due to their high strength-to-weight ratio and excellent corrosion resistance. They are often used in aerospace engineering to construct turbine engine components. Conventional manufacturing processes such as forging and rolling induce microscopic defects (*e.g.* dislocations), combining with the inherent anisotropy in titanium's microstructure, the bulk mechanical properties can be difficult to predict. Certification of turbine engines require rigorous testing which includes simulated ice and bird strike at a high velocity. Any small changes in material supply and manufacturing processes can drastically alter the structural performance under impact loading. Therefore, one must understand the fundamental correlations between the microscopic features

and bulk mechanical properties.

To begin the investigation, a comprehensive literature review is undertaken to consolidate the current understanding of mechanical behaviour of titanium, and to identify gaps in the existing knowledge. The scope of this thesis is then refined and the research objectives are established. Experiments are designed and conducted to generate new evidence to advance the current knowledge in micromechanics in titanium.

1.2 Literature review

1.2.1 Titanium crystallographic structure

Titanium is a crystalline solid material at standard temperature and pressure. The crystallographic structure, or more commonly called the solid "phases", of pure titanium varies depending on the temperature and pressure it is held at [1]. At room temperature and atmospheric pressure, titanium crystallises in a hexagonal close-packed (HCP) unit cell structure, known as the α phase (see Fig. 1.1). As atoms are more close-packed along the a-direction than the c-direction, α-titanium is inherently elastically and plastically anisotropic [2]. When α-titanium is heated, the crystal structure transforms into the β phase, which has a body-centred cubic (BCC) structure [1, 3]. Compared to the α phase which exhibits higher specific strength, the β phase is isometric (as it is cubic), less anisotropic and more ductile compared to α [1, 3].

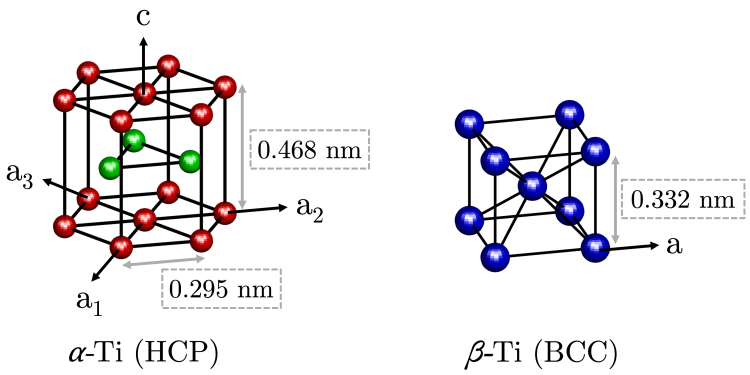


Figure 1.1: The two solid phases of pure titanium. The α phase has a hexagonal close-packed (HCP) structure and the β phase has a body-centred cubic (BCC) structure.

The β-transus temperature is the temperature at which pure titanium completely transforms from α to β phase. For pure titanium, this temperature is approximately 900 °C [3, 4]. Impurities or alloying elements can affect this temperature and are often added to either suppress or encourage the transformation. Upon cooling, the transformation is reversed: the β phase transforms back to the α phase. This phase transformation follows the Burgers Orientation Relationship as shown in Fig. 1.2.

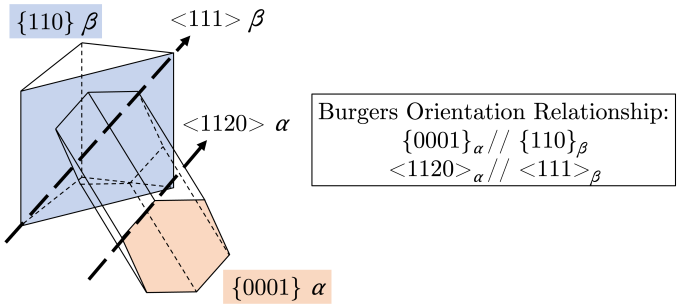


Figure 1.2: The Burgers orientation relationship, adopted from [2].

Other than these two solid phases, titanium can also exist in a hexagonal structured ω phase, distorted HCP [5], distorted BCC [6] and a face-centred cubic structure [7] under extreme conditions, for example extremely high pressure and cryogenic temperature. However, these phases generally only exist at specific laboratory

environments or in an insignificant amount compared to α and β phases.

1.2.2 Effect of alloying elements

To enhance the strength of metals, solution-strengthening or alloying, is a technique where the base metal is mixed with additional alloying elements. These alloying elements are either interstitial or substitutional [3, 8]. Interstitial elements, such as oxygen, fill the gap between titanium atoms, while substitutional elements, such as aluminium, form metallic bonds with titanium. Both cases impose lattice strain in the base metal, acting as barriers to inhibit dislocation movements [1]. In particular, aluminium can also form intermetallic compounds (Ti_3Al) which further strengthen the base metal [1, 3]. Some of these elements also act as phase stabilisers that allow α or β phase to be retained outside of their normal temperature range. For example, aluminium and oxygen stabilise the α phase at higher temperature, while vanadium and niobium stabilise the β phase at lower temperature [1]. The Ti-6Al-4V is the most common titanium alloy. It is a two-phase alloy, combining high strength from the α phase and good ductility from the β phase across different temperatures [1, 3, 9]. This increases the microstructural complexity and the interaction between the two phases can alter the microscopic deformation mechanisms, which is explained in the following section.

1.3 Deformation and strengthening mechanisms

When an external loading is applied to titanium, it first undergoes a reversible elastic deformation, following a linear Hooke's law stress-strain relationship. As the

applied load exceeds the material's yield strength, it undergoes plastic deformation, which refers to the permanent shape change and deviation from the linear Hooke's law. This macroscopic shape change originates from the microscopic deformation mechanisms, which lead to atomic/dislocation movements within the material. Upon unloading, only the elastic deformation is reversed, releasing its elastic strain energy. The energy associated with plastic deformation is partially stored within the material as internal strain energy while the remaining is released as heat [8].

1.3.1 Dislocation slip

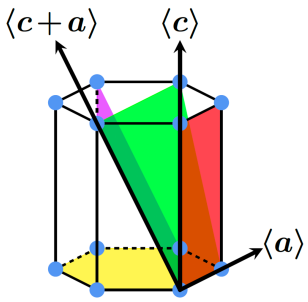
In a perfect crystal lattice structure, the atoms are arranged in a repeated arrangement called the unit cell. In reality, during solidification of the material (*e.g.* casting), there will be defects in the crystal structure. These defects, termed "dislocations", create internal strain fields and are one of the primary mechanisms for facilitating plastic deformation.

Increasing the applied loading causes dislocations to "move" (slip), which involves the continuous breaking and reforming of bonds around the dislocation [8]. To quantitatively describe dislocation character, the slip plane normal and the slip direction are collectively called a slip system. The type and number of slip systems depends on its unit cell structure. High-symmetry structures such as BCC or face-centred cubic (FCC) have more slip systems and hence are more ductile. HCP structures have less slip systems and are therefore less ductile. The applied loading can also be accommodated by dislocation nucleations. As the dislocation density

becomes higher, for example, due to the activation of Frank-Reed sources [10, 11], probability of dislocations encountering each other increases. Several interactions can occur: (1) annihilate or repel each other (strain hardening) if they lie on the same glide plane with opposite or same strain fields respectively, (2) pile up to form low and high-angle grain boundaries, causing grain refinement.

Both strain hardening and grain refinement lead increase the macroscopic strength, as dislocations require higher stress to overcome these obstacles. In particular, the Hall-Petch equation describes the grain refinement strengthening [12, 13], which correlates the grain size (d) to macroscopic yield stress (σ_{y}): $\sigma_{\mathrm{y}} = \sigma_0 + \mathrm{k}/\sqrt{\mathrm{d}}$. Here, σ_0 and k are the material constants, determined experimentally. These properties can be deliberately engineered into the material via severe plastic deformation, *e.g.* equal-channel angular pressing. They can also be the unintentional side effect from conventional processing such as forging and rolling.

Dislocation slip systems in HCP titanium are shown in Fig. 1.3. Slip occurs when the resolved shear stress (RSS) along the slip direction reaches a critical level - the critical resolved shear stress (CRSS). Pure (or commercially-pure) titanium has a c/a ratio of 1.587, which means the atoms are more closely packed along the $\langle \mathrm{a} \rangle$ directions, resulting in the least resistance to dislocation motion [2, 14]. No literature has shown any slip systems along the $\langle \mathrm{c} \rangle$ direction, only $\langle \mathrm{a} \rangle$ and $\langle \mathrm{c} + \mathrm{a} \rangle$ directions.



Slip Systems			
Slip Planes		Slip Directions	
{0001}	Basal	⟨11$\bar{2}$0⟩	⟨a⟩
{10$\bar{1}$0}	Prismatic	⟨11$\bar{2}$0⟩	⟨a⟩
{10$\bar{1}$1}	Pyramidal	⟨11$\bar{2}$0⟩	⟨a⟩
{10$\bar{1}$1}	Pyramidal	⟨11$\bar{2}$3⟩	⟨c+a⟩
{11$\bar{2}$2}	2nd-order Pyramidal	⟨11$\bar{2}$3⟩	⟨c+a⟩

Figure 1.3: Slip systems in HCP titanium. Prismatic slips are favoured due to the c/a ratio of titanium being lower than the ideal c/a of 1.633. Basal and pyramidal slips are less favoured but are still active.

1.3.2 Deformation twinning

To fulfil the von Mises yield criterion, a minimum of five independent deformation mechanisms must be available to accommodate plastic strain [15]. However, as HCP lattices are inherently asymmetric, the number of easily-activated slip systems is low and might not be sufficient to fulfil this criterion [16, 17]. Twinning then becomes an additional, and in some cases dominant, deformation mechanism [18]. When twinning occurs, a portion of the grain rapidly changes its orientation, forming a twinned region within the parent grain, as shown in Fig. 1.4. Twins usually nucleate from the grain boundaries, forming thin and needle-like structures. They propagate into the grain until they reach the opposite side of the grain boundary, forming "twin laths". The twin will then propagate laterally (perpendicular to the twin boundaries) and finally consume the entire grain, effectively changing the orientation of the grain. The twin boundaries also act as obstacles to dislocation slip, causing hardening in the grain.

Within titanium, six types of twins have been identified. They can be cate-

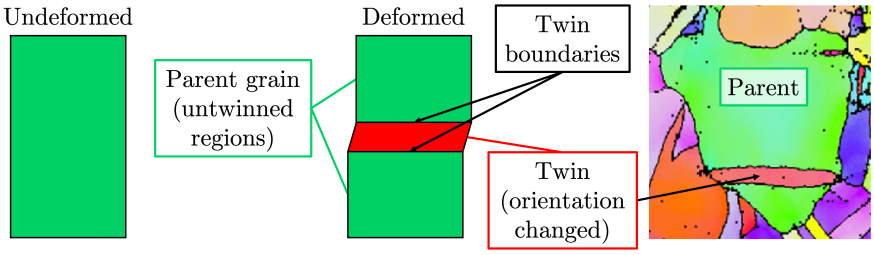


Figure 1.4: Schematic illustrating the process of deformation twinning.

gorised into two groups: extension twins (ET's), and contraction twins (CT's), which lengthen and shorten the grain along the c-axis respectively [15, 19–27]. Twinning activities are greatly influenced by intrinsic (*e.g.* grain orientation [28–31] and grain size [16, 32]) as well as extrinsic (*e.g.* strain-rate [29, 33] and temperature [34, 35]) factors.

Table 1.1: Extension (ET's) and contraction (CT's) twin systems in α-Ti [24].

ET's	**CT's**
$\{10\bar{1}2\}\ \langle 10\bar{1}1\rangle$	$\{11\bar{2}2\}\ \langle 11\bar{2}\bar{3}\rangle$
$\{11\bar{2}1\}\ \langle 11\bar{2}\bar{6}\rangle$	$\{10\bar{1}1\}\ \langle 10\bar{1}\bar{2}\rangle$
$\{11\bar{2}\bar{3}\}\ \langle 11\bar{2}\bar{2}\rangle$	$\{11\bar{2}\bar{4}\}\ \langle 22\bar{4}\bar{3}\rangle$

Both slip and twinning can result in changes in grain orientation. In polycrystals, a drastic change in the global orientation distribution of grains is regarded as a change in "texture", which refers to the generally-favoured grain orientation - *i.e.* a "strong" texture means that most of the grains have the same/similar orientation, and a "weak" texture refers to random grain orientations within the polycrystal. The change in texture can be an accidental/unintended consequence of manufacturing processes, with the shape change (*e.g.* forging a fan blade) being the primary goal. As the specific strength of titanium is tied to its grain orientation and the slip/twin systems available, the texture changes could be beneficial or detrimental depending on the applications.

The following section will discuss the previous attempts from past researchers on the effect of processing on the microstructural characteristics and macroscopic mechanical behaviour of titanium.

1.4 Mechanical processing of titanium

As aforementioned, titanium is strongly anisotropic and its microstructure can be heavily affected by external applied loadings. Consequently, past researchers have investigated the effect of different processing routes on the microstructure and mechanical properties of titanium.

Forging is the most common shaping method as it is versatile and cost effective [36–39]. Jackson *et al.* studied the effect of initial microstructure on the bulk mechanical behaviour of Ti-10V-2Fe-3Al under hot forging with different strain-rates [36]. They found that the flow behaviour of this alloy strongly depends on the initial microstructure, Widmanstätten or globular, of the α phase. They also suggested that the interaction between the two phases, specifically the β phases penetrating the α platelets, had a strong effect on the softening of the alloy. However, they could not explain how different strain-rates caused a different level of softening or hardening.

Ansarian *et al.* later investigated the microstructure evolution of pure titanium through multi-directional forging [40]. They reduced the grain size of the as-received titanium from 64 µm to about 1 µm to 1.2 µm at room temperature and 220 °C re-

spectively. They showed that increasing the number of forging passes greatly increases the sample's tensile and shear strength: the samples with 6 passes of forging at room temperature showed an increase of tensile strength by a factor of 2 and shear strength by a factor of 1.5. While confirming the Hall-Petch yield relationship, their results did not explain in-depth the microscopic deformation mechanisms during the tests, nor how high-rate behaviour would be affected. As forging includes a large range of varying strain level, strain-rate and temperature, it is difficult to predict the actual stress-state of the material, which leads to inconclusive results in the effects of general forging on the mechanical behaviour and microstructure changes.

Another common processing technique is rolling. Material in plate form is drawn through a set of rollers to reduce overall thickness. The material is subjected to a complex stress state of compression along the thickness/normal direction (ND), and tension along the rolling (RD) and transverse directions (TD). Nasiri-Abarbekog *et al.* studied the effect of rolling on the mechanical properties of pure titanium [41]. They rolled pure titanium to different levels, from 25% to 85% reduction in plate thickness, with all samples having the same initial split-basal texture. All samples showed grain elongation and texture changes after the rolling process. They suggested that at the lower level of reduction (less than 50%) the main deformation mode was dislocation slip due to grain orientation, however, twinning was also identified and resulted in randomising the texture. At a higher level of thickness reduction, only dislocation slip occurred and no twinning was detected. Their mechanical testing results showed that increasing the rolling reduction led to an increase

in both tensile and ultimate strength in the rolling and transverse directions.

Won *et al.* conducted a similar study on the anisotropy of rolled pure titanium [42]. They subjected the sample to a total reduction of 80% with multi-step uni-directional rolling at 400 °C and annealed at 700 °C for 1 hour. The rolled sample showed strong yielding anisotropy, with ND having the highest yield strength of 237 MPa, followed by TD of 164 MPa and RD of 126 MPa. They correlated the grain orientation to the Schmid Factor (SF), which is a parameter related to the direction of external loading and the orientation of a slip system:

$$\mathrm{SF} = \cos(\phi)\cos(\theta) \tag{1.1}$$

where ϕ is the angle between the direction of applied stress and the slip plane normal, and θ is the angle between the direction of applied stress and the slip direction. Fig. 1.5 indicates the angles ϕ and θ used in calculating SF. As their rolled titanium also showed a split basal texture on the ND, the yield strength along ND was much higher than TD and RD as the grains were oriented less favourably for easily-activated prismatic slips. Recently Zhou *et al.* studied the high strain-rate tensile behaviour of rolled Ti-6Al-4V alloy [43]. Their results only confirmed the anisotropy nature of titanium and were not well-explained regarding its microstructure.

Sahoo *et al.* later studied the microstructure evolution of pure titanium during different methods of rolling, including uni-directional rolling, multistep cross-rolling and reverse-rolling, with 50% to 90% thickness reduction at 600 °C [44]. In contrast to the previous studies, their rolled samples showed a strong basal texture, which

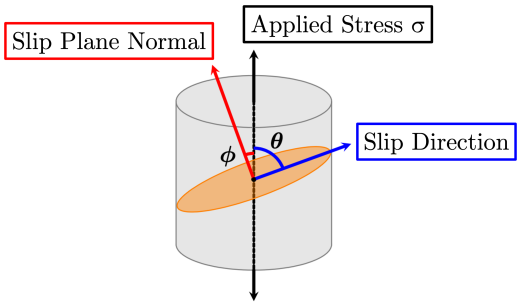


Figure 1.5: The Schmid Factor of a slip system.

they attributed to the thermal activation of basal ⟨a⟩ slip system during deformation. They also found twinning to be active in all uni-directional rolled samples, which contradicts results from Nasiri-Abarbekog *et al.* Both contraction and extension twinning were active due to simultaneous compression and tensile loading during the rolling process. Twinning was the most prominent in the multistep cross-rolled in the early rolling stages (lower reduction percentage), but twin boundary fraction dropped rapidly once the rolling reduction reached 80% and 90%. It is possible that some of the twinned region became grains, essentially reducing grain sizes. However, there was no mechanical testing on the rolled samples, and no conclusion was drawn between the texture and microstructure of rolled samples and their mechanical properties, either low or high-rate.

Li *et al.* investigated the effect of temperature and rolling direction on a type of near-α alloy Ti60 [45]. They studied both uni- and cross-directional rolling within the $\alpha + \beta$ and β temperature ranges, and the quasistatic mechanical properties of the RD and TD of the rolled samples. While both β-rolled samples exhibit weaker texture and similar strength, the $\alpha + \beta$-rolled samples showed drastically stronger texture and different strength. The $\alpha + \beta$ uni-directional rolled had the basal plane

of the grains orientated towards the TD and therefore stronger effect of anisotropy – TD showed much higher yield strength than RD. The $\alpha + \beta$ cross-rolled sample had a strong basal texture in the ND and therefore similar properties on both TD and RD. Their study however, only focused on the quasistatic properties; high-rate behaviour and corresponding deformation mechanisms were not investigated.

Properly characterising material behaviour is challenging as processing routes often subject the material to multi-axial loadings and complex stress states. This results in an unpredictable microstructure as the different types of loading (compression, tension and shear) activate different types of deformation mechanisms. Currently, the most common method for predicting material behaviour is by phenomenological models such as the Johnson-Cook model [46]. These models describe the stress-strain behaviour, the strain-rate effect and temperature dependency by optimising parameters of specific mathematical formula.

Zakaria and Wu studied the stress-strain responses of different titanium alloys, including Ti-6Al-4V and Ti550, from strain-rates of $\dot{\varepsilon} = 0.1\,\mathrm{s}^{-1}$ to $10^3\,\mathrm{s}^{-1}$ [47]. They found that the yield strength increased with the deformation strain-rates, and there were signs of shear band formation and adiabatic heating associated with high strain-rate deformation of these two alloys. Zhang *et al.* studied the stress-strain behaviour of the Ti-0.7Al-4V, Ti-1Al-4V and Ti-3Al-2.5V alloys from quasistatic ($8.5\times10^{-4}\,\mathrm{s}^{-1}$) to strain-rate of order $10^3\,\mathrm{s}^{-1}$ [48]. Similar to Zakaria and Wu's study, the yield stress of these titanium alloys also increased with strain-rate, and high strain-rate deforma-

tion experienced less plastic strain before failure and formed adiabatic shear bands. They then assessed the two phenomenological models, the Johnson-Cook and the Khan-Huang-Liang models, for their abilities to describe the dynamic response of these alloys. Although they concluded that the Khan-Huang-Liang model described the experimental results with better accuracy than Johnson-Cook model, it is most likely due to the form of the equation in Khan-Huang-Liang being a closer fit to the stress-strain curves from their experimental data.

Later, Zhang *et al.* studied the tensile behaviour of a near-α alloy Ti-3Al-12.5V at quasistatic ($10^{-3}\,s^{-1}$) to high (above $10^{3}\,s^{-1}$) strain-rates and evaluated the suitability of a combined Johnson-Cook and Khan-Huang-Liang (CJK) model for describing the dynamic stress-strain behaviour of this alloy [49]. This new model showed resonably good agreement with the experimental results. However, similar to the previous studies, it lacked the correlation between the microscopic deformation mechanisms and the macroscopic stress-strain behaviour, which limits its applicability to other loading cases or alloys based on this finding.

These models are not ideal as they only describe the stress-strain behaviour of a specific microstructure (*e.g.* texture, grain size, defect/phase properties etc.) along a specific direction. Changes to the microstructure will result in changes to the stress-strain behaviour, which then require additional experiments to re-parametrise the models. Therefore, they are not suitable for capturing the changes throughout a multi-stage deformation process, from manufacturing to high strain-rate scenarios.

In order to understand the fundamentals of the deformation mechanisms interactions and their interactions with the microstructure, investigations must be simplified to address a specific mechanism or interaction. Therefore, researchers have studied the effect of isolated types of loading, such as uniaxial compression, carefully applied in a controlled laboratory environment to probe the macroscopic mechanical behaviour and microstructural response.

1.5 Micro-mechanical studies of titanium

As dislocation slip and twinning are the most common deformation mechanisms in titanium, many researchers have studied these individual microscopic mechanisms to characterise their activation criteria, such as the critical resolved shear stress (CRSS) for slips, and twinning nucleation, growth and interaction. This section summarises the key findings from previous attempts to quantify these properties.

1.5.1 Deformation slip characterisation

The CRSS's of the slip systems can be quantified through experimental techniques such as micropillar compression and single crystal deformation, as well as computational simulations such as crystal plasticity modelling to fit experimental data by adjusting the CRSS values [2, 50, 51].

Akhtar studied macroscopic tension and compression on single crystals of titanium and zirconium (another HCP metal) [52, 53]. Loading was applied in such a way to activate a specific slip system for investigation. However, there are two

main drawbacks of such techniques. First, single crystals are usually very soft and must be handled carefully to avoid premature deformation. Second, single crystals of alloys with high impurity contents are difficult to produce even in a laboratory environment [2].

An alternative approach is to perform small-scale tests (*e.g.* nano-indentation) on small-length samples machined from a large sample. Kishida *et al.* investigated the CRSS of 1$^{\text{st}}$-order pyramidal $\langle \text{c} + \text{a} \rangle$ slip of pure titanium by applying compression on micro pillars [50]. These micropillars were milled from a large polycrystal sample using focused ion beam milling. Dimiduk *et al.* investigated the size effect of micropillars and found that smaller pillars could withstand greater applied stress before showing slip [54]. Greer *et al.* found that these micropillars also had an extrinsic size dependency, which refers to the size of the bulk material from which the micropillars were milled from [55]. Dimiduk *et al.* and Greer *et al.* confirmed that the plastic flow behaviour of micropillars is stochastic in nature, leading to difficulty in extracting the true CRSS values [54, 55].

Britton *et al.* performed nano-indentation on polycrystal α-Ti and studied the surface flow field and lattice curvature of the sample. They also adjusted the CRSS values in their crystal plasticity finite element analysis to mathematically model the experimental results [56]. This was further studied by Zambaldi *et al.* who measured and modelled deformation around conical indents [57]. However, they did not consider the size effects [54], which could have led to inaccuracy in their CRSS

calculations. The addition of alloying elements or impurities, such as oxygen and aluminium, has shown to greatly affect the CRSS values. Aluminium increases the c/a ratio in titanium close to the ideal HCP c/a ration of 1.63, which results in the basal slip becoming more favourable [3]. Sakai and Fine, and Williams *et al.* conducted similar studies on the effect of increasing aluminium content in titanium on the CRSS of basal and prismatic slips [58–60].

It is difficult to extract the exact CRSS values experimentally, and there is a lack of high strain-rate micropillar compression/nano-indentation testing. There is also no good agreement of the ranking of the slip systems. While it is understood that prismatic $\langle a \rangle$ is the slip system with the lowest CRSS value (hence easiest to be activated) in titanium, there are arguments about whether basal $\langle a \rangle$ or pyramidal $\langle c + a \rangle$ has the highest CRSS. Zambaldi *et al.*, Wroński *et al.* and Gong *et al.* stated that the order from lowest to highest CRSS is: prismatic $\langle a \rangle$, basal $\langle a \rangle$ and pyramidal $\langle c + a \rangle$ [31, 57, 61]. However, Wu *et al.* [62] used their Taylor-type crystal plasticity model to determine that basal $\langle a \rangle$ has the highest CRSS. Their results were subsequently adopted by Qin *et al.* [63], validating the parameters with experimental results.

1.5.2 Twinning characterisation

The other commonly observed deformation mechanism in titanium is twinning, due to the limited number of slip systems available in HCP. Compared to deformation slip, the experimental techniques required for observing twins are much simpler. A

bulk sample can be compressed with universal testing machines, and the twins can be observed post-mortem under an optical microscope.

Twins form when slip systems alone are insufficient to accommodate the global plastic strain. As the strain increases, the volume fraction of twin also increases. Salem *et al.* studied twin formation in commercially-pure titanium with an initial fibre texture (majority of the grains have the c-axis 20° to 35° from applied stress) and found that as commercially pure titanium experiences uniaxial quasistatic compression to a strain level of 10% or more, there is a noticeable volume fraction of twins, and it increases with increasing strain [14]. Chun *et al.* also studied the twin formation of titanium during room temperature compression [64]. They applied rolling from 10% to 40% strain and found that $\{11\bar{2}2\}\langle 11\bar{2}\bar{3}\rangle$ contraction twin (CT) and $\{10\bar{1}2\}\langle 10\bar{1}\bar{1}\rangle$ extension twin (ET) to be the dominant twin variants. Later, Zeng *et al.* and Tirry *et al.* also studied the twin formation in titanium and had the same findings that these two twin variants are the most common at room temperature [65, 66]. More recently, Meng *et al.* studied the microstructure evolution of commercially pure titanium deformed by rotary swaging, which is an industrial grain refinement process [67]. The samples had an average grain size of 10.7 µm and were deformed to a true strain of 0.40 to 2.00. They found that the same types of twin variants were present in the deformed samples.

The nucleation of deformation twins is also strongly related to the grain size. In general, larger grains twin more easily than smaller (nano-scale) grains [68–70].

Ghaderi and Barnett investigated the twin volume fraction in cold-rolled and extruded commercially-pure titanium with different grain sizes under the same tensile loading [68]. They found that the twin volume fraction increases with grain size, but in larger grains, twins do not extend to the grain boundaries. This is likely due to the steeper stress gradient from grain boundaries in larger grains. Zherebtsov *et al.* further investigated the grain size effect from an average grain size of 1 µm to 30 µm under unidirectional multi-pass rolling [69]. However, the twin volume fraction only increased from samples with grain size 1 µm to 15 µm and did not further increase beyond this grain size. Both studies did not consider the type of twins found in the test samples. To more accurately predict the formation of a specific type of twin, Stanford *et al.* studied titanium under compression with the orientation favourable for the activation of $\{10\bar{1}2\}$ ET [70]. This enabled them to identify if other types of twins were activated in samples with different grain size. They found that all samples with grain sizes from 17 µm to 85 µm showed $\{10\bar{1}2\}$ twins, while in larger grains, $\{11\bar{2}2\}$ ET and $\{11\bar{2}1\}$ ET were also observed. As $\{11\bar{2}1\}$ twins are not commonly observed, it was concluded that this type of twin is associated with larger grain sizes. This satisfied the Hall-Petch equation, which equates larger grain sizes to lower yield strength. The extra twin type was activated in the larger grain to accommodate a higher degree of plastic deformation.

Other methods were used to predict twin formation and interactions, in particular the secondary (twins formed within a twinned region) and sequential twin (other types of primary twins that form after the first type) formation. The most

straightforward method is the Schmid Law [8], which gives each twin type a Schmid factor (SF), similar to slip systems. The type with the lowest SF is expected to be activated first. Ye *et al.* studied the twin variant selection using SF [71]. They found that in general the SF method could predict the formation of $\{10\bar{1}2\}$ ET but not the $\{11\bar{2}2\}$ CT. Qin and Jonas used a different method based on the deformation gradient tensor (DGT) to predict the secondary and tertiary twins formed within titanium [72]. The DGT method was originally developed by Jonas *et al.*, and computes the twin variant selection based on the orientation of neighbouring grains and the strain tensor required to accommodate the twin [73]. The detailed outline of the DGT method can be found in [74]. They found that only twins that require prismatic or basal slip in neighbouring grains were formed, and those that require pyramidal slip could not form due to the high CRSS of pyramidal slip system. Tertiary twins did not follow the Schmid Law as only high SF tertiary twins were observed. Later, Huang *et al.* studied the twin variants during sequential twinning in titanium and found that SF prediction was very accurate for predicting twin formation at each stage of deformation (compression-tension-compression or vice versa) [27], in contradiction to Qin and Jonas'findings. Xu *et al.* used both SF and DGT methods to try to determine the twin sequential formation [75]. They analysed the sequential formation of $\{10\bar{1}2\}$ ET in another primary twin, and concluded that both SF and DGT methods were only good for predicting twin variants in specific scenarios, and neither of them worked particularly well.

Recently, Wroński *et al.* conducted a comprehensive study on twinning forma-

tion with changing strain path of commercially pure titanium [31]. They applied two stages of quasistatic compression loading in different directions of the samples, and used their crystal plasticity model to simulate the microstructure changes and macroscopic stress-strain behaviour. In their model, a Morte-Carlo approach [76] was employed to predict twin formation. Unlike SF and DGT methods which are deterministic, Morte-Carlo is a stochastic approach that uses probability to predict which twin type would form. While this is not physically-based, it showed good agreement their own experimental results, in both the twin formation prediction and macroscopic stress-strain behaviour.

Deformation twinning is also favoured under high strain-rate deformation. Tirry *et al.* studied twinning in pure titanium at $\dot{\varepsilon} = 500\,\mathrm{s}^{-1}$ [66]. They found the formation of $\{10\bar{1}2\}$ ET and $\{11\bar{2}2\}$ CT, similar to the the twins formed in quasistatic tests. Xu *et al.* studied twin formation in small grain (10 µm) pure titanium compressed to 5% to 80% engineering strain at $\dot{\varepsilon} = 400\,\mathrm{s}^{-1}$ to $600\,\mathrm{s}^{-1}$. On top of the usual $\{10\bar{1}2\}$ ET and $\{11\bar{2}2\}$ CT, they identified the activation of $\{11\bar{2}1\}$ ET and $\{11\bar{2}\bar{4}\}$ CT, although the frequency is very low at only 0.5%. This is possibly due to the small grain size, which inhibited the formation of twins [28].

Zhou *et al.* studied the twin formation of large grained (600 µm) pure titanium under high-rate compression ($\dot{\varepsilon} = 2600\,\mathrm{s}^{-1}$), and observed some non-Schmid behaviour [24]. They also reported the formation of $\{11\bar{2}1\}$ ET and $\{11\bar{2}\bar{4}\}$ CT at a much higher frequency. It suggests that the much larger grains led to formation of

more twins, however, their findings could not be explained by either SF or DGT method. Unlike the twin types and variants formed in quasistatic testing, the twins formed under high strain-rate deformation are unpredictable. This uncertainty leads to unpredictable high-rate macroscopic mechanical behaviour.

The twinning mechanism of near-α and $\alpha + \beta$ titanium alloys can be different from that of pure titanium, due to the change in c/a ratio in the α phase and the presence of more than one phase. Lainé *et al.* studied the deformation of Ti-6Al-4V alloy under very high strain-rate using Taylor impact tests. They had two different types of samples, one with small grains (12 µm) and the other one with much larger grains (2 mm) [77]. In both samples, there was only evidence of $\{10\bar{1}2\}$ and $\{11\bar{2}1\}$ twins formed, and no other types were found. It is possible that the secondary-α and the small volume of β had a role in strain accommodation.

1.6 Summary

In the field of engineering, one of the goals of material modelling is to accurately predict their behaviour under external loading. Since titanium is microstructure dependent, developing microstructure-aware models is crucial to predict its bulk mechanical behaviour. Pre-straining induces microscopic defects, including dislocations and twinning, which further complicate the bulk behaviour. While there were investigations on the effect of pre-straining on quasistatic/low strain-rate deformation, their effect on high strain-rate behaviour remains unclear. The existing literature on high-rate focuses on either the mechanics with very little microstructure

awareness, or the microscopic mechanisms of pristine (strain-free) specimens. This presents a great opportunity to study the effect of pre-existing defects on the high strain-rate behaviour, combining mechanical testing and microstructure evolution.

1.7 Objectives

From the literature review above, it is clear that there is a lack of research on high strain-rate behaviour of pre-strained titanium. As titanium alloys (*e.g.* Ti-6Al-4V) contain additional elements, they incur additional complexities such as heat treatment effect and phase distributions. This thesis therefore focuses on the behaviour of **commercially-pure titanium**. The primary objectives of this thesis are the following:

1. Characterising pre-strained microstructures to obtain statistical features which represent the bulk material,

2. Performing interrupted testing to study the microstructure evolutions of different pre-strained titanium,

3. Identifying key features that affect bulk mechanical properties and their strain-rate dependency,

4. Correlating microstructure features and bulk mechanical properties using statistical analyses, and

5. Exploring novel data augmentation techniques to enhance development of modelling frameworks.

1.8 Thesis overview

Chapter 2 details the relevant experimental methodology, including mechanical testing and microscopy. The theoretical aspects and the practical considerations using the in-house equipment at Oxford are discussed in detail.

Chapter 3 contains the first experimental campaign, which is exploratory in nature to determine subsequent experiment design. Chapter 4 consists of further experimentations, novel statistical analysis of microstructure evolutions, as well as features extractions using advanced statistical and machine learning modelling. Chapter 5 assess the suitability of using generative machine learning on data augmentation for materials design. Details of the work are explained in each chapter.

Chapter 6 is the concluding summary of the three bodies of work, outlining the key contributions in scientific discovery. Future works are discussed, from short-term experimental investigations to long-term strategies in more efficient materials discovery and design.

Chapter 2

Experimental Methodology

This chapter covers the experimental methodology employed to generate novel experimental data in Chapters 3 and 4. Here, the background and detailed descriptions of material mechanical testing and microscopy for material characterisation are included. Specifications of experimental procedures in each campaign will be explored in their chapters respectively.

2.1 General Workflow

Data generation in this thesis followed the general workflow in Fig. 2.1. **Commercially-pure titanium grade 2** was used throughout this thesis due to its relatively simple microstructure and supplier availability. In commercial-grade pure titanium, the α-phase is strengthening by oxygen, which does not promote phase stabilisation nor does it for intermetallic phases. First, the "as-received" material (from supplier) was machined to suitable sizes and subjected to a controlled pre-straining to generate microscopic defects. The pre-strained specimens were then deformed in the mechanical testing step to generate the bulk mechanical behaviour (stress-strain curves). Specimens at each stage were subjected to microstructure analysis to determine the

correlations between microscopic defects and bulk stress-strain behaviour.

The following sections will discuss these steps in detail, including the theoretical principles and practical implementations using the facilities available at the University.

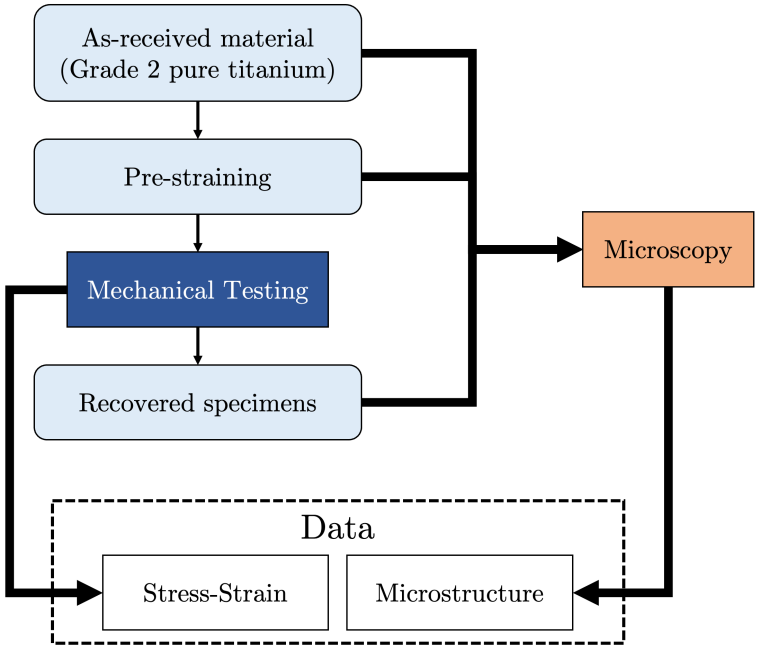


Figure 2.1: The general experimental workflow, including pre-straining to generate defects, mechanical testing of pre-strained specimens and microscopy.

2.2 Quasistatic testing

Static, or quasistatic, deformation is defined as, at any given time, the sum of forces acting on any given region of the deformed body is (or close to) zero, or in other words, it is in static equilibrium [78]. To simulate this deformation, loading is typically applied using a universal testing machine (UTM), which composes of a screw- or hydraulic-driven crosshead to apply the deformation, a load cell to measure

the force response and a data acquisition system (Fig. 2.2). The raw outputs from the system are typically time step (t), crosshead displacement and force (F), which can then be converted to engineering stress ($\sigma_{\text{eng.}} = \text{F}/\text{A}_0$), engineering strain ($\varepsilon_{\text{eng.}} = \Delta\text{L}/\text{L}_0$) and engineering strain-rate ($\dot{\varepsilon}_{\text{eng.}} = \text{d}\varepsilon_{\text{eng.}}/\text{dt}$). Here, A_0 is the initial cross-section area of the specimen, L_0 is the initial length and ΔL is the change in length.

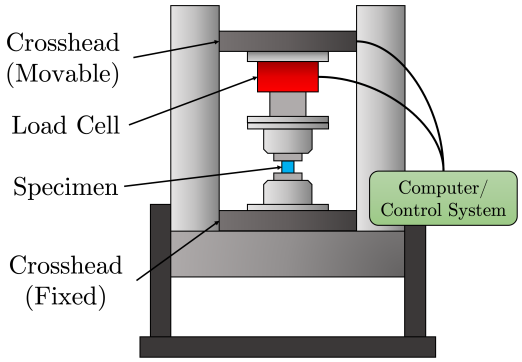


Figure 2.2: Schematic of a typical universal testing machine (UMT).

In many cases, the true stress and strain (σ_{true}, $\varepsilon_{\text{true}}$) are preferred as they provide a more accurate representation of the material behaviour as they account for change in cross-section area in the specimens [8]. These values are typically computed from digital image correlation (DIC) data. As it was not implemented in this study due to practical limitations, the alternative approach is to analytically converting the engineering stress and strain [8]:

$$\sigma_{\text{true}} = \frac{\text{F}}{\text{A}} = \sigma_{\text{eng.}} \left(1 + \varepsilon_{\text{eng.}}\right), \tag{2.1}$$

$$\varepsilon_{\text{true}} = \ln\left(\frac{\text{L}}{\text{L}_0}\right) = \ln\left(1 + \varepsilon_{\text{eng.}}\right), \tag{2.2}$$

where A and L are the instantaneous cross-section area and length respectively.

Note that for compressive strain, the value of $\varepsilon_{\text{eng.}}$ should be negative.

Since UTM's are not perfectly rigid, small amounts of elastic deformation in the machine will affect the readings. Compliance testing, which involves compressing the anvils without specimens, is conducted. The displacement from real test is then corrected at each force interval, as shown in Fig. 2.3. The compliance-corrected data are used to compute $\sigma_{\text{eng.}}$ and $\varepsilon_{\text{eng.}}$.

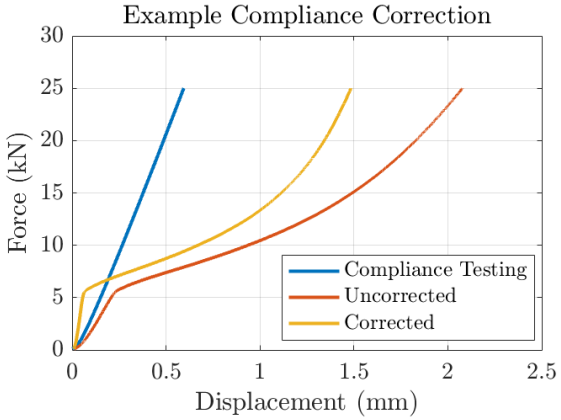


Figure 2.3: An example of the compliance testing, specimen testing uncorrected and corrected for machine compliance.

2.3 High-rate testing

High-rate testing at $10^3\,\text{s}^{-1}$ is conducted using split-Hopkinson pressure bars [79, 80]. When an external force is applied to a body, the body deforms (strains) and experiences an internal stress. It is theoretically considered a dynamic event regardless of the rate of force applied [78]. This is because the internal stress of the region at which force is first applied, is not instantaneously transmitted to the rest of the body. This can be considered a wave propagation problem, in which the stressed

region moves towards the opposite end of the body. The speed of wave propagation varies depending on the material, and is commonly known as “speed of sound” or the “elastic wave speed” - when the internal stress does not exceed the material's yield stress.

2.3.1 Deformation under dynamic loading

When the loading rate is relatively low, such as during a quasistatic test, the effect of wave propagation is relatively insignificant. At each stage of deformation, due to the speed of elastic wave propagation, both the specimen and load cell will reach internal stress equilibrium. Therefore, a calibrated load cell can represent the material stress state.

As the loading rate increases, wave propagation should be carefully considered. In many cases, commercially-available load cells cannot obtain accurate readings. Their compact design cannot accommodate the long stress wave from the specimen. When the material is deforming at a high strain-rate, its internal stress is no longer static within any small time step. The stress wave generated by the material specimen is continuously and rapidly changing. These compact commercial load cells will result in the stress wave reflecting back upon reaching an interface. This reflected wave will then interact with the ongoing incident wave, disturbing the stress state of the load cell and causing erroneous readings. Therefore, a longer load cell is required to ensure wave separation. This led to the development of the split-Hopkinson pressure bars [80].

2.4 Split-Hopkinson pressure bars (SHPB)

The Hopkinson pressure bar was first developed to measure the material response under high-rate loading [79]. It was improved by Davies [81] with more advanced measurement techniques. Kolsky [80] further improved the design by using two elastic pressure bars, with a specimen sandwiched in between, to measure the dynamic stress-strain behaviour of the specimen. This design is later known as the "split-Hopkinson pressure bars" (SHPB), which became widely adopted by researchers.

Since only compressive experiments are conducted in this thesis, the following sections will first discuss the theoretical principles of the compressive SHPB. Followed by the practical considerations of using the in-house systems in the Impact and Shock Mechanics Laboratory at Oxford.

2.4.1 Theoretical principles

A modern compressive SHPB consists of three round bars: the striker bar, the input (or incident) bar and the output (or transmitted) bar, with a specimen sandwiched between the input and output bars. An incident stress wave is generated by launching the striker bar against the input bar using a gas gun powered by compressed air. A schematic of a simple compression SHPB is shown in Fig. 2.4. The bars should be sufficiently long to ensure wave separation, and significantly harder and stronger than the test specimens so that they remain elastic throughout. Both input and output bars are usually made of the same material and cross-section area

to simplify assumptions. The bars should also be straight and coaxially aligned to ensure uniform one-dimensional wave propagation throughout.

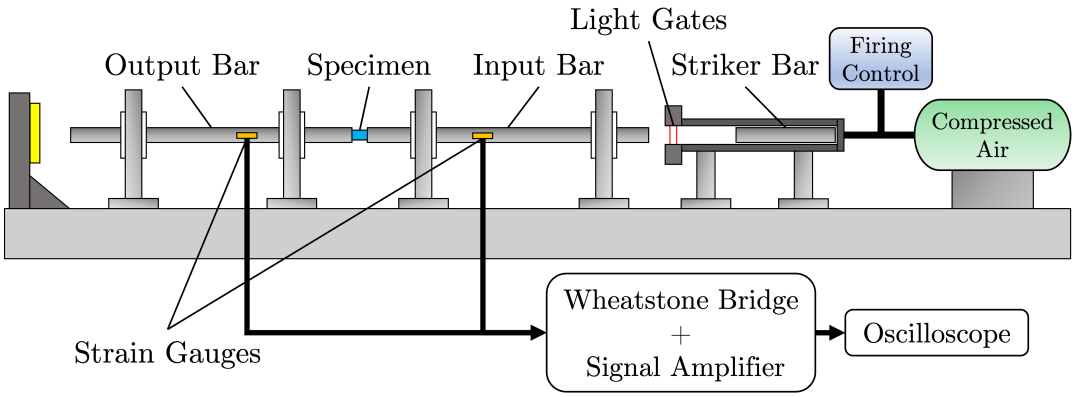


Figure 2.4: Basic components of a simple compression SHPB system.

When the striker bar impacts the input bar, two compressive stress waves are generated: one in the input bar propagating in the same direction as the initial impact, one propagating in the striker bar propagating in the opposite direction, as shown in Fig. 2.5. As the compressive wave in the striker bar reaches the free end, it reflects as a tensile wave. At the same time, the compressive wave front continues to travel along the input bar. At the instance the tensile wave reaches the impact end of the striker bar, the striker bar becomes stress-free. Simultaneously, the stress at the impact end of the input bar reduces to zero, terminating any further compressive wave within the input bar. The length of this stress wave can be identified as twice the length of the striker bar (assuming it is shorter). Using striker bars of different lengths and varying the impact velocities, different amplitude and duration of stress waves can be achieved.

When the incident compressive wave (σ_{i}) in the input bar reaches the specimen,

the impedance difference causes a portion of the wave to be transmitted and the rest reflected. The reflected wave (σ_r) is tensile and the transmitted wave (σ_t) remains compressive. Assuming tensile stress is positive and compression is negative, the stresses at the input-specimen and output-specimen interfaces at time t can be expressed $-\sigma_i(t) + \sigma_r(t)$ and $-\sigma_t(t)$ respectively. Using these three stress waves and information about bar materials and diameters, one can derive the stress-strain relationship of the specimen [78, 82].

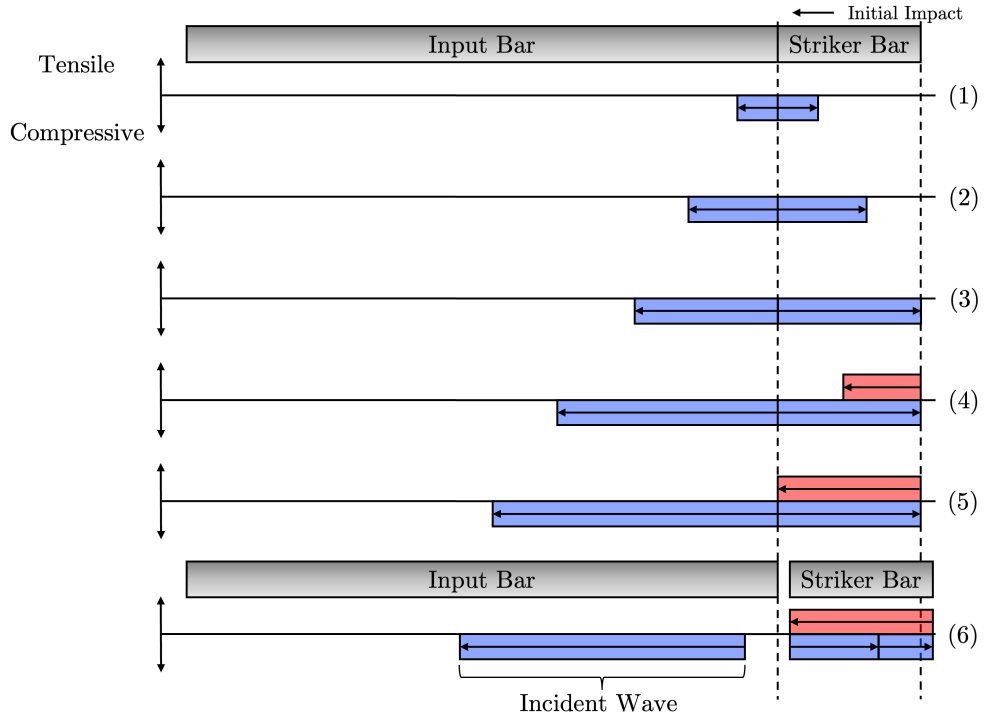


Figure 2.5: Stress wave propagation in the striker and input bars upon impact.

From the D'Alembert wave propagation [83] (Eq. 2.3) ,

$$\frac{\partial^2 u}{\partial t^2} = C_0^2 \frac{\partial^2 u}{\partial x^2}, \tag{2.3}$$

where $u = u(x, t)$ is the displacement at position x along a body and time t, and C_0

is the longitudinal wave speed of the material. The displacement in the input bar u_1 can be expressed as a function:

$$u_1(x,t) = F(x - C_0 t) + G(x + C_0 t) = u_i(x,t) + u_r(x,t), \tag{2.4}$$

$$u_2(x,t) = H(x - C_0 t) = u_t(x,t), \tag{2.5}$$

where F, G and H are non-harmonic functions that describe the wave shapes, u_i, u_r and u_t are the displacements caused by the stress waves. The 1-dimensional strains, ε_i, ε_r and ε_t, caused by the stress waves can be obtained by differentiating the displacements (Eq. 2.6) with respect to the position x.

$$\varepsilon = \frac{\partial u}{\partial x}, \tag{2.6}$$

substituting $A = (x - C_0 t)$ and $B = (x + C_0 t)$, and using chain-rule to differentiate:

$$\varepsilon_i = \frac{\partial u_i}{\partial x} = \frac{\partial F}{\partial A}\frac{\partial A}{\partial x} = \frac{\partial F}{\partial A}\frac{\partial (x - C_0 t)}{\partial x} = \frac{\partial F}{\partial A}, \tag{2.7}$$

$$\varepsilon_r = \frac{\partial u_r}{\partial x} = \frac{\partial G}{\partial B}\frac{\partial B}{\partial x} = \frac{\partial G}{\partial B}\frac{\partial (x + C_0 t)}{\partial x} = \frac{\partial G}{\partial B}, \tag{2.8}$$

$$\varepsilon_t = \frac{\partial u_t}{\partial x} = \frac{\partial H}{\partial A}\frac{\partial A}{\partial x} = \frac{\partial H}{\partial A}\frac{\partial (x - C_0 t)}{\partial x} = \frac{\partial H}{\partial A}. \tag{2.9}$$

The particle velocities can be obtained by differentiating the displacements with

respect to time t, and using Eqs. 2.7, 2.8 and 2.9:

$$\dot{u}_i = \frac{\partial u_i}{\partial t} = \frac{\partial F}{\partial A}\frac{\partial A}{\partial t} = \frac{\partial F}{\partial A}\frac{\partial (x - C_0 t)}{\partial t} = \frac{\partial F}{\partial A}(-C_0) = -C_0 \varepsilon_i, \tag{2.10}$$

$$\dot{u}_r = \frac{\partial u_r}{\partial t} = \frac{\partial G}{\partial B}\frac{\partial B}{\partial t} = \frac{\partial G}{\partial B}\frac{\partial (x + C_0 t)}{\partial t} = \frac{\partial G}{\partial B}(C_0) = C_0 \varepsilon_r, \tag{2.11}$$

$$\dot{u}_t = \frac{\partial u_t}{\partial t} = \frac{\partial H}{\partial A}\frac{\partial A}{\partial t} = \frac{\partial H}{\partial A}\frac{\partial (x - C_0 t)}{\partial t} = \frac{\partial H}{\partial A}(-C_0) = -C_0 \varepsilon_t. \tag{2.12}$$

Therefore, the particle velocities of the bar-specimen interfaces, shown in Fig. 2.6, are expressed as:

$$\dot{u}_1 = \dot{u}_i + \dot{u}_r = C_0(-\varepsilon_i + \varepsilon_r), \tag{2.13}$$

$$\dot{u}_2 = \dot{u}_t = -C_0 \varepsilon_t, \tag{2.14}$$

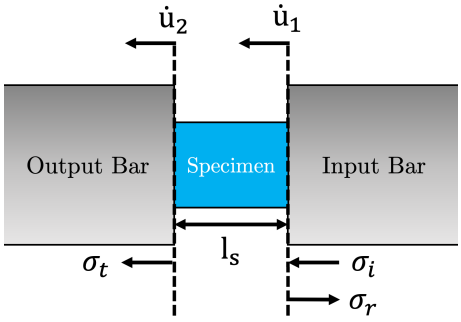


Figure 2.6: Bar velocities and stress waves at the specimen interface, adopted from [82], where $\dot{u}_1$ and $\dot{u}_2$ are the input and output bar end velocities, l_s is the initial specimen length, σ_i, σ_r and σ_t are the incident, reflected and transmitted waves.

The bar-end velocities depend on measurements of strains caused by the stress waves. Clear separation of the waves, incident, reflected and transmitted, can be obtained by mounting strain gauges at appropriate locations of the bar surfaces. To derive the displacements at the bar ends, u_1 and u_2, one can integrate the velocity-time functions numerically by calculating the areas under the curves. The strain

$\varepsilon_{\text{eng.}}$ and strain-rate $\dot{\varepsilon_{\text{eng.}}}$ of the specimen can be computed as follows:

$$\varepsilon_{\text{eng.}} = \frac{u_1 - u_2}{l_s}, \tag{2.15}$$

$$\dot{\varepsilon}_{\text{eng.}} = \frac{\dot{u}_1 - \dot{u}_2}{l_s}, \tag{2.16}$$

Assuming stress equilibrium within the specimen, $\sigma_{\text{eng.}}$ is simply expressed as:

$$\sigma_{\text{eng.}} = \frac{F_{\text{bar}}}{A_{\text{specimen}}}, \text{where} \tag{2.17}$$

$$F_{\text{bar}} = \sigma_{\text{bar}} A_{\text{bar}} = (E_{\text{bar}} \varepsilon_{\text{bar}}) A_{\text{bar}}. \tag{2.18}$$

The above equations for engineering strain, strain-rate and stress are all computed against time. Given the common time axis, the engineering stress-strain can be computed.

2.4.2 Practical considerations

Given a coaxial impact of the striker and input bars, the expected shape of the longitudinal incident wave is rectangular - a sharp rise to the maximum stress amplitude for a duration of $2L_{\text{striker}}/C$ (where L_{striker} is the striker bar length and C is the elastic wave speed), and a rapid drop to zero stress. However, in practice, the strain gauges measure all the stress waves in the bar, rather than solely the rectangular longitudinal wave. Each of these waves have their own amplitudes and frequencies, and they disperse as they travel along the bar. The wave dispersion effect causes the stress to not immediately rise to a steady level but instead ramp up and oscillate before settling down, as shown in Fig. 2.7.

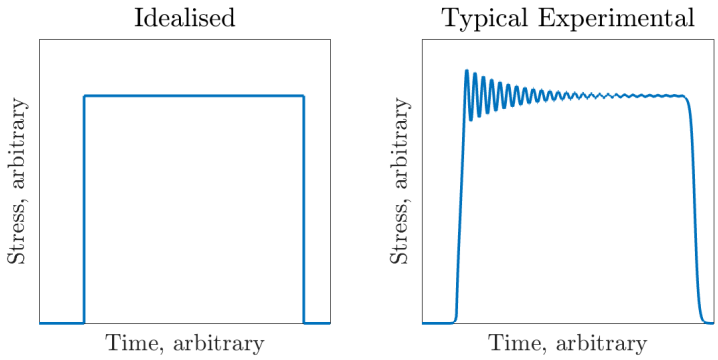


Figure 2.7: The idealised stress wave at the centre of the rod and typical experimental stress wave measured on the rod surface. Note that both waves are artificially generated to represent the two cases. These are not experimental results.

There are several sources of these other waves, including the radial waves, Rayleigh surface waves and other vibrations from the experimental platform. As the compressive wave travels along the bar, the compressed region expands radially due to the Poisson's effect. Pochhammer [84] and Chree [85] have independently studied the wave dispersion effects on cylindrical solids and found that higher frequency waves travel faster than lower frequency waves. Therefore, the wave forms obtained at the gauge region are not identical to the wave forms at the bar ends (or any other regions of the bars). Gama *et al.* [86] described the detailed procedures for the dispersion correction on SHPB data.

Pulse shaping

The wave dispersion, in reality, is less significant with smaller diameter bars, or more precisely, when the longitudinal wavelength is much larger than the bar diameter. The high frequency waves can be minimised by using appropriate pulse shapers. In this study, a small piece of sacrificial material (*e.g.* copper or thin sheets of paper) was placed at the impact end of the input bar for each experiment.

Bar alignment

Bar alignment is one of the most important aspects of SHPB experiments. The striker, input and output bars must be straight and coaxially aligned to minimise bar bending. The bars used in this study were centreless-ground to ensure uniform straightness, and the bar ends were machined on a lathe to achieve flat surfaces. The input and output bars were mounted on adjustable supports, which were bolted onto a rigid and levelled frame. The gas gun was fixed to establish a datum for alignment. To ensure coaxial impact and movement of the bars, a laser beam was first aligned to the gas gun barrel. The laser alignment rig used in this study is shown in Figs. 2.8a and 2.8b. It consisted of a laser source and two mirrors, which were incrementally adjusted to create a coherent diffraction pattern at the muzzle end (Fig. 2.8c).

Each bar support were then be adjusted individually to align with the laser beam. Bushings (or axial bearings) were used to ensure the bar movement was as smooth as possible. It is worth noting that, over-supporting might restrict bar movement and introduce additional boundary conditions, while under-supporting might cause the bars to deflect downward (sag) and bend. A standard practice is to provide minimal support to the bars until they no longer deflect [82].

Strain measurement

Stress waves in a SHPB were measured with strain gauges, which were adhesively bonded to the bar surfaces. In this thesis, titanium alloy Ti-6Al-4V bars were used

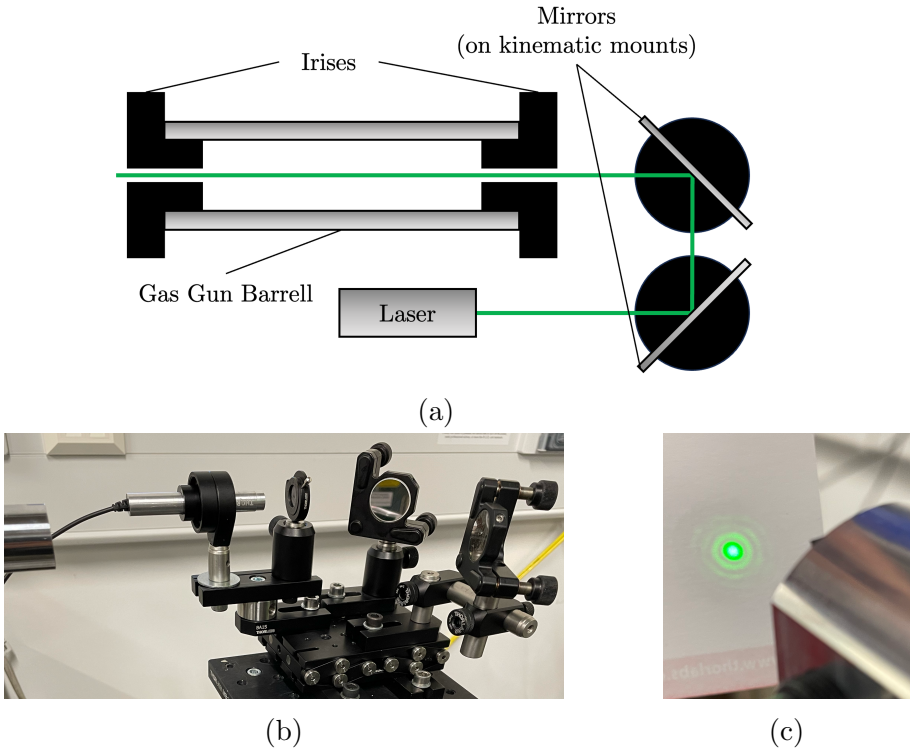


Figure 2.8: An example of laser alignment on the SHPB. (a) A schematic of the alignment components. (b) The actual setup used for the alignment, consisting of off-the-shelf optical components. (c) A laser coherent diffraction pattern at the far end (muzzle) of the barrel.

in the SHPB systems, with the Tokyo Measuring Laboratory FLA-2-8/FLAB-2-8 strain gauges. Prior to strain gauge bonding, the bar surfaces were first abraded with 320-grit silicon carbide sandpapers with phosphoric acid and subsequently neutralised (Micro-Measurement M-Prep Conditioner A and Neutralizer 5A). They were then cleaned with isopropanol alcohol. Gauges were then bonded carefully with cyanoacrylate adhesive. For each gauge region, four strain gauges are placed equidistantly around the bar at the same axial position. The gauges diametrically-opposite are connected in series so that any minor bending effects on the stress wave data is eliminated [82].

To obtain strain measurements, each set of gauges were then connected to a

Wheatstone Bridge in a half-bridge configuration [87]. The bridge was then connected to a signal amplifier, and the output was recorded by a high-speed oscilloscope. The strain ε measurement is expressed as:

$$\varepsilon = \frac{2\,\mathrm{V_{out}}}{\mathrm{N}\,\mathrm{V_{in}}\,\mathrm{GF}} \tag{2.19}$$

where $\mathrm{V_{out}}$ is the output voltage from the amplifier, N is the amplifier gain, $\mathrm{V_{in}}$ is the excitation voltage of the bridge and GF is the strain gauge factor. The forces in the bars can be computed using Eq. 2.18.

Interrupted testing on SHPB

There are currently no feasible methods for *in-situ* microstructure characterisation at high-rate. Interrupted testing is conducted to limit specimen deformation. The microstructures of the specimens are studied *post-mortem*.

While UTM's are easily interrupted by defining the termination criteria (*e.g.* stop at a certain force), interrupted SHPB testing requires additional considerations. Two methods were implemented: momentum trapping in Chapter 3 and stop rings for testing in Chapter 4. The former method was more sophisticated as it removes the stress wave from the incident bar, thus eliminating any subsequent loading. The latter method involved manufacturing rigid stop rings of various thicknesses, which were then placed around the specimen, acting as a hard stop to limit input bar travel. The thicknesses of stop rings were determined by the desired strain levels of interrupted testing. It was far easier to implement as it does not require

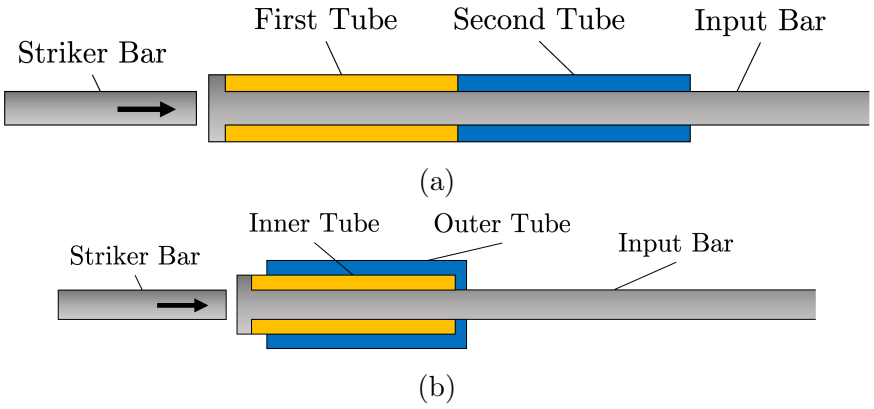


Figure 2.9: The tandem momentum trap design from Prot and Cloete [88]: (a) the conceptual design consisting to two tubes, (b) the actual design with the second tube being wrapped around the inner tube.

careful designing, but secondary impact should still occur.

The momentum trap implemented in Chapter 3 was originally adopted from Prot and Cloete [88]. Their conceptual design consisted of a flanged bar and two tubes, initially in contact with the input bar (Fig. 2.9a). When the striker bar impacts the flanged input bar, two stress waves are generated, one in the input bar as usual, another in the first tube. The bar wave would propagate as usual and reflect at the specimen end. The first tube would transfer its wave into the second tube, assuming matching impedances. Therefore, the first tube remains in contact with the flanged section of the input bar, while the second tube would become separated. When the reflected wave in the input bar reaches the impact end, as the first tube is in contact with the bar via the flange, this reflected wave would be transmitted entirely into the first tube. The stress wave in the input bar is now entirely transferred away, eliminating secondary loading.

As the tubes must be longer than the striker bar, if two tubes are in contact

in series, with the gauges placed in an appropriate position, one would require an extremely long bar. Fig. 2.9b shows the actual design used in [88]. The second tube is redesigned to wrap around the first tube, with an internal flange so that it remains in contact with the first (inner) tube. While this acts as an additional interface for wave interactions, it is still effective at reducing secondary loading.

There are several limitations with this design, from the theoretical and practical points-of-view, which can affect one's decision in using this design:

1. The strain in the specimen is determined by the duration of the stress wave, which in turn is determined by the striker bar length. As the specimen properties are unknown, one could only estimate the length of striker bar required for a desired strain,

2. While in practice the stress wave could never be removed entirely, the components, namely the inner and outer tubes, must be machined to very high tolerance in order to maintain similar impedances. This means the design can only accommodate a specific setup/bar material and the striker bar length is limited. The design should maximise versatility,

3. As the outer tube is free to move due to the "trapped" stress wave, an additional stopper must be used to prevent it from crashing into the strain gauges bonded on the bar, and

4. As the striker bar impacts both the input bar and inner tube, to achieve the same strain-rate as a conventional SHPB setup, the impact velocity is

estimated approximately 1.5 times higher than with the conventional setup [88]. This means higher gas gun pressure is required, which leads to additional safety concerns.

Due to the above considerations and equipment availability at Oxford, the tandem momentum trap design was only used in Chapter 3, while the aforementioned stop ring approach was used in Chapter 4.

2.4.3 In-house SHPB systems at Oxford

Two different compression SHPB systems were used in this thesis due to equipment availability, with the schematics shown in Fig. 2.10. This section serves as a brief description of the two systems. Details about the data produced can be found in Chapters 3 and 4.

The first system used is shown in Fig. 2.10a, with 12.7 mm diameter Ti-6Al-4V bars used throughout. The input and output bars are 1.5 m and 1.1 m long respectively, and two striker bars of length 0.075 m and 0.3 m were used. Four strain gauges are mounted on each bar, with the gauge distances from the specimen end being 647.5 mm and 329.5 mm for the input and output bars respectively. The strain gauge signals were amplified by the Elsys ELSGA-2/B signal amplifier operating at 10 V, with the gain set to 100 for both sets of gauges. The tandem momentum trap mentioned above was used in this system as the strain-limiting device. Standard SHPB data analysis procedure was followed using this setup [82].

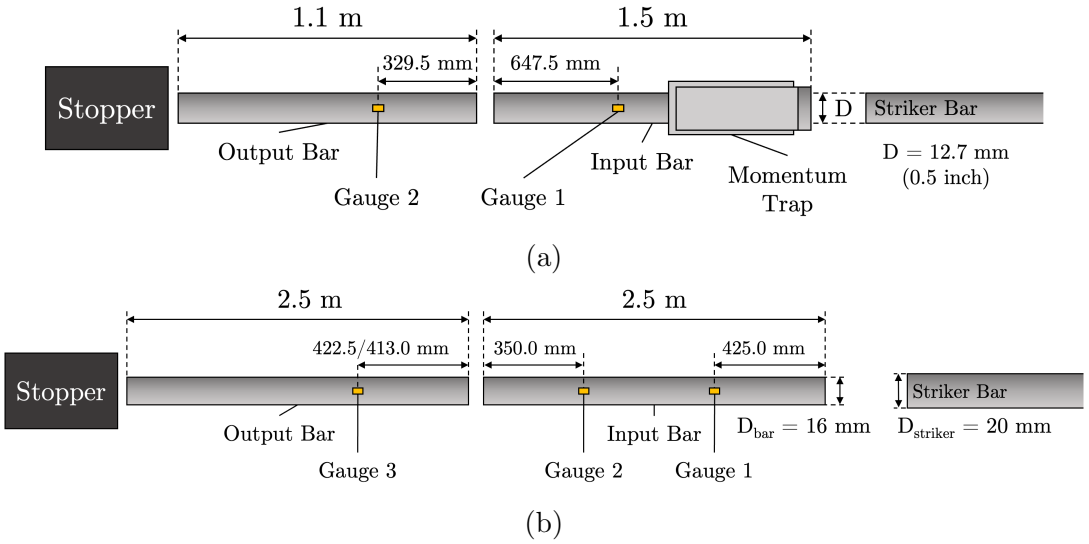


Figure 2.10: The two compression SHPB systems used in this thesis, all bars are made of Ti-6Al-4V: (a) the SHPB with a tandem momentum trap used in Chapter 3, with all bars being 12.7 mm in diameter, and (b) the long SHPB system used Chapter 4, with the input and output bars being 16 mm in diameter and the striker bar being 20 mm in diameter.

The second system (Fig. 2.10b) consists of 16 mm diameter input and output bars made of the same titanium alloy, and are both 2.5 m long. The striker bar is 20 mm in diameter and 2.7 m in length, which would cause the incident and reflected wave to overlap if one were to follow the standard analysis. Therefore, gauges are mounted on two separate regions on the input bar, and the data analysis procedure can be found in [89, 90]. The amplifier used was the Fylde FE-H379-TA, with an excitation voltage of 6 V, the gain on the input bar gauges set to 200, and the output bar gauges to 500. The long striker bar produces a very long stress wave, which is useful in a variety of setups and materials. Coupled with this novel data analysis which allows the use of relatively short input and output bars, making this design practical when laboratory space is limited.

Before discussing the microscopy techniques in the next section, it is worth not-

ing that for any *post-mortem* microscopy of interrupted testing, the microstructure characteristics are not affected by the elastic unloading.

2.5 Microscopy

Microscopy refers to a range of techniques to view objects at a resolution scale higher than what human eyes are capable of. The most common techniques include optical (light) and electron microscopy. While other techniques exist, such as X-ray and atom-force microscopy, they were not used and will therefore not be discussed in this thesis.

Optical microscopes are very common due to their ease of use and relatively inexpensive setup. However, it relies on reflection of visible light with a wavelength of 400 µm to 700 µm, which limits the image resolution [91]. From the wave-particle duality, particles can behave as waves. In particular, electrons can be accelerated to different voltage to obtain different wavelengths, hence higher image resolution. On the other hand, the negatively-charged electrons interact with atoms and produce additional effects. This further enhances the versatility of electron microscopy. The following sections will discuss the uses of electron microscopy to obtain the microstructure data.

2.5.1 Electron microscopy

There are two main types of electron microscopes, the scanning electron microscopes (SEM's) and transmission electron microscopes (TEM's), as shown in Fig.

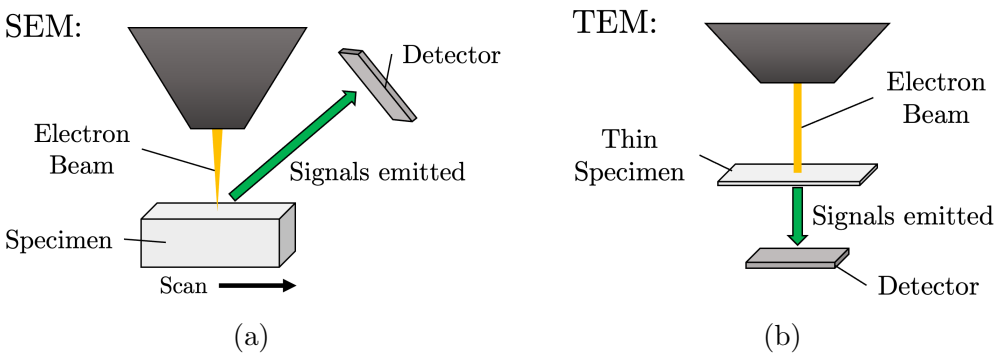


Figure 2.11: Two common electron microscope: (a) a scanning electron microscope (SEM), and (b) a transmission electron microscope (TEM).

2.11. Both of these consist of an electron source (or an electron "gun"), lenses to focus the electron beam, detectors for measuring electron-specimen interactions and a vacuum chamber. As electrons are highly-interactive with matters, which include air molecules, the system and the specimen are kept under vacuum to prevent contamination.

The TEM was the first type of electron microscopes. It uses very high energy of electron beams. This extremely high resolution enables direct imaging of dislocations and atomic arrangements. However, TEM requires a thin specimen that is electron-transparent, and the image size is small relative to a bulk specimen in mechanical testing. Obtaining a statistically-representative dataset will require enormous efforts and resources.

The SEM was later developed to image bulk specimens with reasonably-high resolution. An SEM focuses a low-energy electron beam to a point and sequentially scans across the specimen surface. Although it cannot replace TEM in terms of resolutions, the SEM can still obtain grain-level information across a much larger

area. It is therefore the most common technique in electron microscopy.

With an SEM, when the primary electron beam impacts the specimen surface, several interactions will occur. First, secondary electrons (electrons originated from the specimen) scatter, which are used in the standard imaging mode. Second, characteristic X-rays are emitted, which are used for elemental analysis. Third, primary electrons are backscattered. They carry additional information about lattice orientations based on the diffraction patterns. This is known as the electron backscatter diffraction (EBSD).

2.5.2 Electron backscatter diffraction (EBSD)

When an electron beam impinges on the specimen, the electrons enter the specimen and scatter around in all directions within the "interaction volume", as shown in Fig. 2.12a. The depth of this volume depends on the electron energy/acceleration voltage. Typically, only the electrons at the first few nanometres from the surface can escape from the specimen and be measured by detectors.

The electrons can be backscattered either elastically (no/very little energy loss) or inelastically (with significant energy loss). A diffraction pattern is generated when the electrons are elastically scattered following the Bragg's condition, as shown in Fig. 2.12b. The Bragg's law is expressed as:

$$2\mathrm{d}\sin(\theta) = \mathrm{n}\lambda, \tag{2.20}$$

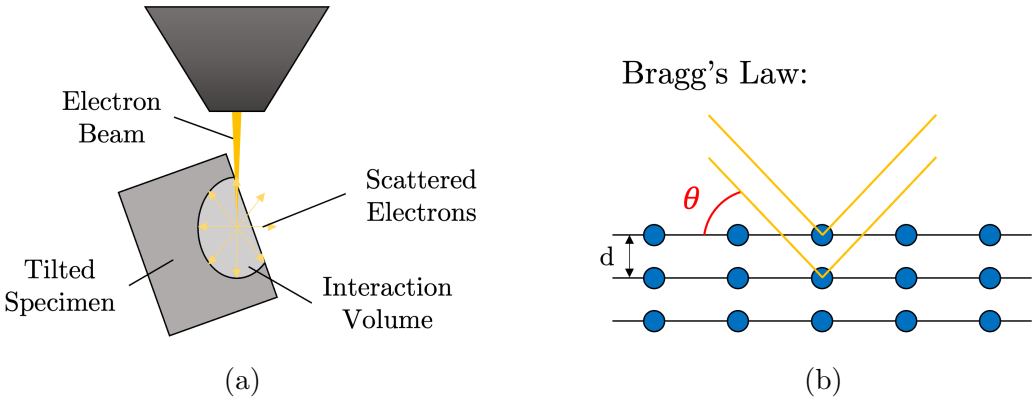


Figure 2.12: The phenomenon of electron scattering: (a) the incident electron beam enters the specimen, and electrons interact with the atoms near the surface. Some electrons backscatter and escape the surface, forming diffraction patterns. (b) Bragg's law that causes electron diffraction to be unique to the lattice structure and orientation.

where d is the interplanar spacing between atoms, θ is the angle between the incident electron beam and the specimen surface, n is the order of reflection and λ is the wavelength of the electron beam, which depends on the acceleration voltage.

This phenomenon was first observed by Nishikawa and Kikuchi, and became known as the Kikuchi pattern [92]. Several researchers later refined this technique for a wide range of materials [93–95]. Nowadays, the EBSD is a mature technique with high-speed detectors and automated data acquisition systems.

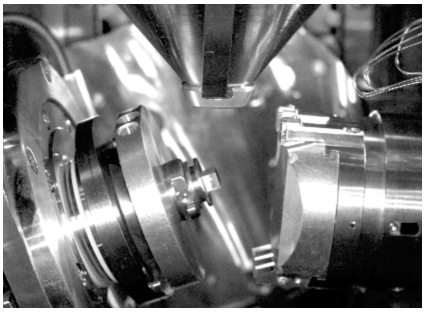
2.5.2.1 Modern EBSD setup

In a modern SEM/EBSD system, the specimen is typically tilted to 70° with respect to the electron beam, and the EBSD detector is placed close to the specimen. The Kikuchi patterns can be captured by the detector and analysed automatically. Given a known material, in this case pure titanium in α-phase, the pattern captured at each pixel point is compared with the material database to identify the lattice orientation. The Kikuchi patterns from the database are generated by simulations of

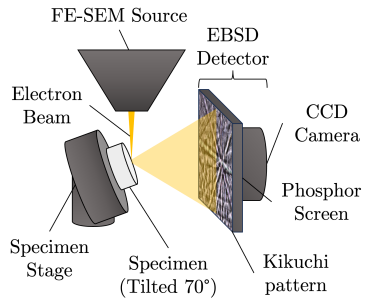
different lattice structures and parameters. As the SEM scans the specimen surface, an EBSD map is generated, showing the lattice orientations across the surface. In post analysis, pixels of similar orientations are then clustered together and defined as a grain. Features such as grain boundaries, grain size distributions, Schmid factor of slip systems can be computed. Subsequently, correlations between microstructures and bulk properties can be evaluated.

The EBSD data in this thesis was obtained from the David Cockayne Centre for Electron Microscopy (DCCEM), Department of Material Science, University of Oxford. The Zeiss Merlin field emission gun SEM equipped with the Bruker eFlash EBSD detector were used. In the EBSD detector, a phosphor screen turns electrons into visible light, and a low-light charge-coupled device (CCD) camera captures the pattern. A typical SEM setup is shown in Figs. 2.13a and 2.13b. The working distance was set to 18 mm, with the electron beam operating at an acceleration voltage of 15 keV to 20 keV and a probe current of 20 nA. The raw data (Fig. 2.13c) was processed by the Bruker eSprit 2.3 software and the post-processing was done using MATLAB MTEX 5.8.1 tool box [96].

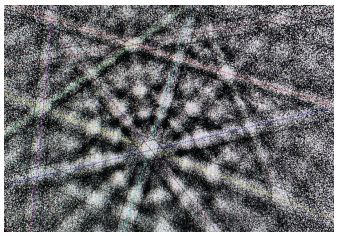
To ensure successful data acquisition using EBSD, the quality of Kikuchi patterns depends heavily on sample (specimen) preparation. Any uneven features on the surface, including small scratches and oxide layers, will prevent electrons from forming Kikuchi patterns. The surface flatness requirement for EBSD is therefore much more stringent than conventional microscopy. Different materials require dif-



(a)



(b)



(c)

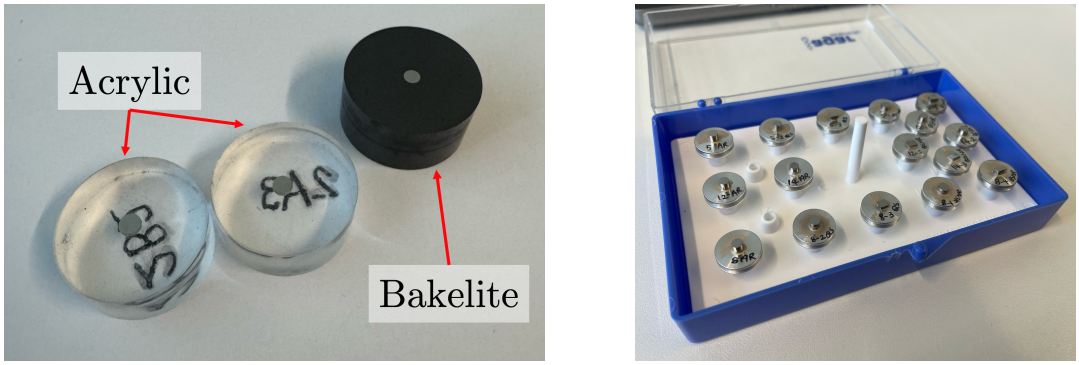
Figure 2.13: The EBSD setup in a SEM: (a) the real setup, (b) a schematic showcasing the components, and (c) an example of Kikuchi patterns.

ferent surface preparation methods. The following section will outline the method developed for obtaining EBSD data in this study.

2.5.2.2 Sample preparation

In this thesis, all specimens were hot-mounted in a 25 mm diameter cylindrical mould (see Fig. 2.14a), which fit the specimen holder in the mechanical grinding-polishing machine. Acrylic powder (Struers ClaroFast) was used as it can be dissolved in acetone, which allowed for easier unmounting after polishing, as shown in Fig. 2.14b.

To ensure consistency and repeatability of results, specimens were polished using the Struers Tegramin-25 grinding-polishing machine. The polishing steps could be generalised: (1) coarse grinding to flatten the surface, (2) fine grinding with diamond slurry to remove scratches, and (3) polishing to create microscopically-flat surfaces. The parameters on the machine, including rotational speed/direction of the specimen



(a) (b)

Figure 2.14: Example of SEM specimens: (a) specimens hot-mounted in acrylic (clear) and conductive Bakelite (black), and (b) unmounted specimens bonded to stubs after mechanical polishing.

holder and polishing pad, and the down force from the specimens, were programmed as follows:

Steps	**Grit/Compound**	**Holder/Disc (RPM)**	**Force (N)**	**Time**
1	500-/800-grit SiC	140/120	10	Until planar.
2	1200-grit SiC	140/120	5	20 secs
3	9 µm, MD-Largo	140/120	10	10 mins
4	3 µm, MD-Dac	140/120	10	10 mins
5	1 µm, MD-Nap	140/120	10	20 mins
6	Colloidal Silica/OP-U, MD-Chem	90/50	10	≥2 hrs

Note that the"SiC" refers to silicon carbide sandpapers, and the "MD-" refers Struers polishing pads. They were used with the Struers DiaDuo-2 diamond slurry of various grain sizes. Since titanium is corrosion resistant, water-based solutions

were used as lubricant without severe oxidation on the surface.

After each step of the grinding and polishing, the specimens were rinsed and ultra-sonically cleaned in a water bath with neutral detergent for a few minutes. The machine was also thoroughly cleaned to prevent contaminations. Before proceeding to the next step, the specimens were visually inspected to ensure the surfaces are uniform. The final step with colloidal silica would take a total of at least 2 hours. During this stage, the surface should gradually become scratch-free and grains should be revealed.

The specimens were unmounted to minimise contamination from polymer degassing under vacuum. The mounts were carefully cut away without damaging the specimens. They were then submerged in acetone to remove any residual acrylic. The polished surfaces of the specimens were carefully wiped with a clean cotton pad with isopropanol alcohol to remove contaminations. The cleaned specimens were then bonded to aluminium stubs (Fig. 2.14b) for the SEM specimen stage and the ion polisher.

Prior to the EBSD scans, the specimens were further polished using the Gatan PIPS II precision ion polishing system Model 695. The specimen was placed on a stage rotating at 6 RPM, the two ion beam guns were tilted to 8° from the specimen surface and operated at 8 keV, as shown in Fig. 2.15. The duration varied between 8 and 32 minutes. This removed the oxide layer and ensured surfaces were free from

mechanical deformation.

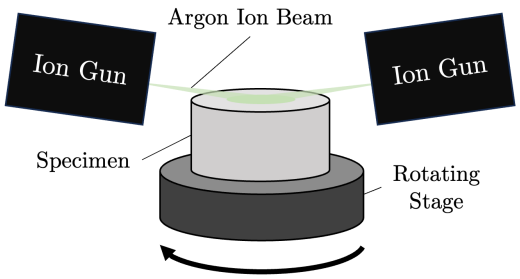


Figure 2.15: A schematic of the ion polisher: the specimen is placed on a rotating stage, with two ion guns mounted at an angle, emitting broad argon ion beams to polish the specimen surface.

To obtain high-quality Kikuchi patterns, the EBSD camera exposure time was adjusted for each specimen to increase the chances of successful pattern capturing and indexing. Large EBSD maps with reasonable resolution required a total scan time of approximately 2 to 4 hours with the Bruker eFlash system.

2.6 Conclusion on Experimental Methodology

Using the mechanical testing and microscopy mentioned in this chapter, this thesis includes two experimental campaigns conducted by the author. The first campaign focuses on the high strain-rate behaviour of pre-strained titanium, and the second one focuses on the strain-rate dependency and statistical analysis of the microstructure evolution. The author also explored the use of machine learning on data augmentation in Chapter 5 using the data obtained from the experiments.

Chapter 3

Effect of strain-path changes on the deformation mechanisms of pure titanium

This chapter covers the first experimental campaign on the two-stage compressive loading, first quasistatic then high-rate, on pure titanium. It explores the pre-straining effects from the quasistatic loading on subsequent high strain-rate behaviour of titanium, with a primary focus on the microstructure evolution throughout the deformation stages.

3.1 Primary objectives

This campaign aimed to investigate the effect of changing the strain-paths with high-rate loading. Here, a two-stage compressive loading was applied to pure titanium, with the first stage being a low-rate/quasistatic (QS) and the second stage being high-rate (HR). Fig. 3.1 shows the general work flow of this experimental campaign. To generate different strain-paths, deformations at the QS stage were interrupted

at different strain levels followed by HR compression, which were also interrupted at different strain levels. The intention of the first QS stage was to generate various levels of microscopic defects. The second interrupted HR testing aimed to study the microstructure evolutions. The primary objectives of this campaign were as follows:

- Conducting high-rate mechanical testing with different strain-paths,
- Analysing the microstructure evolutions and deformation mechanisms, and
- Identifying key microscopic features that lead to changes in bulk mechanical behaviour, specifically on the HR deformation.

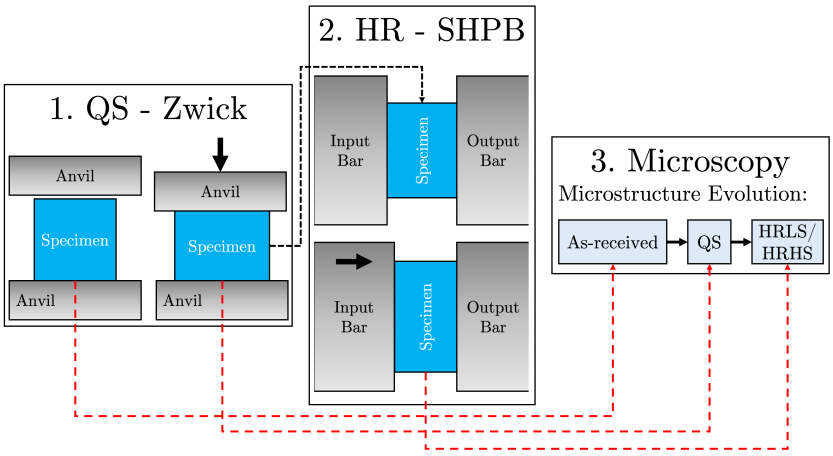


Figure 3.1: The work flow of the first experimental campaign.

3.2 Experimental procedures

3.2.1 Mechanical testing

To study the effect of strain-path changes with an initial QS followed by HR deformation, test specimens were uniaxially compressed to different strain levels at both

stages. The as-received material was a 8 mm diameter round bar of commercially-pure titanium (CP-Ti) grade 2 according to ASTM B348, with the chemical composition shown in Table 3.1. The test specimens were machined on a lathe to the required diameter and sectioned off to the required length through EDM (electrical discharging machining) to ensure good parallelism between both circular faces. The final specimens were 3 mm diameter by 3 mm length cylinders, consistent with the specimens used on similar testing [97]. At the initial QS stage, specimens were compressed to approximately 5%, 8% and 20% engineering strain (labelled as "5%", "8%" and "20%") at a strain-rate of $10^{-3}\,s^{-1}$. At the subsequent HR stage, they were compressed further to approximately 7% and 22% at a rate of $10^{3}\,s^{-1}$, referred to as high-rate low-strain (HRLS) and high-rate high-strain (HRHS) respectively. Under high rate of deformation, effects such as dislocation drag [78] and wave propagation/inertia [82] can drastically change the microscopic and macroscopic properties. This strain-rate sensitive behaviour is commonly observed in titanium [48, 97, 98].

The QS compression was applied on the Zwick-Roell 050 universal testing machine, equipped with a 30 kN load cell. The machine crosshead was programmed to move at a displacement rate of $0.003\,mm\,s^{-1}$. Lubricant was lightly applied to reduce the effect of friction, as to minimise non-uniform radial expansion of the specimens. Prior to the interrupted tests, full compression testing was conducted on the material to obtain the force values corresponding to the desired strain levels. They were 3.3 kN for 5% strain, 3.8 kN for 8% strain and 6 kN for 20% strain. The machine was programmed to terminate the loading at these forces to obtain the different strain

levels, as there was no reliable strain- or displacement-controlled method.

The split-Hopkinson pressure bars (SHPB) system described in Fig. 2.10a in Chapter 2.4.3 was used to apply the HR compression. Prior to the HR testing, the geometries of the QS-compressed specimens were kept unchanged, and the slight barrelling remained. It was impractical to re-machine these specimens due to the small specimen size. To achieve different strain-levels, different lengths of striker bars were used at the HRLS and HRHS stages. The strain gauge signals were recorded by either the Tektronix DPO 4054 or the LeCroy WaveMaster 808Zi-A oscilloscope, at a sampling rate of $\geq$100 million points per second on each channel. Single-use copper pulse shapers were used to reduce the high-frequency components of the incident waves.

An example of the strain gauge signals from the SHPB is shown in Fig. 3.2. The standard 1-wave analysis method was applied throughout this study [82], as the 3-wave analysis shows substantial oscillations from the Pochhammer-Chree effect due to wave dispersion (Fig. 3.3). This is due to the different phases of waves (*e.g.* bending and radial waves) overlapping with the longitudinal wave at the gauge region, leading to difficulty in interpreting the yield and early-stage flow stresses with the 3-wave analysis. The forces at the specimen-bar interfaces are shown in Fig. 3.4. The input bar side shows a slightly higher force than the output bar side, which is likely due to part of the kinetic energy converted into heat energy (adiabatic heating) during deformation and inertial effects from specimen-bar interfaces [82].

No temperature measurements were obtained to verify the differences due to equipment limitations, but could be investigated in the future. To ensure consistency in data interpretation, the output bar forces were used to obtain the engineering stress throughout.

Table 3.1: Chemical composition in weight percentage (Wt. %) of the commercially-pure titanium (grade 2) used in Chapter 3, with oxygen being the primary strengthening element.

Element	**Fe**	**C**	**N**	**O**	**H**	**Other**	**Ti**
Wt. %	0.032	0.017	0.010	0.138	0.00095	≤ 0.4	Balance

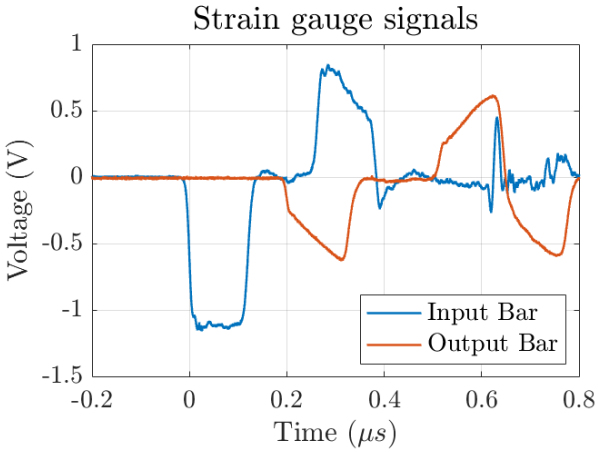


Figure 3.2: An example of the strain gauge signals from the input and output bars with the momentum trapping device.

3.2.2 Microstructure characterisation

The EBSD maps were approximately $(1.117 \times 0.838)\,\mathrm{mm}^2$, with step sizes of approximately 1.995 µm for the as-received material, 1.117 µm for QS specimens and 0.931 µm for HR-recovered specimens, to reveal fine microscopic features. The difference in step sizes was related to the expected features from the specimens. Typically, the as-received material is supplied in the annealed condition, with low internal resid-

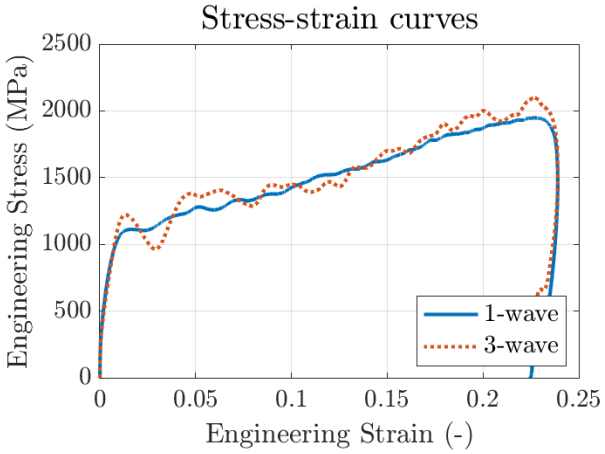


Figure 3.3: Both the 1- and 3-wave analyses are showing similar engineering stress-strain responses. The different phases of waves in the 3-wave analysis overlapped with the longitudinal wave, causing oscillations around the stress-strain behaviour. Therefore, the 1-wave analysis was applied as it produces a cleaner result.

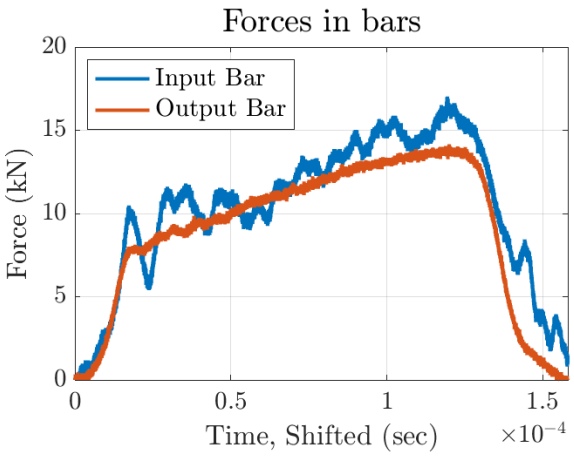


Figure 3.4: The forces at the specimen-bar interface at the input and output bar ends show slight differences, possibly due to adiabatic heating and inertial effects of the specimen.

ual strain and relatively large grain sizes, in the range of tens of µm. A larger step size provides sufficient resolution of the grain structures while significantly reducing the total scan time. While small twins might be omitted, nano-scale twins are commonly observed at cryogenic temperature as opposed to room temperature [34, 99]. As deformation increases, deformation mechanisms (slip and twin) were activated, increasing the severity of sub-grain rotation and reducing grain sizes. Higher resolu-

tion EBSD maps were required to capture these finer features. The Kikuchi patterns were acquired at a relatively low resolutions of 320 × 240 pixels as no analyses were conducted directly on the images of the patterns (*e.g.* lattice strain approximation). This lower resolution allowed high pattern acquisition rate and faster processing by the software to determine the grain orientation at each pixel.

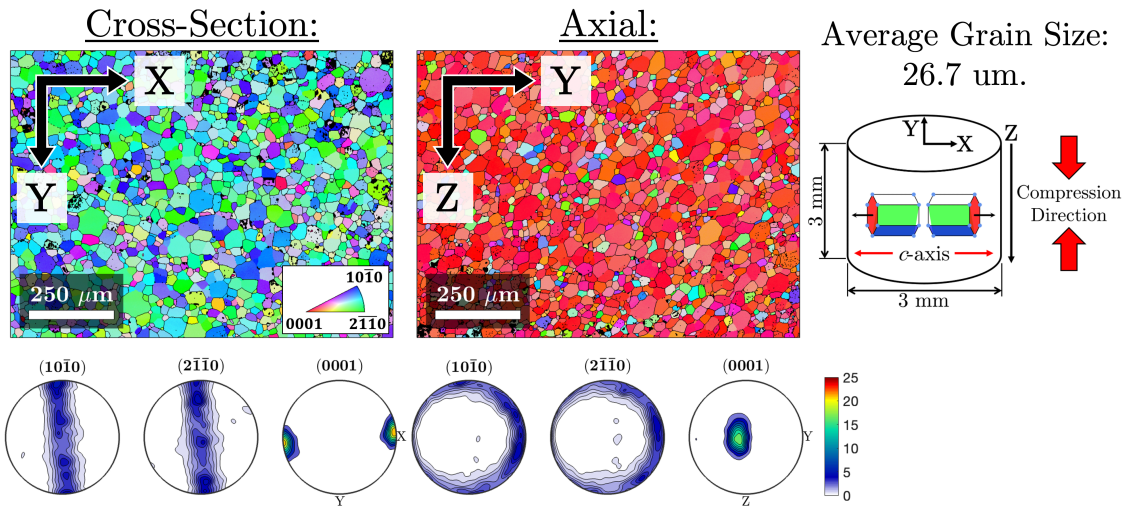


Figure 3.5: As-received CP-Ti Grade 2 used in this study. The cross-section EBSD map is obtained from the plane normal to the Z-direction (loading direction) of the cylinder.

3.3 Results

3.3.1 Mechanical behaviour

Fig. 3.6 shows the engineering stress-strain curves at each stage of loading, from the first quasistatic (QS), to the second stage of high-rate to two different strain levels, termed the high-rate low strain (HRLS, dotted lines), and high-rate high strain (HRHS, solid lines). Table 3.2 shows the length of the recovered specimens at each stage of loading, measured with a caliper after the testing. The average strain-

rate achieved in this experimental campaign is $1807\,s^{-1}$, with a standard deviation of approximately $68\,s^{-1}$ (less than 5% difference). The curves were shifted so that they begin at their respective pre-strained levels. Strain-hardening can be clearly observed as increasing strain at the QS stage led to increased plastic flow stresses at the secondary HR stage. The stress-strain curves at HR show an overlapping when the total strain is low, but at the later stage they all show hardening that deviate from the trend - a linear projection of the flow stress from the specimen without the initial QS compression.

The effect of radial inertia has been investigated following the equation derived by Gorham [100]. However, it was found that the stress difference is negligible, therefore, the correction is not applied to the results. Note that anisotropy was observed from the specimens: the radial expansion along the Y-axis was noticeably more than the X-axis. This is expected as the as-received material shows a strong texture along the X-axis, as shown in 3.5. To quantify this effect, one would need to conduct uniaxial testing along these directions. Due to the small diameter (8 mm) of the rod, it was not possible (within reasonable spending of resources) to conduct these testing.

3.3.2 Microstructure evolution

The EBSD maps, pole figures (texture) and grain boundary misorientation (MO) distributions are shown in Figs. 3.7 and 3.8. The sample plane coordinates are roughly aligned with the ones shown in Fig. 3.5. The high-angle grain boundaries

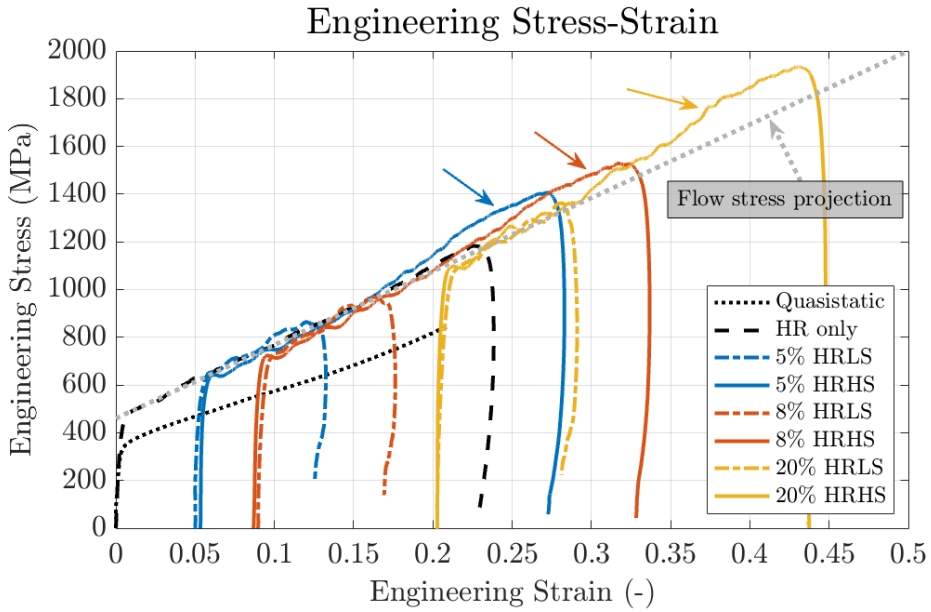


Figure 3.6: Engineering stress-strain curves at the quasistatic stage and the subsequent high strain-rate loading. The high-rate curves are shifted to their respective QS-strained levels. HRLS and HRHS refer to high-rate low strain and high-rate high strain respectively. The arrows indicate deviations in late-stage hardening from the flow stress projection.

Table 3.2: The original length (OL) and engineering strain-rates under high-rate loading of the recovered specimens.

Specimens	OL	Quasistatic		High-rate		Eng. strain-rate
	mm	mm	%	mm	%	s^{-1}
As-received	3.00	-	-	2.35	21.667%	1749
5% QS only	3.00	2.83	5.667%	-	-	-
5% HRLS	3.00	2.85	5.000%	2.64	7.000%	1776
5% HRHS	3.00	2.84	5.333%	2.16	22.667%	1704
8% QS only	3.01	2.74	8.970%	-	-	-
8% HRLS	3.01	2.74	8.970%	2.53	6.977%	1847
8% HRHS	3.00	2.74	8.667%	2.06	22.667%	1851
20% QS only	3.01	2.40	20.266%	-	-	-
20% HRLS	3.01	2.40	20.266%	2.18	7.309%	1901
20% HRHS	3.01	2.40	20.266%	1.69	23.588%	1823

(HAGB's) were defined as boundaries with MO greater than 15°, and low-angle grain boundaries (LAGB's) or sub-grain boundaries were below 15° and above 2°, which is the typical angular resolution of the Hough-based EBSD analysis employed

here [101]. It is also worth noting that the successful indexing rate in the EBSD scans reduces with increasing strain, indicated by the black pixels. This could be related to either poor sample preparation or increase in lattice strain, causing difficulty in identifying Kikuchi bands [28, 102]. This could potentially be remedied by reducing step sizes (increasing resolution) or increasing exposure time. However, they would exponentially increase the total scan time.

To quantify the deformation mechanisms involved, further analyses were performed. The dislocation densities were estimated by the geometrically-necessary dislocation (GND) density, using the method proposed by Pantleon [103], implemented in MATLAB MTEX (version 5.8.1). Traditionally, dislocation densities are measured from transmission electron microscopy (TEM) images. However, one image could only represent a small area and a large number of images would be required to estimate the global dislocation density. Here, it was deemed acceptable to estimate the GND density from the EBSD data, as it gives a good approximation of dislocation density within the context of this study. It is should be noted that GND density approximation typical requires a very high resolution EBSD map (step sizes of approximately 200 nm to 300 nm [56, 104]), therefore the values obtained for this study should be considered comparative and not absolute.

The other common mechanisms within titanium is deformation twinning. Table 3.4 shows the possible twinning systems in titanium [22]. The twinning activities can be identified by the peaks in the grain boundary MO distributions, as twin bound-

aries always follow a specific relationship, depending on the twinning system. Upon nucleation, the twinned regions typically have a thin lathe-like shape that extend from the boundary of the parent grain. As the dataset acquired for this study is very large, to compute the twin volume and boundary fractions, the random forest classifier from the Python package *SciKit-Learn* was employed [105]. The classifier was trained using a smaller dataset of manually-selected twin-parent pairs with features including grain orientations, shapes and MO angles. The classifier was then applied to the entire EBSD maps to identify twins, subsequently the twin volume and boundary fractions were computed. Both dislocation pile-up and twin nucleation lead to Hall-Petch strengthening as new grain/twin boundaries are formed [12, 13]. The grain size was calculated as the equivalent diameter (by assuming a circle with the same area as the grain). The average GND densities, LAGB densities, twinning volume and boundary fractions computed from the data obtained in this study are shown in Table 3.3.

3.4 Discussions

3.4.1 Quasistatic deformation

Prior to applying loading, Fig. 3.8 (a) shows that the as-received material (at the initial state) shows a fairly uniform equiaxed structure with no twinning observed. At the QS stage, uniaxial compression was applied along the Z-direction, normal to the prismatic-pyramidal plane of the grains. The specimens show very little changes

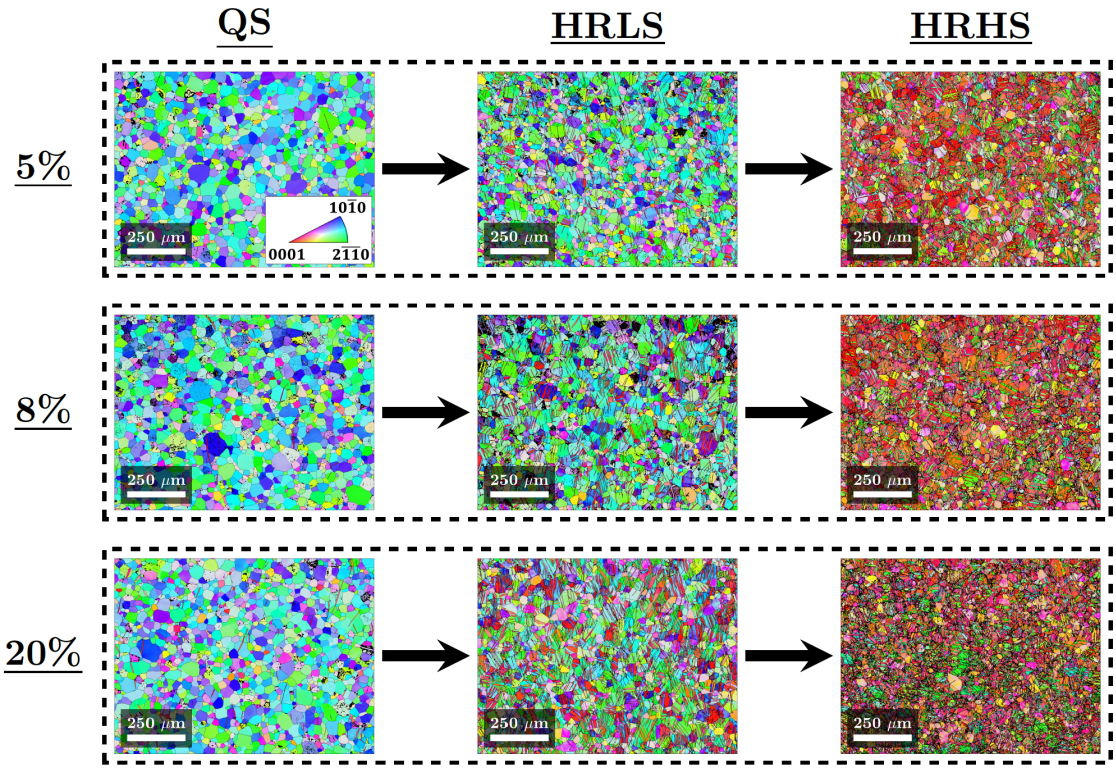


Figure 3.7: EBSD maps of the recovered specimens at different loading stages. The scanned regions were $(1.117 \times 0.838)\,\mathrm{mm}^2$ at the centre of the cross-section planes, with step sizes of approximately 1.117 µm for QS and 0.931 µm for HRLS and HRHS.

Table 3.3: Evolution of low-angle grain boundary density (μ_{LAGB}), average GND density (μ_{GND}), twin volume and twin boundary fractions (TV and TB frac.), and average grain size in equivalent diameter of the specimens.

Specimens	μ_{LAGB}	μ_{GND}	TV frac.	TB frac.	Grain size
	$1/\mu\mathrm{m}$	$1/\mathrm{m}^2$	-	-	µm
As-received	10.9589	4.68×10^{13}	0	0	26.7
5% QS only	13.3687	4.88×10^{13}	0.0033	0.0099	25.2
5% HRLS	244.5398	9.62×10^{13}	0.0764	0.4207	11.4
5% HRHS	2831.7802	1.86×10^{14}	0.5230	0.5482	8.0
8% QS only	21.7611	4.94×10^{13}	0.0079	0.0529	24.0
8% HRLS	251.0342	8.90×10^{13}	0.1401	0.5650	10.9
8% HRHS	2546.8504	1.86×10^{14}	0.5731	0.5514	8.1
20% QS only	22.0075	5.45×10^{13}	0.0109	0.0897	21.5
20% HRLS	831.9604	1.26×10^{14}	0.2531	0.6463	9.6
20% HRHS	6427.2128	2.29×10^{14}	0.3782	0.4446	7.4

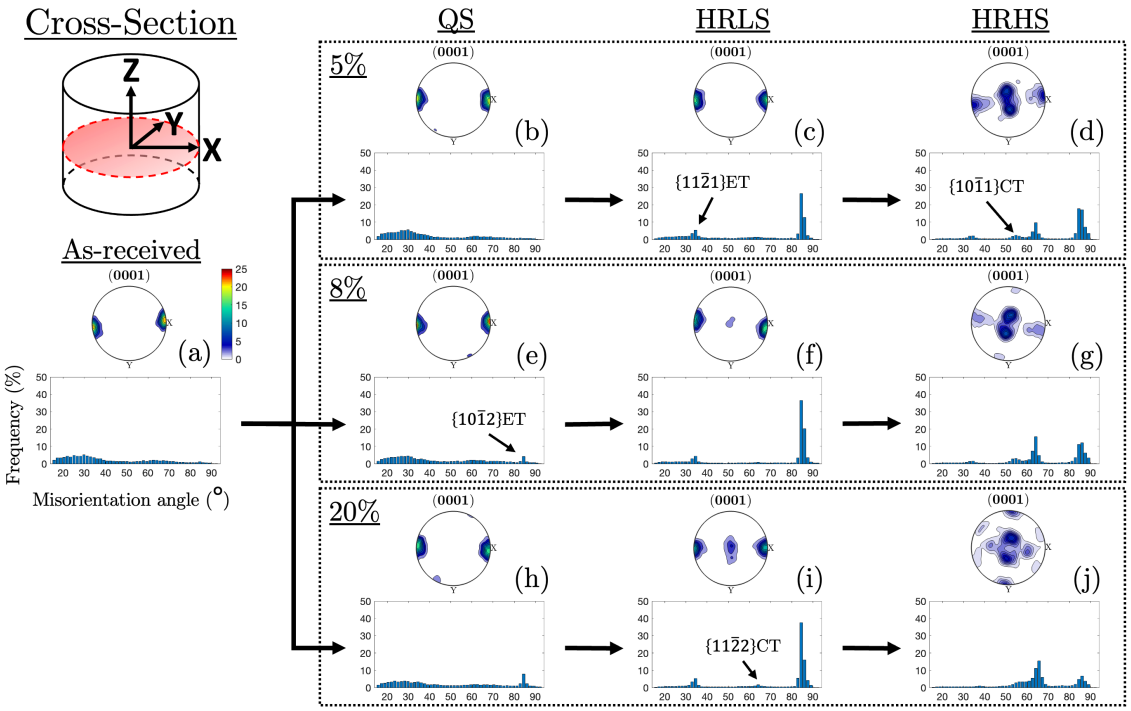


Figure 3.8: Evolution of (0001) pole figures from the cross-section planes of the specimens, obtained from large area $(1.117 \times 0.838)\,\mathrm{mm}^2$ EBSD scans.

in the overall grain orientation and only few twins were formed, as shown in Figs 3.8b, e and h. The only twinning system activated was the $\{10\bar{1}2\}$ ET, with a MO of ∼85°. This twinning system is widely reported in other studies during quasistatic deformation [28, 30, 31, 35, 102, 106, 107], and is often the first twinning system to be activated. As twinning was limited at this stage, dislocation nucleation and slip were responsible for strain accommodation, as shown by the increase in GND density and LAGB density (Fig. 3.12).

3.4.2 High-rate deformation

The most noticeable difference between the microstructures after QS stage and after the secondary HR stage is the increase in twinning activities and texture changes,

Table 3.4: Twinning systems, types (ET: extension twins, CT: contraction twins), twin boundary misorientation angles [22] and shear strains in pure titanium [1, 2, 21].

Twinning Systems	**Twin Type**	**Misorientation Angles**	**Shear strain**
$\{11\bar{2}1\}\langle 11\bar{2}\bar{6}\rangle$	ET	$\sim 35^\circ$	0.638
$\{10\bar{1}1\}\langle 10\bar{1}\bar{2}\rangle$	CT	$\sim 57^\circ$	0.105
$\{11\bar{2}2\}\langle 11\bar{2}\bar{3}\rangle$	CT	$\sim 64^\circ$	0.224
$\{11\bar{2}4\}\langle 22\bar{4}\bar{3}\rangle$	CT	$\sim 77^\circ$	0.254
$\{10\bar{1}2\}\langle 10\bar{1}1\rangle$	ET	$\sim 85^\circ$	0.167

as shown in the EBSD maps of HRLS and HRHS in Fig. 3.7. The pole figures and MO distributions of HRLS stage of the 5%, 8% and 20% QS-strained specimens are shown in Figs. 3.8c, f and i respectively. All specimens show activities of the $\{11\bar{2}1\}$ ET and $\{10\bar{1}2\}$ ET (at $\sim 35^\circ$ and $\sim 85^\circ$ on the MO distributions), and only the 20% QS-strained specimen shows a small peak at $\sim 64^\circ$ which indicates nucleation of $\{11\bar{2}2\}$ CT. While not as active as the other twinning systems, the $\{11\bar{2}1\}$ ET can be found in high strain-rate deformation [24, 106, 108]. The higher peak at $\sim 85^\circ$ in all cases indicates that the $\{10\bar{1}2\}$ ET contributes the most to strain accommodation due to its low twin shear (see Table 3.4). Note that although $\{10\bar{1}1\}$ CT has the lowest shear strain, it was not the first twin type to be activated. Exact mechanisms are not well-known owning to the complexity in experimental studies [2], but could be a thermally-assisted mechanism as shown by Zeng *et al.* [65].

Activation of twinning results in changes in grain orientation [2, 14, 15, 21, 29, 35, 109], and accumulation of twins leads to texture changes. While the 5% HRLS specimen (Fig. 3.8c) did not show a noticeable change in texture, at 8% HRLS (Fig. 3.8f) the increase in twinning activity caused the basal plane of some grains

to rotate, from aligning with the X-direction to aligning with the loading axis (Z-direction). At 20% HRLS (Fig. 3.8i), a stronger effect of twinning-induced grain re-orientation, and forming split poles along the Z-direction, similar to the findings from Xu *et al.* [28] and Sahu *et al.* [30]. As the prismatic/pyramidal planes of parent grains were normal to the loading axis, the $\{10\bar{1}2\}$ ET was activated. The c-axes of the twinned regions rotated towards the loading axis, forming a split-pole texture.

At the HRHS stage, Figs. 3.8d, g and j show that while the $\{10\bar{1}2\}$ ET is still the dominant system (the highest peaks) in the 5% and 8% HRHS specimens, in the 20% HRHS specimen the $\{11\bar{2}2\}$ CT has drastically out-competed the other twinning systems and has become the dominant system. In addition, all specimens display a further small peak at $\sim 55^{\circ}$ indicating the activation of the $\{10\bar{1}1\}$ CT. Examining the corresponding pole figures, at 5% and 8% HRHS, the majority of the fibres (c-axis of the grain) have migrated from aligning with the X-direction to aligning with the Z-direction, forming split-poles. At 8% HRHS, some fibres have even rotated to align with the Y-direction. At 20% HRHS, there is no longer any evidence for grains maintaining their original orientation, instead, two pairs of split-poles formed along the Z-direction, with the stronger pair on the Y – Z plane (similar to the 5% and 8% HRHS specimens) and a weaker pair on the X – Z plane. Similar to the 8% HRHS, some fibres have also rotated to align with the Y-direction. There are also signs of some fibres orienting approximately 45° between the X- and Y-directions. A total of four peaks are identified from the MO distributions. In addition to the previously identified twinning systems, there is a new peak formed

at $\sim$55°, which corresponds to the $\{10\bar{1}1\}$ CT. Throughout the high-rate loading stages, the grain size evolution is shown in Fig. 3.10. It is worth mentioning that as the total strain level increases (see Fig. 3.7), the number of un-indexed points, as shown as the black pixels on the EBSD maps, also increases. While this could be the result of poor sample preparation leading to unsuccessful indexing of Kikuchi patterns, it could also be due to formation of sub-micron features, essentially features much smaller than the pixel size. Therefore the actual grain sizes could be much smaller than the detectable ones.

3.4.3 Distributions of twin types

Further investigation of the twinning activities, the twin volume and boundary fractions are compared in Figs. 3.9b and 3.9a respectively. As the MO angles of normal grain boundaries are randomly distributed, grains could be misidentified as twins during the calculations, and therefore, the following quantitative result should be treated with caution. In general, an increase in twinning activity can be observed with increasing pre-straining level at the QS stage, which results in increased yield stress and plastic flow stress of the polycrystalline materials [34].

At the HRLS stage, in all cases both the $\{10\bar{1}2\}$ ET and $\{11\bar{2}1\}$ ET were found, with the former being the dominant twin mode. The boundary fraction of $\{10\bar{1}2\}$ ET increases rapidly from 5% to 8%, but only slightly from 8% to 20%, while the volume fraction increases rapidly across all specimens. This suggests that at lower initial fractions of the $\{10\bar{1}2\}$ ET (at 5% and 8% QS-strained), there is still room

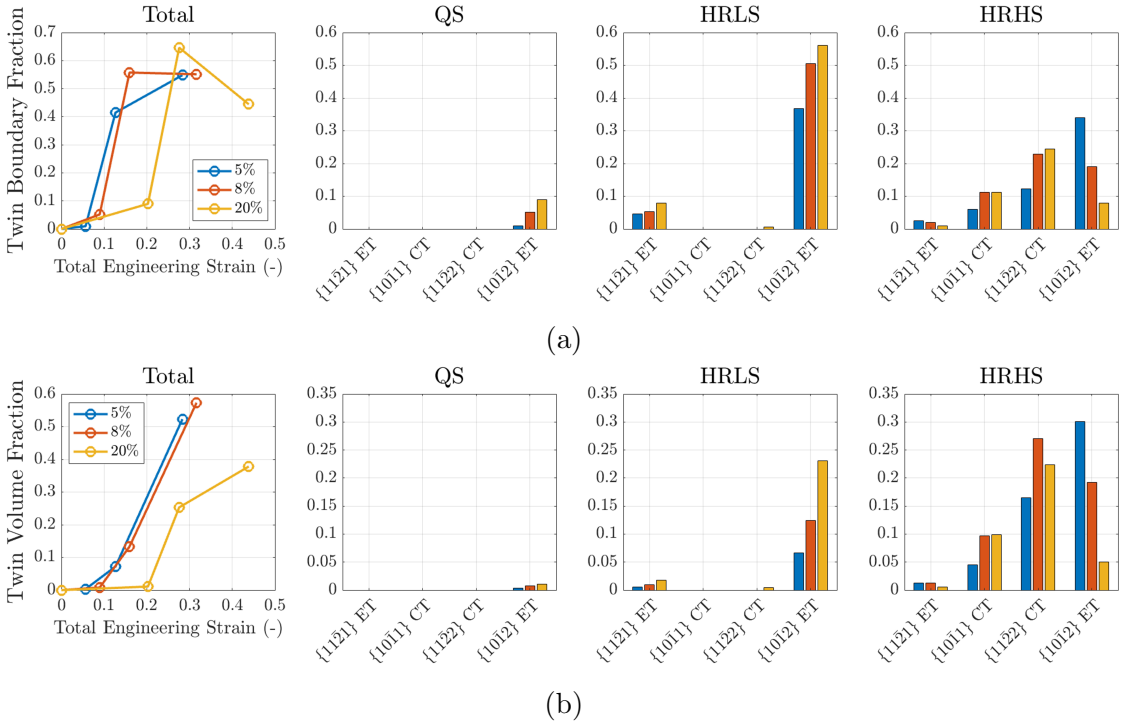


Figure 3.9: Twin boundary fractions (a) and twin volume fractions (b) of {11$\bar{2}$1} ET, {10$\bar{1}$1} CT, {11$\bar{2}$2} CT and {10$\bar{1}$2} ET twinning systems.

for this particular twinning system to nucleate, indicated by both the increase in boundary and volume fractions. This finding is similar to that from Zhang *et al.* [110] and Siska *et al.* [111]. Both studies also found that formation of multiple twins is more favourable due to the fact that more stress can be accommodated, as stress is concentrated around the tip of twin lathes. However, as more twins were pre-activated in the 20% QS-strained specimen, twin growth of {10$\bar{1}$2} ET became more favoured. This is similar to the findings from Zhang *et al.* [110] who suggested that once twins nucleate, twin growth can occur at relatively low stress, leading to plateau in boundary fraction but increase in volume fraction of {10$\bar{1}$2} ET. However, the activation of {11$\bar{2}$2} CT in the 20% QS-strained specimen remains unclear. It is possible that the {10$\bar{1}$2} ET system has become exhausted - it has reached the critical volume fraction of this particular twinning system.

At the HRHS stage, all specimens show an increase in twin volume fraction, but only the 5% HRHS specimen also shows an increase in boundary fraction. In the 5% and 8% HRHS case, the $\{11\bar{2}2\}$ CT and $\{10\bar{1}2\}$ ET are the dominant mode, however at 20% HRHS, $\{10\bar{1}1\}$ CT outcompeted the $\{10\bar{1}2\}$ ET. In all cases, $\{11\bar{2}1\}$ ET was found only in small fractions. Judging by activities of each twin mode, the sequence of nucleation can be considered as: $\{10\bar{1}2\}$ ET $\rightarrow$ $\{11\bar{2}1\}$ ET $\rightarrow$ $\{11\bar{2}2\}$ CT $\rightarrow$ $\{10\bar{1}1\}$ CT. This is a surprising observation as for a similar textured CP-Ti under QS deformation in literature [31, 35], the $\{11\bar{2}2\}$ CT was usually activated after $\{10\bar{1}2\}$ ET. This confirms a fundamental strain-rate dependency in deformation mechanisms. Note that the 20% HRHS specimen shows the lowest twin boundary and volume fractions at this stage, while also containing the highest LAGB density (Fig. 3.12), by a significant margin. The combination of these characteristics can signify that the early stage of a phenomenon known as dynamic recrystallisation [102, 112]. As high LAGB leads to high degrees of subgrain rotation and dislocation pile-up at the twin boundaries, this effectively disturbs the ideal MO relationship between the twinned region and its parent grain [64, 102], which then led to difficulty in identifying twin boundaries through MO angles. Continuous dislocation pile-ups also further evolve the LAGB's into HAGB's, and turning some twin boundaries into HAGB's, which reduces the grain size and in conjunction with twinning (Fig. 3.10), enhances the effect of Hall-Petch hardening. The high internal residual plastic strain, stored within LAGB's also acts as short-range obstacles that limit dislocation mobility, leading to further hardening of the material system.

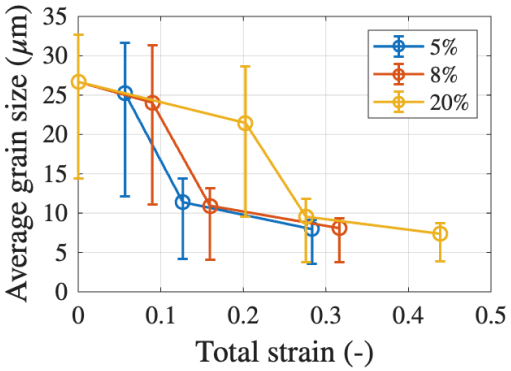


Figure 3.10: The average grain sizes in equivalent diameters of the pre-strained specimens at different loading stages. Total strain was measured *post-mortem*. The error bars indicate the interquartile range (middle 50%) of the grain sizes.

3.4.4 Dislocations and Schmid Factors

The twinning-induced grain rotation also has an effect on the Schmid factors (SF's) of the slip systems. Although other factors, for example critical resolved shear stress (CRSS), affect the activation of slip systems, SF's indicate the geometrical likelihood of the system to be activated. It is generally agreed that in HCP-Ti, the prismatic (Pris) $\langle a \rangle$ has the lowest CRSS, followed by basal (Ba) $\langle a \rangle$ and pyramidal (Py) $\langle a \rangle$, with the pyramidal (Py) $\langle c + a \rangle$ having the highest CRSS. Here Fig. 3.11 shows the area fraction of grains with high SF (SF = 0.4 to 0.5) for each slip system. At the QS stage, in all cases, the area fraction of Pris$\langle a \rangle$ slip increases while that of Py$\langle c + a \rangle$ decreases. As the HR strain increases, Pris$\langle a \rangle$ became less favourable and the Ba$\langle a \rangle$ and Py$\langle c + a \rangle$ became more favourable. This reduces the activity of the easily-activated Pris$\langle a \rangle$ slip, which can be attributed to the flow stress hardening observed in all HR stress-strain curves.

The overall GND and LAGB density evolution are shown in Fig. 3.12. Through-

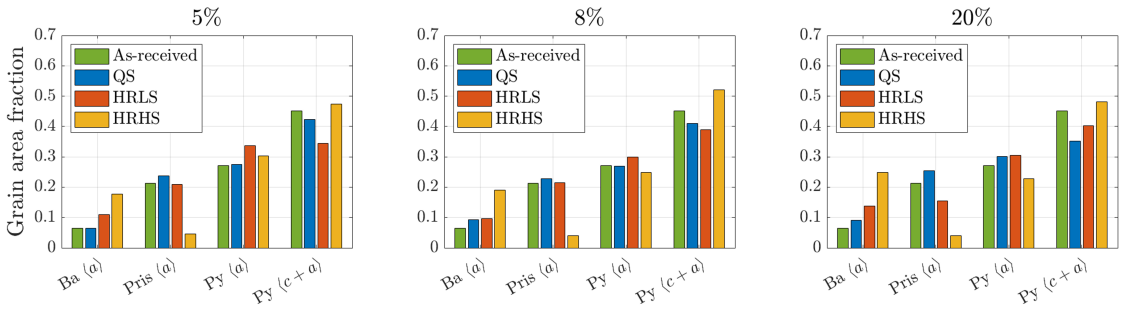


Figure 3.11: Area fractions of grains with high Schmid Factors (SF = 0.4 to 0.5) for each slip system at different loading stages.

out the HR deformation, the GND density increases linearly while the LAGB density increases exponentially. Comparing to the QS stage, while the GND density increases from 5% to 20% strain, the magnitude is incomparable to that from HR deformation. As dislocations were continuously generated from homogeneous nucleation and Frank-Read sources, the mobile dislocations swept through the crystal lattice, forming LAGB's when they encountered each other. These LAGB's, together with sessile dislocations, act as obstacles for slip, causing macroscopic strain hardening.

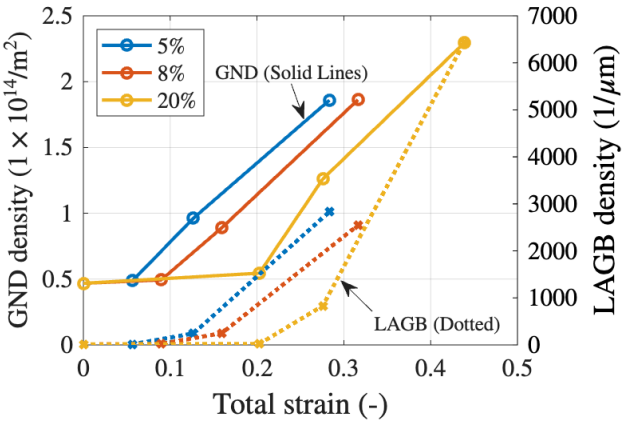


Figure 3.12: The average GND densities (solid lines) and average LAGB densities (dotted lines) of the specimens at different loading stages.

3.4.5 Changes in yield stress

The increase in dislocation density directly increases the yield stress [8]. Comparing the GND densities against macroscopic flow stress at $\varepsilon_{\text{eng.}} = 0.01$ shown in Fig. 3.13, a simple linear regression model (the dotted line) using the least squares method shows a fairly good fit with the experimental data (solid points). The value of $\varepsilon = 0.01$ was used because in a typical SHPB experiment, force equilibrium is not reached until after approximately 1% strain [82]. Although this is different from the conventional 0.2% offset point taken as the yield stress, the stress at $\varepsilon = 0.01$ is considered as a close approximate of the yield stress. The Taylor dislocation hardening model [113] describes the yield stress as a function of the square root of dislocation density,

$$\sigma_{\text{Taylor}} = \text{M}\alpha\text{Gb}\sqrt{\mu_{\text{D}}} \tag{3.1}$$

where M is the Taylor factor, α is a material constant, G is the shear modulus, b is the magnitude of the Burgers vector, and μ_{D} is the dislocation density.

Previous studies also show that other microscopic features such as grain/sub-grain boundaries and grain size also contribute to strain hardening. The effect of grain size on yield stress is often predicted by the Hall-Petch equation [12, 13]. To include the effect of grain/sub-grain boundaries, Luo *et al.* proposed a modified

Hall-Petch equation which takes into account the LAGB's features [114], as follows:

$$\sigma_{\text{mod.HP}} = \sigma_0 + \sigma_{\text{LAGB}} + \sigma_{\text{HAGB}}, \tag{3.2}$$

$$\sigma_{\text{mod.HP}} = \sigma_0 + \text{M}\alpha\text{Gb}\sqrt{\mu_{\text{GB}} + \mu_{\text{LAGB}}} + \text{k}\left(\frac{\text{d}}{\text{f}}\right)^{-\frac{1}{2}}, \tag{3.3}$$

$$\sigma_{\text{mod.HP}} = \sigma_0 + \text{M}\alpha\text{Gb}\sqrt{\rho_{\text{GB}} + \frac{3(1-\text{f})\bar{\theta}_{\text{LAGB}}}{\text{bd}}} + \text{k}\left(\frac{\text{d}}{\text{f}}\right)^{-\frac{1}{2}}, \tag{3.4}$$

where σ_0 and k are respectively the frictional stress (= 78 MPa) and Hall-Petch slope (= 0.4) from [115], M = 3.0 and $\alpha = 0.2$ are taken from [114], G = 45 GPa (for Ti), b is taken as the weighted average magnitude of the Burgers Vector [116], d is the boundary spacing, which is taken as the average grain size in equivalent diameter, f is the HAGB fraction and $\bar{\theta}_{\text{LAGB}}$ is the average misorientation of LAGB's[114].

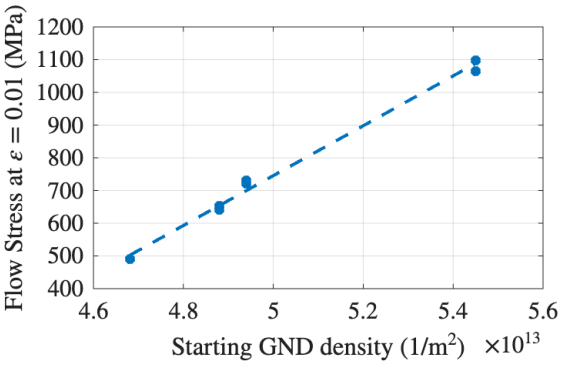


Figure 3.13: Flow stresses at 1% engineering strain against different starting GND densities. Experimental data is shown as the blue dots and the linear regression is shown as the red dotted line.

Applying these models to predict the yield stress under high-rate loading from this study, as shown in Fig. 3.14, the Taylor model shows a gross underestimation of yield stress across all specimens, and the modified Hall-Petch model shows a closer approximation for the specimen with no QS-strain only. However, both models fail

to capture the increase in yield stress. Combining with the fact that the texture at the QS stage across all specimens does not change drastically, as discussed earlier in Figs. 3.8a, b, e and h, one could conclude that, under high strain-rate loading, the initial dislocation density, grain size (grain/sub-grain boundaries) and orientation do not contribute significantly to the change in macroscopic yield stress. This naturally points to the twinning activities - the twin volume and boundary before the high-rate loading in particular.

To establish a correlation between the pre-activated twins and yield stress, Fig. 3.15 shows the experimental data and the linear regression fit for the total twin boundary and volume fractions. The equations of these fittings are as follows,

$$\sigma_{\mathrm{YS}} = 5.6548 \times 10^{9} \times \mathrm{TB}_{\mathrm{frac}} + 5.2656 \times 10^{8}, \tag{3.5}$$

$$\sigma_{\mathrm{YS}} = 4.9595 \times 10^{10} \times \mathrm{TV}_{\mathrm{frac}} + 4.5883 \times 10^{8}, \tag{3.6}$$

where σ_{YS} is the yield stress, $\mathrm{TB}_{\mathrm{frac}}$ is the twin boundary fraction and $\mathrm{TV}_{\mathrm{frac}}$ is the twin volume fraction. Due to the limited data available within this study, the results should be considered qualitative and the authors are not proposing a model that can be applied universally. More investigations and data must be obtained before determining the constitutive relationship between these aspects. From Fig. 3.15, the gradient of the twin volume fraction fit is very steep, suggesting that from the statistical standpoint, the yield stress is very sensitive to the change in twin volume fraction. This is supported by the lack of significant changes of the texture due to twinning (Figs. 3.8a, b, e and h), and the minor changes in slip activities and

Schmid factors within these twinned regions are relatively small. Hence, it is difficult to correlate twin volume fraction and yield stress. This contradicts with findings from Salem *et al.* [14], albeit with a different starting texture, who observed strain-hardening in titanium with increasing twin volume fractions. However, hardening is likely due to the texture changes, which resulted in high CRSS slips being more active [116]. In contrast, increasing twin boundary fraction shows a more stable increase in yield stress, and therefore a more meaningful representation to correlate the two features. At a fundamental level, the twin tends to first propagate and extend across the grain, then thickens perpendicular to its length. The previous study by Guo *et al.* [117] reveals that the high GND density at twin tip, coupled with the negative stress field surrounding it, resist twin propagation. From the results in this study, it seems to suggest that the amount of pre-activated twins directly affects the yield point, particularly in high-rate loading which promotes twinning in titanium. Comparing to the results at the HRLS stage, where there is a drastic increase in both the twin boundary and volume fractions, it is not entirely clear whether the additional twins nucleate at yield, or at a later stage of plastic deformation. This will require further investigations to consolidate the relationship between pre-activated twins and their effect of yielding, and the strain-rate sensitivity of this mechanism.

3.5 Conclusions on strain-path changes

In this study, the effect of strain-path changes on commercially-pure titanium was investigated. The first stage was quasistatic compression to approximately 5%, 8% and 20% strain, and the secondary high-rate compression was interrupted at an

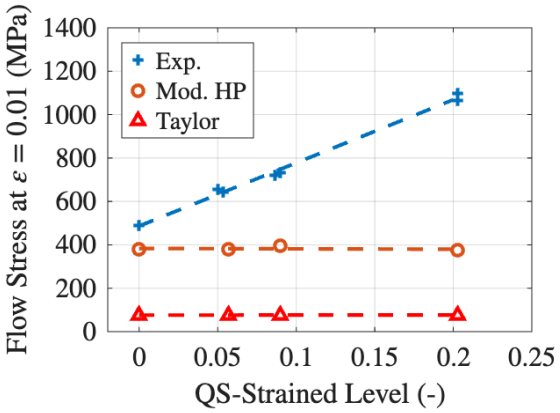


Figure 3.14: Linear regression of the yield stress obtained from experiments, the prediction using the modified Hall-Petch model and the Taylor dislocation hardening model. The x-axis indicates the level of strain at the initial QS stage, from no QS-strain (0%), to 5%, 8% and 20% QS-strain.

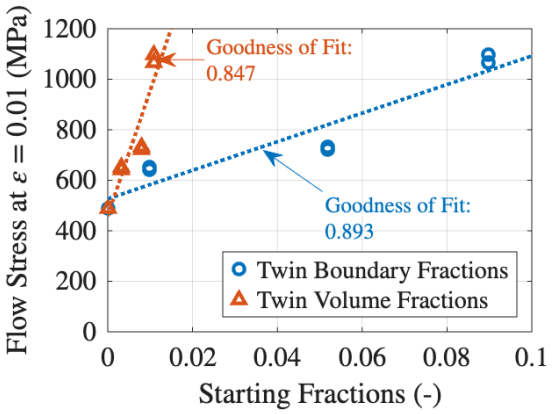


Figure 3.15: Twin boundary and volume fractions against yield stress (taken as flow stress at 1% engineering strain) under high-rate compression. The straight dotted lines show the linear regression of the data points.

additional of $\sim$ 7% and 22% strain. Tests were repeated and the specimens were recovered at each stage for microstructure analysis using EBSD to reveal their grain-level features. The key findings are as follows:

1. The twinning nucleation sequence is identified to be: $\{10\bar{1}2\}$ ET $\rightarrow$ $\{11\bar{2}1\}$ ET $\rightarrow$ $\{11\bar{2}2\}$ CT $\rightarrow$ $\{10\bar{1}1\}$ CT. The $\{10\bar{1}2\}$ ET system was first activated at the QS stage, and remained the dominant system at the early stages of high-rate compression, until the $\{11\bar{2}2\}$ CT overtook at high strain levels,

2. The widening of the peaks at the grain boundary MO distribution suggested that dynamic recrystallisation occurred at high strain levels. This could be due to dislocations sinking into the twin boundaries, disturbing the ideal twin-parent MO relationship,

3. In the absence of significant changes in dislocation density and grain orientation (texture), twin boundary fractions played an important role in determining the yield stress. This is shown by the unsuccessful prediction of yield stress using existing models on dislocation density and grain size.

This chapter has revealed the effect of pre-activated twinning on the high strain-rate compression of this specific batch of pure titanium. Based on the above observations and findings, the following questions were raised regarding the behaviour of titanium with pre-strained features:

- As the microscopic deformation mechanisms often differ with respect to the strain-rates, what is the strain-rate sensitivity in microstructure evolutions with pre-existing defects?

- Nucleation of new twins or growth of existing twins - which mechanism is more dominant at the early stage of deformation?

- What are the incipient failure mechanisms in titanium?

The following experimental campaign (Chapter 4) aimed at statistically correlating the microscopic features with the bulk mechanical behaviour.

Chapter 4

Effect of pre-existing defects on the strain-rate dependent deformation mechanisms of pure titanium

This chapter covers the second experimental campaign, which aims at further exploring the effect of pre-straining on titanium by applying novel statistical analyses and modelling on microstructure-bulk behaviour correlations. The discussions will be presented in three parts. First, novel statistical analyses will be performed on the EBSD data to extract global features. Second, the early stage and incipient failure mechanisms will be investigated under different strain-rates. Third, key microstructure features will be identified and extracted, and correlations between microstructure features and bulk yield and flow stresses will be established using advanced statistical models .

4.1 Primary objectives

The campaign of experiments aims to investigate the strain-rate effect on the early-stage deformation and incipient failure mechanisms. The primary objectives of this study are as follows:

- Conducting interrupted testing, particularly at very low and very high plastic strain levels, before reaching material failure,
- Extracting statistical features from the microstructures,
- Identifying the key microstructure features and their correlations with bulk properties.

4.2 Experimental procedures

A second batch of commercially-pure titanium (CP-Ti grade 2), was used throughout this campaign. Reviewing the methodology employed in Chapter 3 revealed uncertainties in the effect of barrelling (from the first stage of compression) on the second high-rate compression. This was difficult to mitigate due to practical limitations - specimens could not be re-machined to remove barrelling prior to the high-rate loading. In this campaign, a novel approach of generating pre-strained materials was developed.

4.2.1 Novel pre-straining method

The barrelling effect comes from the uneven strain distribution within a specimen during compression. The radial expansion of the specimen near the specimen-anvil interfaces is smaller due to friction between the two surfaces, while the middle section is less restricted and can expand more freely. Experimentally, this effect cannot be eliminated but only minimised. This is achieved by grinding the specimen faces and anvils are typically ground to a smooth finish (not to a mirror finish) and applying lubricant to the interfaces, to reduce the friction. While non-uniform strain distribution still exists regardless, if one were to look at a local region, the strain variation is much smaller.

Since the specimens used in mechanical testing and microscopy are relatively small (approximately 3 mm diameter $\times$ 3 mm length), it was hypothesised that if a suitably large cylinder was compressed, small test specimens could be machined from the local regions with relatively uniform strain. To determine the feasibility of this approach, finite element analysis (FEA) was conducted.

Fig. 4.1 shows the Abaqus FEA model for the simulations [118]. Assuming radial symmetry, a simplified 2D rectangular structure was used to represent the large cylindrical specimen. The cylinder has a diameter of 60 mm and a length of 120 mm, forming a L/D ratio of 2:1. The top and bottom anvils were defined as analytical rigid and friction was applied to the interfaces. Three values of coefficient of friction were used: 0.1, 0.2 and 0.3. These values were chosen to cover a range

of possible friction conditions with lubricants applied [119]. The bottom anvil was fixed and the top anvil was displaced to apply the strain. To simulate a low-rate compression loading, the FEA model was run in the implicit integration.

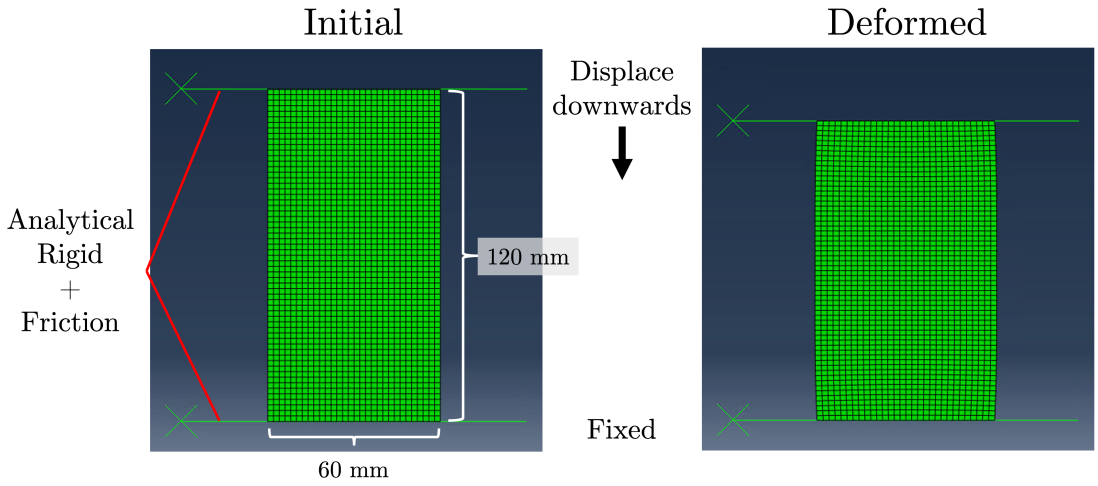


Figure 4.1: The Abaqus FEA model for determining the strain distribution of a CP-Ti (grade 2) cylinder of 60 mm diameter by 120 mm height. The top and bottom "anvils" were analytical rigid with friction added to the interfaces. The bottom anvil was fixed while the top anvil displaced downwards.

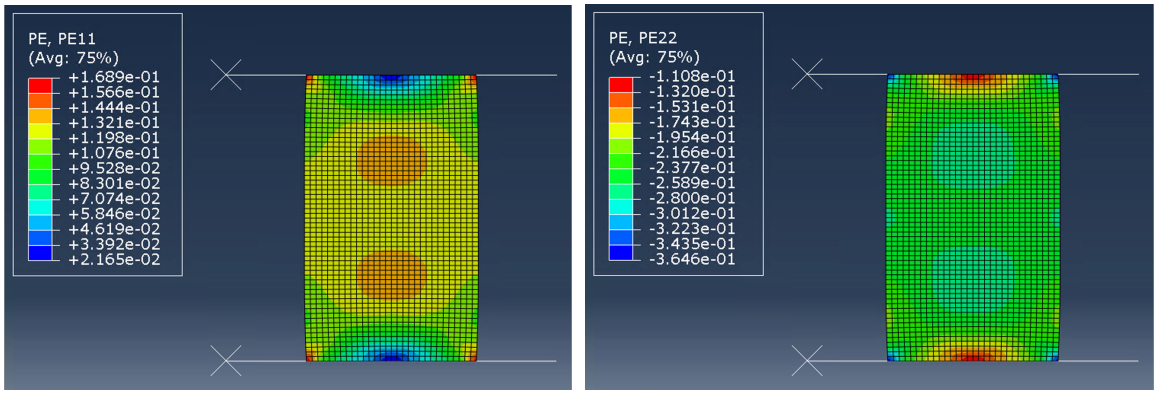
The standard Johnson-Cook plasticity model [46] was used, with the parameters for CP-Ti were obtained from [120] (see Table 4.1). Note that C, $\dot{\varepsilon_0}$ and m were omitted (set to 0 in the model) as only there is no temperature and strain-rate dependency here. It was assumed that the material was isotropic.

Table 4.1: The material properties and standard Johnson-Cook plasticity model parameters of CP-Ti (grade 2) [120] used in the model. The parameter **A** is the reference yield stress, **B** and **n** are strain-hardening constants.

Density	**Young's Modulus**	**Poisson's Ratio**	**A**	**B**	**n**
4510 kg m^{-3}	115 GPa	0.33	330 MPa	753 MPa	0.42

The top anvil was displaced by 30 mm linearly throughout 10 time steps. The tensile and compressive plastic strains, PE11 and PE22, in Fig. 4.2, were used to determine the strain variations within a specific region, as shown in Fig. 4.3b. This

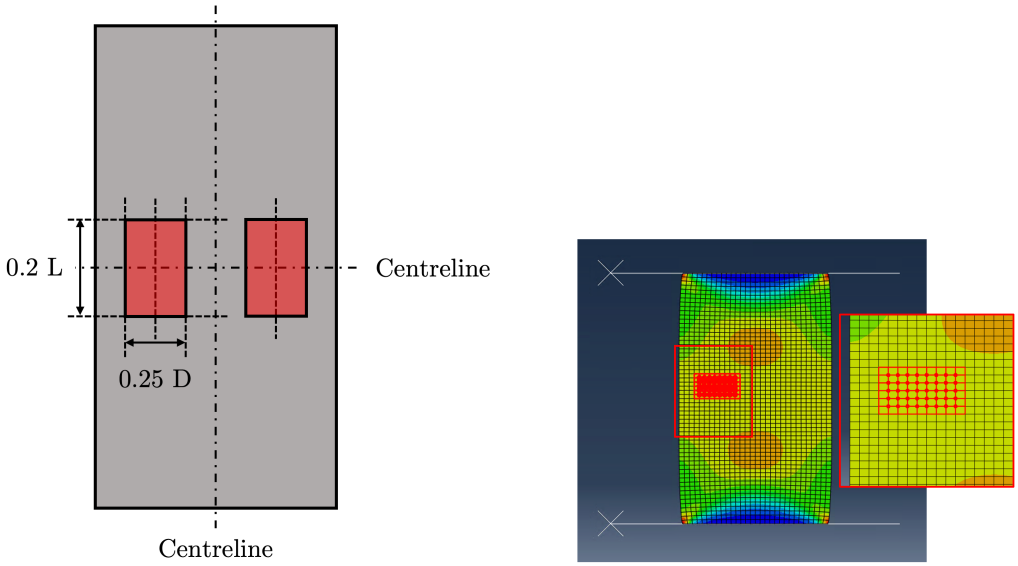
region corresponds to the top half (assuming plane symmetry from the mid-plane) of the middle ring section of the material (Fig. 4.3a). The centre region of the cylinder was discarded as it only represents a smaller volume in 3D, thus limiting the number of test specimens that could be extracted through subsequent machining. The ring section provides a higher volume of material for specimens.



(a) (b)

Figure 4.2: Examples of tensile and compressive plastic strain distributions: (a) PE11 for tensile strain, and (b) PE22 for compressive strain.

To quantify the strain distributions, Figs. 4.4 and 4.5 show the results of the deformed cylinders at 5% and 20% strains (height reduction) respectively. These results were obtained from time steps 2 and 8, which correspond to 6 mm and 24 mm of displacements respectively. Although the strain levels are not uniform at each step, calculating the percentage difference of the maximum and minimum strain in each case reveals that the percentage differences are all below 5% (see Table 4.2). Therefore, it can be concluded that given a sufficiently large cylinder, along with the assumptions above, this ring section of material should provide a sufficiently uniform strain for specimen extractions.



(a) (b)

Figure 4.3: The centre region to be studied for the strain variations, with a width of 0.25 D and height of 0.2 L: (a) This ring section of material (assuming radial symmetry about the centre axis) was selected to maximise the number of test specimens that could be machined from one large cylinder, and (b) elements selected (highlighted in red) to calculate the strain distributions.

Table 4.2: The percentage differences of the maximum and minimum values of absolute tensile (PE11) and compressive (PE22) strain distributions. Displacements of 6 mm and 24 mm correspond to $\varepsilon_{\text{eng.}}$ =5% and 20% respectively.

Friction Coefficient	**Displacement**	**%-diff. in PE11**	**%-diff. in PE22**
$F_c = 0.1$	6 mm	2.307%	2.886%
	24 mm	1.728%	1.362%
$F_c = 0.2$	6 mm	3.422%	4.299%
	24 mm	2.517%	2.303%
$F_c = 0.3$	6 mm	3.487%	4.405%
	24 mm	2.622%	2.396%

Following the FEA model, larger cylinders of CP-Ti grade 2 were obtained from a material supplier and subsequently compressed to generate pre-strained materials. The chemical composition of the titanium cylinders is shown in Table 4.3. This material has been double vacuum remelted, annealed at 650 °C and air-cooled. The diameter of the cylinders was kept as supplied (60 mm), and the cylinders (120 mm

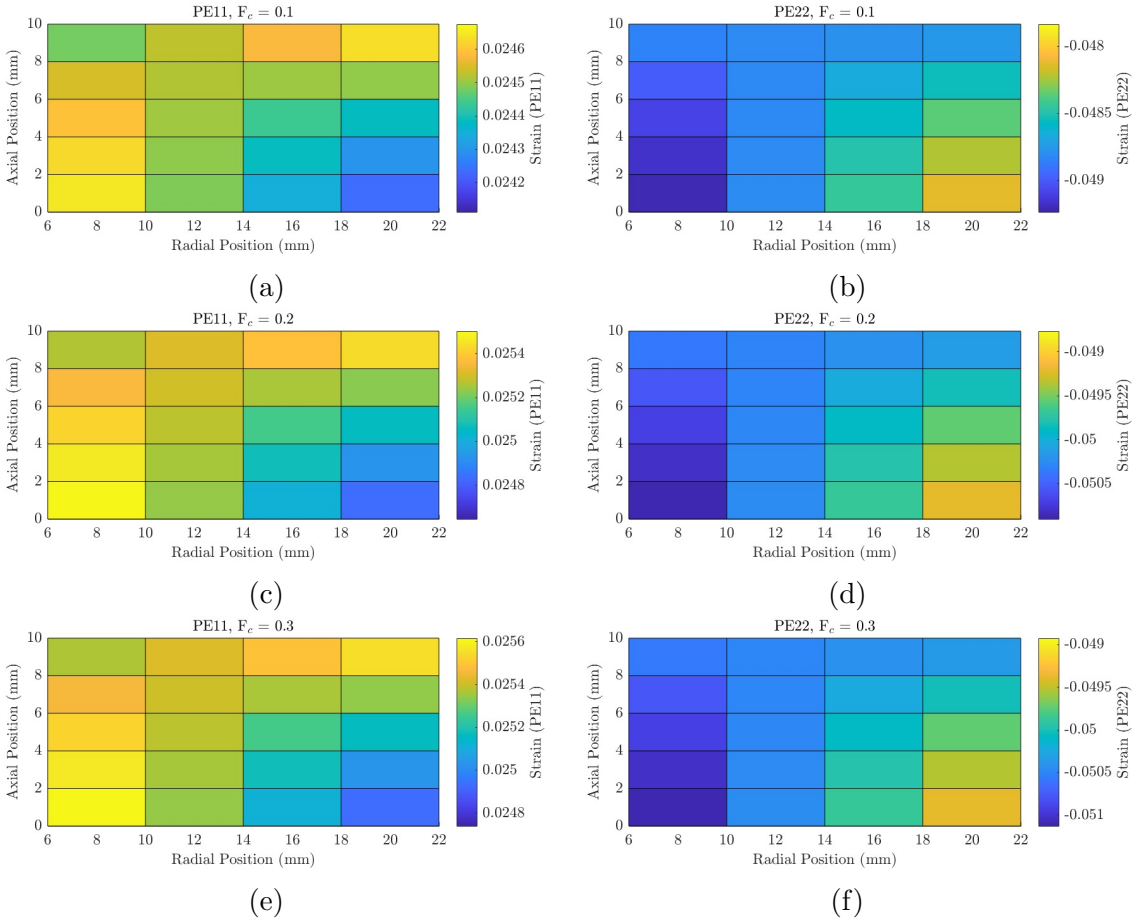


Figure 4.4: The tensile and compressive strain distributions at 5% strain, with different coefficient of friction (F_c) at the interfaces.

in length) were first sectioned to length using EDM to ensure an uniform surface finished and good parallelism. Fig. 4.6 shows that the top and bottom sections from the as-received cylinder were sectioned off, and a slice of material between the two large cylinders was kept to study the as-received microstructure. They were then compressed using an Instron hydraulic machine (SATEC 3500 kN) located at Imperial College London, United Kingdom (see Fig. 4.7). A silicon-based lubricant was applied between the titanium cylinders and the steel anvils to minimise the friction effect. The machine was programmed to terminate at a specific displacement, corrected for the machine compliance. The displacement rate was set to 0.12 mm s^{-1}

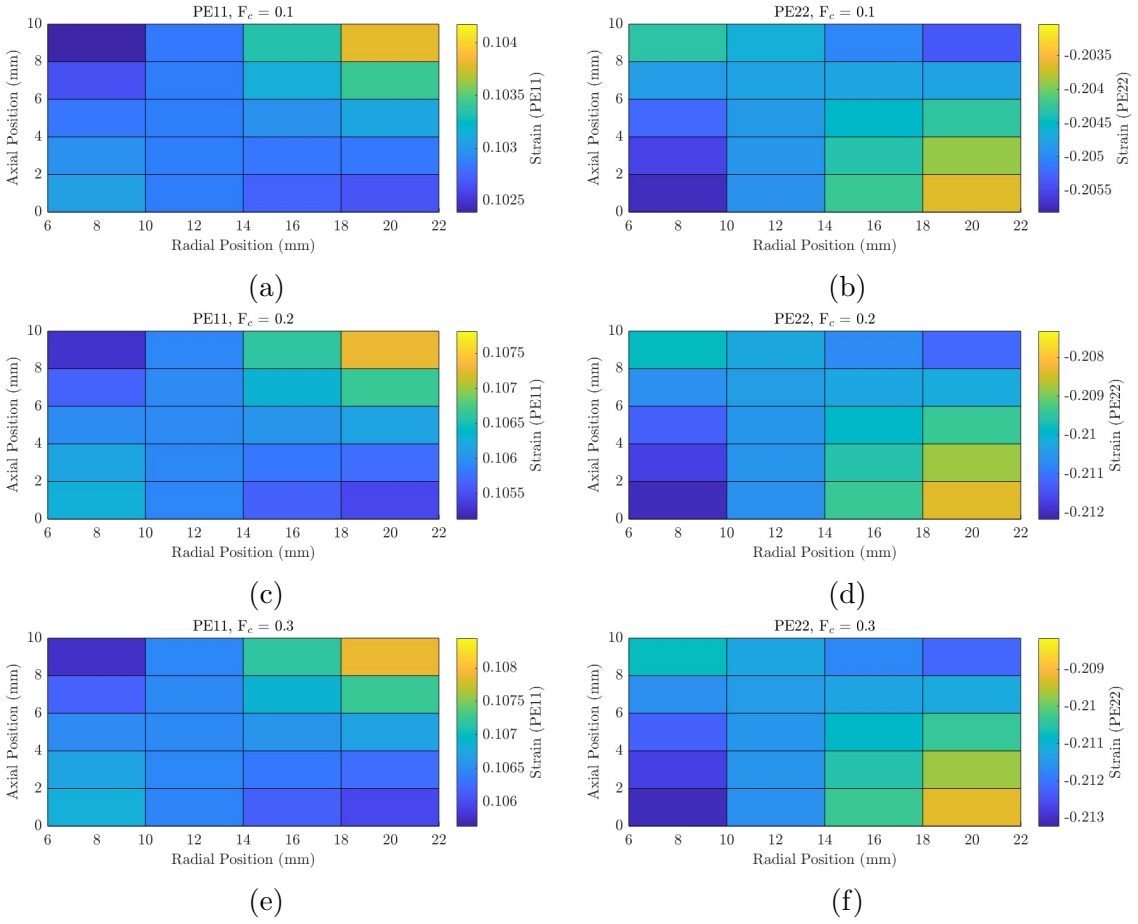


Figure 4.5: The tensile and compressive strain distributions at 20% strain, with different coefficient of friction (F_c) at the interfaces.

for a strain-rate of $1 \times 10^{-3}\,s^{-1}$. Based on the operating technician's experience, the machine compliance was corrected by setting the displacements 3 mm higher than the desired values - *i.e.* 9 mm (6 mm + 3 mm) and 27 mm (24 mm + 3 mm) for approximately 5% and 20% strain, labelled the "PS 5" and "PS 20" respectively. The displacement-force curves are shown in Fig. 4.8. The off-set of the "PS 20" curves is possibly due to early triggering of the data recording system. However, this does not affect the subsequent experiments as the goal was to generate different pre-straining conditions and the cylinders were characterised based on their microstructures. The length of the cylinders were measured as 113.58 mm and 96.93 mm for PS 5 and PS

20 respectively.

Table 4.3: Chemical composition in weight(Wt. %) of the large bar of commercially-pure titanium (grade 2) used in Chapter 4.

Element	**Fe**	**C**	**N**	**O**	**H**	**Other**	**Ti**
Wt. %	0.173	0.010	0.021	0.157	0.0095	≤ 0.4	Balance

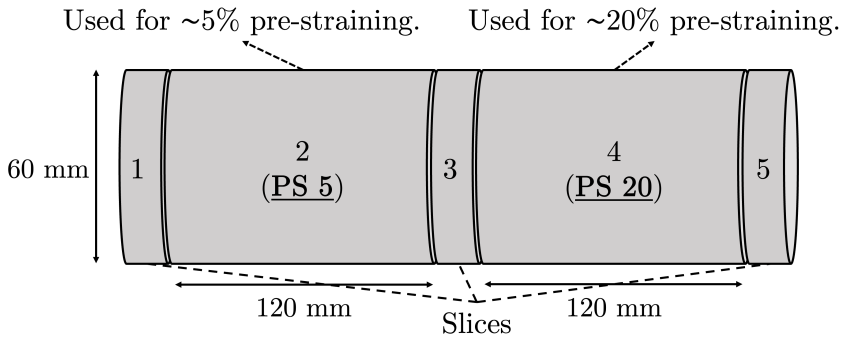


Figure 4.6: The as-received large cylinder was sliced into 5 pieces. The top and bottom sections (Slices 1 and 5) were discarded to ensure good parallelism of Bars 2 and 4, which were subsequently compressed to generate pre-strained specimens, labelled "PS 5" and "PS 20" respectively. Slice 3 was reserved for microscopy of the as-received material.

The deformed cylinders are shown in Fig. 4.9a. Small test specimens were extracted from the region identified from the FEA. Smaller rods were first extracted using EDM (see Fig. 4.9b). Then, they were machined on a lathe to the desired diameter and cut to length using EDM. The final dimensions of these small specimens were 3 mm diameter by 2.4 mm length. This L/D ratio of 0.8 was within the standard SHPB specimen requirements for materials with a Poisson's ratio of ~0.33 [82]. These pre-strained specimens were then used to generate the data for this study.



Figure 4.7: The Instron hydraulic machine (model SATEC 3500 kN), located at Imperial College London, was used to compress the large CP-Ti cylinders.

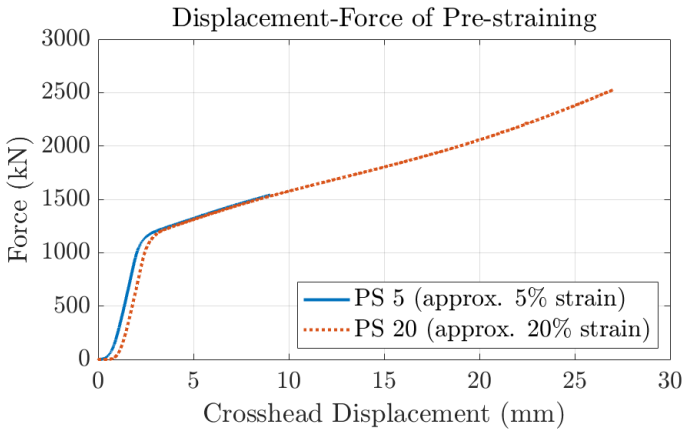
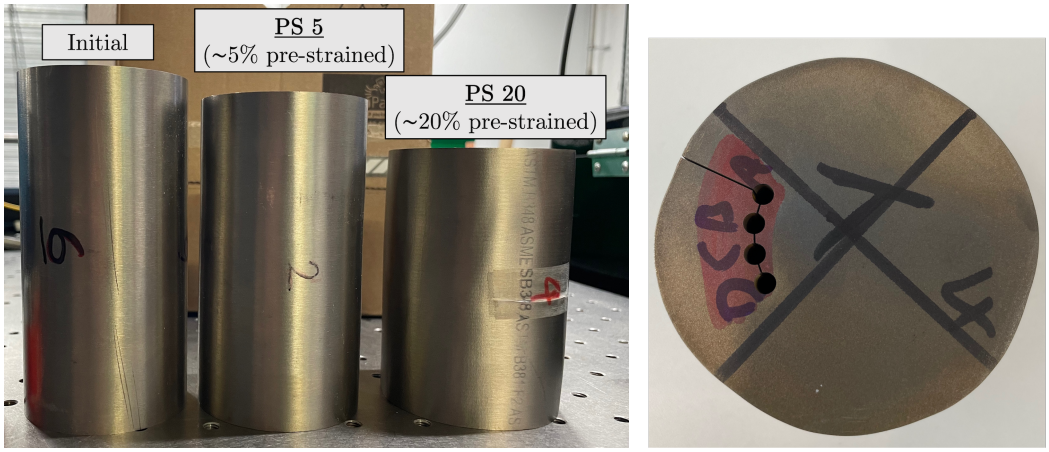


Figure 4.8: The displacement-force curves from the Intron hydraulic machine for the compression loading on the two cylinders of CP-Ti.



(a) (b)

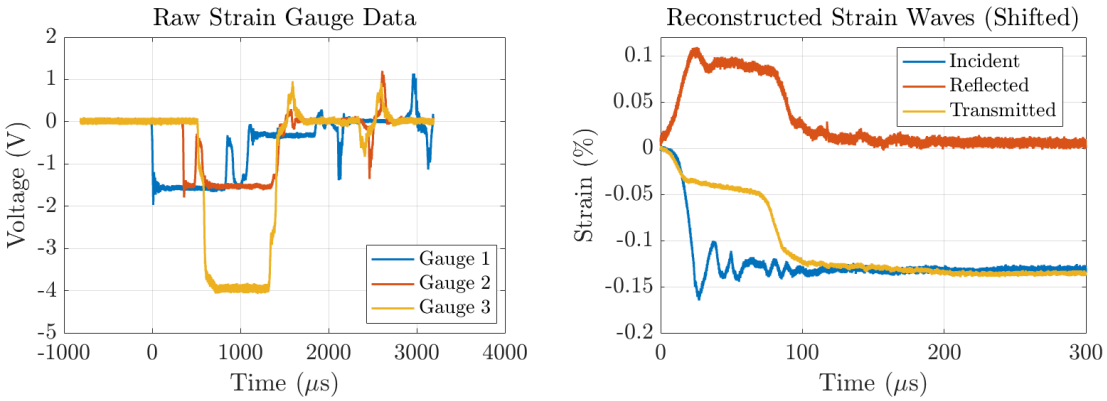
Figure 4.9: (a) The large (60 mm diameter × 120 mm length) cylinders of CP-Ti grade 2 used to generate pre-strained specimens: (left) an undeformed bar, not used in this study, (middle) PS 5 - ∼5% strain and (right) PS 20 - ∼20% strain. The strain levels were characterised by the height reduction, and (b) the cross-section of the PS 20 cylinder. Test specimens were extracted from the ring section of the cylinder, which was identified to have similar strain distributions.

4.2.2 Mechanical testing

To study the effect of strain-rate, the specimens were subjected to quasistatic (QS) and high-rate (HR) compressive loading. The Zwick-Roell 050 machine was used, with the crosshead displacement rate of $0.005\,\mathrm{mm\,s^{-1}}$ to achieve a strain-rate in the range of $10^{-3}\,\mathrm{s^{-1}}$. For the full deformation testing, the machine was programmed to terminate when the load cell reached 25 kN. For the interrupted testing, the machine was programmed to terminate at low force values which correspond to the desired strain levels. These force values were determined from the respective full deformation curves. Note that for the QS full deformation, both pre-strained materials did not exhibit failure.

The HR testing was conducted on the long SHPB at Oxford (Fig. 2.10b). The

strain gauge signals were recorded by the Tektronix DPO 3034 at an acquisition rate of 250 million points per second on each channel. An example raw strain gauge data is shown in Fig. 4.10a. The time 0 here refers to the triggering time of the oscilloscope. The reconstructed stress waves are shown in Fig. 4.10b. The average impact velocity of the striker bar was approximately $10.6\,\mathrm{m\,s^{-1}}$ to achieve a strain-rate of approximately $3500\,\mathrm{s^{-1}}$. Full deformation testing was conducted to obtain stress-strain behaviour and failure strain. The HR interrupted testing was conducted using stop rings of various thicknesses, made from Ti-6Al-4V. For all SHPB testing, sacrificial discs (same material and diameter as the bars) were used to prevent damage to the bar ends.



(a) (b)

Figure 4.10: An example of the long SHPB data: (a) the raw strain gauge data from the long SHPB with three sets of strain gauges, and (b) the reconstructed waves using the data analysis from [90]. Waves were shifted to the specimen-bar interfaces at time = 0.

Details of individual specimens are shown in Table 4.4. The values are accurate to 2 decimal places as this is the resolution of the callipers used for measurements. Since fragments from the full HR compression were re-compressed by the bars, no *post-mortem* measurements were made. For each testing condition (PS 5 and PS 20,

Table 4.4: Geometries of pre-strained specimens before and after the mechanical testing: OD and OL are the original diameter and length, and L_{test} is the length post-test. The specimen labelling convention is: PS 5/20 (pre-strained ∼5% or ∼20%), QS/HR indicates the strain-rate, followed by the strain levels. For example, PS 5 QS 10 refers to the ∼5% pre-strained specimen which was quasistatically-compressed to ∼10% strain.

Specimen	Testing	OD (mm)	OL (mm)	L_{test} (mm)	Eng. Strain (%)
PS 5, approx. 5% pre-strained					
PS 5 QS 3	QS, 4.5 kN	3.00	2.38	2.30	3.36%
PS 5 QS 10	QS, 6 kN	3.00	2.38	2.14	10.08%
PS 5 QS Full	QS, Full	3.00	2.38	0.97	59.24%
PS 5 HR 2	HR, 2%	3.00	2.38	2.35	1.26%
PS 5 HR 8	HR, 8%	2.99	2.37	2.19	7.59%
PS 5 HR 34	HR, 35%	3.00	2.39	1.59	33.47%
PS 5 HR Full	HR, Full	3.00	2.38	-	-
PS 20, approx. 20% pre-strained					
PS 20 QS 3	QS, 6 kN	3.00	2.39	2.33	2.51%
PS 20 QS 10	QS, 7.2 kN	3.00	2.39	2.16	9.62%
PS 20 QS Full	QS, Full	3.00	2.39	0.97	59.41%
PS 20 HR 2	HR, 2%	2.99	2.39	2.35	1.67%
PS 20 HR 5	HR, 5%	2.99	2.38	2.26	5.04%
PS 20 HR 25	HR, 25%	2.99	2.38	1.78	25.21%
PS 20 HR Full	HR, Full	3.00	2.38	-	-

QS and HR), testing was interrupted at two strain levels to study the early-stage deformation. As failure did not occur at QS, only the HR incipient failure mechanisms were investigated. Specimens were interrupted approximately 5% to 10% engineering strain before failure occured. The microstructures of these specimens would reveal the mechanisms leading to failure.

4.3 Results

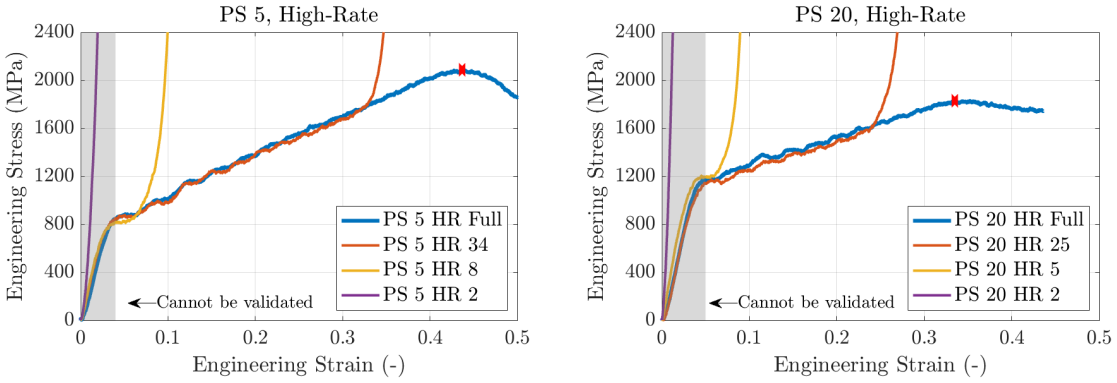
4.3.1 High-rate interrupted testing

The full and interrupted HR testing results are shown in Fig. 4.11. For both materials at HR, failure occured at the peak stresses. The values are shown in Table 4.5. Note that while the failure $\sigma_{\text{eng.}}$ are noticeably different, the failure σ_{true} are similar. Comparing the stress-strain curves of each pre-strained material, most of them show good agreement with each other, indicating that testing was repeatable and the assumption that specimens extracted from the ring section of uniform strain held true. For the larger interrupted strain levels, they clearly overlap with the full deformation curves, with the sudden increase in stress indicating collision between the input bar and stop rings. For the low strain levels (PS 5 HR 2 and PS 20 HR 2), they do not have the same trend as the other curves, and are instead a very sharp rise of stress.

Table 4.5: Failure engineering stresses ($\sigma_{\text{eng.}}$) and strains ($\varepsilon_{\text{eng.}}$) of HR compression on PS 5 and PS 20, shown in Fig. 4.11. The true stress strain values (σ_{true} and $\varepsilon_{\text{true}}$) were computed using the standard analytical conversions.

Specimen	$\sigma_{\text{eng.}}$ (MPa)	$\varepsilon_{\text{eng.}}$ (-)	σ_{true} (MPa)	$\varepsilon_{\text{true}}$ (-)
PS 5 HR, Failure	2086.509	0.437	1174.705	0.574
PS 20 HR, Failure	1831.447	0.335	1217.912	0.408

At the early stage of deformation (except for the low strain cases), as previously discussed, stress equilibrium was not achieved until after 1% strain [82]. Visually inspecting the "elastic" slopes of the stress-strain curves, they are much lower than the literature value of ∼120 GPa for pure titanium [1]. To further investigate the



(a) (b)

Figure 4.11: Engineering stress-strain curves (smoothed) of the PS 5 ($\sim$ 5% pre-strained) and PS 20 ($\sim$ 20% pre-strained) specimens. The red "X" symbols indicate failure occurring at $\varepsilon_{\text{eng.}} > 40\%$ and $\varepsilon_{\text{eng.}} > 30\%$ for PS 5 and PS 20 respectively. The other curves were from the interrupted testing. Results from the early stages cannot be validated due to stress not being in equilibrium.

validity of the data, Davies *et al.* stated that stress equilibrium is only achieved when the stress wave propagates back and forth across the specimen at least three times [121]. In this case, with a specimen length of 2.4 mm and assuming the longitudinal wave speed of pure titanium of 5000 m s^{-1} [122], the time required for the three cycles of wave propagations (wave travelling across six times the length):

$$\mathrm{t}_{\text{required}} = \frac{2.4 \times 10^{-3} \times 6}{5000} = 2.880 \times 10^{-6}\mathrm{s}, \tag{4.1}$$

assuming the deformation was minimal and the total distance travelled was approximately six times the original length of the specimen. At a constant strain-rate of 3500 s^{-1}, stress equilibrium should reached at $\varepsilon_{\text{eng.}} \approx 1\%$:

$$\varepsilon_{\text{eng.}} = 2.88 \times 10^{-6} \times 3500 = 0.01008 \approx 1\%. \tag{4.2}$$

Practically speaking, this slow-rising stress-strain curve is likely an experimen-

tal artifact - gaps between bars, sacrificial discs and specimens, leading to delay in wave propagation. This gap could originate from the rough surfaces and excessive lubricant used, and is usually reduced when the bars are sufficiently compressed during the impact. First, regarding the effect of excessive lubricant, assuming the silicone lubricant is a thin (50 µm) layer of solid material, with a wave speed of $\sim$980 m s^{-1} [123, 124], and a total of 4 possible layers at the specimen-disc and disc-bar interfaces. Using the above assumption of stress equilibrium would yield $\sim 1.224 \times 10^{-6}$ s, which alone has negligible effect on this phenomenon. Next, consider a surface roughness of 15 µm, which is produced by 1200-grit sandpapers. Assuming this is the gap between components, given the four interfaces, this is approximately: $\left(15 \times 10^{-6} \times 4\right) / \left(2.4 \times 10^{-3}\right) = 0.025 = 2.5\%$ strain. While the specimens could still be deforming during this stage, this could explain obscurity of the stress state from the strain gauge data. Note that these calculations should not be considered formal explanations, but only as preliminary assumptions. To reduce this error experimentally, before each test, the discs were ground flat, and the bars, with the specimen sandwiched in between, were pressed together lightly to minimise the gaps. Nevertheless, comparing the data presented here with a published study using the identical compression SHPB system from Zhang *et al.* [97], the initial elastic slopes also have a similar trend. This seems to be an ongoing issue of the SHPB system, or to the extent of other similar SHPB setups.

Continuing onto the issue with the low strain data (PS 5 HR 2 and PS 20 HR 2), it may arise from bar misalignment and wave propagation. The bars in this

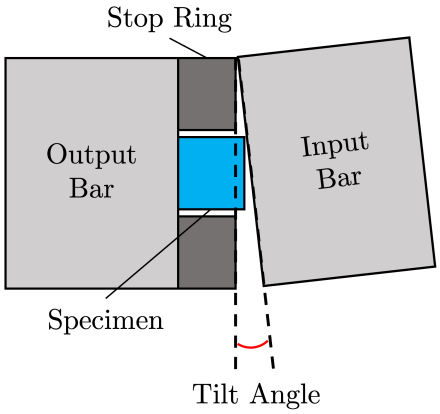


Figure 4.12: A tilted input bar (exaggerated) can cause contact with one side of the stop ring to transmit the incident wave into the output bar before deformation of the specimen occurs.

system were much longer, which could lead to difficulty in maintaining straightness along the entire bars. The stacking of interfaces, bar-disc and disc-specimen, could also lead to accumulation of unparallel surfaces, further worsening the misalignment. Fig. 4.12 shows an exaggerated misalignment of bars. With a bar diameter of 16 mm and the small gap present being 0.06 mm ($L_{specimen} = 2.38$ mm, $L_{ring} = 2.32$ mm), a tilt angle of only $\sim 0.25°$ would result in the input and output bars being in contact via the stop ring. Hence, stress wave could transmit through this interface. This misalignment and the early transmission of stress waves could overlap with the specimen stress waves, rendering the data unusable.

In summary, due to the combined the practical and the theoretical limitations of SHPB at the early stages of deformation, it will be worth revisiting these issues in the future with new experimental and diagnostic techniques. Moving forward, as these tests were conducted in the same condition - same SHPB system and same impact velocities, and the main interest lies in the microstructure characteristics,

the tests were deemed acceptable for subsequent microstructure studies.

4.3.2 Strain-rate dependent mechanical behaviour

The engineering stress-strain curves of the full QS and HR compressions are shown in Fig. 4.13. For both pre-strained materials, the hardening rates remained similar but flow stresses increased with strain-rate. This agrees with the literature that deformation behaviour of titanium is strain-rate sensitive [98].

To extract the hardening rates from the stress-strain curves, a linear regression is fitted to the plastic flow stresses. For the QS curves, Figs. 4.14a and 4.14c show clearly when the stress-strain behaviour deviate significantly from the linear fits at $\varepsilon_{\text{eng.}} \approx 0.3$, indicating the possibility of structural hardening: when the specimen was compressed, the cross-section area increased, leading to a higher force required to continue the deformation. For the HR curves in Figs. 4.14b and 4.14d, the linear fits also serve as extrapolations of the early-stage behaviour which were obscured by the practical and theoretical limitations of SHPB as discussed earlier. The linear fit of the flow stresses is expressed as:

$$\sigma_{\text{eng.}} = \text{a} \times \varepsilon_{\text{eng.}} + \text{b}. \tag{4.3}$$

The parameters a and b are shown in Table 4.6. Both PS 5 and PS 20 exhibit similar hardening rates at different strain-rates.

To quantify the interrupted testing, Young's modulus slopes originating from the recovered (plastic) strain levels, were plotted in each curve. The maximum $\sigma_{\text{eng.}}$

Table 4.6: Parameters of linear regression of plastic flow stresses in Fig. 4.14.

Specimen	a (MPa)	b (MPa)
PS 5 QS	3204.911	482.225
PS 5 HR	3283.494	718.419
PS 20 QS	2490.729	776.501
PS 20 HR	2313.163	1062.390

and $\varepsilon_{\text{eng.}}$ were determined by the intersections between these shifted slopes and the stress-strain curves. For the QS data, the initial stress-strain curves were used. For HR, the linear regression of flow stresses were used instead of the initial curves. This is because Fig. 4.11 does not show the clear maximum $\sigma_{\text{eng.}}$ of the recovered specimens and the earlier stages of deformation were obscured. The yield stresses were obtained using the same method, except slopes started from 0.2% strain. The standard analytical conversions (Eqs. 2.1 and 2.2) were used to compute the maximum σ_{true} and $\varepsilon_{\text{true}}$. These values are shown in Table 4.7, which were then used to correlate with the microstructures. For QS interrupted testing, comparing the maximum forces programmed to the machine and the maximum $\sigma_{\text{eng.}}$ extracted above, they show good agreement and the errors were <5%. For these recovered specimens, it was assumed that no significant microstructural changes occured during elastic unloading. Comparing these against the results from the previous experimental campaign in Chapter 3, Fig. 3.6 shows that the stress-strain behaviour of pre-strained titanium could be closely approximated by shifting to the respective pre-strained levels, while the hardening rate was maintained. Since the results here show that the hardening rates are different, and the approximation did not hold true. The differences show that there are no simple pre-straining metric for titanium, further emphasising the importance of investigating the microstructure features.

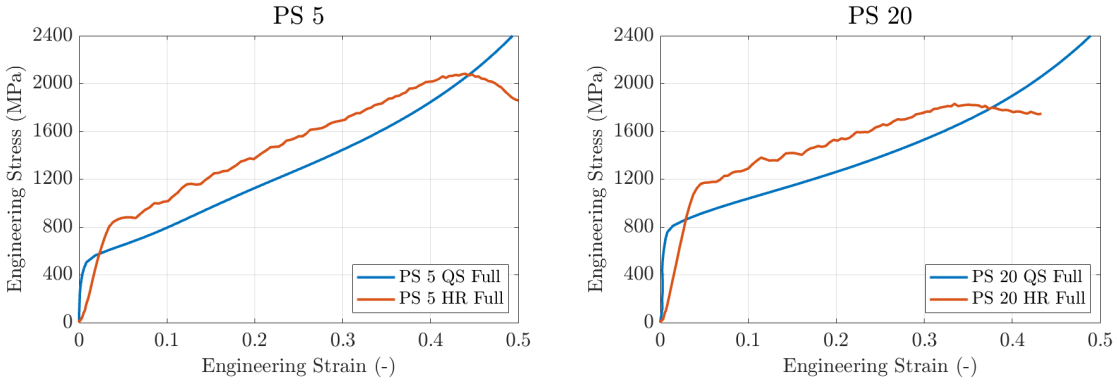


Figure 4.13: The engineering stress-strain curves of QS and HR compressions on PS 5 and PS 20. Note that the HR curves were the same as those from Fig. 4.11. It is clear that the flow stresses increased with strain-rate.

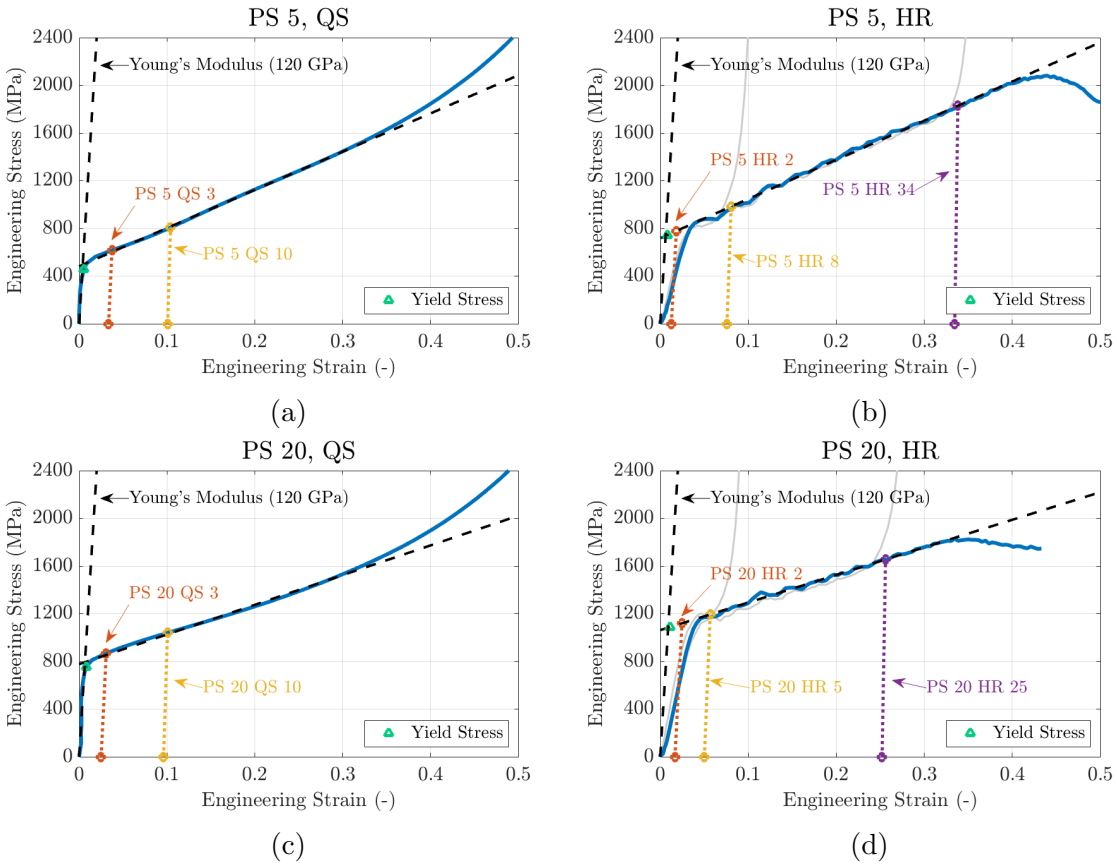


Figure 4.14: Stress-strain curves of the QS and HR compressions on PS 5 and PS 20, with Young's modulus plotted on each curve. For each curve, a linear regression was fitted to the plastic deformation region.

Table 4.7: The maximum engineering stresses and strains ($\sigma_{\text{eng.}}$, $\varepsilon_{\text{eng.}}$), and the analytically-converted true stresses and strains (σ_{true}, $\varepsilon_{\text{true}}$) of the recovered specimens as shown in Fig. 4.14.

Specimen	$\sigma_{\text{eng.}}$ (MPa)	$\varepsilon_{\text{eng.}}$ (-)	σ_{true} (MPa)	$\varepsilon_{\text{true}}$ (-)
PS 5 QS (YS)	458.238	0.006	455.606	0.006
PS 5 QS 3	616.851	0.037	593.751	0.038
PS 5 QS 10	807.552	0.104	723.444	0.110
PS 5 HR (YS)	744.965	0.008	738.941	0.008
PS 5 HR 2	778.709	0.018	764.409	0.019
PS 5 HR 8	982.921	0.081	903.740	0.084
PS 5 HR 34	1828.922	0.338	1210.362	0.413
PS 20 QS (YS)	760.229	0.008	753.987	0.008
PS 20 QS 3	867.996	0.031	841.190	0.031
PS 20 QS 10	1039.138	0.101	934.586	0.106
PS 20 HR (YS)	1069.545	0.011	1058.060	0.011
PS 20 HR 2	1101.857	0.025	1074.786	0.025
PS 20 HR 5	1176.998	0.057	1110.227	0.058
PS 20 HR 25	1642.531	0.256	1222.063	0.296

4.3.3 Microstructures

The EBSD maps were obtained from the centre region of the circular face of each specimen, with the scan area of approximately $(744.10 \times 557.91)\,\mu\text{m}^2$, with an image resolution of 1000 by 750 pixels. The grain boundary misorientation (MO) angle distributions were plotted as histograms with 256 bins, normalised to the probability density. During the pre-straining and the subsequent mechanical testing, loading was applied along the Z-direction, normal to the EBSD maps.

Fig. 4.15 shows the as-received microstructure characteristics, taken from Slice 3 as shown in Fig. 4.6. This batch shows a ring-like radially symmetrical texture - with the c-axis of the grains orienting radially when viewed from the X-Y plane. Each grain exhibited non-uniform orientations, indicated by the colour variations. No twinning was observed from the as-received material.

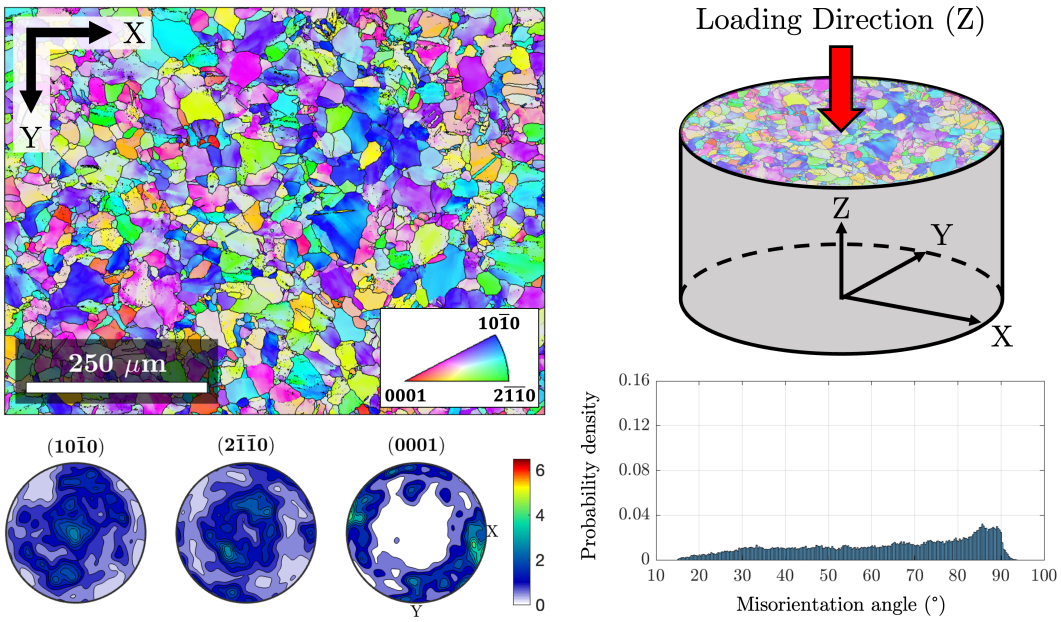


Figure 4.15: The as-received large cylinder of CP-Ti (grade 2) for this study. All the EBSD maps were scanned from the circular face, X-Y plane, and the loading was applied in the Z direction (out-of-plane).

A qualitative description of the recovered microstructures is given here. The EBSD maps, texture plots and MO distributions of PS 5 ($\sim$ 5% pre-strained) and PS 20 ($\sim$ 20% pre-strained) are shown in Figs. 4.16 and 4.17. Qualitatively, the EBSD maps and texture plots of the pre-strained materials, PS 5 and PS 20, are visually different. Both the difference in colours and their respective texture plots indicate a significant difference in the grain orientation distributions. During the pre-straining in PS 5, a small number of grains rotated their c-axis to align with the Z-direction, while PS 20 shows significant grain reorientation, forming a strong basal texture.

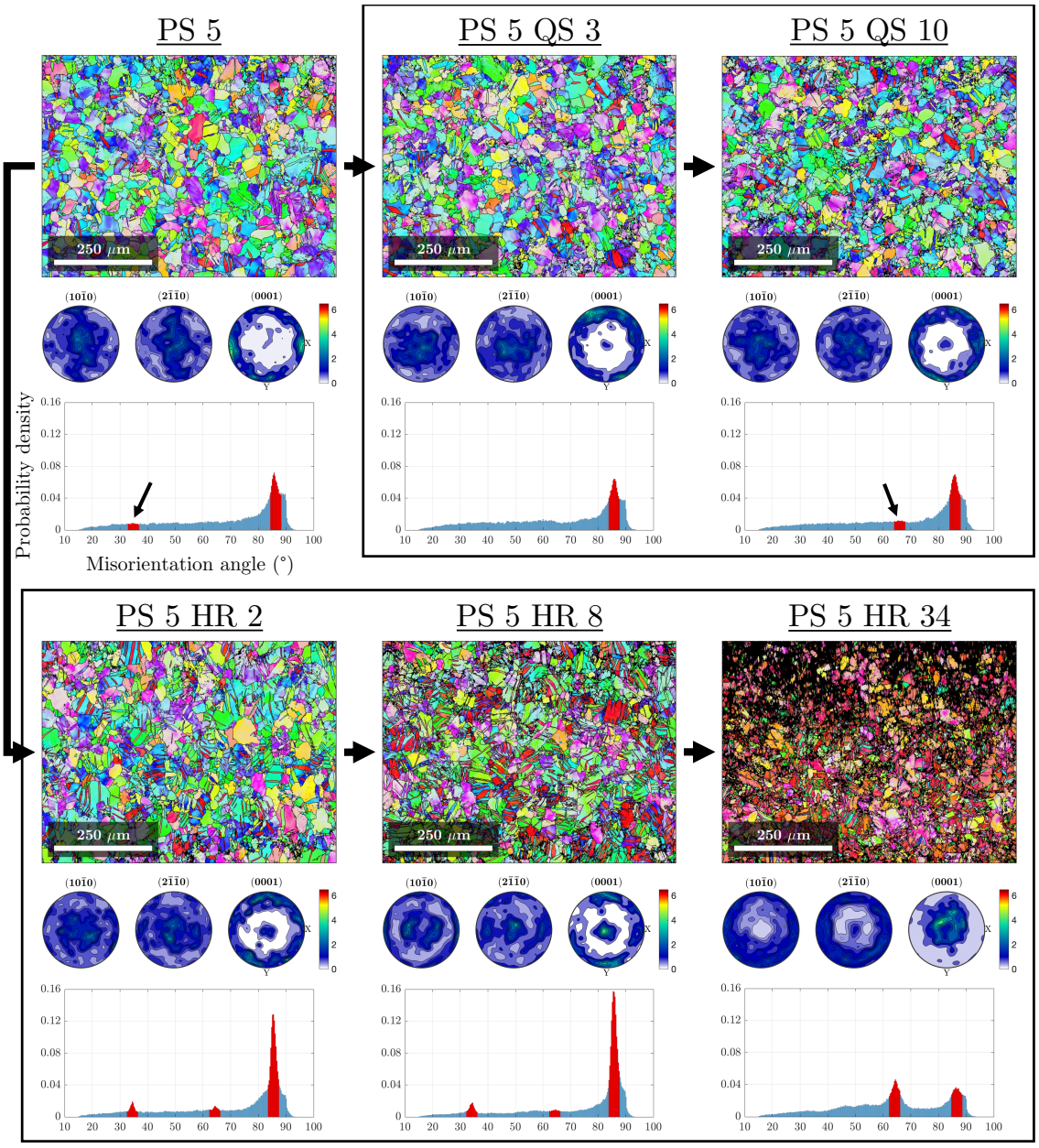


Figure 4.16: The EBSD maps, texture plots and MO distributions of recovered specimens from mechanical testing on PS 5 ($\sim$ 5% pre-strained). Peaks identified in PS 5 and PS 5 QS 10 are likely not twins - possibly due to the sensitivity in peak detections.

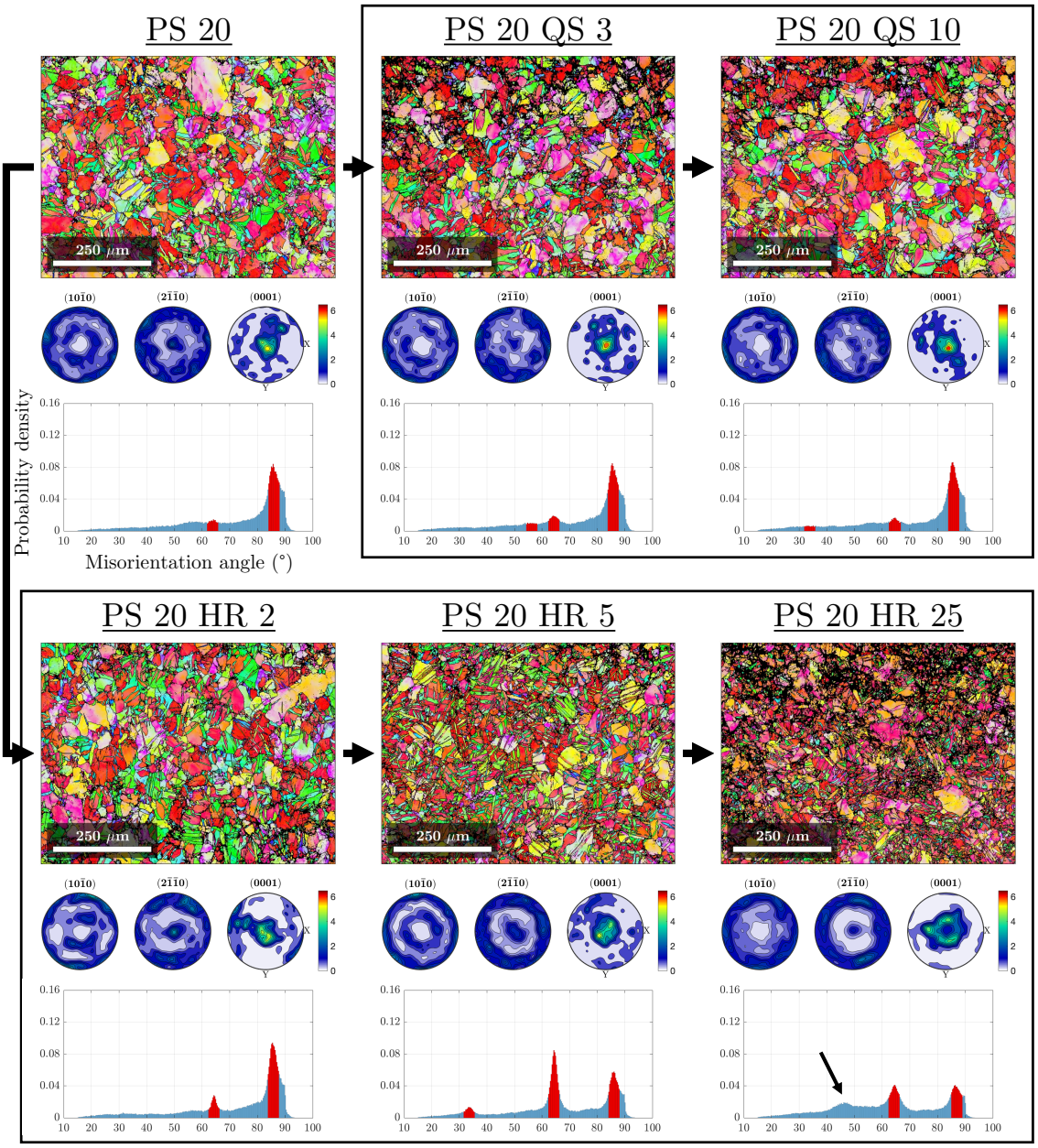


Figure 4.17: The EBSD maps, texture plots and MO distributions of recovered specimens from mechanical testing on PS 20 (∼ 20% pre-strained). In PS 20 HR 25, a peak was identified between 40° and 50°, however it does not correlate to any twin systems from literature.

During the QS compression, PS 5 QS 3/10 show an increase in intensity of the basal orientation (at the centre) in the (0001) plots, gradually forming a weak basal texture, implying grain rotation continued to occur. PS 20 QS 3/10 in contrast, do not show a significant change in texture, which means grain rotation does not occur

at a large scale.

During the HR compression, both pre-strained materials exhibit significant changes in the EBSD maps and texture plots . In PS 5 HR 2, even the onset of yielding caused a rapid occurrence of grain rotation, shown as the increasing intensity of the basal orientation in the (0001) plot. In PS 5 HR 8, grains continued to rotate, gradually transitioning from a ring texture to a basal texture. At the later stage, PS 5 HR 34 shows a moderate basal texture, and even signs of split-poles or formation of multiple poles. On the other hand, PS 20 HR 2 shows a less drastic change in the texture when comparing to PS 5 HR 2. The (0001) plot shows two peaks of similar intensities were formed near the centre, which could indicate the early stage of pole-splitting. In PS 20 HR 5, more significant split poles could be observed. Finally in PS 20 HR 25, multiple poles were formed. It should be noted that, visually inspecting both PS 5 HR 34 and PS 20 HR 25, which were interrupted close to their respective failure strain levels, display very similar microstructure features - namely very strong basal textures and multiple poles forming.

4.4 Discussion 1 - Feature extractions from microstructures

To quantify the differences and changes in the microstructures, various microscopic features were extracted and studied with their respective bulk mechanical properties (stress and strain levels). As the material is a pure, single-phase α titanium, the main differences in the microstructure are primarily the grain features: (1) grain sizes and shapes, (2) grain orientations which affects the Schmid Factors of slip systems, and (3) grain boundary MO angles. No direct measurement of dislocations was obtained. Their activities were instead interpreted by the low-angle grain boundary (LAGB) density and grain orientation spread (GOS). This is because dislocations can pile up to form grain boundaries and can cause small degree of sub-grain rotation [8]. Therefore, the following features were the primary focus of this study:

- MO distributions for twin activities,
- Average grain size, in equivalent diameter,
- Grain shape, the average long and short radii (a and b) of the equivalent ellipses, and the aspect ratios, defined as: a/b,
- LAGB density, sub-grain features from dislocations pile-up,
- GOS, similar to above, but is defined as the average of the misorientation angles of each pixel within a grain, referencing the grain mean orientation,
- Area fraction of grains with the highest Schmid Factor (SF) among all slip

systems considered, and

- Grain orientation in Euler angles: φ_1, ϕ, φ_2.

For some features, such as grain sizes, grain shapes (aspect ratios) and LAGB densities, the mean (average) values will be considered since their distributions are in the form of a skewed normal distribution, as shown in Fig. 4.18. For GOS, the maximum values will be used to compare with literature findings. To analyse the activities of the common dislocation slip systems, the area fractions of high SF indicate the geometric-likelihood of the particular slip system. Here, the critical resolved shear stresses (CRSS's) were not used because the absolute values are often debated [31, 76, 125–127], as many factors including neighbouring grains and dislocation density can affect the measured values. However, it is typically accepted that the Prismatic slip (Pris<a>) has the lowest CRSS, followed by Pyramidal <a> (Py<a>) and Basal (Ba<a>), and the Pyramidal <c+a> slip (Py<c+a>) has the highest CRSS. While the 2nd-order Pyramidal slip (Py II<c+a>) is a possible system, it was not considered in this study due to the high CRSS, and the difficulty to compare with literature as it is often neglected [76, 125, 128, 129].

Other features including MO distributions and Euler angles (for grain orientations), their mean values cannot accurately describe the differences. The following sections will cover the novel methods developed to extract quantifiable metrics from both of these features.

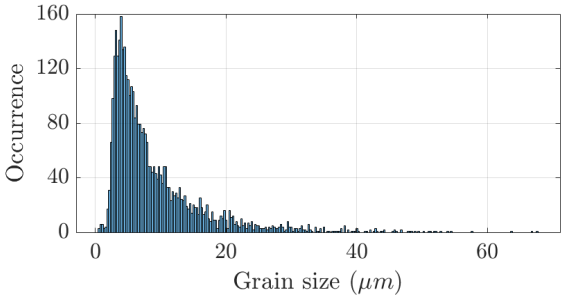


Figure 4.18: An example of the grain size distribution - it has the form of a skewed normal (Gaussian) distribution. As only one peak was identified, the mean value (the average grain size) was considered.

4.4.1 Novel twin identification - Kernel Density Estimation

The twin systems of interest and their corresponding MO angles are shown in Table 4.8. Here, since the goal was to identify the global features of the microstructures, twin activities were determined statistically. The novel method developed to extract quantitative metrics is illustrated in Fig. 4.20, and as follows:

1. The MO angles were plotted as normalised histograms of 256 bins, ranging from 15° (the lowest MO angle of a high-angle grain boundary) to 95°,

2. A Kernel Density Estimation (KDE) model was fitted to the MO data. KDE is a non-parametric probability density model that uses a kernel (function) and a defined bandwidth to estimate the underlying probability density (PD) [130]. Here, a Gaussian kernel was used, and the KDE is expressed as:

$$\rho(\mathrm{x}) = \frac{1}{\mathrm{nh}\sigma} \sum_{\mathrm{i}=1}^{\mathrm{n}} \exp\left(\frac{-(\mathrm{x}-\mathrm{z_i})^2}{2\mathrm{h}^2\sigma^2}\right), \tag{4.4}$$

where **x** is the sequence of 256 values evenly spaced between 15° and 95°, **n** is the the number of MO data points, **z** is the MO dataset, σ is the stan-

dard deviation of dataset **z** and **h** is a user-defined bandwidth. Here a fixed bandwidth of $\mathbf{h} = 256/(95-15)/2 = 1.6$ was used throughout the dataset,

3. From the KDE, peaks were then identified by comparing each point with its neighbouring points to determine the local maxima. As twins are known to appear at certain MO angles, after the initial algorithm, extra peaks that did not fall into the range of possible twin systems were manually removed,

4. After the twin peaks were identified, the MO data points that fell within the range of $\pm 2^\circ$ of the peak values were counted towards the "twin boundary fractions" - the ratios of "twin boundaries" to"total grain boundaries", and were highlighted in the MO plots in Figs. 4.16 and 4.17.

All these operations were executed using the *Python* packages *SciKit-Learn* [105] and *SciPy* [131].

Regarding the choices of parameters, first, the number of points (256) were chosen as a good balance between the smoothness of KDE and computation speed. Second, the $\pm 2^\circ$ for the twin boundary fractions was chosen for its ability to reconstruct the MO distributions, which will be discussed in details in Chapter 5.3.1. Third, for the bandwidth value, there are debates whether a fixed or a dynamic value is more suitable [132–134]. In general, a large **h** will lead to over-smoothing and obscure the peaks, and a small **h** will lead to under-smoothing. The most common dynamic bandwidth calculation is the Scott's Rule, which yielded bandwidths of 1.23 to 2.44, with a mean of 1.90, for this study. Fig. 4.19 shows that the KDE's with a fixed and dynamic bandwidth are mostly overlapping. However, subsequent analyses showed

that dynamic bandwidths led to more false peaks (not twin-related) being identified. Due to the small dataset in this study and the fixed value of 1.6 showing good fitting to the histogram data, it was chosen for this analysis.

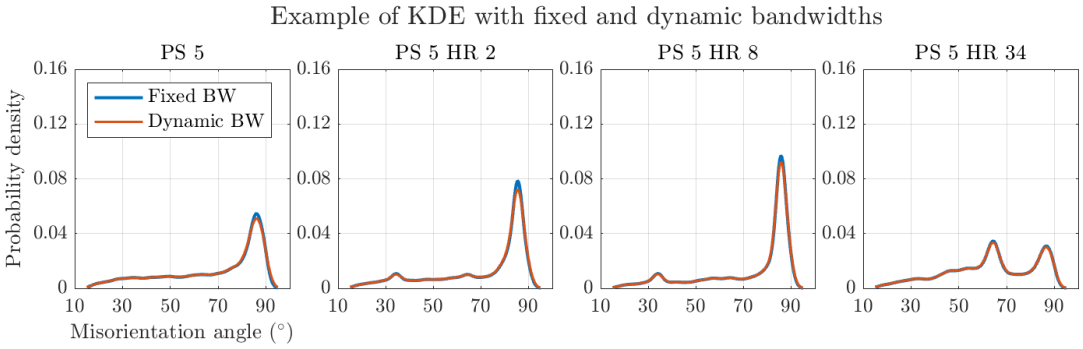


Figure 4.19: Examples of KDE with a fixed (1.6) bandwidth and a dynamic bandwidth using Scott's Rule.

Table 4.8: Twin boundary fractions of individual twin systems. Note that the $\{11\bar{2}4\}$ ($\sim$77°) system was not detected statistically from any of the specimens in this study.

Specimen	$\{11\bar{2}1\}$	$\{10\bar{1}1\}$	$\{11\bar{2}2\}$	$\{11\bar{2}4\}$	$\{10\bar{1}2\}$	Total
	$\sim$35°	$\sim$57°	$\sim$64°	$\sim$77°	$\sim$85°	-
PS 5	0.031	0	0	0	0.228	0.259
PS 5 QS 3	0	0	0	0	0.207	0.207
PS 5 QS 10	0	0	0.044	0	0.229	0.273
PS 5 HR 2	0.044	0	0.041	0	0.336	0.421
PS 5 HR 8	0.046	0	0.031	0	0.421	0.498
PS 5 HR 34	0	0	0.147	0	0.130	0.276
PS 20	0	0	0.048	0	0.288	0.336
PS 20 QS 3	0	0.037	0.066	0	0.281	0.384
PS 20 QS 10	0.023	0	0.054	0	0.285	0.362
PS 20 HR 2	0	0	0.073	0	0.308	0.382
PS 20 HR 5	0.042	0	0.232	0	0.190	0.465
PS 20 HR 25	0	0	0.136	0	0.141	0.277

1. The grain boundary misorientation angles are plotted as a normalised histogram (256 bins, as probability density) to show the distribution.

2. A KDE (kernel density estimation) is fitted to the MO data and plotted against the histogram.

3. Peaks are identified from the KDE.

4. Data around each peaks (± 2°) are highlighted and counted towards "twin boundary fractions".

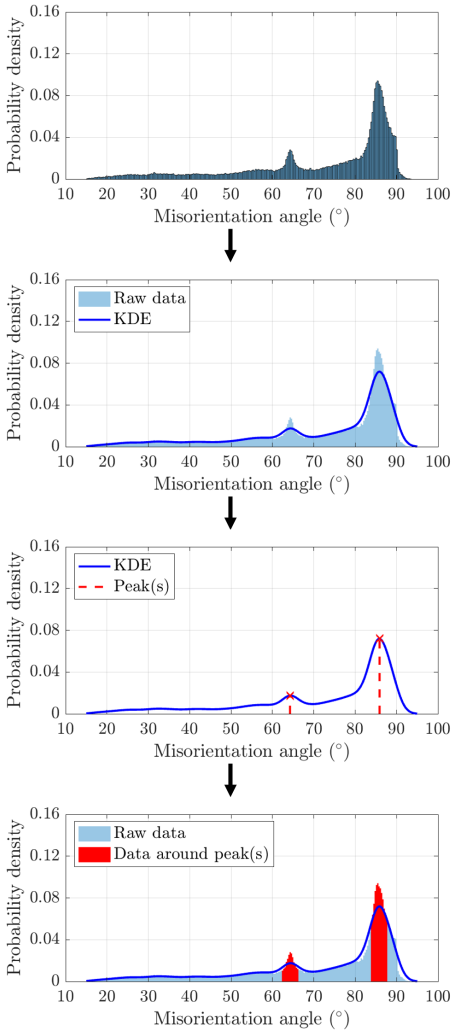


Figure 4.20: The twin system identification method: (1) the grain boundary MO angles are plotted as a histogram with 256 bins and normalised to a probability density, (2) a KDE (Kernel Density Estimation) is fitted to the data and plotted against the histogram, (3) peaks are identified from the KDE - a smoother transition than the histogram heights, and finally (4) data around the peaks are highlighted, and counted as the twin boundary fraction of the specific twin system.

4.4.2 Grain orientations - Gaussian Mixture

Using MTEX for data processing, the average grain orientations were computed as Euler angles (φ_1, ϕ and φ_2), as shown in Fig. 4.21. The reference grain, with Euler angles of (0, 0, 0), is positioned with the basal plane normal to the EBSD map Z-axis (out-of-plane), and one of the prismatic planes normal to the X-axis. The

grain rotation is described by the Bunge convention [135]: z(φ_1) → x(ϕ) → z(φ_2). Here, the x axis identical to the c axis of the HCP crystal.

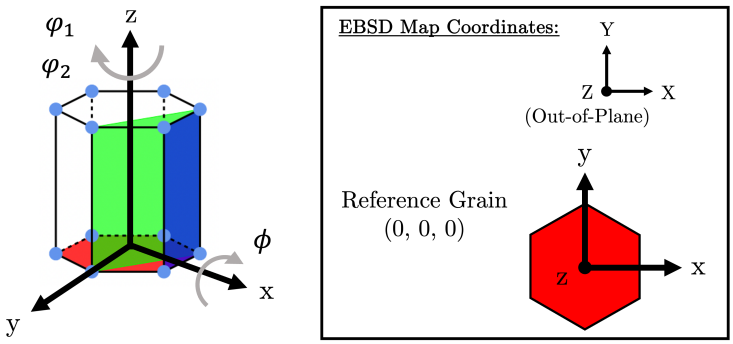


Figure 4.21: Grain orientation expressed as Euler angles (φ_1, ϕ, φ_2). The reference grain with Euler angles (0, 0, 0) is shown against the EBSD map (global) coordinates.

To extract quantitative features from the Euler angles, an example of the distributions is shown in Fig. 4.22. As the deformation increased from PS 5 to PS 5 HR 34, changes in φ_1 and φ_2 do not follow any clear trends, while ϕ shows a 2-component mixed distribution in each case. From the reference grain, it becomes obvious that the ϕ angle (rotation around the x-axis) is directly correlated to the c-axis rotation, and therefore the grain orientation distribution and the overall texture of the microstructure. This feature strongly affects the bulk yield and flow stress as it changes the Schmid Factors (SF) of slip systems. Here, as the c-axis rotates and becomes more aligned with the bulk coordinate Z-axis, the SF's of all slip systems with slip direction <a> will gradually reduce to zero (cos(90°)=0). As both B<a> and Pris<a> slip systems have low CRSS's, grains with this orientation are then considered hard grains due to the increased in stress required to activate other slip systems and mechanisms [136–138].

Gaussian Mixture models were fitted to the ϕ distributions to obtain the means (μ), standard deviations (σ) and weights (relative ratios) of the two underlying

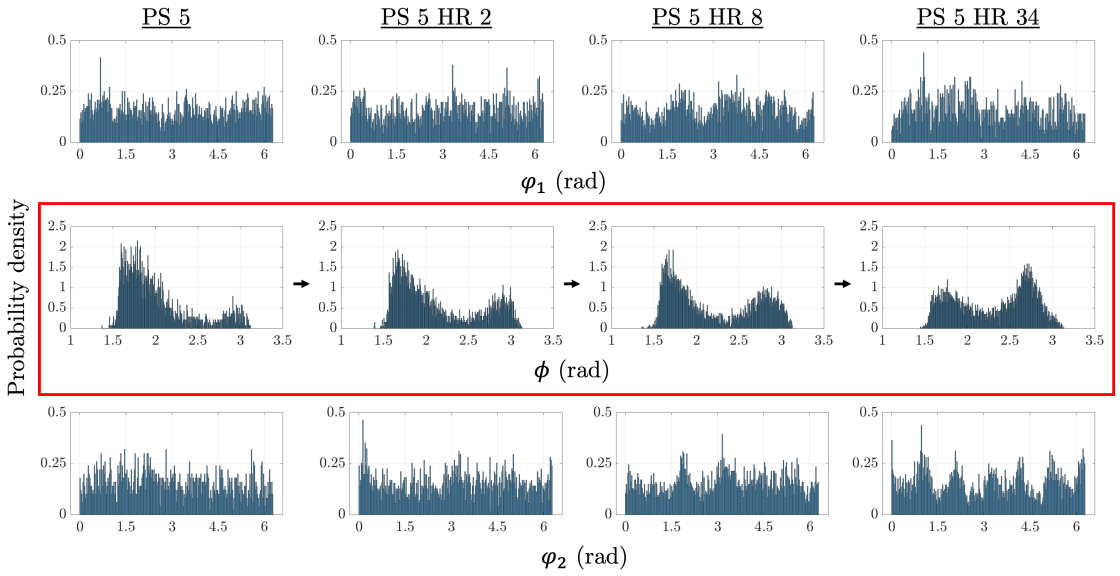


Figure 4.22: Examples of Euler angles (φ_1, ϕ, φ_2) distributions for the PS 5 HR specimens. Only ϕ shows quantifiable differences and was therefore considered as the metric for grain orientation evolution.

components. Fig. 4.23 shows the general steps taken to obtain these quantities. The component with the smaller mean value is labelled "GM1", while the larger one is labelled "GM2". A brief description of the Gaussian Mixture (GM) model fitting is given here:

1. The GM model assumes the dataset can be described by a mix of Gaussian distributions, with the probability density function with **K** components:

$$\mathrm{p}\left(\mathcal{X}\right) = \sum_{\mathrm{k}=1}^{\mathrm{K}} \left[\mathrm{w_k}\, \mathcal{N}\left(\mathcal{X}|\mu_\mathrm{k}, \Sigma_\mathrm{k}\right)\right] \tag{4.5}$$

where $\mathcal{X}$ is the dataset with D dimensions, $\mathrm{w_k}$ is the weight of the k-th component, $\mathcal{N}$ is a multi-variate Gaussian distribution with mean μ and covariance

Σ:

$$\mathcal{N}\left(\mathcal{X}|\mu_{\mathrm{k}},\Sigma_{\mathrm{k}}\right)=\frac{1}{\left(2\pi\right)^{\mathrm{D}/2}\left|\Sigma_{\mathrm{k}}\right|^{1/2}}\exp\left(-\frac{1}{2}\left(\mathcal{X}-\mu_{\mathrm{k}}\right)^{\mathrm{T}}\Sigma_{\mathrm{k}}^{-1}\left(\mathcal{X}-\mu_{\mathrm{k}}\right)\right). \tag{4.6}$$

2. The parameters, w, μ and Σ for each component **k** are estimated using the Expectation-Maximisation algorithm [139]. The **Expectation** step computes the "responsibility" γ_{ik}, which is the posterior probability that a data point $\mathrm{x_i}$ (from $\mathcal{X}$) falls in the k-th component of mixture:

$$\gamma_{\mathrm{ik}}=\frac{\mathrm{w_k}\,\mathcal{N}\left(\mathrm{x_i}|\mu_{\mathrm{k}},\Sigma_{\mathrm{k}}\right)}{\sum_{\mathrm{j}=1}^{\mathrm{K}}\left[\mathrm{w_j}\,\mathcal{N}\left(\mathrm{x_i}|\mu_{\mathrm{j}},\Sigma_{\mathrm{j}}\right)\right]}. \tag{4.7}$$

After the random initialisation of parameters, the **Maximisation** step then iteratively updates the parameters until convergence is reached. The parameters are updated as follows:

$$\mathrm{N_k}=\sum_{\mathrm{i}=1}^{\mathrm{N}}\gamma_{\mathrm{ik}}, \tag{4.8}$$

$$\mu_{\mathrm{k}}=\frac{1}{\mathrm{N_k}}\sum_{\mathrm{i}=1}^{\mathrm{N}}\left[\gamma_{\mathrm{ik}}\mathrm{x_i}\right], \tag{4.9}$$

$$\Sigma_{\mathrm{k}}=\frac{1}{\mathrm{N_k}}\sum_{\mathrm{i}=1}^{\mathrm{N}}\left[\gamma_{\mathrm{ik}}\left(\mathrm{x_i}-\mu_{\mathrm{k}}\right)\left(\mathrm{x_i}-\mu_{\mathrm{k}}\right)^{\mathrm{T}}\right], \tag{4.10}$$

$$\mathrm{w_k}=\frac{\mathrm{N_k}}{\mathrm{N}}, \tag{4.11}$$

where N is the number of data points in the dataset $\mathcal{X}$, and $\mathrm{N_k}$ is the number of data points in the k-th component with the parameters.

1. One of the components of Euler angles, $\boldsymbol{\phi}$, is plotted as a histogram and normalised as the probability density.

2. A 2-component Gaussian Mixture (GM) is fitted to each histogram. The component with a lower mean value is labelled as "GM1", and the larger component is labelled "GM2".

3. Each component (GM1 and GM2) contains the mean, standard deviation and weight (relative ratio).

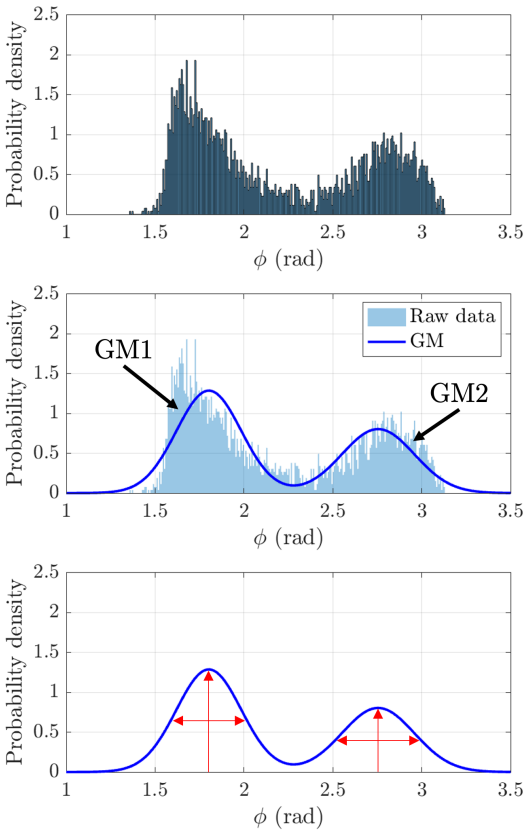


Figure 4.23: Extracting statistical features from the distributions of Euler angle Phi (ϕ): (1) plot a histogram, normalised to the probability density, (2) fit a Gaussian Mixture (GM) model with 2 components on each histogram to extract two underlying Gaussian distributions, (3) for each component, GM1 and GM2, extract the means, standard deviations and weights - which represents the ratio of each component.

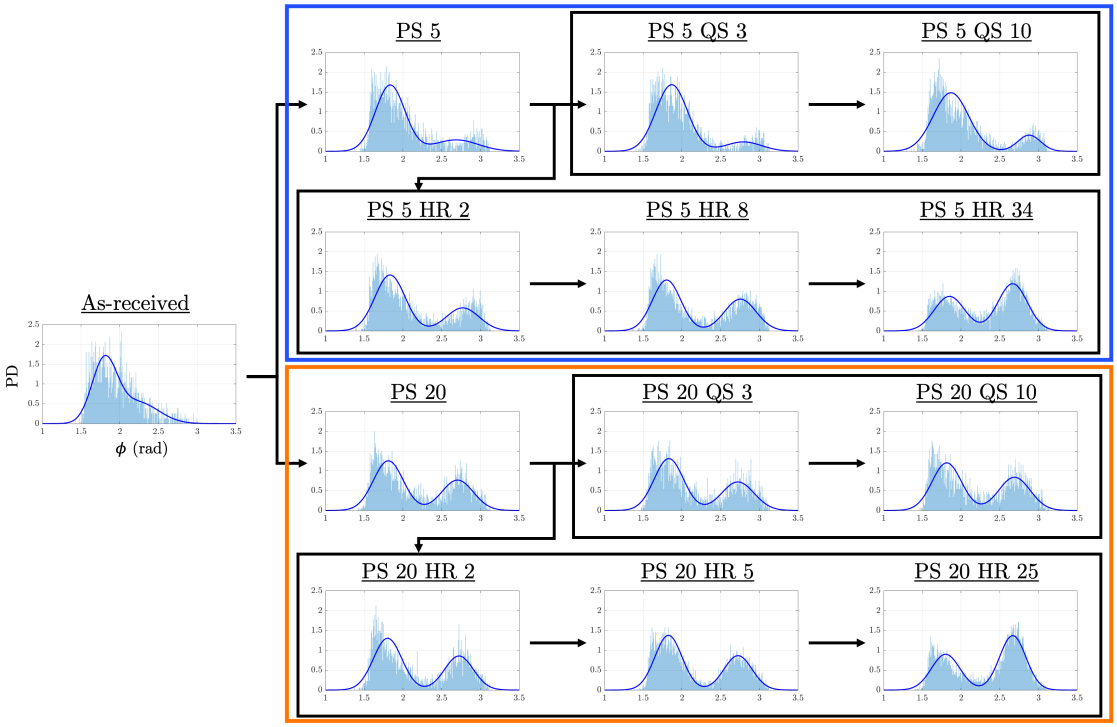


Figure 4.24: The evolution of ϕ distributions, with a two-component Gaussian Mixture model fitted to each histogram. The histograms are normalised to the probability density (PD).

Table 4.9: Mean, standard deviation (Std. Dev.) and weight of the components, GM1 and GM2, of the Gaussian Mixture fitted to each ϕ distributions.

Specimens	GM1			GM2		
	Mean	Std. Dev.	Weight	Mean	Std. Dev.	Weight
As-received	1.801	0.162	0.634	2.230	0.270	0.366
PS 5	1.835	0.189	0.796	2.686	0.282	0.204
PS 5 QS 3	1.868	0.204	0.860	2.796	0.234	0.140
PS 5 QS 10	1.870	0.229	0.849	2.880	0.147	0.151
PS 5 HR 2	1.833	0.195	0.690	2.771	0.212	0.310
PS 5 HR 8	1.803	0.183	0.589	2.755	0.204	0.411
PS 5 HR 34	1.850	0.197	0.431	2.667	0.190	0.569
PS 20	1.811	0.193	0.607	2.704	0.204	0.393
PS 20 QS 3	1.831	0.189	0.621	2.723	0.210	0.379
PS 20 QS 10	1.815	0.189	0.572	2.691	0.203	0.428
PS 20 HR 2	1.802	0.184	0.601	2.723	0.186	0.399
PS 20 HR 5	1.826	0.175	0.606	2.725	0.181	0.394
PS 20 HR 25	1.801	0.183	0.414	2.668	0.170	0.586

4.5 Discussion 2 - Microstructure evolutions

4.5.1 Early-stage deformation

This section aims at investigating the early stages of deformations of both pre-strained materials, PS 5 and PS 20, at QS and HR compression. Both materials exhibit distinctive differences in the microstructure characteristics at different strain-rates, which in turns affect the yield stresses, flow stresses and hardening.

Pre-strained microstructures

Comparing the textures of the pre-strained microstructures, PS 5 had a strong prismatic/pyramidal texture, and PS 20 had a strong basal texture. This can be quantitatively identified by the ϕ distributions shown in Fig. 4.30. Since PS 5 showed less changes compared to the as-received material, the first component, GM1, of the Gaussian Mixture distribution can be associated with the prismatic/pyramidal orientation. The significantly higher weight of GM2 shown in Fig. 4.30c is then associated with the basal orientation. When comparing the mean values, GM1 has a mean of 1.8 rad$\approx$103°, and GM2 2.7 rad$\approx$155°, which indicate that GM1 grains have their c-axes rotated $\sim$77° forming a prismatic/pyramidal orientation, and GM2 grains $\sim$25° forming a split-pole basal texture.

The MO distributions in Figs. 4.16 and 4.17 show that the $\{10\bar{1}2\}$ ($\sim$85°) twin was activated in both materials. The higher peak in PS 20 indicates a higher fraction of twin boundaries. Note that the $\{11\bar{2}2\}$($\sim$35°) twin was possibly misidentified

from the PS 5 specimen due to sensitivity of the analysis method. While existing literature suggests that hardening due to twinning is often associated with grain orientation changes [140] and Hall-Petch effect from grain size reduction [141], the current results do not suggest that they are the main contributing factors. When examining the grain sizes of PS 5 and PS 20 (Fig. 4.25a), they are still within the range of 7 µm to 13 µm, which do not increase the yield stresses according the Hall-Petch equation [12, 13]. Instead, hardening is likely caused by twin boundaries acting as a specific type of grain boundaries. When mobile dislocations within a parent grain encounter a twin boundary, El Kadiri and Oppedal [142] found that they would undergo a transmutation process which increases the number of dislocations in the twinned region. Guo *et al.* [117] proposed that the high stress concentration around twin tips, combined with twin-induced internal stresses identified by Fitzner *et al.* [143] further support that hardening due to twinning should be treated as a separate mechanism.

Microstructure evolutions

Figs. 4.16 and 4.17 show that the microstructures changed more drastically under HR. This is due to the transient nature of dislocation slips, twinning was more active at HR [15, 24, 108]. This resulted in more significant changes in grain orientation [2, 29], as shown in the EBSD maps and texture plots.

Since grain sizes were computed as the diameters of equivalent circles, this metric neglects the shape of twins, which were thin laths when they first nucleate. Fig.

4.26c shows a common method for quantifying grain shapes. With an equivalent ellipse (instead of a circle) fitting to a grain, the long and short (a and b) radii can be obtained (Figs. 4.26a and 4.26b). The aspect ratio is defined as a/b. Fig. 4.25b shows that both PS 5 and PS 20 display very little changes in the aspect ratios in QS, while in HR the aspect ratios both increase at the early stages. This indicates that at the early stages of deformation, twin nucleations occured more frequently in HR than in QS. This confirms that twinning is a strain-rate sensitive mechanism, and both orientation and pre-activated twins do not seem to affect it in a statistical sense.

Although the starting orientations of the two materials are different, the changes in microstructures of both under QS compression are very small. It suggests that other mechanisms such as dislocation activities and grain rotation contributed to strain accommodation. As dislocations were not directly observed, LAGB density and GOS are used to deduce dislocation activities [8, 144]. From Fig. 4.27, in PS 5 QS, while LAGB density increases, GOS first increases then decreases. In PS 20 QS, LAGB decreases while GOS is essentially unchanged. Considering that PS 20 has been pre-strained to a higher degree than PS 5, and the as-received microstructure exhibits a high GOS (Table 4.12), similar behaviour was observed by Muñoz *et al.* [145]. They showed that both GOS and LAGB increased at the initial stages, and GOS began to decrease at an earlier stage than LAGB. It implies that in PS 5 QS, new dislocations were generated first, causing a higher variation in sub-grain orientation, hence a higher GOS value. Dislocation slips then occured, which either piled up to form LAGB's, or annihilated each other causing recrystallisation as indicated

by the decrease in GOS.

In contrast, PS 20 QS shows an initially higher LAGB density, which decreases with deformation. Zhou *et al.* [146] proposed that as mobile LAGB's can be annihilated by HAGB's by mechanisms such as dislocation absorption and interpenetration, which likely occured due to the higher initial LAGB density. Twinning was also involved in strain accommodation, as shown in Figs. 4.29c and 4.31. The $\{11\bar{2}2\}$ ($\sim$64°) was activated in PS 20 QS 10, which is usually activated in "hard grains" unfavourable for Pris<a> slip [16, 31, 147, 148].

Inspecting the area fractions of the highest Schmid Factor (SF) of each slip systems (Fig. 4.28) reveals that in PS 5 QS, no particular slip system was highly geometrically-favoured. Table 4.10 shows the CRSS values obtained from literature [76, 125, 128, 129, 149]. The activities of Pris<a> and Py<a> slips were geometrically-favoured. This increased dislocation interactions, which could lead to an increase in dislocation generation and pile-ups [10, 11], causing the high hardening rate in the stress-strain curve. In PS 20 QS, the lower area fraction of Pris<a> slip led to the opposite effect. The slip system with a higher CRSS, Py<c+a>, was geometrically-favoured. This increased the threshold for yielding, which caused higher flow stress. However, the reduced dislocation interactions led to a lower hardening rate. The overall QS deformation mechanisms are in good agreement with existing literature findings, which state that mechanical behaviour of titanium is texture-dependent [28, 30, 150].

Table 4.10: The CRSS values (in MPa) of titanium obtained from literature.

Reference	**Ba<a>**	**Pris<a>**	**Py<a>**	**Py<c+a>**
[128]	175	68	120	250
[129]	180	90	140	210
[125]	127	96	-	>240
[149, 151]	332	155	202	363
[76]	170	90.5	-	210

The mechanisms in HR are different from those in QS due to the involvement of twinning, despite the stress-strain curves (Fig. 4.13) indicating similar hardening rates with the same material. Figs. 4.29b and 4.29d show that twin boundaries increased at the early stages of HR deformation. At the onset of yielding, Fig. 4.32 shows that twin nucleation occured at a higher rate in PS 5 HR when compared to PS 20 HR. Investigating the individual twinning systems (Fig. 4.31), in PS 5 HR, the pre-activated $\{10\bar{1}2\}$ ($\sim$85°) twin continued to nucleate rapidly, while simultaneously activating the $\{11\bar{2}1\}$ ($\sim$35°) and $\{11\bar{2}2\}$ ($\sim$64°) twins. The $\{11\bar{2}2\}$ twin was far less active due to the high shear strain it imposed on the grains [106]. Twin growth was also prominent as shown by the rapid increase in GM2 weight in Figs. 4.30b. Compared to PS 20 HR, the $\{11\bar{2}2\}$ and $\{10\bar{1}2\}$ twins were pre-activated in the pre-straining stage. While both twins continued to nucleate, the $\{11\bar{2}2\}$ nucleated more rapidly. The $\{11\bar{2}1\}$ twin also nucleated at this stage. However, twin growth was likely limited due to the relatively small changes in texture.

The reason for the difference in activities of specific twin systems could have been suggested by several studies [71, 143, 147, 148]: the $\{10\bar{1}2\}$ twin occurs at "soft grains" well-oriented for Pris<a> slip (in PS 5), and the $\{11\bar{2}2\}$ occurs in

"hard grains" (in PS 20). Since growth of $\{10\bar{1}2\}$ is less restricted due to the easier accommodation by Pris<a> slip, this twin tends to consume the entire grain, thus changing the grain orientation from prismatic/pyramidal to basal [152]. Compared to the $\{11\bar{2}2\}$ twin which nucleated in hard grains, since less slip systems are available to accommodate the twin shear, growth is restricted but nucleation is favoured, leading to more twin boundaries [71, 152]. The quantitative differences of the twinning activities are shown in the changes in twin boundary fractions (Fig. 4.32) and GM2 weights of ϕ distributions (Fig. 4.33f). In PS 5 HR, since both aspects increase, it indicates that twin nucleation and growth were present. In PS 20 HR, only the twin boundary fractions increase, which implies twin nucleation occured more frequently than twin growth. Since twin boundaries act as barriers to dislocation mobility, the higher fraction in PS 20 HR explains the higher flow stresses. The lower twin growth corresponds to less changes in grain orientation, therefore the hardening rate of PS 20 HR remained low.

Twin-induced grain reorientation directly affects the SF's of different slip systems [147, 148]. In the early stages of PS 5 HR, the higher growth rate of the $\{10\bar{1}2\}$ twin resulted in more severe changes to the area fractions of geometrically-favoured slip systems. Fig. 4.28 shows that the area fraction of Py<a> increased with deformation, while the area fraction of Pris<a> first decreased then increased, and the area fractions of Py<c+a> first decreased then increased. The low CRSS Pris<a> was still highly favoured, which resulted in lower flow stresses. Conversely, in the early stages of PS 20 HR, the area fraction of Pris<a> remained low, while the

area fractions of Py<a> and Py<c+a> increased. The high CRSS of Py<c+a> led to higher flow stresses required to activate it. In both PS 5 and PS 20, while the starting area fractions of Ba<a> were different, they converged and overlapped, leading to difficulty in delineating its contributions.

Inspecting the LAGB densities and GOS in Figs. 4.27a and 4.27c, PS 5 HR shows a slow increase in LAGB densities, and an initial increase then slight decrease in GOS. Since GOS remained high, it signifies that there is a high level of dislocation activities. Existing literature identified that grain and twin boundaries can act as dislocation multiplication sources [142, 153]. As twin growth was favoured in PS 5 HR, the twin boundaries swept through their parent grains, increasing the chances of encountering dislocations. This could lead to an increase in dislocations in the twinned regions, subsequently leading to a high hardening rate. In PS 20 HR, the LAGB densities increased rapidly, but GOS remained low and virtually unchanged. Chen and Yu [154] proposed that LAGB's could act dislocation nucleation sites, and allowed partial transmission of dislocations, unlike regular HAGB's. Mobile dislocations likely piled up to form additional LAGB's. The migration of LAGB's themselves acted as strain accommodation mechanism. The mechanisms involving LAGB's reduced dislocation interactions, resulting in a low hardening rate.

The mechanisms involved in the **early stages of deformation** can be described as below:

- **QS vs HR**: As dislocation slip occurs at a lower rate than deformation twin-

ning, more twinning activities can be observed at HR deformations in both pre-strained materials as suggested by the increase in grain aspect ratios.

- **PS 5 QS**: Pre-straining increased the dislocation densities but did not change the texture. The low CRSS Pris<a> and Py<a> were geometrically-favoured, more dislocation interactions occured, resulting in high hardening rate. The pre-activated twinning did not play an important role.

- **PS 20 QS**: The strong basal texture meant the Pris<a> slip was less favoured while the high CRSS Py<c+a> slip was more favoured. This led to a higher threshold for yielding, but lowered the chances of dislocation interactions, hence lower hardening rate. Additionally, the $\{11\bar{2}2\}$ twin was activated.

- **PS 5 HR**: Although the hardening rate is similar only with higher flow stresses, the fundamental mechanisms were different. In particular, statistical evidence suggests that the $\{10\bar{1}2\}$ twin growth and Pris<a> slip were favoured. The twin boundary migration due to twin growth likely increased the chances of encountering dislocations in the parent grains. Since twin boundaries acted as a dislocation multiplication source, the dislocation densities in twinned regions likely increased, as indicated by the high GOS. This resulted in a high hardening rate.

- **PS 20 HR**: Nucleation of the $\{11\bar{2}2\}$ twin nucleation was favoured, and the Py<c+a> was geometrically-favoured. The high CRSS of this slip system and the increase in twin boundaries acting as obstacles drastically increased the flow stresses. The high LAGB density suggests that mobile dislocations piled

up. The migration of LAGB's acted as a strain accommodation mechanism, and dislocations were allowed to transmit them. This reduced dislocation interactions, causing a low hardening rate.

4.5.2 Incipient failure

As no failure was observed in QS compression, only failure in HR will be studied. The EBSD maps (Figs. 4.16 and 4.17) show that both microstructures, PS 5 and PS 20, were rather similar when approaching failure. While the failure $\sigma_{\text{eng.}}$ (Table 4.5) are different (∼13% difference), the failure σ_{true} were quite similar (∼3.6% difference).

From the statistical features at the incipient failure stages, both specimens show a decrease in aspect ratios (Fig. 4.25b) and decrease in twin boundary fractions (Fig. 4.31), indicating a decrease level of twinning activities when deformation reached a certain level. Interestingly, both twin boundary fractions were quite similar, with the remaining twin types being $\{11\bar{2}2\}$ and $\{10\bar{1}2\}$, which also show similar levels in both specimens. Fig. 4.25 shows that while the grain size in PS 20 HR 25 was slightly smaller than that of PS 5 HR 34, both aspect ratios reverted back to the starting values. This strongly suggests that recrystallisation occured. The ϕ distributions show that the grain orientations are similar, with the GM2 weight being significantly higher than GM1, as shown in Figs. 4.33e and 4.33f. The GM2 mean values were slightly shifted (Table 4.9). Together, it means both materials show a split-basal texture.

Fig. 4.27a shows that the LAGB densities increased in both PS 5 HR and PS 20 HR. Combined with the reduction in grain sizes and reduced twin boundaries identified above, dynamic recrystallisation likely occured, supported by existing literature [102, 112] and the similar results from Chapter 3. The LAGB density in PS 20 HR 25 was much higher than that of PS 5 HR 34, while the GOS in PS 5 HR 25 remained high. This implies the fundamental differences in the dislocation structures, with the dislocations in PS 5 were less likely to pile up and therefore maintaining a high internal stress, and PS 20 formed more ordered arrays of dislocations in terms of LAGB's. Slip activities from Fig. 4.28 shows that in both PS 5 and PS 20, the Pris<a> slip was essentially inactive, Ba<a> and Py<c+a> slip activities increased while Py<a> slip decreased to similar levels. As dislocations have been accumulating through deformation, the CRSS's for slip systems would increase due to the hardening effect, as suggested by existing literature, [128, 149], which assigned hardening parameters to slip systems in numerical models. PS 5 likely experienced low dislocation mobility due to high internal stresses, limiting the use of slip and twin nucleation/growth as effective plasticity carriers. PS 20 contained extremely high LAGB density, which led to difficulty in using boundary migration as a plasticity carrier due to the stresses around LAGB's as observed by [154]. Eventually, the tremendous amount of dislocations would pile up forming stress concentration zones, eventually leading to failure through micro-void coalescence [8]. It is hypothesised that the high LAGB density in PS 20 HR resulted in a delayed failure due to the ability of LAGB's to resist crack growth, previously suggested by Li *et al.*

[155]. The failure mode could therefore be considered more ductile compared to PS 5 HR. Although current experimental limitations did not allow for investigation of compressive failure (the fragments were simply re-compressed together), this will be worth investigating in the future with more advanced design of experiments.

To summarise the findings in HR incipient failure (no failure observed in QS), evidences from microstructure features suggest that, regardless of the starting microstructure of the specimens, they eventually evolve and converge into very similar twin boundary fractions (MO distributions) and grain orientation (ϕ distributions). To explain the differences in failure $\sigma_{\text{eng.}}$, it is linked to the dislocation structures and activities. The differences in LAGB density and GOS suggest that PS 5 maintained a high-degree of internal stresses, while PS 20 formed ordered dislocation arrays in the form of LAGB's. Analysing the slip activities revealed that both materials could no longer employ slip as a strain accommodation mechanisms due to the high dislocation densities and the low CRSS slip (Pris<a>) being unfavoured. This ultimately initiated material failure.

Table 4.11: The average grain sizes (Fig. 4.25a) , grain shapes in aspect ratios AR (Fig. 4.25b), and the average long and short radii, labelled a and b respectively, of an equivalent ellipse, shown in Fig. 4.26.

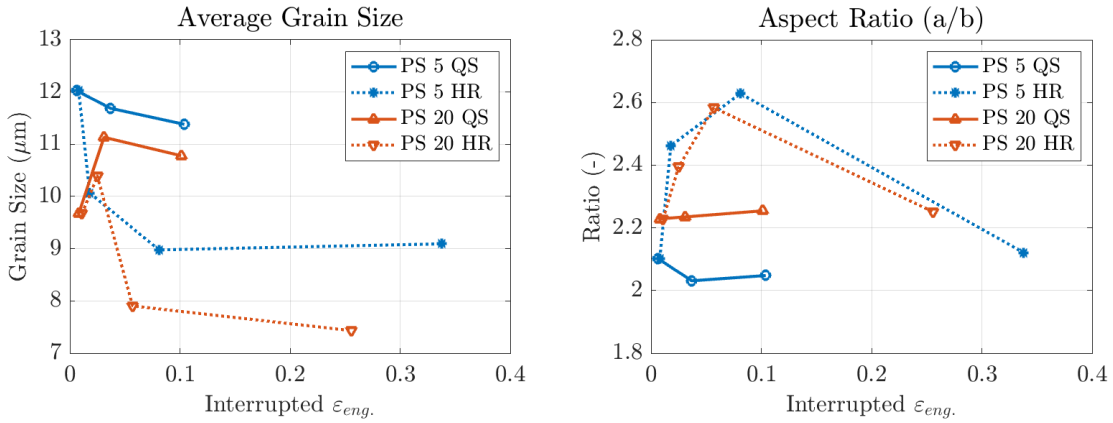
Specimen	Grain Size (µm)	AR (-)	Ellipse, a (µm)	Ellipse, b (µm)
As-received	15.634	1.848	10.794	5.842
PS 5	12.028	2.102	8.960	4.262
PS 5 QS 3	11.688	2.031	8.515	4.193
PS 5 QS 10	11.381	2.048	8.328	4.067
PS 5 HR 2	10.067	2.462	8.235	3.345
PS 5 HR 8	8.978	2.628	7.539	2.868
PS 5 HR 34	9.093	2.121	6.751	3.183
PS 20	9.670	2.229	7.410	3.325
PS 20 QS 3	11.134	2.235	8.548	3.825
PS 20 QS 10	10.781	2.254	8.310	3.687
PS 20 HR 2	10.390	2.394	8.310	3.471
PS 20 HR 5	7.904	2.583	6.562	2.540
PS 20 HR 25	7.431	2.251	5.694	2.530

Table 4.12: The LAGB densities of the entire EBSD maps (μ_{LAGB}, total), the per-grain average (μ_{LAGB}, per grain), and the maximum grain orientation spread (GOS) in degrees. These values are plotted on Fig. 4.27.

Specimen	$\mu_{\mathbf{LAGB}}$**, total** (1/µm)	$\mu_{\mathbf{LAGB}}$**, per grain** (1/µm)	**GOS, max.** (°)
As-received	142.502	0.113	23.143
PS 5	281.755	0.139	15.798
PS 5 QS 3	310.710	0.142	21.994
PS 5 QS 10	374.043	0.159	19.322
PS 5 HR 2	531.079	0.184	23.865
PS 5 HR 8	706.846	0.186	22.867
PS 5 HR 34	1170.845	0.300	21.630
PS 20	923.412	0.328	0.362
PS 20 QS 3	603.809	0.267	0.348
PS 20 QS 10	575.987	0.257	0.371
PS 20 HR 2	563.014	0.221	0.320
PS 20 HR 5	1264.861	0.266	0.374
PS 20 HR 25	2296.637	0.404	0.421

Table 4.13: Area fraction of grains with the highest Schmid Factor (SF) among all four slip systems considered in this study, as shown in Fig. 4.28.

Specimen	**Ba<a>**	**Pris<a>**	**Py<a>**	**Py<c+a>**
As-received	0.284	0.216	0.195	0.305
PS 5	0.178	0.185	0.305	0.333
PS 5 QS 3	0.216	0.232	0.279	0.273
PS 5 QS 10	0.204	0.245	0.279	0.271
PS 5 HR 2	0.182	0.215	0.347	0.257
PS 5 HR 8	0.169	0.162	0.376	0.293
PS 5 HR 34	0.375	0.020	0.169	0.436
PS 20	0.291	0.064	0.269	0.377
PS 20 QS 3	0.300	0.060	0.272	0.368
PS 20 QS 10	0.300	0.067	0.233	0.399
PS 20 HR 2	0.200	0.053	0.320	0.427
PS 20 HR 5	0.194	0.038	0.328	0.440
PS 20 HR 25	0.300	0.019	0.152	0.529



(a) (b)

Figure 4.25: Evolution of the average grain sizes and grain shapes in their aspect ratios during QS and HR compression of PS 5 and PS 20.

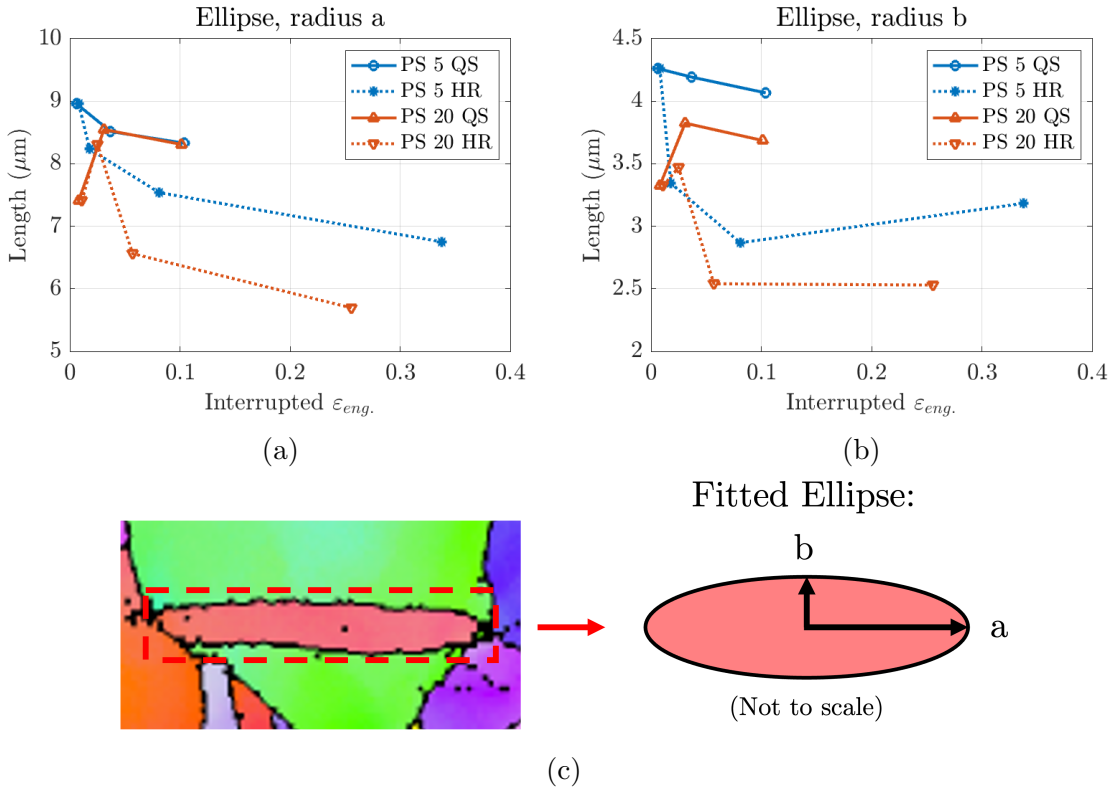


Figure 4.26: The average values of the long and short radii, labelled "a" and "b" respectively, of the equivalent ellipses fitted to each grain from the EBSD maps.

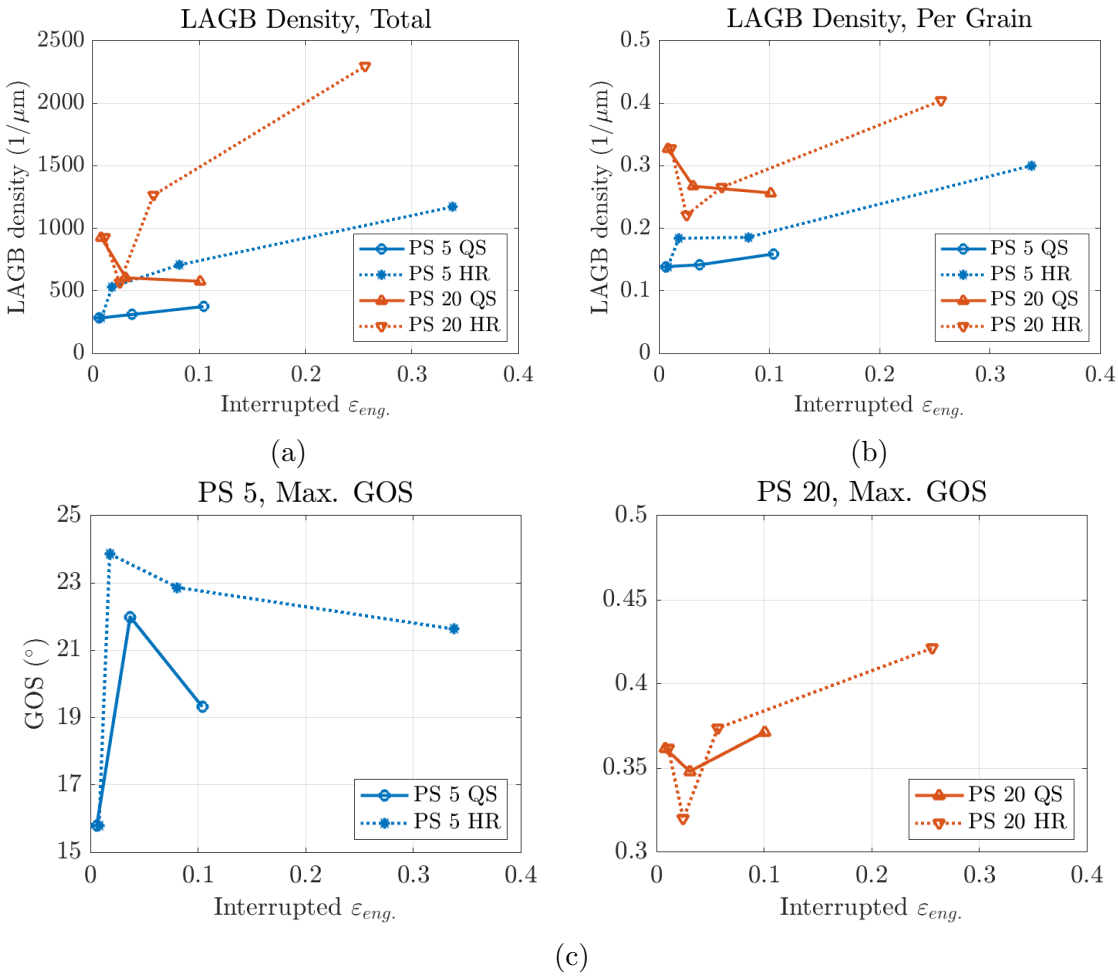


Figure 4.27: The evolution of (a) the total low-angle grain boundary (LAGB) densities, taken as: $\text{LAGB}_{\text{total}}/\text{Area}_{\text{total}}$ (b) LAGB densities per grain (μ_{LAGB}/N, where N is number of grains) , and (c) maximum grain orientation spread (GOS).

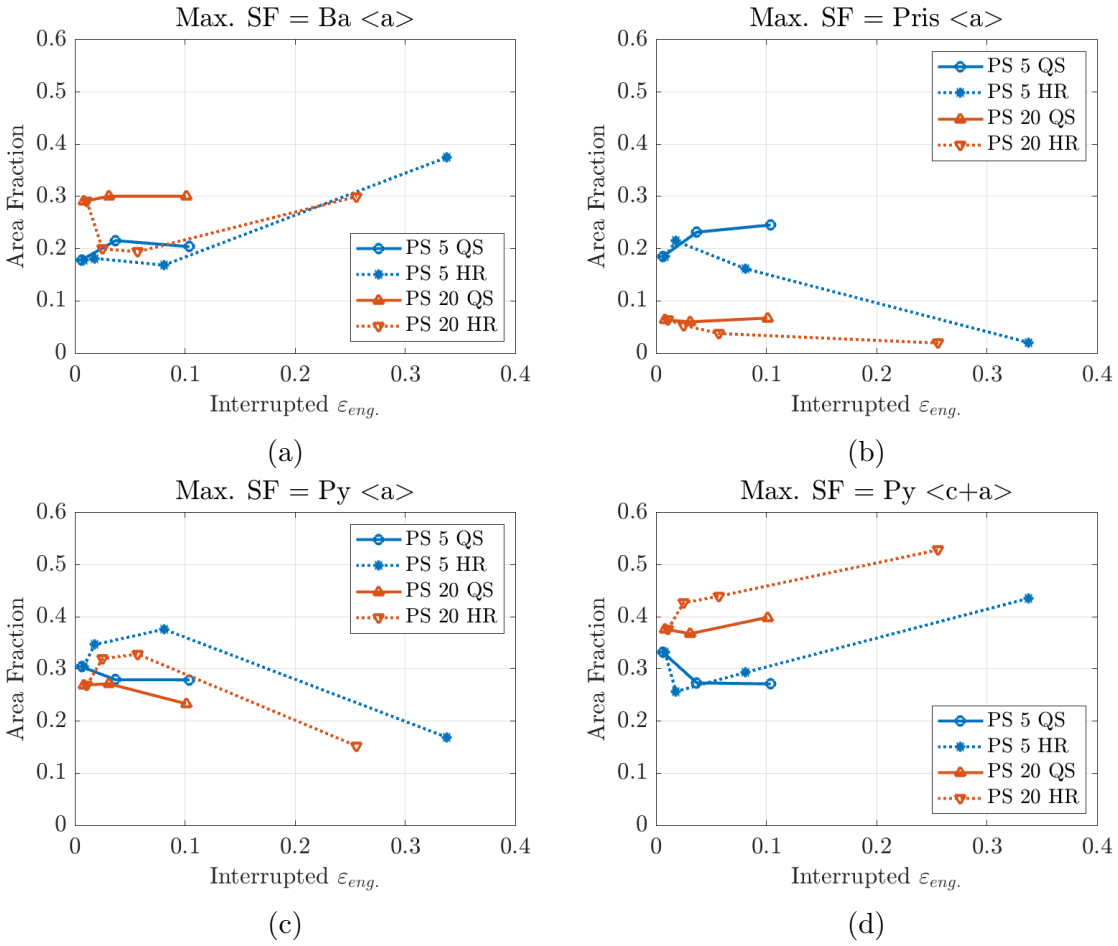


Figure 4.28: The area fractions of grains with the highest SF for each slip systems in α-phase (HCP) titanium. Here only four slip systems are considered: Basal <a>, Prismatic <a>, Pyramidal <a> and Pyramidal <c+a>.

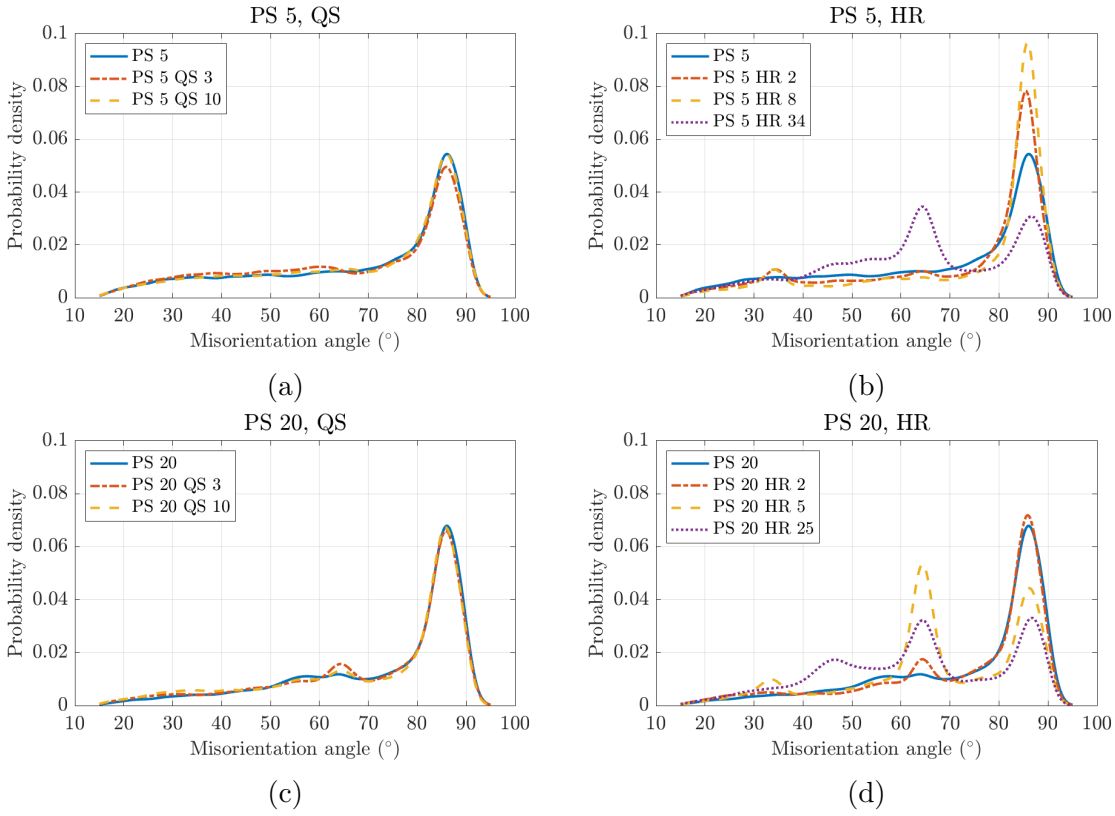


Figure 4.29: The evolution of the KDE curves fitted to the MO distributions of PS 5 and PS 20, QS and HR loading.

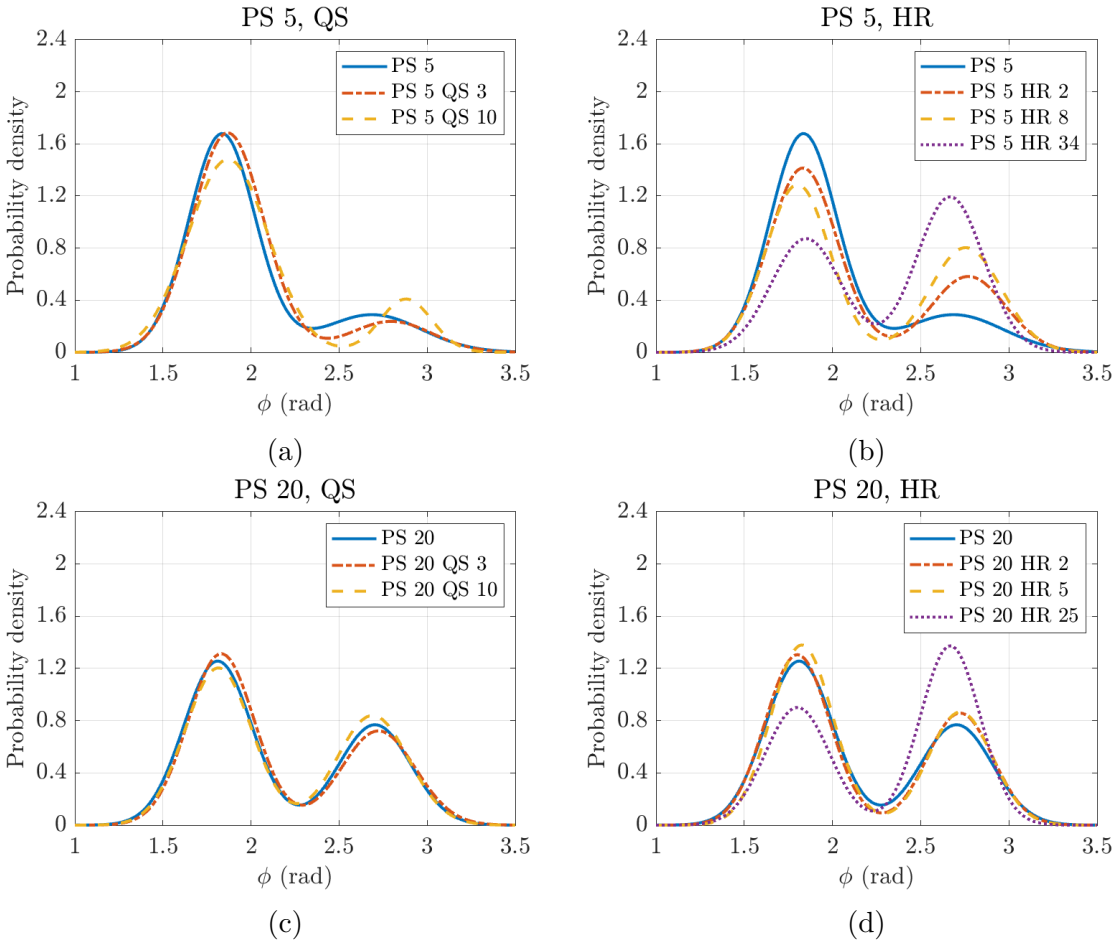


Figure 4.30: The evolution of the Gaussian Mixture (GM) curves fitted to the Phi (ϕ) distributions of PS 5 and PS 20, QS and HR loading.

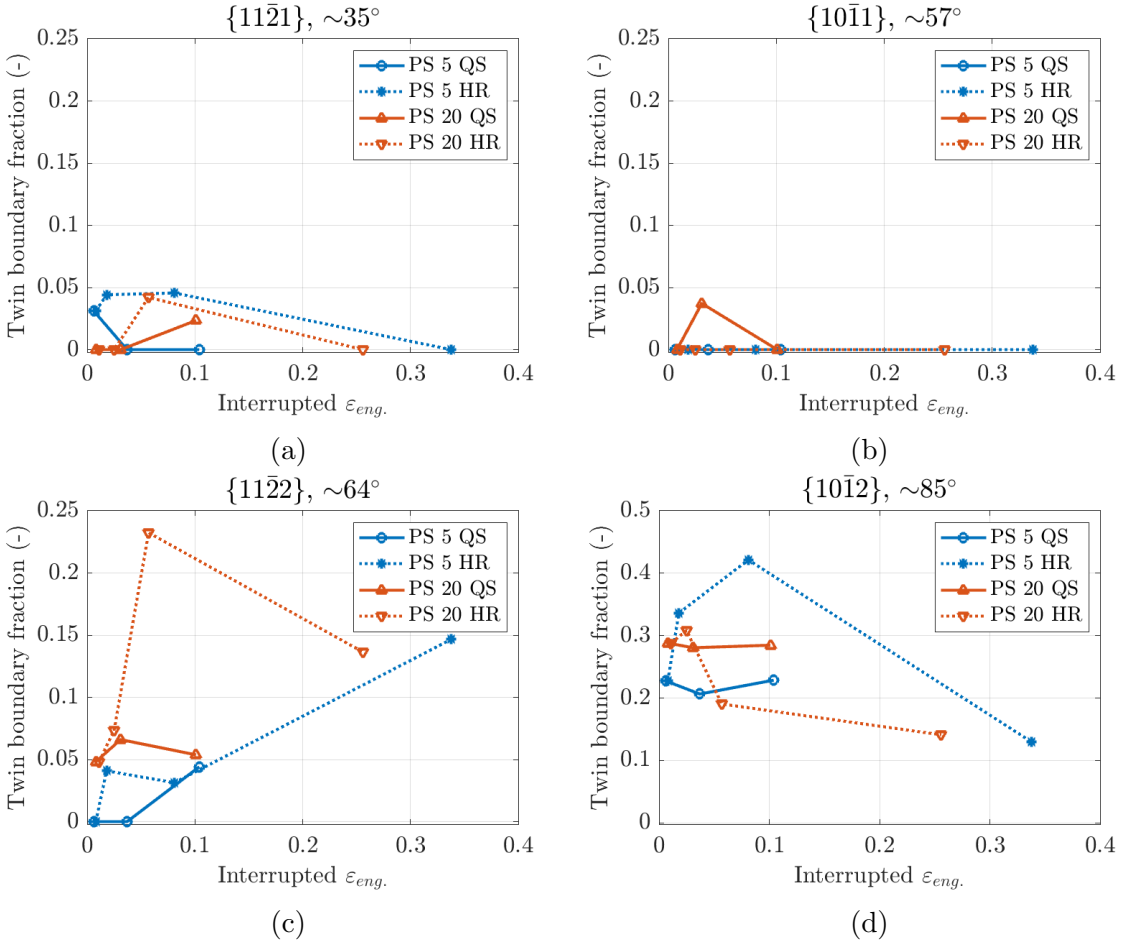


Figure 4.31: Evolutions of twin boundary fractions of each twin systems, except the {11$\bar{2}$4} twin (~77°) as it was not detected.

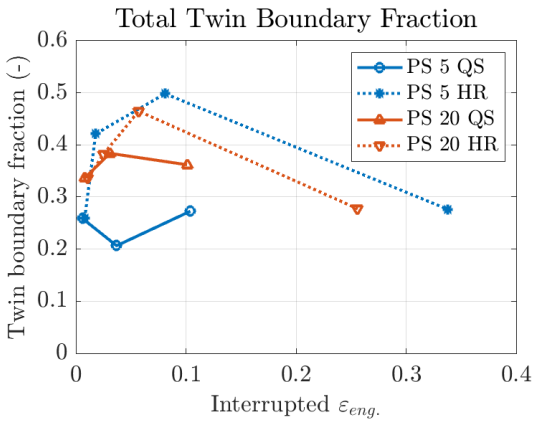


Figure 4.32: Evolution of the total twin boundary (TB) fractions of PS 5 and PS 20, QS and HR loading.

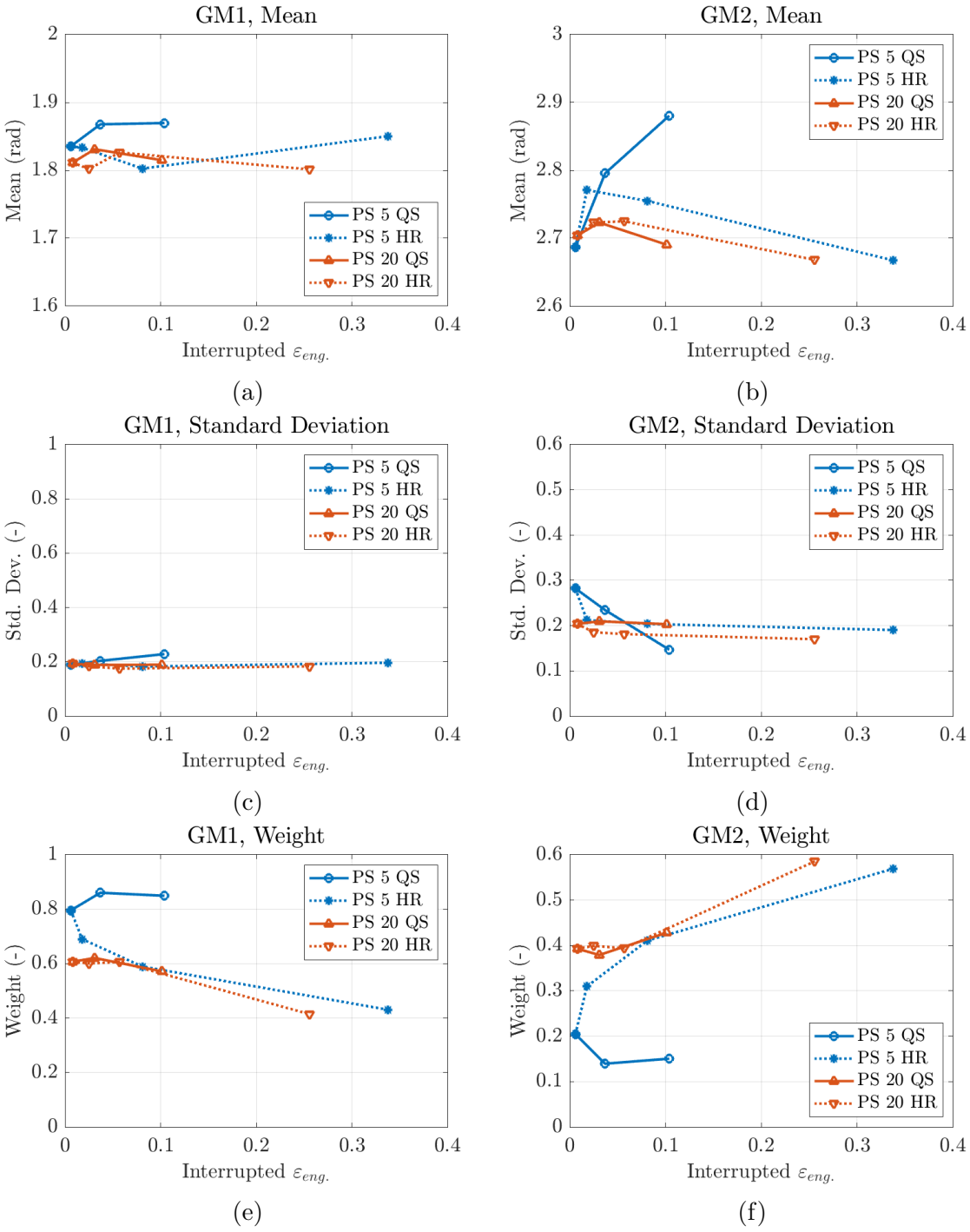


Figure 4.33: The changes in means, standard deviations and weights (relative ratios) of GM1 and GM2 in the Gaussian Mixtures fitted to the ϕ distributions.

4.6 Statistical analyses of microstructures

4.6.1 Motivations

The main reason for conducting novel experiments is to uncover new scientific findings. So far in this thesis, the data generation was motivated by the lack of existing studies in the high strain-rate regime. New findings from this thesis, including contributions of twinning and incipient failure mechanisms, have been obtained through conventional means - manually identifying features and comparing with literature. This high amount of human inputs on analysing complex microstructure datasets will inevitably lead to biases and misinterpretations of the features. For instance, the dislocation slip systems were implied solely by their geometrical likelihood (SF's of slips) and relative CRSS values, and no *in-situ* observations were made using TEM. While existing literature has studied these mechanisms in isolations, the combined effects on the bulk behaviour remained inconclusive, as indicated by the inconsistent slip systems and CRSS values in Table 4.10. Besides, when new features are identified, such as twin boundaries, the implementation on existing models might be challenging.

These issues can be avoided by employing statistical models, which analyse the underlying correlations and patterns from datasets, without resolving to deterministic physical or phenomenological laws [156–160]. The literature review in Chapter 1 has shown that while some aspects are deterministic, such as activation of slip systems, other features (*e.g.* twinning [73, 76]) can be stochastic. The relatively

small dataset in this study is not suitable to propose phenomenological or physical laws beyond arbitrary curve-fitting. However, a data-driven approach can help statistically identify important features and correlations between microstructures and bulk properties.

In this section, a data analysis pipeline is proposed, which consists of first identifying important **features from microstructures**, then applying statistical and machine learning (ML) models to correlate these key features to their respective **bulk mechanical properties**.

4.6.2 Feature correlations

From the point-of-view of a material scientist, it is obvious that some features are inherently correlated to each other, such the grain orientation and Schmid Factors of slip systems, and twin boundaries and grain sizes/shapes. However, correlations between other features might often be overlooked. To build a more efficient model for predicting the yield and flow stresses using microstructure features as inputs, the initial high-dimensional dataset could be transformed to extract the more important and relevant features. Dimensionality reduction techniques are typically used to transform the datasets from high to low dimensions. This process allows one to either select only the important features, or use the transformed features as the input for subsequent models. In either case, this reduces the input features for the model, increasing the computational (training) speed and reducing the risk of over-fitting the training datasets.

Principal component analysis (PCA) is the most common dimensionality reduction technique due to the fast computation, ease of implementation and high degree of interpretability [161–163]. With a given dataset of correlated features, PCA creates new uncorrelated features called principal components (PC's), which capture the directions of variations in the dataset. The creation of these "features" (PC's) is considered feature engineering as new features are generated without additional data acquisition. Latypov *et al.* have successfully employed PCA to obtain additional information from traditional 2-dimensional microstructure images for improved quantification of grain morphology [164]. Alternatively, by selecting PC's with the highest variations, the initial dataset can be simplified and noise can be reduced. Xu *et al.* have used PCA for material design, by first reducing the dimension of the initial dataset and forming new correlations with the desired physical properties [165]. This created a more precise description of microstructure and increasing the speed of model optimisation. Sengodan used PCA for a similar purpose of simplifying the initial dataset for a deep-learning based stress-strain prediction of composite materials [166]. Before discussing the use of PCA in this study, a brief summary of the PCA methodology is described as follows.

1. Starting from a given set of n number of data points with p number of features, each features ($x_{n,p}$) are standardised ($\mathcal{X}_{std.}$) by their means and variances,

$$\mathcal{X}_{std.} = \frac{x_{n,p} - \mu_p}{\sigma_p}. \tag{4.12}$$

2. The covariance matrix Σ, with shape p $\times$ p, is then computed:

$$\Sigma = \frac{1}{n-1}\mathcal{X}_{std.}^{T}\mathcal{X}_{std.}. \tag{4.13}$$

3. The direction and variance explained by each PC are obtained by computing the eigenvectors (v) and eigenvalues (λ) respectively, $\Sigma v = \lambda v$.

4. The PC's are then sorted based on their eigenvalues, from largest to smallest. The larger the eigenvalue of the principal component, the more it can represent the underlying correlations between features. The explained variance ratio is then expressed as:

$$\text{Explained Variance Ratio} = \frac{\lambda_i}{\sum_{i=1}^{p}\lambda_i}. \tag{4.14}$$

   Note that, the maximum number of PC's is equal to the number of features (p), and the sum of all explained variance ratios is 1.

5. The importance of each feature of a given PC is expressed in the eigenvector - with the first element in the vector correlated to the loading w (or the weight)

of the first feature and so forth. For example, with PC1:

$$v_1 = \begin{bmatrix} w_{11} \\ w_{12} \\ \vdots \\ w_{1p} \end{bmatrix} \tag{4.15}$$

$$PC1 = w_{11}x_1 + w_{12}x_2 + \cdots + w_{1p}x_p \tag{4.16}$$

From the PC's computed, the initial features can be processed in multiple ways, depending on the acceptable combined explained variance. For example, if PC1 and PC2 have a combined explained variance ratio of $\geq$80%, one can either qualitatively assess the loadings of each features, or quantitatively transform the initial high-dimensional dataset into a lower dimension space:

$$Z = \mathcal{X}_{std} V_m \tag{4.17}$$

where Z is the transformed lower-dimensional dataset and V_m is the matrix containing the eigenvectors of top m PC's. Although PCA assumes linear correlations and is sensitive to outliers, its high degree of interpretability of the results makes it a value tool for investigating relationships between features.

4.6.3 PCA on Microstructure Features

As discussed before, due to the chemical consistency in the material studied, the main differences in the microstructure lie in the grain morphology, grain orientation

and grain boundaries. The 11 features explored using PCA are as follows:

- Average **grain size** is equivalent diameter,
- Grain shape in aspect ratio (**AR**) computed from the long and short radii of an equivalent ellipse,
- Total **LAGB density**,
- Grain orientation spread (**GOS**),
- Area fractions of the highest SF among all four slip systems considered, including **Ba<a>, Pris<a>, Py<a>** and **Py<c+a>**,
- The weights **GM1** and **GM2** from the Gaussian Mixture models fitted to the ϕ distributions, and
- Total **twin boundary fraction**.

Following the procedures described, Fig. 4.34 shows the absolute loadings of the features of the first four PC's, and their respective explained variance ratios. For each PC's, the top three features with the highest loadings are highlighted. Since the combined ratio of PC1, PC2 and PC3 is $\geq$85% and the ratio of PC4 is less than 10%, only the first three PC's will be considered. The eigenvectors of these three

PC's are shown as follows:

$$\mathrm{PC1} = \begin{bmatrix} 0.350 & -0.068 & -0.407 & 0.331 & -0.343 & 0.420 & 0.323 & -0.419 \\ -0.019 & -0.107 & 0.107 & & & & & \end{bmatrix} \tag{4.18}$$

$$\mathrm{PC2} = \begin{bmatrix} -0.247 & 0.538 & 0.061 & -0.089 & -0.240 & -0.113 & 0.340 & 0.053 \\ 0.514 & -0.304 & 0.304 & & & & & \end{bmatrix} \tag{4.19}$$

$$\mathrm{PC3} = \begin{bmatrix} -0.163 & 0.218 & 0.0261 & -0.126 & -0.146 & 0.129 & 0.224 & -0.194 \\ 0.219 & 0.607 & -0.607 & & & & & \end{bmatrix} \tag{4.20}$$

Evaluating the top three features, PC1 shows that most features generally contribute evenly to direction of the highest variation, with the total LAGB densities and area fractions of Pr<a> and of Py<c+a> being the top features. However, the grain aspect ratios, twin boundary fractions and the weights from the ϕ Gaussian Mixture models have the lowest contributions. PC2 shows a wider distribution of loadings of features, with the aspect ratios, twin boundary fractions and area fractions of Py<a> having the highest loading. Note that two of these features have the lowest loadings in PC1. In PC3, only the weights of Gaussian Mixture components show very high loadings. The only features that do not have high loadings are the grain sizes, GOS and area fractions of Ba<a>. These results do agree reasonably well with the previous discussions in 4.5 - the changes in grain sizes were not significant according to the Hall-Petch equation; the GOS is while drastically different from PS 5 to PS 20, it did not change meaningfully within each material; the area fractons of Ba<a> slip were similar in most cases. The statistical results indicate that since only some features are correlated, the dataset can be further simplified

before being used as input for predictive models. Two approaches are considered, (1) constructing a lower-dimension dataset from the first PC's, and (2) manually selecting important features based on the loadings. The following section will discuss the modelling using these two interpretations of the initial dataset.

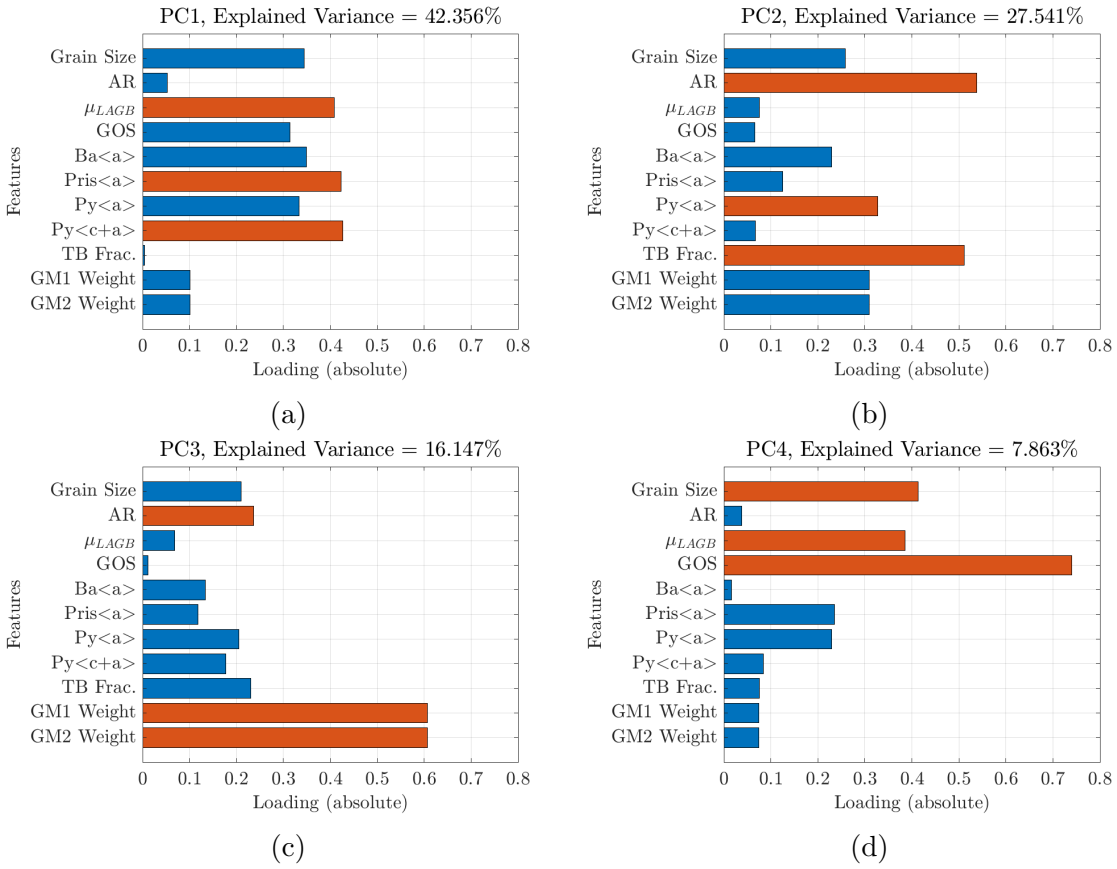


Figure 4.34: Absolute loadings of features from PC1, PC2, PC3 and PC4. The top three features with the highest loadings are highlighted.

4.6.4 Microstructure and bulk behaviour correlations

Advanced statistical models, or machine learning (ML) models, have gained significant attention in the field of solid mechanics to predict bulk stress-strain behaviour [157]. In general, supervised regression ML models are used for these tasks as the goal is to map input features (of the specimens) to the bulk behaviour, which are

continuous quantities rather than discrete class labels [167]. A few examples as follows: Yasniy *et al.* successfully applied ML in prediction of stress-strain behaviour of aluminium alloy at room and high temperatures from experimental data [159]; Lizarazu *et al.* incorporated several ML techniques for microstructure-aware finite element simulations, from standardising features for synthetic microstructure generation, to prediction of stress-strain behaviour [160]; Liu and Wu used ML to predict the stress values of additively-manufactured lattices based on applied strain and parameters from manufacturing (printing) processes [168]; Bhaduri *et al.* used an image-based U-Net approach to predict the stress fields in composite materials [158].

There are two common types of advanced statistical and ML models [169]: (1) high-dimensional non-linear approximators (*e.g.* neural networks) and (2) Bayesian approach to predict posterior future events based on prior observations (*e.g.* Gaussian Process). The neural network (NN) is the most popular ML model due to its versatility, scalability with larger datasets and ability capturing complex behaviour [170]. However, its output is often deterministic and the uncertainty is difficult to quantify. In contrast, Gaussian Process (GP) naturally offers uncertainty quantification as it essentially defines a (Gaussian) distribution over functions that would fit the data [167, 171]. The mean value is used as the prediction while the standard deviation is used as the confidence band for uncertainty quantification. GP is also exceptionally good at handling smaller datasets, which is the main limitation in this study [172, 173].

These two models were employed to map microstructure features to **engineering yield and flow stresses**, and were compared against each other to assess their predictive capabilities and applications in long-term deployment. Here, the engineering stresses were used as they are the absolute metric from the experimental measurements, while the true stresses were simply analytically-converted. Strains were omitted as they depended on the starting point of measurements, hence unsuitable for this purpose.

4.6.4.1 Overview of Neural Network

Before describing the features of artificial neural networks (or simply "neural network"), one should consider the three general approaches to solving scientific problems, which can be categorised as analytical, empirical and numerical. Analytical models can output the exact solution for a given problem, and are often based on fundamental/scientific governing laws. Empirical models rely on data gathered from real life (*e.g.* experiments) and use mathematical equations to describe the phenomena. This is sometimes called phenomenological models and is widely used in different fields as the fundamental laws can be difficult to derive and mathematical equations typically yield satisfactory results for practical applications. An example of empirical/phenomenological model is the Johnson-Cook model which uses power law to describe the plastic deformation of various metals [46]. Finally, numerical methods use computational algorithms to approximate solutions that are too complicated to derive analytically, such as the finite element method used to compute the stress-strain distribution in a complex geometry. However, when the computer is programmed search through all possible solutions numerically, it is often extremely

inefficient and the algorithms are unique to specific problems.

There was an idea to create a general purpose algorithm to solve any problems. An algorithm can learn the underlying pattern of a given dataset, and generate predictions based on pattern recognised. This is the foundation of artificial intelligence and thus machine learning became an active field of research [174]. Out of all machine learning models, the neural network architecture has become the most popular type of machine learning algorithm due to their versatility and scalability [175, 176].

The neural network was inspired by the function of the human brain - an input feeding into a neuron, which processes the information and produces an output. Mathematically, in a neural network , it is simply a function that accepts an input value, and computes an output value. While not strictly enforced, typically the input value is fed into a linear function, and the output of the linear function is fed into a non-linear function, which generates the output of the neuron. A visual illustration of a single neuron is shown in Fig. 4.35. An input z is first processed by the linear function: $z = wx + b$, where w and b are the learnable parameters weight and bias. The z value is then processed by a non-linear function, denoted as $a = \sigma(z)$, where the a represents the output of a particular neuron. The reason for this being non-linear is, since a neural network is essentially a collection of many neurons, if all the functions are linear, the network would function as a basic linear model which limits its flexibility. This non-linear function is typically called the activation function, and depending on the application, there are several common

activation functions. For example, for a classification task, the sigmoid activation can be used. Fig. 4.36a shows that the output value of the sigmoid function either converges to 0 or 1, which is useful for a binary classification task. For regression tasks, if the prediction value is a continuos positive variable, rectified linear unit (ReLU), as shown in Fig 4.36b.

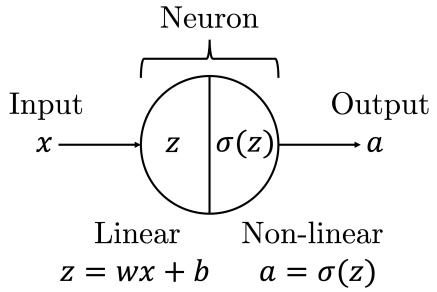
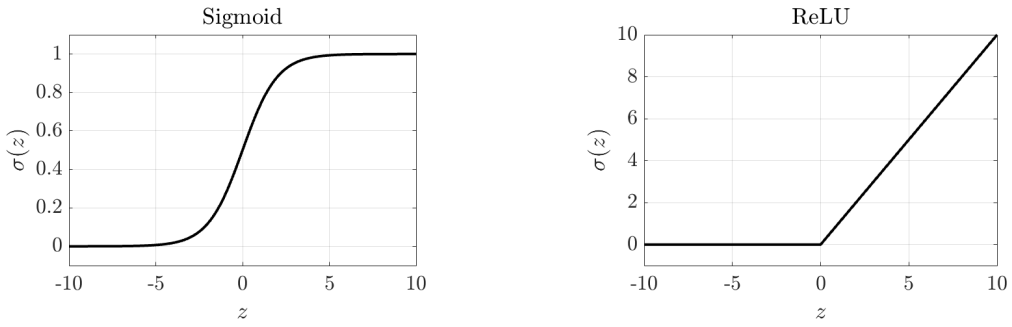


Figure 4.35: A visual illustration of a single neuron in a neural network: an input x is passed onto the first half of the neuron, which is a linear function z = wx + b, the z value is then passed onto the second half which is a non-linear function that generates an output a (or ŷ for the final output).



(a) (b)

Figure 4.36: Two commonly used activation functions in a neural network, the sigmoid function for classification tasks and ReLU function for regression tasks.

Since these functions do not have a learnable parameter, the learning relies only on the linear function prior. In practice, since neural networks are often used to solve complex problems, multiple neurons are used in a model. Fig. 4.37a shows an example of a 2-feature input and output fully-connected neural network, which

is also referred to as a "multi-layer perceptron". The number of input and output features, as well as the number of neurons and number of layers within a network (or the hidden layer/state) can be adjusted depending on the applications. For the purpose of this study, the size of the input layer corresponds on the number of microstructure features of interest, and the output is a single value that represents the predicted stress.

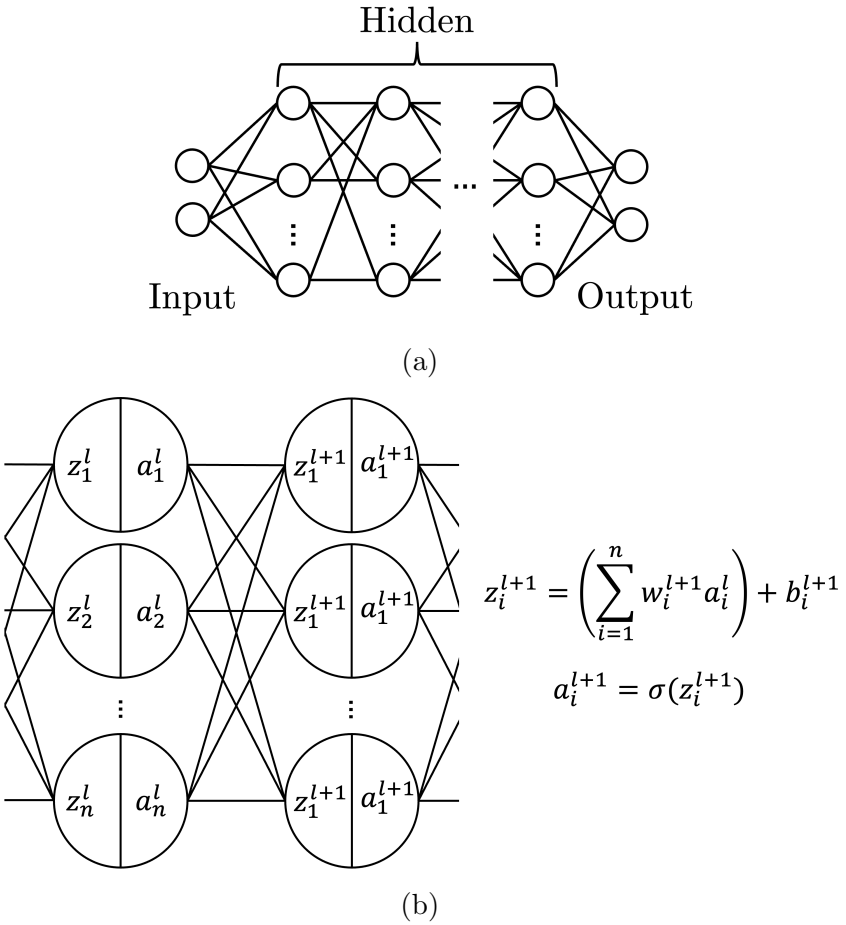


Figure 4.37: A visual illustration of a typical neural network consisting of multiple layers of neurons. The output of neurons of layer (l) are passed onto the neurons in the next layer $(l+1)$. The number of neurons in each layer is denoted as n.

Within a neuron network, a visual illustration of how information is passed down in shown in Fig. 4.37b. Assuming n number of neurons in layer l, the output from the i-th neuron is a_i^l. The linear function from the neurons in the following layer

$l+1$ takes in all outputs from the layer, multiply them by corresponding weights w_i^{l+1}, and a bias value b_i^{l+1} is added. The linear output is then passed onto the activation function, and the output is denoted as a_i^{l+1}. For the final layer, the output is denoted as $\hat{\mathrm{y}}$.

During the training process, the learnable parameters w and b are updated to reduce the error between the predicted ($\hat{\mathrm{y}}$) and the real output (y). This is achieved using the gradient descent optimisation algorithm, which requires the loss function (which computes the error, denoted as $\mathcal{L}(\hat{\mathrm{y}}_i - \mathrm{y}_i)$) and the activation function to be differentiable [177, 178]. A commonly used loss function for regression tasks it the mean-squared error (MSE) function, and its derivative with respect to $\hat{y}$ is:

$$\mathcal{L} = \frac{1}{\mathrm{m}} \left(\hat{\mathrm{y}}_\mathrm{i} - \mathrm{y}_\mathrm{i}\right)^2 \tag{4.21}$$

$$\frac{\partial \mathcal{L}}{\partial \hat{\mathrm{y}}} = \frac{1}{\mathrm{m}} \left(2\hat{\mathrm{y}} - 2\mathrm{y}\right). \tag{4.22}$$

where m is the batch size (number of data points in smaller subset of data). Note that the loss function computes the average error of the entire batch. In some cases, the loss can be computed after every data point, however very rarely. The gradient descent optimisation updates the parameter by iteratively adjusting their values:

$$\mathrm{w} := \mathrm{w} - \alpha \frac{\partial \mathcal{L}(\mathrm{w}, \mathrm{b})}{\partial \mathrm{w}}, \tag{4.23}$$

$$\mathrm{b} := \mathrm{b} - \alpha \frac{\partial \mathcal{L}(\mathrm{w}, \mathrm{b})}{\partial \mathrm{b}}, \tag{4.24}$$

where α is the learning rate, which determines how much the parameters are adjusted

at each epoch (iteration). The learning rate determines how much the values are adjusted at each epoch. An example of different learning rates is shown in Fig. 4.38. During training, the learning rate typically starts from a larger value to speed-up the search for the close approximation of optimised parameters, and is reduced to fine-tune these parameters.

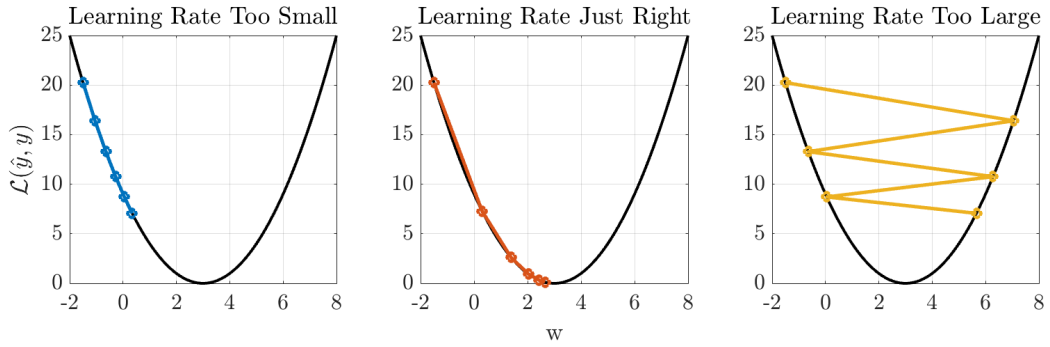


Figure 4.38: An example of different learning rates for the gradient descent optimisation after 5 epochs. The black curves are the true loss against different weight w. When the learning rate is too small (left) or too large (right), the parameter w cannot quickly converge and more epochs are required to compute to the optimised value. When the learning rate is at its optimal (middle), the parameter w quickly converges to give the lowest loss.

From Eqs. 4.23 and 4.24, the partial derivatives can be expanded using chain-rule:

$$\frac{\partial \mathcal{L}(\mathrm{w},\mathrm{b})}{\partial \mathrm{w}} = \frac{\partial \mathcal{L}(\mathrm{w},\mathrm{b})}{\partial \mathrm{a}} \frac{\partial \mathrm{a}}{\partial \mathrm{z}} \frac{\partial \mathrm{z}}{\partial \mathrm{w}}, \tag{4.25}$$

$$\frac{\partial \mathcal{L}(\mathrm{w},\mathrm{b})}{\partial \mathrm{b}} = \frac{\partial \mathcal{L}(\mathrm{w},\mathrm{b})}{\partial \mathrm{a}} \frac{\partial \mathrm{a}}{\partial \mathrm{z}} \frac{\partial \mathrm{z}}{\partial \mathrm{b}}. \tag{4.26}$$

Here, using ReLU as an example, the partial derivates of the activation function a

and linear function z are:

$$\frac{\partial \mathrm{a}}{\partial \mathrm{z}} = 1, \text{ if } \mathrm{z} > 0 \text{ (or 0 otherwise)}, \tag{4.27}$$

$$\frac{\partial \mathrm{z}}{\partial \mathrm{w}} = \mathrm{x}, \tag{4.28}$$

$$\frac{\partial \mathrm{z}}{\partial \mathrm{b}} = 1. \tag{4.29}$$

This demonstrated the importance of differentiable activation functions when using gradient descent. Note that for ReLU, it is not differentiable at $\mathrm{z} = 0$. However, it is usually not an issue computationally as the value of z is rarely exactly zero. There are several practical considerations when using neural networks:

1. For a multi-layer neural network, although different activation functions can be used, neurons within the same layer typically use the same activation function for simplicity. The activation function at the final layer typically dictates what the model is used for,

2. Although the mathematical formulae and computer algorithms are known, the lack of interpretability of the learnable parameters often leads to trial-and-error when building a model,

3. Intuitively speaking, the suitable model size (number of neurons and layers) is correlated to the training dataset size, *e.g.* smaller dataset requires a smaller model. This can prevent over-fitting as less learnable parameters makes the model better at generalising the correlation of input and output,

4. Since neural networks have gained significant popularity due to their versatility

and high-performance, *PyTorch* [179] (a *Python* package) was employed to construct the neural network model.

4.6.4.2 Overview of Gaussian Process

Gaussian process regression is a Bayesian approach to predictive modelling, which takes in the known observations (prior) and generate predictions (posterior). Traditional predictive models often follow a pre-defined format, for example:

$$\mathrm{y} = \mathrm{f}(\mathrm{x}) = \mathrm{w}^{\mathrm{T}}\mathrm{x} + \varepsilon \tag{4.30}$$

where f(x) is defined as a linear model (Fig. 4.39) with input x and output y, parameter w as the gradient and ε as the uncertainty, defined as a Gaussian noise $\mathcal{N}(\mu = 0, \sigma^2)$. The model can therefore be defined as a Gaussian distribution as a whole, with the mean being the prediction and the variance being the uncertainty:

$$\mathrm{P}(\mathrm{y}) \sim \mathcal{N}(\mathrm{w}^{\mathrm{T}}\mathrm{x}, \sigma_{\mathrm{n}}^2\mathrm{I}). \tag{4.31}$$

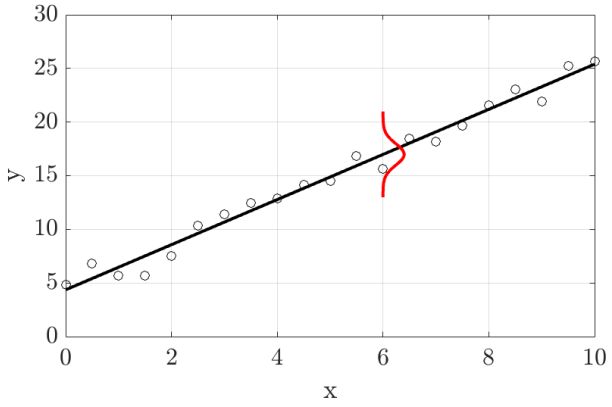


Figure 4.39: An example of a linear regression model with uncertainty shown as a Gaussian distribution (in red).

Model parameters can then be optimised for a given set of training data. However, problems can arise when new data is added to the training set, which would require re-optimisation of model parameters (*e.g.* re-train a NN model).

An alternative approach to prediction models would be to use a probabilistic model to determine the likelihood of new predictions based solely on the training dataset, without committing to a single model. This is essentially a model with an infinite number of possible parameters. The main difference is that traditional parametric models assume only one function is the best fit for the training dataset and hence can be used for future prediction, while this approach assumes multiple functions can fit the data. This can be described as, following a prior observation of the training data, the model draws a prediction (posterior) from a multi-variate Gaussian distribution. This is known as the Gaussian process (GP).

In GP, the probability of a function f that fits a given dataset D, using Bayes'rule, is expressed as:

$$\mathrm{P(f|D)} = \frac{\mathrm{P(D|f)P(f)}}{\mathrm{P(D)}}. \tag{4.32}$$

The assumption here is for any finite subset in X, the marginal likelihood of P(f) is a multi-variate Gaussian [171, 180]. With this, the joint probability of two output $\mathrm{y} = \mathrm{f(x)}$ and $\mathrm{y_*} = \mathrm{f(x_*)}$, given the two inputs x and $\mathrm{x_*}$ is:

$$\mathrm{P(Y|X)} = \mathrm{P(y, y_*|x, x_*)} \sim \mathcal{N}\left(\begin{bmatrix} \mu(\mathrm{x}) \\ \\ \mu(\mathrm{x_*}) \end{bmatrix}, \begin{bmatrix} \mathrm{K} + \sigma^2\mathrm{I} & \mathrm{K_*} \\ \\ \mathrm{K_*^T} & \mathrm{K_{**}} \end{bmatrix}\right), \tag{4.33}$$

where the mean function (μ) is usually set to zero, the $K = K_{ij} = K(x_i, x_j)$ is the kernel function describing the covariance matrix, with σ^2 representing the noise in the initial data. To predict the output of a new input, the probability will need to be conditioned to y_* only. This can be achieved by marginalising the likelihood [171]:

$$P(y_*|x, y, x_*) = \int_w P(y_*|x_*, D, w)dw \tag{4.34}$$

$$P(y_*|x, y, x_*) = \int_w P(y_*|x_*, w)P(w|D)dw. \tag{4.35}$$

where w is the parameter of the function f. Since the resulting marginal likelihood is Gaussian, the mean and variance are derived as [181]:

$$P(y_*|x, y, x_*) \sim \mathcal{N}\left(\mu = K_*^T K^{-1} y,\, \Sigma = K_{**} - K_*^T K^{-1} K_*\right) \tag{4.36}$$

The prediction and uncertainty are obtained from the mean μ and the bottom right element of the covariance matrix Σ. Here, one issue remained unsolved - the kernel function for computing the covariance matrix. Selecting a suitable kernel and its hyperparameters are extremely important in ensuring the GP model's ability to generalise data [182]. The most common kernel is the radial basis function (RBF):

$$K(x_i, x_j) = v_f^2 \exp\left(-\frac{1}{2l}\left(x_i - x_j\right)^T \left(x_i - x_j\right)\right) \tag{4.37}$$

where v_f and l are the hyperparameters for vertical scaling and length scaling. These parameters can be optimised using MLE. This kernel is designed to compare simi-

larities between two inputs x_i and x_j, as the output would tend towards one when similar, and zero when the difference is large. This kernel can then find the most similar point (from the training dataset) to the testing point (x_*), and the output can be predicted. Other kernels, and a mix of kernels can also be used depending on the data [182].

4.6.4.3 Neural Network vs Gaussian Process

From the aforementioned features of these two model types, their advantages and disadvantages are summarised as below: **Neural Network:**

- Advantages:
  - Easy to implement due to existing packages/software libraries in *Python*,
  - The improvement of GPU technology has increased the computation speed during training, which depends largely on the model size/complexity,
  - It is very flexible, with many model variations which are suitable for a wide variety of tasks.
- Disadvantages:
  - It only generates predictions without uncertainty quantification,
  - It is more suitable for larger dataset,
  - The "black box" nature of neural network lacks interpretability, which leads to difficulty in model optimisation.

Gaussian Process:

- Advantages:
  - It is easy to implement due to existing packages in *Python*,
  - It works very well for small datasets, and uncertainty quantification is inherently computed,
  - Since no function/parameters are learnt, the model gradually improves its performance when more training data is available.
- Disadvantages:
  - It is unsuitable for very large datasets due to scaling issues,
  - The inherent assumption that the data follows a multi-variate Gaussian distribution might not be valid for some datasets, it is not suitable for very complex datasets,
  - The choice of kernel (for covariance matrix) is extremely important, and often requires manual selection to find an optimal kernel.

In this study, both models were used to correlate microstructures (as inputs) to the respective stress values. The important microstructure features were identified using PCA previously. Three different sets of features were used:

1. The 11 initial features before PCA,
2. Reduced-dimension dataset using the first three PC's and Eq. 4.17,
3. Manually selecting important features (and eliminating irrelevant ones) from only PC1 and PC2, which includes:

- Average **aspect ratio** of grains,
- Total **LAGB density**,
- Area fraction of **Pris<a>**,
- Area fraction of **Py<a>**,
- Area fraction of **Py<c+a>**, and
- **MO distributions**.

Additionally, since the specimens were subjected to different strain-rates of compression, the magnitudes of **strain-rate** were added to the microstructure features, with $10^{-3}\,s^{-1}$ and $10^{3}\,s^{-1}$ for QS and HR testing respectively. Note that, the twin boundary fractions from PCA were replaced by bin heights of normalised histograms of MO distributions (using 8 bins). This has shown to massively improve of the GP models, though no significant effect on the NN models. The features were then standardised to improve model training stability.

As the dataset is very small, with only 14 data points (pairs of microstructures and stresses), both models were evaluated using the "leave-one-out" cross validation (LOOCV) [183, 184]. In this method, one data point was removed and used as the validation set, while the remaining 13 were used for training. This process was repeated until each data point has served as the validation set once, which resulted in 14 models.

A standard feed-forward NN was constructed using *PyTorch* [179], and architecture is shown in Table 4.14. The input dimension is denoted as n, which is either 11

(initial pre-PCA), 3 (for the PCA-reduced dataset) or 7 (manually-selected dataset). The MSE loss function was used, along with the Adam optimiser [185]. The L_2 weight decay regularisation ($=10^{-4}$) was used to reduce the effect of over-fitting of the training data. [186]. The training schedule was programmed as: 300 epochs at a learning rate (lr) of 1×10^{-3} for accelerating the initial search of optimal parameters, followed by 250 epochs at lr of 1×10^{-6} for stable convergence, and finally 250 epochs at lr of 1×10^{-9} for fine-tuning. The losses of the models during training are shown in Fig. 4.40. All models converged at around 300 epochs with the high learning rate, and further training at lower learning rates help converge the learnable parameters.

Table 4.14: Architecture of the simple neural network used to correlate microstructure features and strain-rates to their respective yield and flow stresses. The input dimension is denoted as n.

Layers	Functions	Dimensions
Input	Linear $\rightarrow$ ReLU	n $\rightarrow$ 256
Hidden 1	Linear $\rightarrow$ ReLU	256 $\rightarrow$ 256
Hidden 2	Linear $\rightarrow$ ReLU	256 $\rightarrow$ 128
Hidden 3	Linear $\rightarrow$ ReLU	128 $\rightarrow$ 64
Hidden 4	Linear $\rightarrow$ ReLU	64 $\rightarrow$ 32
Output	Linear	32 $\rightarrow$ 1

The GP regressor was implemented using *SciKit-Learn* [105]. A combined kernel of "DotProduct" and "WhiteKernel" was used. The WhiteKernel acted as the base line noise, or the variance in the each data point (diagonal elements of the covariance

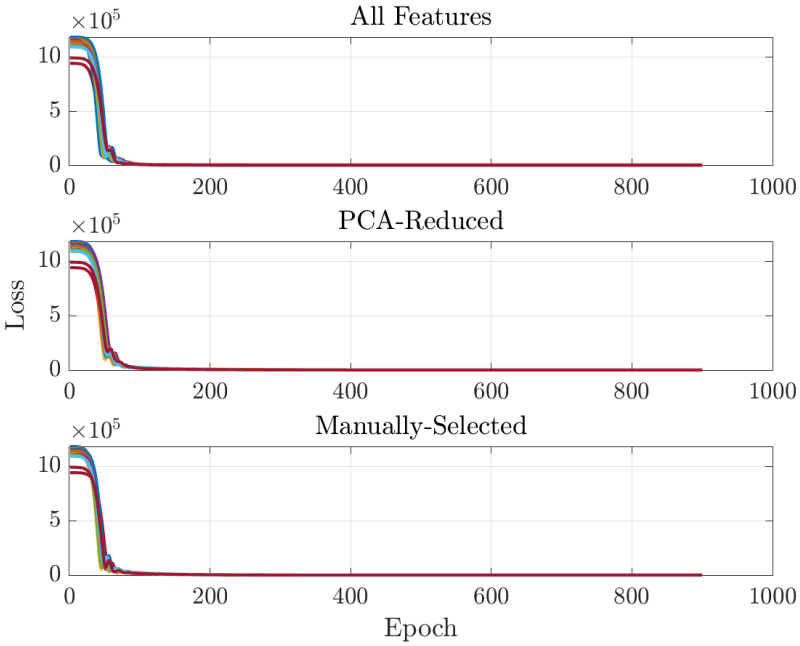


Figure 4.40: The losses of neural networks during training. All models quickly converged at around 300 epochs with the high learning rate, and were trained further to fine-tune the learning parameters. Each line represents a model trained using LOOCV.

matrix). The combined kernel had the following form:

$$\text{Kernel (K)} = \text{DotProduct} + \text{WhiteKernel} \tag{4.38}$$

$$\text{K} = \left(\sigma_0^2 + \text{x}_\text{i}\text{x}_\text{j}\right) + \left(\text{noise, if } \text{x}_\text{i} = \text{x}_\text{j},\ \text{else } 0\right). \tag{4.39}$$

The upper and lower bounds of the hyperparameters σ_0^2 and "noise" were set to $(10^{-6}, 10^2)$, and $(10^{-6}, 10^6)$ respectively, which were then optimised using the log-marginal-likelihood function.

The results are shown in Fig. 4.42, with the x-axis representing the real values and the y-axis representing the predicted values. Ideally, the results should be aligned diagonally (black dotted lines in each graph, x = y), which indicates perfect

predictions. The further the result is from this line, the worse the prediction. For the NN models, predictions are plotted as singular points, while for the GP models, the uncertainties (standard deviations) are also plotted as error bars. The mean absolute percentage errors (MAPE) are also shown for each model.

Comparing both model types, the NN models show similar MAPE's of ∼29% with both all features and PCA-reduced features, and a smaller error of ∼25% when with the manually-selected features. While the predictions show a quantitative improvement, visually inspecting the results, one could observe very small changes in the predictions. In contrast, GP models show lower MAPE's with all datasets, and the errors and uncertainties gradually decrease from the first to the last datasets, reaching <6% with the manually-selected dataset. The uncertainties here are also very low with virtually no outliers in the predictions.

It is not surprising that GP outperforms NN with the given dataset, due to the fundamental differences between how these two model types handle datasets. As NN's contain many learnable parameters, they are generally flexible given a large training dataset. However, in this case since the training set contains only 14 data points, it is insufficient for the model to generalise, increasing the risk to learn the noise in the data rather than the underlying correlations between inputs and outputs. This is often referred to as over-fitting, with an example shown in Fig. 4.41. A NN model functions similar to a high-degree polynomial, which attempts to fit all the data points, while a lower-degree polynomial fits the general trend. The inherent

complexity of NN's can easily lead to over-fitting while training on small datasets.

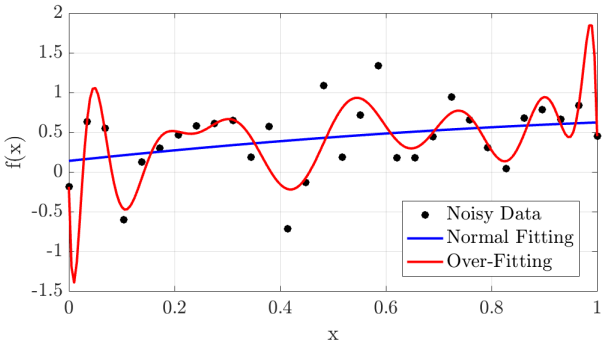


Figure 4.41: An example of normal fitting against over-fitting. When the dataset is too small or NN model is too complex, it can often lead to over-fitting.

GP in contrast, does not have this limitation as it does not rely on fitting parameters of a function. Instead, it uses a Bayesian approach to learn the probability of functions given the training data as a prior. A kernel function is used to define the assumed underlying correlations between input features, and predictions are generated based on the similarity between test and train sets. This allows GP to work well when interpolating between sparse data points while avoiding over-fitting. The probabilistic prediction of GP also quantifies uncertainties, highlights regions where the prediction confidence is low, which directly informs feature correlations. A similar approach was applied in yield and ultimate tensile stress prediction by Lee *et al.* [187], which concluded that GP is amongst the few suitable model types that map the correlation of microstructure features to bulk behaviour.

In general, the results show that using PCA as a tool to identify key features, rather than reducing the dimension of the initial dataset, has led to more accurate predictions in both model types. GP in particular has shown that the features

identified by PCA are indeed the dominating features that dictate the yield and flow stresses. The results re-emphasised the finding from Chapter 3, that the twin boundary fractions (expressed as the MO distributions here) are indeed an important mechanism. They also identified new features such as LAGB densities and grain shapes, as well as confirming the SF of slip systems, though the Ba<a> slip was omitted by PCA. Although recent advancements in GP has overcome its limitation on larger datasets [188–190], only one property (stress) can be predicted using a single GP model. Multiple models would be required for predicting more than one property. On the other hand, a single NN model can predict multiple properties at the same time. NN's can become more advantageous when the dataset is sufficiently large and when modelling all features. Therefore, both models could be employed, with PCA and GP identifying key features and verifying their correlations with bulk properties. This can aid in experiment design, *e.g.* the lack of variance in a certain feature, such as grain size and GOS, could mean more experiments needed in that area. This can also advance the development of physically-based models by incorporating these additional features, *e.g.* twin boundaries, grain shapes and LAGB densities, which are often neglected [76, 125, 128, 129, 149]. When the dataset becomes larger, the NN can be used for high-dimensional/full-feature correlations and predictions. This can serve as a surrogate model due to the ease of implementation and high computing speed, before a robust physically-based model is developed [158, 159, 168].

While these statistical models have shown to predict bulk properties from mi-

crostructures, they lack the underlying physical laws governing deformation mechanisms. This might limit its predictive capability in extrapolation. Although obtaining more real experimental data will improve model performance, it is often very expensive and time-consuming. If the training input features were arbitrarily created, the lack of realism will deteriorate the model performance. From the experimental dataset, one could attempt to "interpolate" between existing microstructures. While features like grain sizes could be easily interpolated, for example curve-fitting of stress/strain against grain size, other features such as MO distributions will pose a challenge, since they are modelled as non-parametric probability densities. A reliable microstructure generation tool is then needed in order to artificially populate a dataset by interpolating the existing microstructures.

4.7 Summary and conclusions

This chapter explored the strain-rate effect on the compression behaviour of pre-strained pure titanium, with a particular focus on the initial stages of deformation and incipient failure mechanisms. Novel statistical approaches were proposed to extract quantitative features from MO distributions for twin nucleation analyses, and ϕ distributions for twin growth (grain reorientation) analyses. To identify correlations between microstructures and bulk mechanical properties, advanced statistical models were used to extract key features from the microstructures, and verify their correlations with their respective yield or flow stresses.

In summary, the results show that while the microscopic mechanisms were strain-

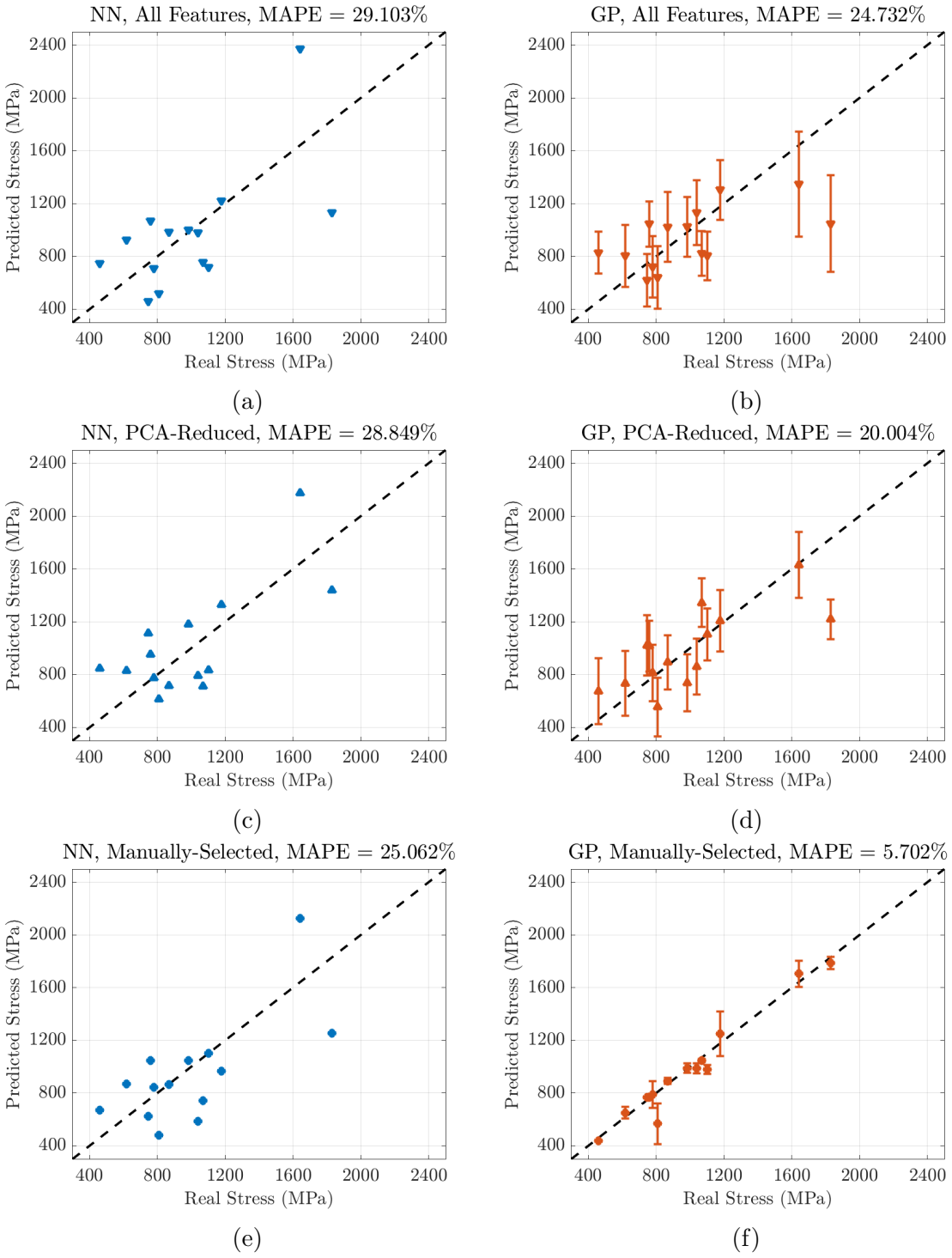


Figure 4.42: Predictions of yield and flow stresses using neural network (NN) and Gaussian process (GP) regressor, with (a), (b): initial 11 features, (c), (d): PCA-reduced dataset and (e), (f): manually selected features. The mean-squared percentage error (MAPE) values are shown for each model and dataset.

rate dependent, the bulk hardening rates for the same material, PS 5 and PS 20, were similar in QS and HR compression. At the early stages of QS, deformation of both PS 5 and PS 20 was mediated by dislocation slip. Pre-straining seemed to have no effect beyond twin-induced texture changes. At the early stages of PS 5 HR, twin growth was favoured and the GOS remained high. Less twin boundaries were formed, which reduced obstacles for dislocations. These effects led to lower flow stresses but a higher hardening rate. In PS 20 HR, twin nucleation was favoured and LAGB density increase drastically. Increasing dislocation obstacles led to higher flow stresses. Since LAGB's acted as plasticity carriers and allowed partial transmission of dislocations, the hardening rate was low.

At the later stages of deformation, as both materials approached failure, their microstructures were very similar. In particular, the decrease in twin boundary fractions and grain aspect ratios indicate a possible dynamic recrystallisation similar to the earlier findings in Chapter 3. Both specimens also displayed a split-basal texture, indicated by the high GM2 weights (in the ϕ distribution) and the slight shift in the GM2 mean values. Differences in dislocation structures were also observed. The high GOS in PS 5 HR indicates a high number of mobile dislocations, while the high LAGB density in PS 20 HR suggest more ordered dislocation arrays.

Following the experimental investigation, PCA was employed to extract key features from the microstructures. The NN and GP models were then used to verify their correlations with bulk engineering yield and flow stresses. The prediction ac-

curacy shows that GP outperformed NN with the small dataset in this study, with a mean percentage error of <6%. The results reinstated the importance of twin boundaries in terms of MO distributions, and identified new features: LAGB densities and grain shapes. They also confirmed the importance of SF's of most slip systems, although the Ba<a> was excluded by PCA. The method employed here suggests that while a small dataset (as in this study) cannot accurately derive the phenomenological or physical laws, statistical models can identify the underlying correlations and patterns of the dataset. This can aid in experiment design by conducting targeted experiments with features of low variance. Moreover, it can also advanced the development of physically-based models by identifying missing features (*e.g.* twin boundaries) that showed high correlations.

Besides feature extractions, machine learning models can often act as surrogate models. However, they often require a large dataset, with thousands or millions of data points, for training. Since experimental data is expensive and time-consuming to generate, there is a need to artificially generate synthetic data points. Interpolating between existing data points (microstructures) is a possible strategy to ensure the synthetic data remains realistic. The next chapter will explore several ways of employing generative artificial intelligence (GenAI) in creating synthetic microstructure features.

Chapter 5

Application of generative machine learning on data augmentation of microstructural data

This chapter discusses the potential use of generative machine learning in creating synthetic microstructural data, specifically non-parametric features. From the previous chapter, it was identified that the use of existing data was perhaps not optimised. The study here uses generative models to attempt to recreate the grain boundary misorientation (MO) distributions. The results from different models are discussed, along with their implications on the future of materials design.

5.1 Introduction

Generative machine learning, or generative artificial intelligence (GenAI), refers to the family of machine learning models that create new data (images, videos, texts etc.) by learning the underlying patterns of existing data [191–193]. This is different from other conventional modelling which analyses the data to make predictions with

a new input. Generative models have seen significant improvements in the past two decades due to the advancements in computer technology and interest in AI development. Some notable generative models include: Transformers (*e.g. ChatGPT*), Latent Diffusion Model, Variational Auto-Encoder (VAE) and Generative Adversarial Networks (GAN).

While generative models are commonly known for their entertainment purposes, such as text-to-image generations and in-filling of corrupted images, they have recently gained popularity in scientific applications, including: creating synthetic (artificial) medical images (*e.g.* MRI scans) to train diagnostic models [194, 195], and developing personalised medicine in drug discovery [196, 197]. Another usage of generative model is data augmentation, for example, Sela *et al.* [198] used GAN to convert images of eye regions from 3D modelling to realistic images of eye gazes.

Within the field of solid mechanics/materials science, researchers study the underlying mechanisms that dictate the material properties, for the purpose of creating materials with higher performance. In reality, all materials have their limits and trade-off's [199, 200], and require careful decisions and engineering to select the most appropriate material (and processes) for a specific application. *Materials by Design* is an emerging field that reverses the traditional process of obtaining test results from a given material specimen. Instead, the material is designed from the ground up based on the desirable applications. With the complex correlations between different material features and their performance, the use of machine learning,

including generative models, have accelerated materials discovery [201, 202].

This process requires two key features: datasets of material features (*e.g.* microstructures) and robust predictive models, both require a large amount of data. In some cases, the limited data available has driven the need to develop a generative model to artificially increase the dataset size. A particular study from Bhaduri *et al.*[203] has inspired the work in this chapter. In their study, they took several real X-ray scans of a ceramic material, studied its pore sizes and recreating statistically-representative synthetic material descriptors for finite element modelling. The material in this thesis, titanium, is comparatively more complex, higher dimensions and the pre-strained features, namely the MO distributions, are difficult to recreate. This presents the opportunity to investigate the possibility to adopt generative models to create realistic features, which is the core objective of this chapter.

5.1.1 Objectives

Since the experimental data within this thesis is sparse, attempting to interpolate within the dataset will likely result in inaccurate representation of the microstructure features. However, the use of generative models on creating non-parametric features for engineering/scientific applications remains limited.

The objective of this chapter is to **investigate the suitability of generative models for recreating the MO distributions**. The three models to be studied are: Diffusion, GAN and Recurrent Neural Network with Gated Recurrent Units

(GRU). A brief overview of each model will be given, and the performances of the models will be assessed by their abilities to recreate the real experimental data.

5.2 Models overview

Three types of models were used in this investigation, that being latent diffusion, generative adversarial networks and recurrent neural network, specifically with the gated recurrent unit. The general overviews of the models will be discussed below with the aim to describe the architectures, advantages and disadvantages and how they were used for the purpose of microstructure feature generation.

5.2.1 Overview of Diffusion models

Diffusion models are a type of generative models that are inspired by the non-equilibrium statistical physics, where particles flow from regions of high concentration to regions of low concentration [204]. The model works by gradually adding noise to the initial clean data, known as the forward process, and learning to incrementally remove the added noise, known as the reverse process, as illustrated in Fig. 5.1.

A condensed summary of the diffusion model is given here. Details can be found in [204, 205].The forward process gradually adds noise to the initial clean data x_0, over T timesteps, as defined:

$$q\left(x_t|x_{t-1}\right) = \mathcal{N}\left(x_t; \sqrt{1-\beta_t}x_{t-1}, \beta_t I\right), \tag{5.1}$$

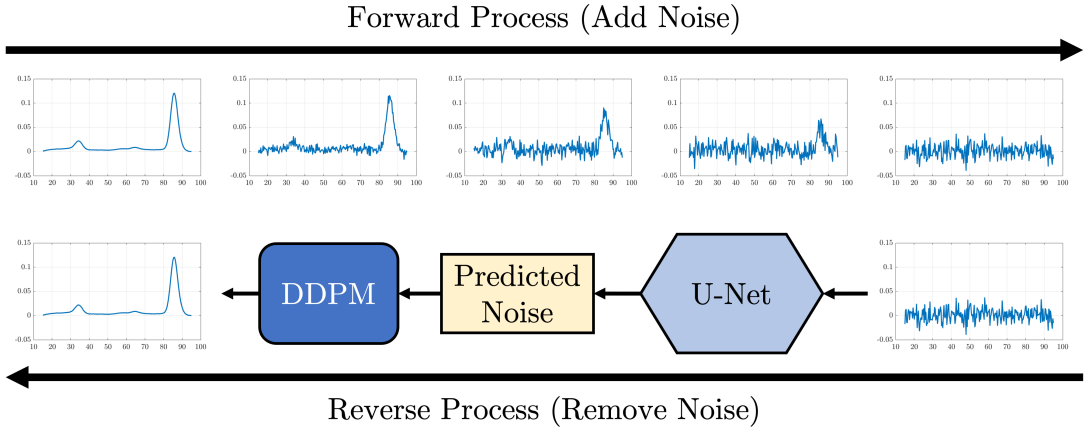


Figure 5.1: The forward and reverse processes of a diffusion model. The U-Net is trained to predict noise, which is gradually removed to obtain a clean input.

where $\beta_{t=1,\ldots,T}$ are pre-defined constants to gradually increase the noise. The term

x_t can be expressed as:

$$x_t = \sqrt{\bar{\alpha}_t} x_0 + \sqrt{1 - \bar{\alpha}_t}\varepsilon, \tag{5.2}$$

where $\varepsilon \sim \mathcal{N}(0, I)$ is the Gaussian noise component, and the term $\bar{\alpha}_t$ is:

$$\bar{\alpha}_t = \prod_{t=1}^{T} (1 - \beta_t)\,. \tag{5.3}$$

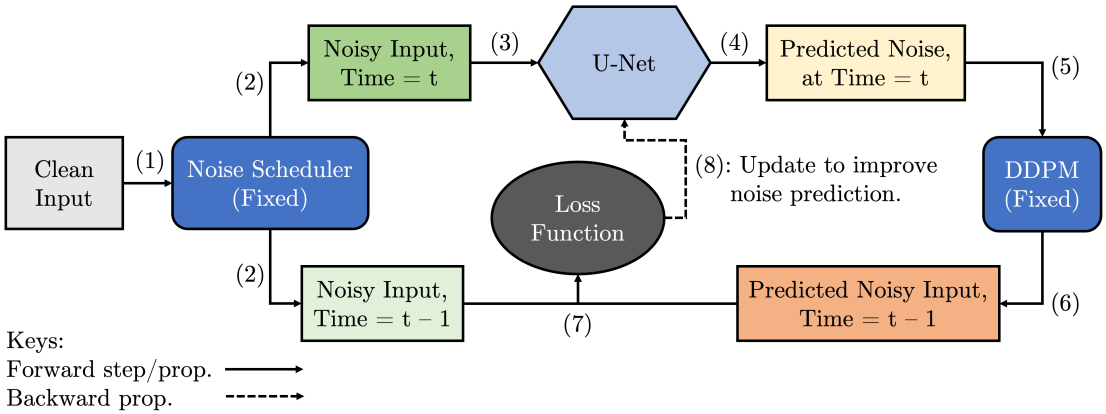


Figure 5.2: Schematic of a Diffusion model, which consists of a (fixed, untrained) noise scheduler, a U-Net for noise prediction, and a fixed DDPM (Denoising Diffusion Probabilistic Model).

The reverse process then gradually removes noise from x_t to generate a less noisy x_{t-1}:

$$p_\theta\left(x_{t-1}|x_t\right) = \mathcal{N}\left(x_{t-1}; \mu_\theta\left(x_t, t\right), \Sigma_\theta\left(x_t, t\right)\right). \tag{5.4}$$

In practice, since the mean μ_θ and variance Σ_θ are unknown, one could only approximate these values. Moreover, Ho *et al.* [205] showed that directly predicting the denoised data is unfeasible. Instead, they proposed that prediction of noise led to more stable training. Therefore, the objective (loss function) of the diffusion model becomes:

$$\mathcal{L} = \mathbb{E}_{x_t, t, \varepsilon_t}\left[\left\|\varepsilon_t - \varepsilon_\theta\left(x_t, t\right)\right\|^2\right], \tag{5.5}$$

with x_t coming from Eq. 5.2, ε_t being the real noise at timestep t, and ε_θ being the prediction noise given the noisy input x_t and timestep t. This prediction is generated by training a neural network, more specifically the U-Net architecture from the original work [205]. From the predicted noise ε_θ, the noisy data can then be denoised:

$$x_{t-1} = \frac{1}{\sqrt{\alpha_t}}\left(x_t - \frac{1-\alpha_t}{\sqrt{1-\alpha_t}}\varepsilon_\theta\right) + \sigma_t z, \tag{5.6}$$

where the variance $\sigma_t = \sqrt{\left(1-\bar{\alpha}_t\right)/\left(1-\bar{\alpha}_{t-1}\right)}\beta_t$ and $z \sim \mathcal{N}\left(0, I\right)$ is the Gaussian noise component. This step is then repeated until $t = 0$ - when the initial data is supposedly noise-free. During training, although it was advised not to directly generate the denoised data, one could either train using noise as the metric (Eq. 5.5), or apply the denoising step (Eq. 5.6) to generate the predicted less-noisy data at $t-1$: $\hat{x}_{t-1} = x_t - \varepsilon_\theta(x_t)$, and train with the real x_{t-1}.

Since the initial proposed model, there have been improvements made to the model, for example the conditional latent diffusion by Rombach *et al.* [206], which uses the attention mechanisms to encode text prompts for conditional image generation purposes [207–209]:

$$\text{Attention}(\text{Q}, \text{K}, \text{V}) = \text{softmax}\left(\frac{\text{QK}^{\text{T}}}{\sqrt{\text{d}_{\text{K}}}}\right)\text{V} \tag{5.7}$$

where Q, K and V are the query, key and value. The self-attention mechanism is used to compute the long-range dependencies within the output features, *i.e.* the global structure of the output, while the cross-attention mechanism is used to compute the correlation between the prompt and the output features. These mechanisms have since been widely used in different generative tasks for creating specific outputs, for example text-to-image generation [206].

5.2.2 Overview of Generative Adversarial Networks (GAN)

Generative adversarial networks were first proposed by Goodfellow *et al.* [210–212], and are a type of neural network architecture which consist of two networks, a generator and a discriminator (or a critic). The main function of the generator is to create synthetic features (the initial paper used images), while the discriminator is to distinguish between real and fake (synthetic) features. The difference between a discriminator and a critic is, the former will predict where the features are real or fake, and the latter will output the degree of realism of the features, *i.e.* how real they are, rather than simply labelling them as absolutely real or fake. The goal of the generator is to "fool" the discriminator into thinking the fake features are

real, while the discriminator aims to separate the fake features from the real ones. The adversarial nature thus comes from the competition between the two models, or one could interpret it as the two models are learning from each other so they could perform better than each other.

The basic GAN proposed by Goodfellow *et al.* [210], as illustrated in Fig. 5.3. A typical training cycle is as follows:

1. The generator (G) takes in an input prompt - a random noise vector z, and outputs a fake set of features (*e.g.* images): G(z),
2. This fake set and a real set (x) are used as inputs for the discriminator model,
3. The discriminator (D) will learn to distinguish the fake sets from the real sets by maximising the log-likelihoods of predicting the correct labels ("real" and "fake"): $\log(\mathrm{D}(\mathrm{x}))$,
4. The generator will learn to create better fake sets that can fool the discriminator by minimising the log-likelihoods of $\log(1 - \mathrm{D}(\mathrm{G}(\mathrm{z})))$.

This is considered a two-player minimax game, with the value function $\mathrm{V}(\mathrm{G}, \mathrm{D})$ defined as below [210]:

$$\min_{\mathrm{G}}\max_{\mathrm{D}} \mathrm{V}(\mathrm{G}, \mathrm{D}) = \mathbb{E}_{\mathrm{x}\sim \mathrm{p}_{\mathrm{data}}(\mathrm{x})}\left[\log(\mathrm{D}(\mathrm{x}))\right] + \mathbb{E}_{\mathrm{z}\sim \mathrm{p}_{\mathrm{z}}(\mathrm{z})}\left[\log(1 - \mathrm{D}(\mathrm{G}(\mathrm{z})))\right]. \quad (5.8)$$

For this basic GAN architecture, the objective is to minimise the Jensen-Shannon divergence between the distribution of the real set and the distribution of the fake

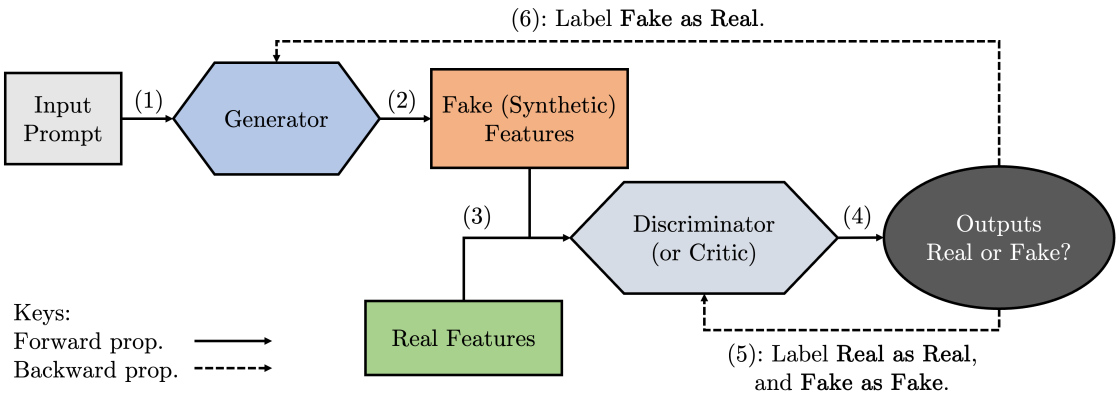


Figure 5.3: Schematic of a GAN model, which consists of a generator model and a discriminator (or critic) model. The typical labels for real and fake are "1" and "0" respectively.

set. However, this has been shown to cause two major issues [213, 214]. First, training can become unstable due to the discriminator being too rigid in real/fake prediction. The binary cross-entropy loss (BCE Loss) function, commonly used in the basic GAN, has the following form:

$$\text{BCE Loss} = -\frac{1}{m}\sum_{i=1}^{m}\left(y^{(i)}\log\left(D\left(x^{(i)}\right)\right) + \left(1-y^{(i)}\right)\log\left(1-D\left(x^{(i)}\right)\right)\right), \quad (5.9)$$

where the first and second terms correspond to the first and second terms in the Jensen-Shannon divergence. When the difference between the real and fake distributions are too large, this loss function can cause vanishing gradient. The generator can no longer learn effectively to create realistic features that can fool the discriminator. The second issue is mode collapse, which refers to the ability of the generator to create only one type of features [215, 216], restricting the diversity of synthetic data points.

This led to the development of Wasserstein GAN (WGAN) by Arjovsky *et al.*

[217] and later WGAN-GP by Gulrajani *et al.* [218] with GP referring to gradient penalty. Instead of minimising the Jensen-Shannon divergence (or other divergence such as Kullback-Leibler), it aims to minimise the Wasserstein-1 distance, also known as the Earth Mover's Distance, which can be qualitatively described as the effort (distance and amount) required to move the fake distribution to the real distribution [219]. The detailed can be found in original paper [217]. In short, the loss function in a WGAN becomes:

$$\min_{G} \max_{D \in D} V(G, D) = \mathop{\mathbb{E}}_{x \sim \mathbb{P}_r} [\log (D(x))] + \mathop{\mathbb{E}}_{\tilde{x} \sim \mathbb{P}_g} [\log (D(\tilde{x}))], \tag{5.10}$$

where $\mathbb{P}_r$ is the data distribution, $\mathbb{P}_g$ is the model distribution defined by $\tilde{x} = G(z)$, $z \sim p(z)$, and the discriminator D must be 1-Lipschitz continuous, meaning the gradient of D at any point can be at most 1. This enables training stability by preventing vanishing gradient. To enforce 1-Lipschitz continuous in the discriminator, Arjovsky *et al.* [217] used weight-clipping, essentially constraining the discriminator weights to be within a certain range of values. They also proposed the idea of training the discriminator (critic) a few epochs for each training epoch of the generator.

In the same year, Gulrajani *et al.* [218] addressed some issues with the weight-clipping approach and proposed an alternative gradient penalty (GP) approach, with

an extra term added to the loss function and some slight rearranging, as follows:

$$\min_{G}\max_{D\in D} V(G,D) = \mathop{\mathbb{E}}_{\tilde{x}\sim\mathbb{P}_g}\left[\log\left(D\left(\tilde{x}\right)\right)\right] - \mathop{\mathbb{E}}_{x\sim\mathbb{P}_r}\left[\log\left(D(x)\right)\right] + \lambda \mathop{\mathbb{E}}_{\hat{x}\sim\mathbb{P}_{\hat{x}}}\left[\left(\|\nabla_{\hat{x}} D\left(\hat{x}\right)\|_2 - 1\right)^2\right], \quad (5.11)$$

where $\hat{x} = \epsilon x + (1-\epsilon)\tilde{x}$, a simple interpolation between the predictions of the real (x) and fake ($\tilde{x}$) feature with a factor of ϵ, the term $\|\nabla_{\hat{x}} D\left(\hat{x}\right)\|$ represents the norm of the gradient of the discriminator with respect to $\hat{x}$, and a scaling term λ. The combined Wasserstein GAN with gradient penalty (WGAN-GP) has since become the most common variation of GAN due to its ability to avoid vanishing gradient and mode collapse.

5.2.3 Overview of Recurrent Neural Network

Recurrent Neural Networks (RNN) are a type of neural network architecture that handles sequential data, for example time-series data like stock prices or text/speech generation and translation, where the previous output affects the subsequent outputs (Fig. 5.4). The main difference between RNN and feed-forward neural network is that the feed-forward NN passes the inputs through the network once and generates an output, while RNN takes the inputs and loops through a computation unit, with the output being fed back into the unit for the next loop (Fig. 5.5).

The main drawback of this basic RNN is its tendency to lose long-term memories when the sequences are long. This happens because of the training process (back-

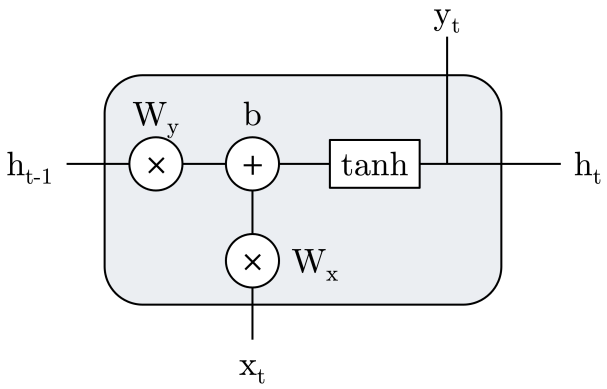


Figure 5.4: The computation of a single unit in a RNN: the input vector at the current timestep t (x_t) is multiplied by a weight matrix W_x, and the output (or the hidden state) from the previous timestep y_{t-1} is multiplied by W_y, and a bias b is added. This is then passed onto an activation function, usually a hyperbolic tangent, generating an output of this current timestep. This process is then repeated to generate a desired sequence.

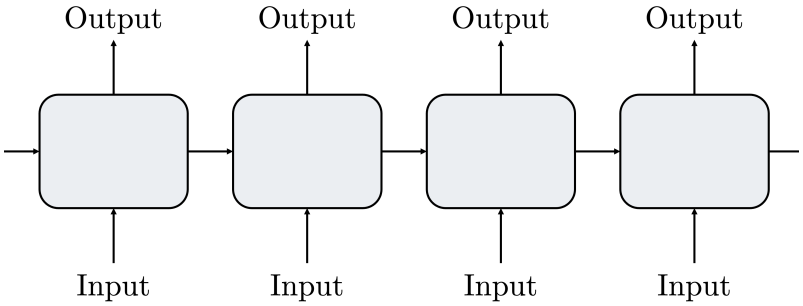


Figure 5.5: A standard RNN architecture with the output from the previous computation unit passing onto the current unit.

propagation through time), leading to vanishing or exploding gradient. Hochreiter *et al.* proposed an alternative gated RNN called the long short-term memory (LSTM) [220], which uses three gates: input, output and forget gates, to control the information flow within the network. A similar, but simplified version of LSTM was proposed by Cho *et al.*, known as the Gated Recurrent Unit (GRU) [221]. These two units are generally considered superior to the original non-gated unit with traditional RNN with a tanh activation unit [222]. While there are debates regarding which unit, LSTM or GRU, is better in general [223, 224], it is generally accepted

that GRU is sufficient for smaller datasets. Due to the relatively small dataset within this study, GRU was chosen for the purpose of synthetic data generation.

A schematic of GRU is shown in Fig. 5.6. It consists of a reset gate and an update gate. The reset gate controls how much of the previous hidden state h_{t-1} is discarded for computing the current hidden state h_t, and the update gate controls how much the previous hidden state to keep. Both gates use a sigmoid activation function, before the outputs from the gates are combined with the input x_t and passed onto the tanh function, and the output (hidden state) is computed. The computation is shown as follows:

$$z_t = \sigma\left(W_z \cdot [h_{t-1}, x_t]\right), \tag{5.12}$$

$$r_t = \sigma\left(W_r \cdot [h_{t-1}, x_t]\right), \tag{5.13}$$

$$\hat{h}_t = \tanh\left(W \cdot [r_t \times h_{t-1}, x_t]\right), \tag{5.14}$$

$$h_t = (1 - z_t) \times h_{t-1} + z_t \times \hat{h}_t. \tag{5.15}$$

While RNN architectures are usually used for prediction tasks, a prompt can be added to (concatenated with) the hidden state h at each time to help the model "remember" what the prediction sequence should be. In addition, a multi-layer GRU can also be employed, by having another layer of units above the current layer, and the output h_t from the current layer is used as the input for the upper layer.

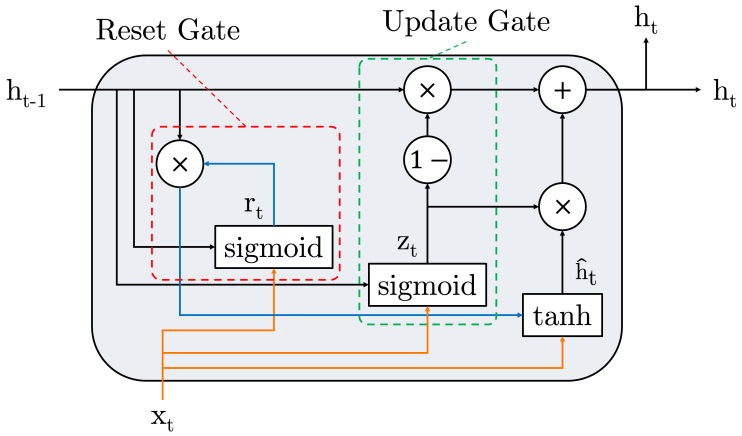


Figure 5.6: Schematic of a GRU used to resolve the issue with long-term memory loss in a traditional RNN unit, while being faster and lighter weight than LSTM.

5.3 Methodology

The goal of this exploratory study is to generate non-parametric features, namely the MO distributions. For conditional generations, one would still require some tangible input prompts for the generator to create desirable features. Here, a method of extracting human-interpretable quantitative features is proposed, along with the model architectures used for each model type.

5.3.1 Pre-processing of misorientation distributions

The non-parametric probability density was computed using the kernel density estimation (KDE), and the peaks were identified using the method mentioned in Chapter 4.4.1. Here, extra steps were taken to extract some parameters to describe each distribution, with the assumption that there are underlying Gaussian distributions, as shown in Fig. 5.7. First, for each peak, a Gaussian distribution is fitted over the peak region ($\pm 2^{\circ}$). Then, the Gaussian mean (very similar to the peak value but

not identical), standard deviation and the data ratio are extracted to represent each twin system.

There are two ways to use these peak features, (1) an array ("peak statistics") to be used as an input prompt to generate a distribution from scratch, and (2) use these parameters to generate a (perfect) combined Gaussian distribution, and use a generator model to turn this ideal distribution to a realistic distribution. The peak statistics array consists of 15 values for the 5 possible twin peaks, with each peak represented by 3 values: the twin mean, standard deviation and data ratio. Zero's were used as placeholders for peaks (twins) that were not identified. Comparing this idealised combined Gaussian and the real distributions (Figs. 5.7 and 5.8), one could see that while the ideal one resembles the real one quite well at the peak regions, it is missing the baseline distribution. The $\pm 2^{\circ}$ was determined to recreate the closest resemblance, which was the reason this metric was previously used in Chapter 4.4.1. For each model type, both approaches of the input prompts, peak statistics and combined Gaussian, were attempted, but it was found that only one would work well for each model.

A bottleneck for training any machine learning models is the dataset size. Since there are only 24 data points (EBSD maps of microstructures) from Chapters 3 and 4, there is a need to artificially increase the dataset size. Although the EBSD maps were not treated as images, image cropping could still be applied here, as shown in Fig. 5.9. Each 24 EBSD maps were cropped to 16 smaller maps with no

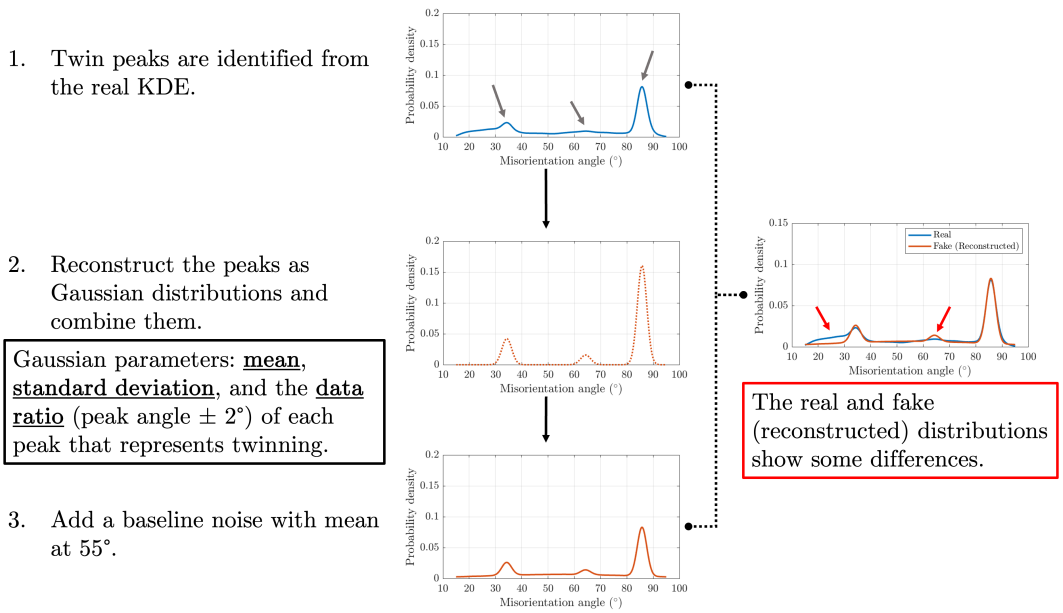


Figure 5.7: An example of pre-processing of the non-parametric KDE for the MO distribution.

overlapping, and only 12 maps from each original set were chosen as the training set, and were subjected to the pre-processing as mentioned above. The two main reasons for this structured cropping of 16 smaller EBSD maps are: (1) cropping into more maps decreases the map size, deviating from the global representation of the microstructures, (2) random-cropping of up to 50 maps (with overlapping allowed) was attempted, however it only increased the training time without affecting the behaviour of the models.

Although only 288 data points were generated, it was a significant increase over the original 24 data points. This larger dataset enabled the use of batch training, meaning the model parameters are updated based on the average loss of each batch (containing a pre-defined number of data points). This speeds up the training and less computation is needed. To assess the performances of the model, the initial 24

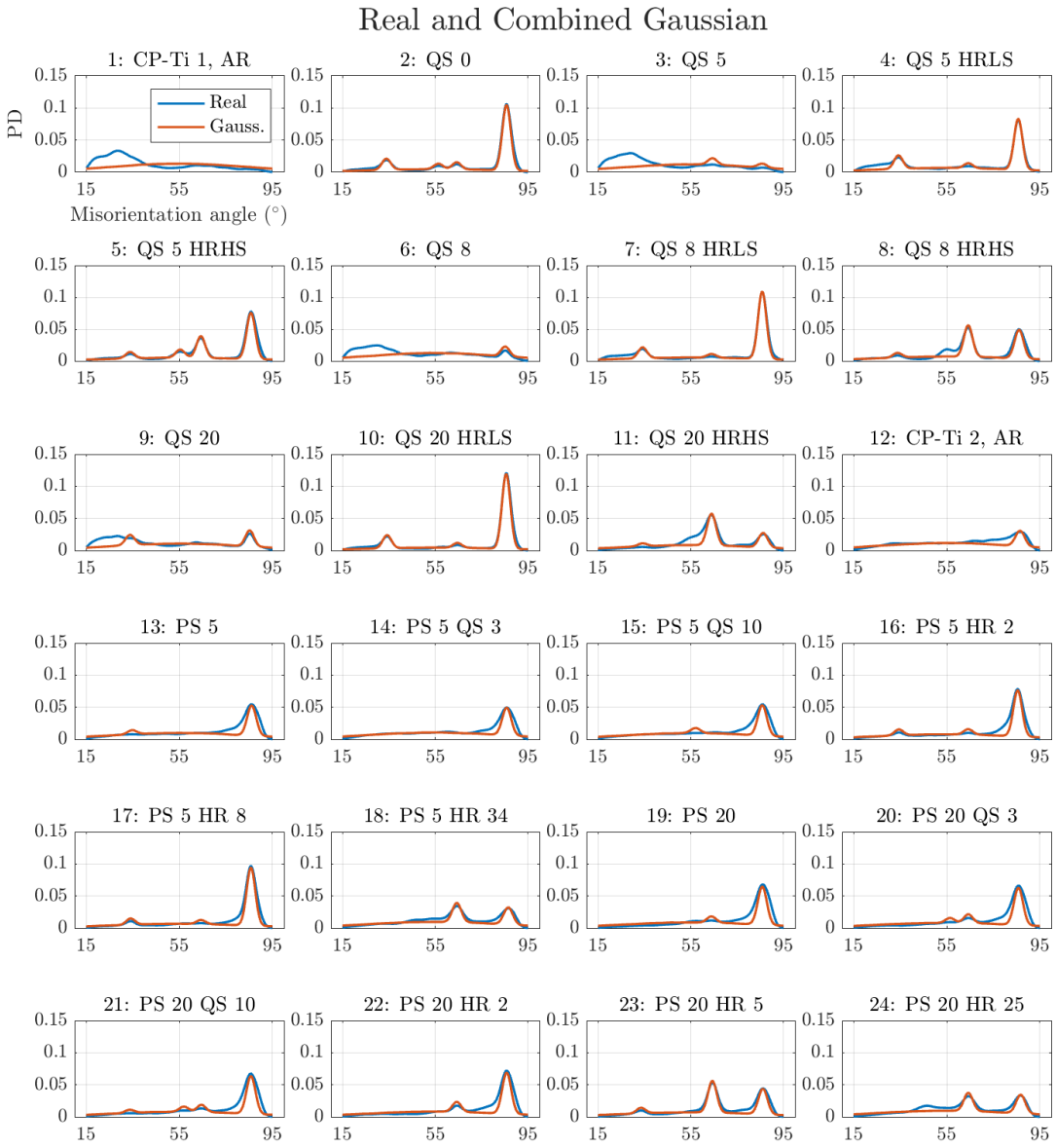


Figure 5.8: Synthetic MO distributions generated by combined Gaussian distributions, as shown in Fig. 5.7.

data points of full size EBSD maps, were used as the testing set. The model architectures and their training input prompts, peak statistics or combined Gaussian, will be discussed in the following section.

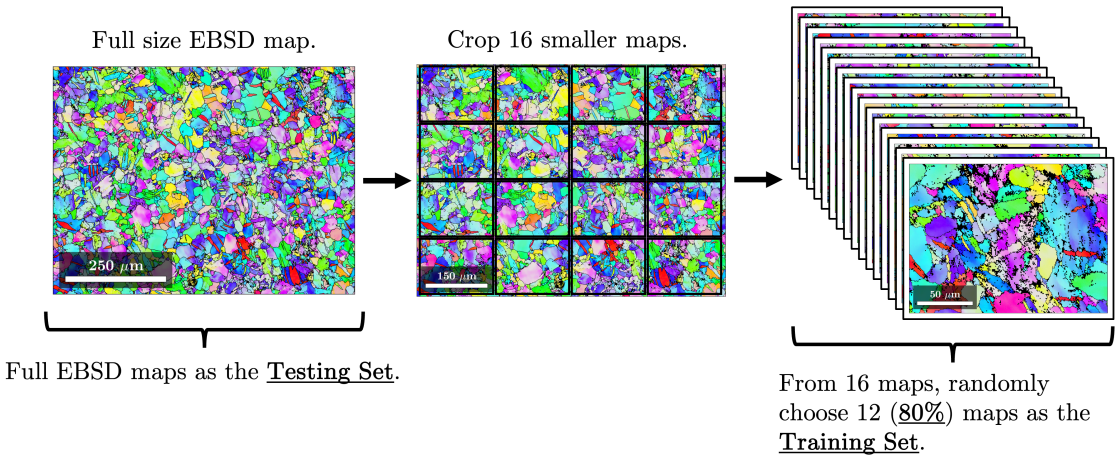


Figure 5.9: To generate more training data points, each 24 original EBSD map (from Chapters 3 and 4) was cropped to 16 smaller EBSD maps with no overlapping. From each set of 16 EBSD maps, only 12 (80%) were chosen for training.

5.3.2 Diffusion model

The standard diffusion model (Fig. 5.10) takes in random noise and the trained model, U-Net and denoiser, gradually removes certain noise components and generates a clean output. However, the purpose here is to conditionally generate features (realistic MO distributions) and not randomly generate plausible features. A prompt (or sometimes called a context) is then needed to guide the model into generating desirable features. A simple diffusion model was built, with a standard neural network used instead of a U-Net with convolution layers, and a context (peak statistics) encoder to generate a numerical prompt. With the dataset in this study, the model failed to generate any meaningful outputs.

An alternative, and more complex model architecture was adopted, which consists of a context encoder, a U-Net, a time embedding and self- and cross-attention mechanisms. It was first proposed by Rombach *et al.*, called the Latent Diffusion

Model [206]. It first compresses the data using a VAE, the diffusion is then done in the latent space. The compressed noisy data is denoised using the U-Net, and is decoded (or reconstructed) to revert to the original dimension. The commercial text-to-image generator *Stable Diffusion* is based on this Latent Diffusion architecture. As this architecture requires a pre-trained VAE to accurately encode and decode the original data, the model adopted in this study was a simplified version without the VAE, and the U-Net size was reduced drastically. The convolution layers were also converted to 1-dimension (or 1-channel) only.

For the forward noise scheduler, the number of timesteps was set to 128, with the β start and end values set to $\beta_1 = 0.0001$ and $\beta_{128} = 0.08$. The noise strength was set to 0.015, which is approximately 10% of the maximum value in the distribution (signal strength). The Adam optimiser was used, with parameters $\beta_{1,2} = 0.9, 0.999$. Multiple combinations of learning rates and epochs were used for training. However, the model could not learn to generate desirable predictions. This is likely due to the high complexity of the model relative to the dataset. Here, an example model is presented as a demonstration. This model used a learning rate of 1×10^{-4} and was trained for 100 epochs. In each epoch, 51 timesteps evenly spaced between 1 and 127 were used to train the U-Net noise predictor.

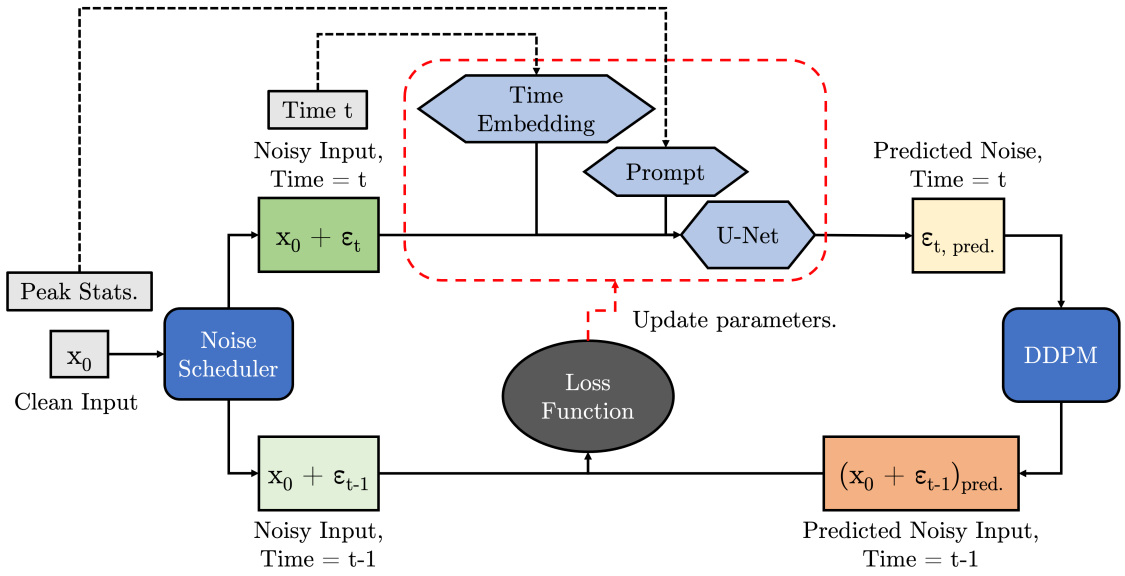


Figure 5.10: The diffusion model with time embedding and prompt encoding for conditional generation of output features. This model failed to learn to generate desirable features, which could be attributed to the model's complexity relative to the dataset.

5.3.3 WGAN-GP

The architectures of the generator and critic are shown Fig. 5.11, and the details of the neural networks are listed in Tables 5.1 and 5.2. The "Leaky ReLU" activation function used here is similar to ReLU, except it applied a gradient (rather than 0 in ReLU) to the negative inputs. This ensured the learning was not stopped when the values within the network became negative. However, at the final layer of the generator, the ReLU was used to ensure the output values must be positive (or zero) for probability density prediction. The critic also used the Leaky ReLU activation in the hidden layers, with a linear function in the final output layer, as required by the Wasserstein distance loss function. The exact number of neurons and layers were determined through trial-and-error. Larger and smaller models, in both depth (number of layers) and breadth (number of neurons per layer), were attempted but

they tended to lead to unstable training or no improvement in predictions.

Table 5.1: The generator architecture in the WGAN-GP used in this study, where n is the number of input features: the number of MO histogram bins. The Leaky ReLU had a negative slope of 0.2 and the drop out probability of 0.5. The total number of learnable parameters in this generator model was 2624768.

Layers	Functions	Dimensions
Input	Linear → Leaky ReLU → Dropout	n=256 → 1024
Hidden 1	Linear → Leaky ReLU → Dropout	1024 → 1024
Hidden 2	Linear → Leaky ReLU → Dropout	1024 → 1024
Output	Linear → ReLU	1024 → 256

Table 5.2: The critic architecture in the WGAN-GP used in this study. The Leaky ReLU activation functions all had a negative slope of 0.1. The total number of learnable parameters in this critic was 2560513.

Layers	Functions	Dimensions
Input	Linear → Leaky ReLU	n=256 → 768
Hidden 1	Linear → Leaky ReLU	768 → 768
Hidden 2	Linear → Leaky ReLU	768 → 768
Hidden 3	Linear → Leaky ReLU	768 → 768
Hidden 4	Linear → Leaky ReLU	768 → 768
Output	Linear	768 → 1

For the model training process, the batch size of the training dataset was set to 4. It was kept small as it was found to improve model convergence [225]. The critic was trained 5 times before each training loop of the generator. For both networks, the Adam optimiser was used, the parameters $\beta_{1,2}$ were set to 0.2 and 0.999, and the learning rate was 1×10^{-4}. The model was trained for a total of 300 epochs, but started to become unstable (generating worse outputs) after 240 epochs. The losses of the first 240 epochs are shown in Fig. 5.12. It should be noted that the

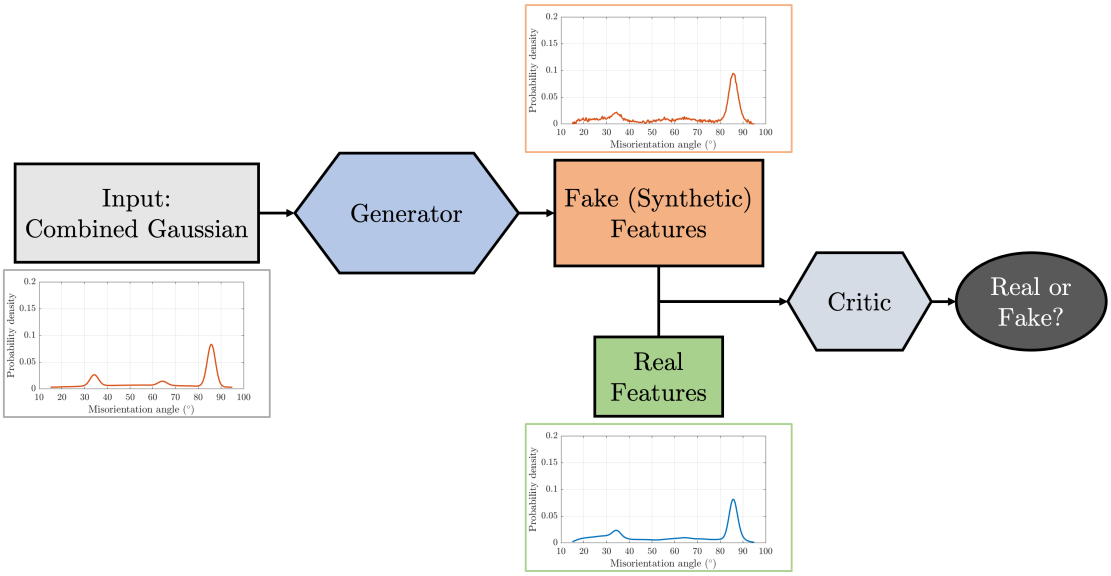


Figure 5.11: Architecture of the WGAN-GP used to convert the combined Gaussian to a realistic MO distribution. The generator essentially added the baseline "noise" to the input, and the critic helped the generator learn the appropriate noise.

losses in GAN are generally considered obsolete, and the actual synthetic (fake) output should be used to assess its performance. Although GAN's are known to be challenging to train [226], the combination of the models sizes, optimiser and epochs here have shown to produce good results.

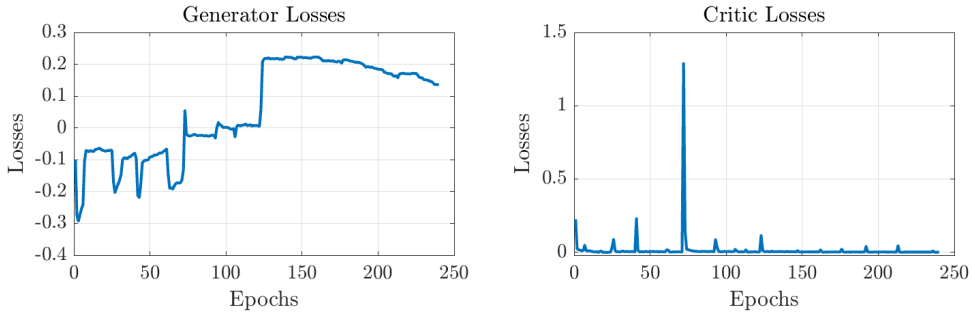


Figure 5.12: Training losses of the generator and critic of the WGAN-GP used.

5.3.4 RNN with GRU

For the RNN with 2-layer GRU, the combined Gaussian was used as input sequence $(x_1, x_2, ..., x_{256})$, and the peak statistics were used as the prompts (c for "context"), which were the initial hidden states $h_{0,1}$ and $h_{0,2}$. The peak statistics were first encoded using a linear→tanh encoder and the dimension was increased from 15 to 128. A dropout layer with a probability of 0.1 was added between the two GRU layers, and a ReLU was added after the second GRU layer.

The model was trained with a schedule of varying learning rates (lr), first 100 epochs of lr = 0.001 then 120 epochs of lr $=1 \times 10^{-5}$. The model losses are shown in Fig. 5.14. The Adam optimiser, with parameters $\beta_{1,2}$ =0.9 and 0.999 respectively, was used, along with the Cross Entropy loss function. A large batch size of 256 was used, which is in contrast with the small batch size in WGAN-GP. A smaller batch size did not lead to improvements in the results, therefore a large batch size was used to increase the training speed.

5.4 Results and discussions

The real and predicted outputs from each model are shown in Figs. 5.15, 5.16 and 5.17. As previously mentioned, qualitatively, the Diffusion model yielded the worst results as the predictions do not follow the general trends of the real distributions. As both the smaller lighter-weight Diffusion model (not shown here due to extremely unstable training) and this larger Diffusion model (adopted from Latent Diffusion)

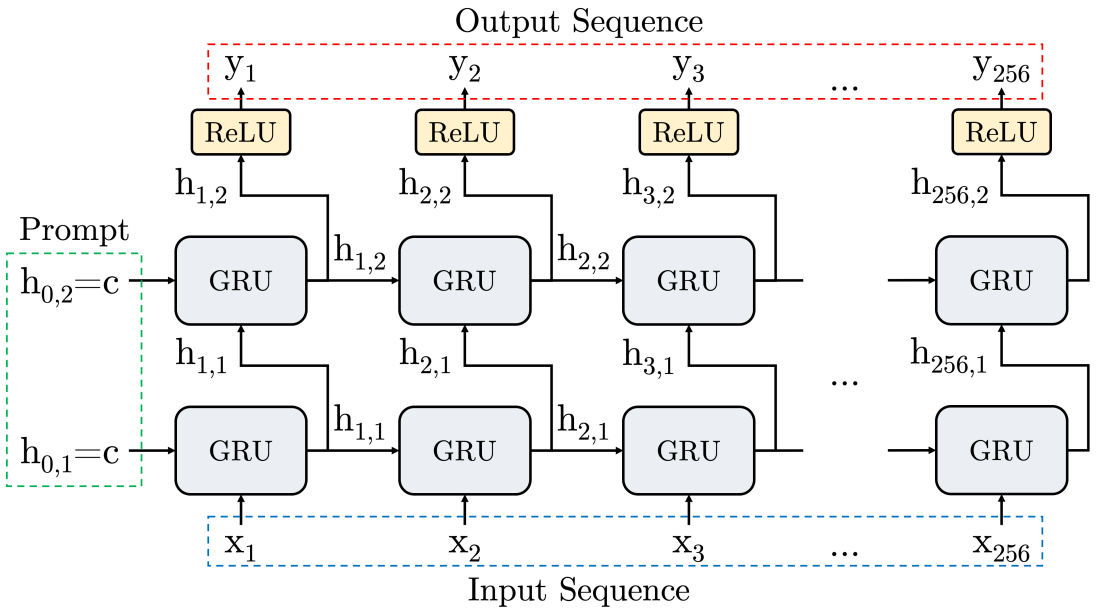


Figure 5.13: Architecture of the RNN with 2-layer GRU used as a sequential generation model, using the peak statistics as prompt to convert an input sequence of combined Gaussian to a realistic MO distribution.

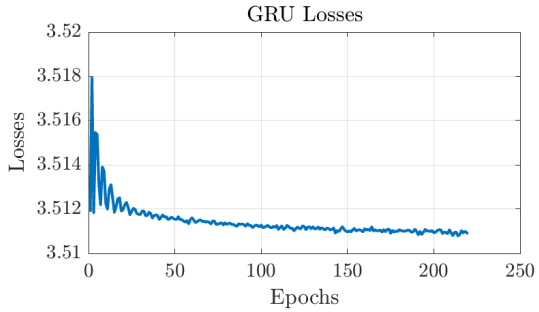


Figure 5.14: Training losses of the RNN with 2-layer GRU, using a prompt as the initial hidden state.

do not produce desirable outputs, it can be concluded that, the training was unsuccessful. Further discussions about the accuracy will not include this model type.

The WGAN-GP (Fig. 5.16), in stark contrast to the Diffusion model, is remarkably good at recreating the MO distributions. The main issue here is the noisy predictions, which would require further post-processing. However, the peaks were mostly maintained, and the added baseline distributions are also visually similar.

As the real and predicted outputs are very similar, one might naturally point to the possibility of over-fitting - essentially the model fitting the training data too well and limiting its ability to generate future predictions. Two things should be noted, first, the training data essentially consists of only 80% of the full dataset, and each cropped EBSD map has its own statistical features, including MO distributions. Therefore, the model has never truly "seen' the testing set (full EBSD maps). Second, although the datasets, both training and testing, are small, they contain a wide range of distributions with varying peaks and underlying distributions. Having the generator recreating all data points to a (qualitatively) good standard might not indicate over-fitting but rather good generalisation.

The RNN with GRU (Fig. 5.17) in contrast did not produce accurate predictions. Although the curves are smoother and the peaks are mostly preserved, it failed to learn the underlying distributions. Moreover, the peak locations seem to be shifted slightly for the majority of the predictions. Overall, while the results are not as bad as the Diffusion model, this RNN with prompted GRU does not seem to be suitable for this generative task.

5.4.1 Accuracy of generative models

Since the Diffusion model has shown poor outputs, it is excluded in the following quantitative analysis. The mean-squared errors (MSE) between the real and synthetic outputs were calculated for the combined Gaussian (as a baseline), WGAN-

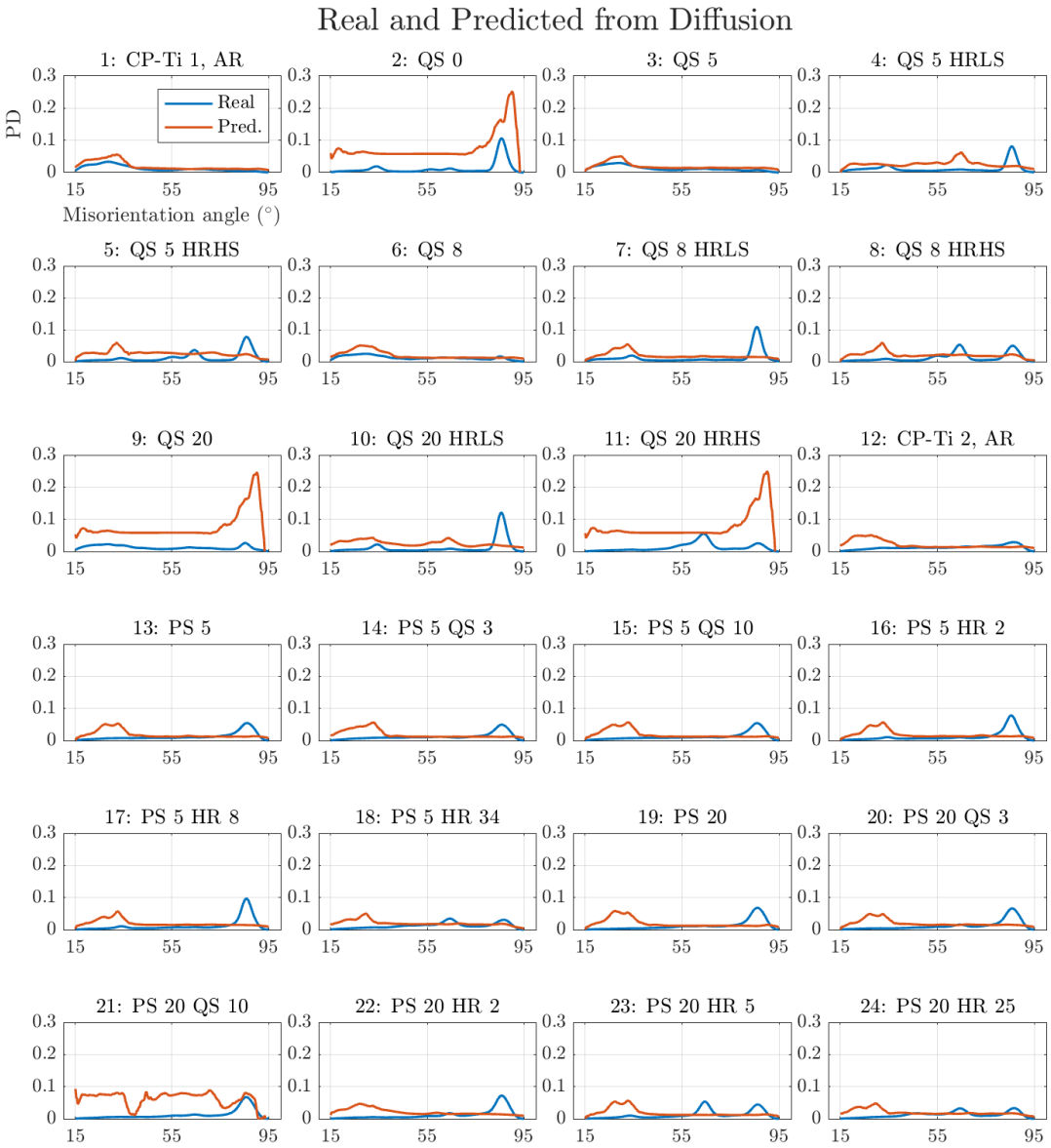


Figure 5.15: Synthetic MO distributions generated by diffusion.

GP and RNN with GRU, shown in Fig. 5.18. The errors from the combined Gaussian outputs are generally low. GRU has worse all the outputs, while WGAN-GP lowers the errors overall.

Inspecting the outliers from the combined Gaussian errors, Specimens 1,3,6 and 9 represent the as-received (undeformed) and the pre-strained (QS 5, 8, 20) con-

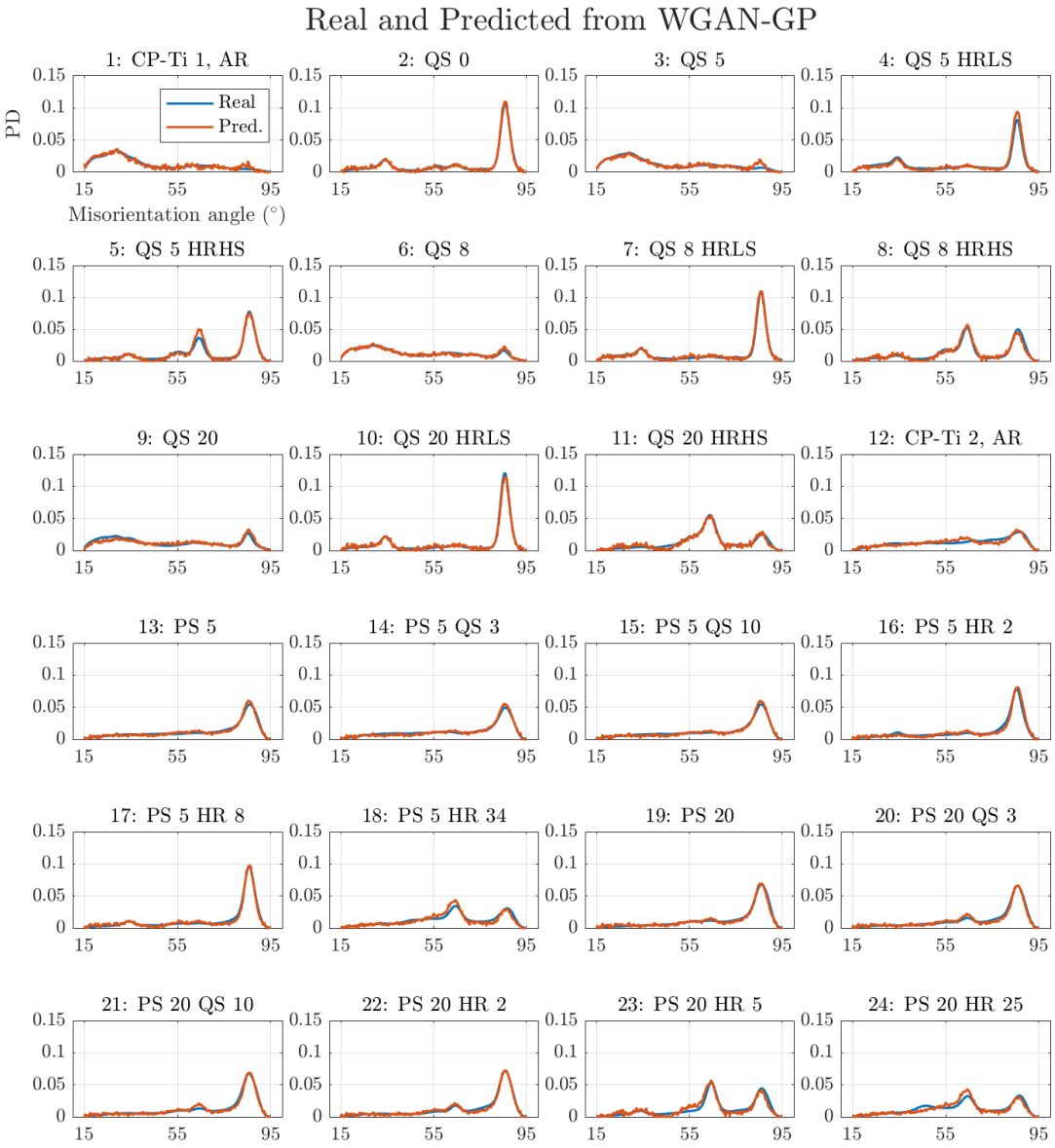


Figure 5.16: Synthetic MO distributions generated by WGAN-GP.

ditions from the experimental campaign in Chapter 3. The low twinning activities means the unquantifiable baseline distributions of MO angles are the highest, since this combined Gaussian was constructed from peak statistics (and a Gaussian noise from 55°) only. A selected few (specimens 2,4 and 5) show very good reconstruction from combined Gaussian only, which supports the previously stated reason for choosing the ±2° around peaks as the data ratios. For the specimens from Chap-

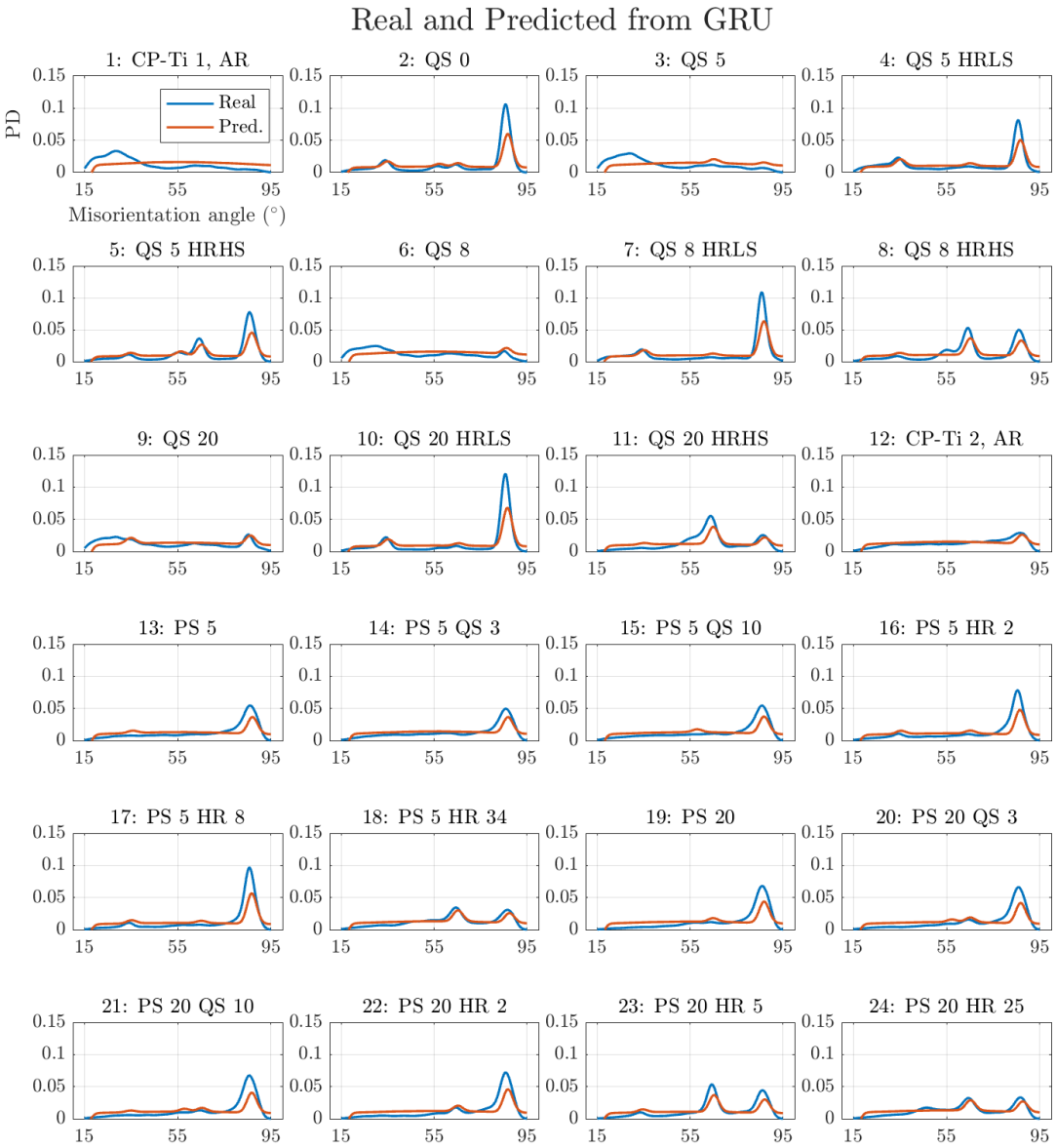


Figure 5.17: Synthetic MO distributions generated by GRU.

ter 4 (specimens 12 to 24), the errors from combined Gaussian do not deviate as much, indicating it is consistently missing the underlying distributions of MO angles. These results show that the combined Gaussian method alone could not consistently generate similar features as the real specimens.

Using WGAN-GP to learn the baseline distributions seems to be the best ap-

proach. The errors overall are not only lower but also more stable. While it shows marginally higher error in a few specimens than the combined Gaussian, its consistent error and good overall performance outweigh this drawback. Both qualitative and quantitative analyses point at the WGAN-GP for being the best model in this study. The goal of the generative model here is, to use the twin peak statistics (parameters) to create a realistic distributions (non-parametric) of MO angles.

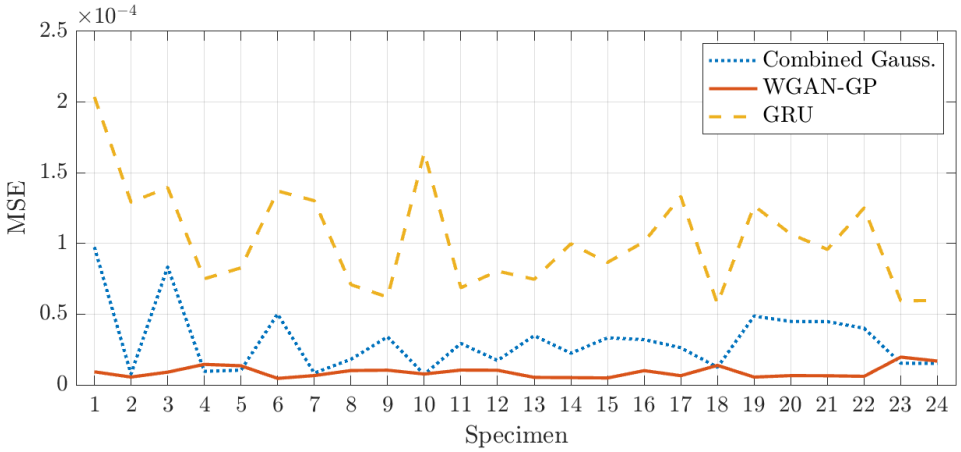


Figure 5.18: The mean squared errors (MSE) between the synthetic and real MO distributions. The specimen labels (1 to 24) are as defined previous figures (*e.g.* Fig. 5.16).

As previously mentioned, although the dataset here is too small for accurate interpolations to generate real training data (for microstructure-bulk behaviour predictions), to determine the potential application of this model, synthetic peak statistics were created as test inputs. Fig. 5.19 shows two examples of the WGAN-GP predictions of synthetic peak statistics interpolated from QS 5/QS 5 HRLS and PS 5 HR 2/PS 5 HR 8. The synthetic peak statistics were first used to create combined Gaussian, then passed onto the trained generator in WGAN-GP. Note that, since the underlying changes in peak statistics are assumed to be non-linear (*e.g.* the

peaks statistic at the mid-point stress between QS 5 and QS 5 HRLS are not the average of the two), an arbitrary ratio of 0.85/0.15 was used. Although the true accuracy of these results cannot be verified, qualitatively, they captured some of the underlying features (red arrows in the Fig. 5.19). Most importantly, the model did not drastically change the peak features, further supporting that over-fitting did not occur.

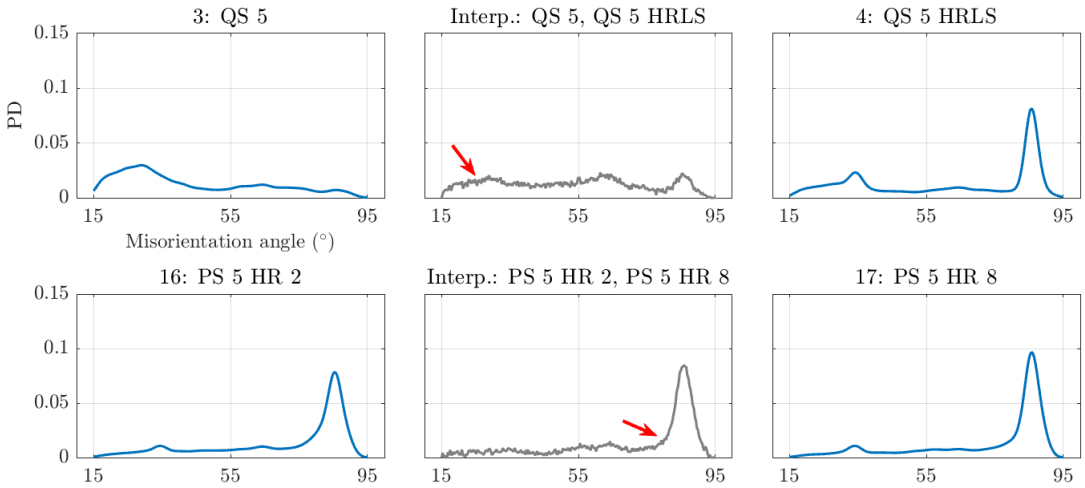


Figure 5.19: Predictions (middle figures) using interpolated twin peak statistics from real specimens (left and right figures). The arrows indicate the underlying features generated from the trained WGAN-GP model.

While only one of these models shows positive results, the small dataset is the bottleneck in utilising machine learning models to their fullest potentials. The most important conclusion here is that there is a future for generative machine learning models to be used in scientific data augmentation. The results here are not indicative towards any specific models or approaches for this purpose, but rather the need to further develop a routine in applying these models. In this case, it could simply be (1) collecting more data from experiments and existing literature for interpolations,

(2) conducting sensitivity analyses of parameters in this workflow (*e.g.* changing the $\pm 2^{\circ}$ in the combined Gaussian) and (3) investigating the use of different model types, features and validate with experimental data and physically-based modelling.

5.5 Conclusions

To conclude this chapter, it was identified that due to the expensive and time-consuming nature in experimental data collection, there is a need to maximise the use of existing data. In the field of solid mechanics/materials science, creating realistic and plausible microstructure features is crucial in both data-driven physically-based approaches for better predictive capabilities. The microstructure data is high-dimensional and some features cannot be studied easily due to the non-parametric nature. This chapter aimed at exploring the possibility of using generative machine learning models in recreating non-parametric features in the dataset in this study.

Since the goal was to create a non-parametric MO distribution using generative ML models, human-interpretable parameters correlated to the peaks in distributions were first extracted with assumption of underlying Gaussian distributions. These peak statistics features were then used as prompts for the generative models to control the output predictions. Three model types were used in this study, Diffusion, GAN and RNN with GRU. Diffusion models were quickly ruled out due to the unsatisfactory performance of both a simple Diffusion and a Latent Diffusion-inspired model with attention mechanisms. The RNN with GRU also did not yield acceptable results. The GAN model, specially using WGAN-GP architecture, has shown

to be able to convert an idealised combined Gaussian into a realistic distribution with unquantifiable underlying distribution. The positive results indicate there are potentials in adapting generative models in data augmentation, however, further development including larger datasets is required.

The possibility of using generative models has paved ways to creating realistic synthetic data points, further enhancing the current capabilities of inverse materials engineering (Materials by Design). While existing models primarily focus on alloying elements, for example the Alloys by Design framework [200, 227], the potential in engineering grain morphology (*e.g.* dislocation density, grain/twin boundaries) could significantly improve the possibility of using pure metals as structural/load bearing components. This will aid in lowering manufacturing barriers as pure metals are easier to produce without exotic alloying elements, and allowing more choices from a wider range of materials.

Chapter 6

Conclusions

This chapter serves as the final concluding remarks of the scientific contributions from the previous chapters in this thesis, including the experimental campaigns, statistical analyses and investigations on generative models on data augmentation. Previous discussions have identified areas that will be worth revisiting, as well as the future implications of the work here.

6.1 Summary and key contributions

This thesis investigates the high strain-rate deformation mechanisms of pre-strained pure titanium (CP-Ti, grade 2). As titanium is inherently anisotropic, pre-straining from manufacturing processes induces microscopic defects and changes overall texture, further influencing the mechanical properties. From the literature review in Chapter 1, while effect of pre-straining has gained some interest in recent years with studies on strain-path changes, they were confined to quasistatic loading. However, titanium is a strain-rate sensitive material in both the bulk and micro scales. Due to the lack of published studies, this thesis conducts experimental investigations on the effect of pre-straining on the high strain-rate deformation of pure titanium, with

a strong focus on the microstructure evolution. The main questions to address were:

1. What features from pre-straining affect the high-rate behaviour?

2. How to extract statistically-representative features from the microstructures which relate to mechanical properties?

3. How to correlate microscopic features and their respective bulk behaviour?

To minimise microstructure variations due to alloying effects, pure titanium (CP-Ti grade 2) was used throughout this thesis. Interrupted testing was performed and the recovered specimens were subjected to EBSD analysis. The first experimental campaign in Chapter 3 studied the role of strain-path with two stages of compression, first quasistatic (QS) then high-rate (HR). The HR testing was conducted on a modified SHPB with a momentum trap, which allowed interrupted testing. The **novel findings** from this campaign are:

- The **HR twin nucleation sequence** for a prismatic-pyramidal textured titanium was identified as: $\{10\bar{1}2\}$ ET $\rightarrow$ $\{11\bar{2}1\}$ ET $\rightarrow$ $\{11\bar{2}2\}$ CT $\rightarrow$ $\{10\bar{1}1\}$ CT. This is different from existing literature on QS deformation of titanium with similar textures [31, 35], which often shows that the $\{11\bar{2}2\}$ twin was the second system to be activated, and

- The twin boundaries generated from the first QS compression had a significant effect on the yield stress under the second HR compression. Therefore, **pre-existing twin boundaries acted as a key strengthening mechanism** of titanium at the high strain-rate deformation. This feature is rarely considered in literature as studies on high-rate are limited. It is also neglected in

microstructure-aware modelling which limits their applications on pre-strained titanium. This new finding therefore expands on the current understanding of strengthening mechanisms in titanium, indicating further studies are required to elucidate the role of twin boundaries.

Several questions were raised from the first campaign, including the mechanisms involved at the onset of yielding and failure mechanisms of titanium with different levels of pre-straining. Chapter 4 investigated the **strain-rate effect on early-stage and incipient failure** of pre-strained titanium. A novel approach was developed to generate two different pre-strained titanium. This involved compressing substantially large cylinders and machining smaller test specimens from the regions of uniform strain. **Advanced statistical approaches** were employed to quantitatively **identify twin systems** from the grain boundary misorientation distributions, and to extract **grain orientation distributions** information from the Euler angles. Other statistical features, such as average grain sizes and shapes (aspect ratio), were also analysed. A summary of findings from the microstructure evolution is as follows:

- In **QS deformation**, dislocation slips were the primary deformation mechanisms, and pre-straining seemed to have no effect on the mechanical behaviour beyond changing the overall texture. This is in **good agreement with existing literature** that the mechanical behaviour of titanium is simply texture-dependent,

- At the early stages of HR deformation, the hardening rates were related to the twinning and dislocation activities. When **the growth of** $\{10\bar{1}2\}$ **twin and**

low CRSS slip (Prismatic<a>) were favoured in the prismatic/pyramidal-textured titanium, the flow stresses were low but a **hardening rate was high**. It was postulated that as twin boundaries swept through the parent grains during twin growth, dislocations were generated within the twinned regions, which is supported by the **high GOS** (grain orientation spread),

- Conversely, with a basal texture, **nucleation of** $\{11\bar{2}2\}$ **twin** was favoured, twin boundary fractions increased but the overall texture remained. The Py<c+a> slip was still geometrically-favoured, leading to higher flow stresses than the prismatic/pyramidal-textured titanium. Dislocations likely piled up which led to **high LAGB densities**. Since LAGB's only acted as partial obstacles for slips, and the migration of LAGB's also acted as a strain accommodation mechanism, it resulted in a **lower hardening rate**.

- At the **incipient failure** stage in HR, both pre-strained materials exhibited very **similar microstructures**. Evidences suggest that **dynamic recrystallisation** occured. However, the dislocation structures were different. In the pre-strained titanium with an initial prismatic/pyramidal texture, the maximum GOS was high, while the initial basal texture displayed high LAGB density. To ability of LAGB's to resist crack growth could suggest a more ductile failure. This is only a hypothesis since the fragments were destroyed at secondary loading during the experiment.

Following the investigation of pre-strained effects, the **correlations between microstructures and bulk behaviour** were established using statistical modelling.

Following the investigation of pre-strained effects, since the small dataset was unsuitable for deriving phenomenological or physical governing laws, statistical models were employed due to **explore the underlying correlations and patterns in the dataset**. Key microstructure features were extracted using PCA, and their correlations with the respective bulk mechanical properties were examined using machine learning models. The results **re-emphasised the importance of twin boundaries** through MO distributions, and identified **new features including grain shapes and LAGB densities**. It also confirmed the correlations of SF's of most slips systems, however the Ba<a> slip was omitted by the analysis possibly because of the low variance. This signifies the limitations of existing microstructure-aware models which often neglect the features identified from this study. Incorporating additional features could help extend the applications of these models, such as the pre-strained materials in this study. On the other hand, this workflow can also inform experiment design by targeting features with low variance, such as grain sizes from this study.

Prior to the development of a robust physically-based model, machine learning models are often used as surrogate models. However, they require a large amount of data for training. Since experimental data is expensive and time-consuming to obtain, the final body of work aimed to explore the possibility of using generative machine learning (GenAI) to **create synthetic microstructure data**. Although the small dataset inhibited meaningful interpolation, there was an opportunity to assess how non-parametric features can be created. Three different generative mod-

els were assessed. In particular, the **Generative Adversarial Networks (GAN)** demonstrated its ability to **create non-parametric MO distributions**. Although there are short-comings, this positive result has shown huge potential in applying GenAI to create realistic synthetic data in the field of materials science.

6.2 Future works

6.2.1 Limitations and potential improvements

There are several areas worth revisiting in relation to experimental testing. Regarding the testing conducted in this thesis, the first area is the uncertainty in **using SHPB to conduct low-strain interrupted testing**. It is well-known that the very early stages of SHPB data are typically disregarded, and practically this might extend further due to the laboratory limitations. This restricts the validity of testing using SHPB, leading to uncertainties in the microstructure studies. The real strain-rate of the specimens at the early stage is difficult to quantify due to the initial wave propagations (ring-up). The second area is capturing the failure mechanisms of the specimens in a dynamic compressive test. This is because the fragments/fractured pieces are re-compressed using both their own momentum and the movement of the SHPB bars. This creates a secondary loading and damages the fracture surfaces, and the recovered specimens will no longer represent the exact condition at failure. Overcoming this issue with compressive testing might be very challenging, therefore other methods, such as tensile testing, could be employed.

Another key limitation is the microstructure analysis, mainly on the **2-dimensional EBSD maps**. Since the specimens were 3-dimensional, obtaining EBSD maps from only the plane normal to the loading direction might be insufficient if the specimen is not homogeneous. Features such as grain geometries, volumes and any highly-localised features (*e.g.* shear bands) might be overlooked. Besides, the resolution of SEM is insufficient to directly observe dislocation slip and nucleation. The analyses made regarding slip systems in this thesis, although based on existing literature, remain speculative. A possible solution is to obtain TEM images to confirm the findings inferred from grain-level observations.

The defined scope of this project did not account for all possible pre-straining conditions. The studies conducted here still leave a sizeable gap, for example an additional strain-level between 5% and 20% strain could serve as an intermediate state, as well as using heat-treatment to reduce internal stress without removing pre-activated twins. The loading conditions, including **direction, strain-rate and temperature**, could also be incorporated in future studies. In particular, since twinning in titanium becomes much more active in either low temperature or high strain-rate loading, the microstructure evolution under this combined effect could lead a high degree of grain refinement through twinning. This might be helpful in engineering nanocrystalline materials, and understanding the behaviour in extreme conditions.

The **statistical analyses** proposed in this thesis could also be refined by conducting **parametric analyses using a larger dataset**. The parameters include: (1) number of bins of misorientation (MO) distribution histograms, as more bins produce smoother trends but increase the computation time, (2) bandwidth selection of Kernel Density Estimation, and (3) the $\pm 2^{\circ}$ around peaks for the MO distribution. For the machine learning models, more data could be obtained from experiments or existing literature, and they should also increase in complexity with more data points.

6.2.2 Future implications on materials discovery

The future work proposed above aimed to advance the current understanding in solid mechanics and materials science. The expensive and time-consuming nature of experiments results in only a selected (hence limited) number of testing being conducted. The assessment on generative models aimed to determine how these high-dimensional and non-parametric features can be created synthetically. With the promising results from the assessment, the generative models should be further developed alongside experimental investigations. Using a more systematic approach to obtain experimental data, such as with the workflow in Chapter 4.6.4, and a well-trained generator to interpolate between the experimental data, the process of realistic synthetic data generation could be greatly simplified.

A large and ever-growing material database will advance statistical-based mate-

rials discovery frameworks, as they rely on learning the underlying correlations between different parameters and the bulk properties. By inverting modelling, it can create, or discover, new possible materials features and parameters for manufacturing (*e.g.* grain morphologies, alloy compositions, casting and additive-manufacturing parameters) based on the required properties (*e.g.* yield stress at a certain temperature and strain-rate). Specifically, this thesis shows that pure titanium can be significantly strengthened with pre-straining alone, without alloying elements. Carefully selecting materials features can reduce the traditional trial-and-error testing of creating new materials. This will also aid the development of physically-based models by providing more data points for parameter calibration.

Bibliography

[1] G. Lütjering and J. C. Williams. *Titanium*. 2nd ed. 2007. ISBN: 9780891182047. DOI: 10.2134/agronmonogr9.2.c15.

[2] T. B. Britton, F. P. E. Dunne, and A. J. Wilkinson. "On the mechanistic basis of deformation at the microscale in hexagonal close-packed metals". In: *Proceedings of the Royal Society A: Mathematical, Physical and Engineering Sciences* 471.2178 (2015). DOI: 10.1098/rspa.2014.0881.

[3] C. Leyens and M. Peters. *Titanium and Titanium Alloys: Fundamentals and Applications*. Vol. 1. Wiley, 2003. ISBN: 3527305343.

[4] A. Foul et al. "Dynamic transformation of $\alpha \rightarrow \beta$ titanium at temperatures below the β-transus in commercially pure titanium". In: *Materials Science and Engineering: A* 722.March (2018), pp. 156–159. ISSN: 09215093. DOI: 10.1016/j.msea.2018.02.097.

[5] Y. K. Vohra and P. T. Spencer. "Novel γ-phase of titanium metal at megabar pressures". In: *Physical Review Letters* 86.14 (2001), pp. 3068–3071. ISSN: 00319007. DOI: 10.1103/PhysRevLett.86.3068.

[6] Y. Akahama, H. Kawamura, and T. Le Bihan. "New δ (distorted-bcc) titanium to 220 GPa". In: *Physical Review Letters* 87.27 (2001), pp. 275503–1–275503–4. DOI: 10.1103/PhysRevLett.87.275503.

[7] I. Manna et al. "Formation of face-centered-cubic titanium by mechanical attrition". In: *Journal of Applied Physics* 93.3 (2003), pp. 1520–1524. DOI: 10.1063/1.1530718.

[8] W. D. Callister and D. G. Rethwisch. *Materials science and engineering: An introduction*. 8th ed. Vol. 12. 1. John Wiley & Sons, Inc., 2007. DOI: 10.1016/0261-3069(91)90101-9.

[9] K. K. Sankaran and R. S. Mishra. *Metallurgy and Design of Alloys with Hierarchical Microstructures*. Elsevier, 2017. ISBN: 9780128120682. DOI: 10.1016/B978-0-12-812068-2.00005-9.

[10] F. C. Frank and W. T. Read. "Multiplication processes for slow moving dislocations". In: *Physical Review* 79.4 (1950), pp. 722–723. ISSN: 0031899X. DOI: 10.1103/PhysRev.79.722.

[11] D. Hull and D. J. Bacon. *Introduction to Dislocations*. Butterworth-Heinemann, 2011. ISBN: 9780080966724. DOI: 10.1016/s1369-7021(11)70217-6.

[12] E. O. Hall. "The deformation and ageing of mild steel: III Discussion of results". In: *Proceedings of the Physical Society. Section B* 64.9 (1951), pp. 747–753. ISSN: 03701301. DOI: 10.1088/0370-1301/64/9/303.

[13] N. J. Petch. "The cleavage strength of polycrystals". In: *Journal of the Iron and Steel Institute* 174.19 (1953), pp. 25–28.

[14] A. A. Salem, S. R. Kalidindi, and R. D. Doherty. "Strain hardening of titanium: Role of deformation twinning". In: *Acta Materialia* 51.14 (2003), pp. 4225–4237. ISSN: 13596454. DOI: 10.1016/S1359-6454(03)00239-8.

[15] J.W. Christian and S. Mahajan. "Deformation Twinning". In: *Progress in Materials Science* 39.2 (1995), pp. 1–157. ISSN: 15213951. DOI: 10.1002/pssb.2221910204.

[16] B. Wang et al. "Effect of grain size on twinning behavior of pure titanium at room temperature". In: *Materials Science and Engineering A* 827 (2021). ISSN: 09215093. DOI: 10.1016/j.msea.2021.142060.

[17] X. Li et al. "Interaction of $\{112\bar{}2\}$ twin variants in hexagonal close-packed titanium". In: *Journal of Materials Science and Technology* 35.4 (2019), pp. 660–666. ISSN: 10050302. DOI: 10.1016/j.jmst.2018.09.049.

[18] J.-r. Luo, X. Song, and M. -y. Wang. "Effects of different types of twinning on microstructure and mechanical properties of a strongly textured TA2 commercially pure titanium alloy subjected to rolling at ambient and cryogenic temperatures". In: *Journal of Iron and Steel Research International* 25.3 (2018), pp. 275–281. ISSN: 22103988. DOI: 10.1007/s42243-018-0026-2.

[19] L. Nervo et al. "A study of deformation twinning in a titanium alloy by X-ray diffraction contrast tomography". In: *Acta Materialia* 105 (2016), pp. 417–428. ISSN: 13596454. DOI: 10.1016/j.actamat.2015.12.032.

[20] Q. Luan, T. B. Britton, and T.S. Jun. "Strain rate sensitivity in commercial pure titanium: The competition between slip and deformation twinning". In: *Materials Science and Engineering A* 734.June (2018), pp. 385–397. ISSN: 09215093. DOI: 10.1016/j.msea.2018.08.010.

[21] M. H. Yoo. "Slip, twinning, and fracture in hexagonal close-packed metals". In: *Metallurgical Transactions A* 12.3 (1981), pp. 409–418. DOI: 10.1007/BF02648537.

[22] Y. Zhong, F. Yin, and K. Nagai. "Role of deformation twin on texture evolution in cold-rolled commercial-purity Ti". In: *Journal of Materials Research* 23.11 (2008), pp. 2954–2966. ISSN: 08842914. DOI: 10.1557/JMR.2008.0354.

[23] T. R. Bieler et al. "In situ characterization of twin nucleation in pure Ti using 3D-XRD". In: *Metallurgical and Materials Transactions A: Physical Metallurgy and Materials Science* 45.1 (2014), pp. 109–122. DOI: 10.1007/s11661-013-2082-3.

[24] P. Zhou et al. "Twin Interactions in Pure Ti Under High Strain Rate Compression". In: *Metallurgical and Materials Transactions A: Physical Metallurgy and Materials Science* 48.1 (2017), pp. 126–138. ISSN: 10735623. DOI: 10.1007/s11661-016-3832-9.

[25] S. Xu et al. "Secondary twin variant selection in four types of double twins in titanium". In: *Acta Materialia* 152 (2018), pp. 58–76. ISSN: 13596454. DOI: 10.1016/j.actamat.2018.03.068.

[26] M. A. Kumar et al. "Role of microstructure on twin nucleation and growth in HCP titanium: A statistical study". In: *Acta Materialia* 148 (2018), pp. 123–132. ISSN: 13596454. DOI: 10.1016/j.actamat.2018.01.041.

[27] Z. W. Huang et al. "Evolution of twinning systems and variants during sequential twinning in cryo-rolled titanium". In: *International Journal of Plasticity* 112 (2019), pp. 52–67. ISSN: 07496419. DOI: 10.1016/j.ijplas.2018.08.008.

[28] F. Xu et al. "Effect of twinning on microstructure and texture evolutions of pure Ti during dynamic plastic deformation". In: *Materials Science and Engineering A* 564 (2013), pp. 22–33. ISSN: 09215093. DOI: 10.1016/j.msea.2012.11.097.

[29] M. S. Lee et al. "The role of strain rate and texture in the deformation of commercially pure titanium at cryogenic temperature". In: *Materials Science and Engineering A* 827 (2021). ISSN: 09215093. DOI: 10.1016/j.msea.2021.142042.

[30] V. Sahu, S. Gupta, and N. P. Gurao. "Effect of Initial Texture on the Evolution of Microstructure and Texture During Rolling of Commercially Pure Titanium at Room and Cryogenic Temperature". In: *Metallurgical and Materials Transactions A: Physical Metallurgy and Materials Science* 51.11 (2020), pp. 5848–5860. ISSN: 10735623. DOI: 10.1007/s11661-020-05979-8.

[31] M. Wroński et al. "Deformation behavior of CP-titanium under strain path changes: Experiment and crystal plasticity modeling". In: *International Journal of Plasticity* 148 (Jan. 2022). DOI: 10.1016/j.ijplas.2021.103129.

[32] C. Zhu et al. "Grain size and specimen thickness effects on twinning behaviors in high strain rate deformation of ultra-thin pure titanium sheet". In: *Materials Science and Engineering A* 832 (2022). ISSN: 09215093. DOI: 10.1016/j.msea.2021.142417.

[33] S. J. Lainé and K. M. Knowles. "Deformation twinning in commercial purity titanium at room temperature". In: *Philosophical Magazine* 95.20 (2015), pp. 2153–2166. ISSN: 14786443. DOI: 10.1080/14786435.2015.1051157.

[34] S. V. Zherebtsov et al. "Formation of nanostructures in commercial-purity titanium via cryorolling". In: *Acta Materialia* 61.4 (2013), pp. 1167–1178. DOI: 10.1016/j.actamat.2012.10.026.

[35] M. S. Lee et al. "In-situ neutron diffraction study of lattice deformation behaviour of commercially pure titanium at cryogenic temperature". In: *Scientific Reports* 12.1 (2022), pp. 1–10. DOI: 10.1038/s41598-022-07640-3.

[36] M. Jackson et al. "Effect of initial microstructure on plastic flow behaviour during isothermal forging of Ti-10V-2Fe-3Al". In: *Materials Science and Engineering: A* 501.1-2 (2009), pp. 248–254. DOI: 10.1016/j.msea.2008.09.071.

[37] N. Gey et al. "Texture and microtexture variations in a near-α titanium forged disk of bimodal microstructure". In: *Acta Materialia* 60.6-7 (2012), pp. 2647–2655. ISSN: 13596454. DOI: 10.1016/j.actamat.2012.01.031.

[38] Q. Zhao et al. "High-strength titanium alloys for aerospace engineering applications: A review on melting-forging process". In: *Materials Science and Engineering: A* 845.May (2022), p. 143260. ISSN: 09215093. DOI: 10.1016/j.msea.2022.143260.

[39] M. Jackson et al. "The microstructural evolution of near beta alloy Ti-10V-2Fe-3Al during subtransus forging". In: *Metallurgical and Materials Transactions A: Physical Metallurgy and Materials Science* 36.5 (2005), pp. 1317–1327. ISSN: 10735623. DOI: 10.1007/s11661-005-0223-z.

[40] I. Ansarian et al. "Microstructure evolution and mechanical behaviour of severely deformed pure titanium through multi directional forging". In: *Journal of Alloys and Compounds* 776 (2019), pp. 83–95. ISSN: 09258388. DOI: 10.1016/j.jallcom.2018.10.196.

[41] H. Nasiri-Abarbekoh et al. "Effects of rolling reduction on mechanical properties anisotropy of commercially pure titanium". In: *Materials and Design* 34 (2012), pp. 268–274. DOI: 10.1016/j.matdes.2011.06.024.

[42] J. W. Won et al. "Anisotropic yielding behavior of rolling textured high purity titanium". In: *Materials Science and Engineering A* 637 (2015), pp. 215–221. ISSN: 09215093. DOI: 10.1016/j.msea.2015.03.096.

[43] B. Zhou et al. "Effect of high strain rates and different orientations on tensile behavior and microcosmic evolution of Ti-6Al-4V sheet". In: *Materials Research Express* 6.9 (2019). ISSN: 20531591. DOI: 10.1088/2053-1591/ab2a60.

[44] S. K. Sahoo et al. "Texture and microstructure evolution of commercially pure titanium during hot rolling: Role of strain-paths". In: *Materials and Design* 91 (2016), pp. 58–71. ISSN: 18734197. DOI: 10.1016/j.matdes.2015.11.073.

[45] W. Li et al. "Rolling texture and its effect on tensile property of a near-α titanium alloy Ti60 plate". In: *Journal of Materials Science and Technology* 35.5 (2019), pp. 790–798. ISSN: 10050302. DOI: 10.1016/j.jmst.2018.10.032.

[46] G. R. Johnson and W. H. Cook. "Fracture characteristics of three metals subjected to various strains, strain rates, temperatures and pressures". In: *Engineering Fracture Mechanics* 21.1 (1985), pp. 31–48. ISSN: 00137944. DOI: 10.1016/0013-7944(85)90052-9.

[47] M. Zakaria and X. Wu. "Response of titanium alloys to high strain rate deformation". In: *Materials Science and Technology* 21.2 (2005), pp. 225–231. ISSN: 02670836. DOI: 10.1179/174328405X20950.

[48] L. Zhang et al. "Rate dependent behaviour and dynamic strain localisation of three novel impact resilient titanium alloys: Experiments and modelling". In: *Materials Science and Engineering: A* 771 (2020), pp. 1–30. ISSN: 09215093. DOI: 10.1016/j.msea.2019.138552.

[49] L. Zhang, A. Pellegrino, and N. Petrinic. "Dynamic necking of a near α titanium alloy at high strain rates: Experiments and modelling". In: *Defence Technology* 17.4 (2021), pp. 1126–1134. ISSN: 22149147. DOI: 10.1016/j.dt.2020.07.002.

[50] K. Kishida et al. "Experimental evaluation of critical resolved shear stress for the first-order pyramidal c + a slip in commercially pure Ti by micropillar compression method". In: *Acta Materialia* 196 (Sept. 2020), pp. 168–174. ISSN: 13596454. DOI: 10.1016/j.actamat.2020.06.043.

[51] S. Hémery et al. "Influence of Microtexture on Early Plastic Slip Activity in Ti-6Al-4V Polycrystals". In: *Metallurgical and Materials Transactions A: Physical Metallurgy and Materials Science* 49.6 (2018), pp. 2048–2056. DOI: 10.1007/s11661-018-4569-4.

[52] A. Akhtar. "Basal slip in zirconium". In: *Acta Metallurgica* 21.1 (1973), pp. 1–11. ISSN: 00016160. DOI: 10.1016/0001-6160(73)90213-7.

[53] A. Akhtar. "Basal slip and twinning in α-titanium single crystals". In: *Metallurgical Transactions A* 6.5 (1975), pp. 1105–1113. DOI: 10.1007/BF02661366.

[54] D. M. Dimiduk, M. D. Uchic, and T. A. Parthasarathy. "Size-affected single-slip behavior of pure nickel microcrystals". In: *Acta Materialia* 53.15 (2005), pp. 4065–4077. ISSN: 13596454. DOI: 10.1016/j.actamat.2005.05.023.

[55] J. R. Greer and J.Th.M. De Hosson. "Plasticity in small-sized metallic systems: Intrinsic versus extrinsic size effect". In: *Progress in Materials Science* 56.6 (2011), pp. 654–724. DOI: 10.1016/j.pmatsci.2011.01.005.

[56] T. B. Britton et al. "The effect of crystal orientation on the indentation response of commercially pure titanium: Experiments and simulations". In: *Proceedings of the Royal Society A: Mathematical, Physical and Engineering Sciences* 466.2115 (2010), pp. 695–719. DOI: 10.1098/rspa.2009.0455.

[57] C. Zambaldi et al. "Orientation informed nanoindentation of α-titanium: Indentation pileup in hexagonal metals deforming by prismatic slip". In: *Journal of Materials Research* 27.1 (2012), pp. 356–367. ISSN: 08842914. DOI: 10.1557/jmr.2011.334.

[58] J. C. Williams, R. G. Baggerly, and N. E. Paton. "Deformation behavior of HCP Ti-Al alloy single crystals". In: *Metallurgical and Materials Transactions A: Physical Metallurgy and Materials Science* 33.13 (2002), pp. 837–850. ISSN: 10735623. DOI: 10.1007/s11661-002-1016-2.

[59] T. Sakai and M.E. Fine. "Basal slip of Ti-Al single crystals". In: *Scipta Metallurgica* 8.5 (1974), pp. 545–548.

[60] T. Sakai and M. E. Fine. "Plastic deformation of Ti-Al single crystals in prismatic slip". In: *Acta Metallurgica* 22.11 (1974), pp. 1359–1372. ISSN: 00016160. DOI: 10.1016/0001-6160(74)90036-4.

[61] J. Gong and A. J. Wilkinson. "Anisotropy in the plastic flow properties of single-crystal α titanium determined from micro-cantilever beams". In: *Acta Materialia* 57.19 (Nov. 2009), pp. 5693–5705. DOI: 10.1016/j.actamat.2009.07.064.

[62] X. Wu et al. "Prediction of crystallographic texture evolution and anisotropic stress-strain curves during large plastic strains in high purity α-titanium using a Taylor-type crystal plasticity model". In: *Acta Materialia* 55.2 (2007), pp. 423–432. ISSN: 13596454. DOI: 10.1016/j.actamat.2006.08.034.

[63] H. Qin et al. "Initiation and accommodation of primary twins in high-purity titanium". In: *Acta Materialia* 71 (2014), pp. 293–305. ISSN: 13596454. DOI: 10.1016/j.actamat.2014.03.025.

[64] Y. B. Chun et al. "Effect of deformation twinning on microstructure and texture evolution during cold rolling of CP-titanium". In: *Materials Science and Engineering A* 398.1-2 (2005), pp. 209–219. ISSN: 09215093. DOI: 10.1016/j.msea.2005.03.019.

[65] Z. Zeng, S. Jonsson, and H. J. Roven. "The effects of deformation conditions on microstructure and texture of commercially pure Ti". In: *Acta Materialia* 57.19 (2009), pp. 5822–5833. DOI: 10.1016/j.actamat.2009.08.016.

[66] W. Tirry et al. "The importance of secondary and ternary twinning in compressed Ti". In: *Scripta Materialia* 64.9 (2011), pp. 840–843. ISSN: 13596462. DOI: 10.1016/j.scriptamat.2011.01.012.

[67] A. Meng et al. "Microstructure evolution and mechanical properties of commercial pure titanium subjected to rotary swaging". In: *Journal of Alloys and Compounds* 859 (2021), p. 158222. ISSN: 09258388. DOI: 10.1016/j.jallcom.2020.158222.

[68] A. Ghaderi and M. R. Barnett. "Sensitivity of deformation twinning to grain size in titanium and magnesium". In: *Acta Materialia* 59.20 (2011), pp. 7824–7839. ISSN: 13596454. DOI: 10.1016/j.actamat.2011.09.018.

[69] S. V. Zherebtsov et al. "The Influence of Grain Size on Twinning and Microstructure Refinement During Cold Rolling of Commercial-Purity Titanium". In: *Metallurgical and Materials Transactions A: Physical Metallurgy and Materials Science* 47.10 (2016), pp. 5101–5113. DOI: 10.1007/s11661-016-3679-0.

[70] N. Stanford, U. Carlson, and M. R. Barnett. "Deformation twinning and the Hall-Petch relation in commercial purity Ti". In: *Metallurgical and Materials Transactions A: Physical Metallurgy and Materials Science* 39 A.4 (2008), pp. 934–944. DOI: 10.1007/s11661-007-9442-9.

[71] P. Ye et al. "A comparative study between {1122} twinning and {1012} twinning variant selection mechanisms during uniaxial compression in pure titanium". In: *Materials Characterization* 162.July 2019 (2020), p. 110188. ISSN: 10445803. DOI: 10.1016/j.matchar.2020.110188.

[72] H. Qin and J. J. Jonas. "Variant selection during secondary and tertiary twinning in pure titanium". In: *Acta Materialia* 75 (2014), pp. 198–211. ISSN: 13596454. DOI: 10.1016/j.actamat.2014.04.065.

[73] J. J. Jonas et al. "The role of strain accommodation during the variant selection of primary twins in magnesium". In: *Acta Materialia* 59.5 (2011), pp. 2046–2056. ISSN: 13596454. DOI: 10.1016/j.actamat.2010.12.005.

[74] P. Zhou and G. Z. Zhu. "Strain accommodations among twin variants in Ti and Mg". In: *Crystals* 11.4 (2021). DOI: 10.3390/cryst11040453.

[75] S. Xu et al. "Sequential {101¯2} twinning stimulated by other twins in titanium". In: *Acta Materialia* 132 (2017), pp. 57–68. DOI: 10.1016/j.actamat.2017.04.023.

[76] M. Wronski et al. "Deformation behavior of CP-titanium: Experiment and crystal plasticity modeling". In: *Materials Science and Engineering A* 724 (2018), pp. 289–297. ISSN: 09215093. DOI: 10.1016/j.msea.2018.03.017.

[77] S. J. Lainé, K. M. Knowles, and D. Rugg. "Very high strain rate deformation twinning behaviour of Ti–6Al–4V". In: *Materialia* 12.May (2020). ISSN: 25891529. DOI: 10.1016/j.mtla.2020.100762.

[78] M. A. Meyers. *Dynamic behavior of materials*. Wiley, 1994, p. 668. ISBN: 047158262X.

[79] B. Hopkinson. "A method of measuring the pressure produced in the detonation of high, explosives or by the impact of bullets". In: *Philosophical Transactions of the Royal Society of London. Series A, Containing Papers of a Mathematical or Physical Character* 213.497-508 (1914), pp. 437–456. ISSN: 0264-3952. DOI: 10.1098/rsta.1914.0010.

[80] H. Kolsky. "An investigation of the mechanical properties of materials at very high rates of loading". In: *Proceedings of the Physical Society. Section B* 62.11 (1949), pp. 676–700. ISSN: 03701301. DOI: 10.1088/0370-1301/62/11/302.

[81] R.M. Davies. "A critical study of the Hopkinson pressur bar". In: 240.January (1948), pp. 375–457.

[82] G. T. Grey III. "Classic Split-Hopkinson Pressure Bar Testing". In: *Mechanical Testing and Evaluation*. Vol. 8. ASM International, 2000, pp. 462–476. DOI: 10.31399/asm.hb.v08.a0003296.

[83] Agamenon R. E. Oliveira. "D'Alembert and the Wave Equation: Its Disputes and Controversies". In: *Advances in Historical Studies* 09.04 (2020), pp. 229–239. DOI: 10.4236/ahs.2020.94019.

[84] L. Pochhammer. "About the Initiation of the Velocities of Small Oscillations in Unbounded Isotropic Circular Cylinders". In: *Journal für die reine und angewandte Mathematik* 81 (1876), pp. 324–336.

[85] C. Chree. "The equations of an isotropic elastic solid in polar and cylindrical coordinates, their solution and application". In: *Transactions of the Cambridge Philosophical Society* 14 (1889), pp. 250–369.

[86] B. A. Gama, S. L. Lopatnikov, and J.W. Gillespie. "Hopkinson bar experimental technique: A critical review". In: *Applied Mechanics Reviews* 57.1-6 (2004), pp. 223–250. ISSN: 00036900. DOI: 10.1115/1.1704626.

[87] C. Wheatstone. "XIII. The Bakerian lecture.—An account of several new instruments and processes for determining the constants of a voltaic circuit". In: *Philosophical Transactions of the Royal Society* 133 (1843), pp. 303–327. DOI: 10.1098/rstl.1843.0014.

[88] M. Prot and T. J. Cloete. "A Tandem Momentum Trap for Dynamic Specimen Recovery During Split Hopkinson Pressure Bar Testing of Cancellous Bone". In: *Journal of Dynamic Behavior of Materials* 2.1 (2016), pp. 50–58. DOI: 10.1007/s40870-016-0046-6.

[89] R. Gerlach, C. Kettenbeil, and N. Petrinic. "A new split Hopkinson tensile bar design". In: *International Journal of Impact Engineering* 50 (2012), pp. 63–67. ISSN: 0734743X. DOI: 10.1016/j.ijimpeng.2012.08.004.

[90] F. De Cola et al. "Effect of Particle Morphology, Compaction, and Confinement on the High Strain Rate Behavior of Sand". In: *Experimental Mechanics* 58.2 (2018), pp. 223–242. ISSN: 17412765. DOI: 10.1007/s11340-017-0331-x.

[91] B. J. Inkson. *Scanning Electron Microscopy (SEM) and Transmission Electron Microscopy (TEM) for Materials Characterization*. Elsevier Ltd, 2016, pp. 17–43. ISBN: 9780081000571. DOI: 10.1016/B978-0-08-100040-3.00002-X.

[92] S. Nishikawa and S. Kikuchi. "Diffraction of Cathode Rays by Calcite". In: *Nature* 122.0 (1928), p. 726.

[93] M. N. Alam, M. Blackman, and D. W. Pashley. "High-angle Kikuchi patterns". In: *Proceedings of the Royal Society of London. Series A. Mathematical and Physical Sciences* 221.1145 (1954), pp. 224–242.

[94] J. A. Venables and C. J. Harland. "Electron back-scattering patterns—a new technique for obtaining crystallographic information in the scanning electron microscope". In: *Philosophical Magazine* 27.5 (1973), pp. 1193–1200. ISSN: 00318086. DOI: 10.1080/14786437308225827.

[95] J. A. Venables and R. Bin-Jaya. "Accurate microcrystallography using electron back-scattering patterns". In: *Philosophical Magazine* 35.5 (1977), pp. 1317–1332. ISSN: 00318086. DOI: 10.1080/14786437708232955.

[96] F. Bachmann, R. Hielscher, and H. Schaeben. "Texture analysis with MTEX-Free and open source software toolbox". In: *Solid State Phenomena* 160 (2010), pp. 63–68. ISSN: 10120394. DOI: 10.4028/www.scientific.net/SSP.160.63.

[97] L. Zhang et al. "Thermomechanical constitutive behaviour of a near α titanium alloy over a wide range of strain rates: Experiments and modelling". In: *International Journal of Mechanical Sciences* 189.May 2020 (2021), p. 105970. ISSN: 00207403. DOI: 10.1016/j.ijmecsci.2020.105970.

[98] S. Nemat-Nasser, W. G. Guo, and J. Y. Cheng. "Mechanical properties and deformation mechanisms of a commercially pure titanium". In: *Acta Materialia* 47.13 (1999), pp. 3705–3720. ISSN: 13596454. DOI: 10.1016/S1359-6454(99)00203-7.

[99] S. Zhao et al. "Cryoforged nanotwinned titanium with ultrahigh strength and ductility". In: *Science* 376.6594 (2022), pp. 1363–1368. ISSN: 10959203. DOI: 10.1126/science.abe7252.

[100] D. A. Gorham. "Specimen inertia in high strain-rate compression". In: *Journal of Physics D: Applied Physics* 22.12 (1989), pp. 1888–1893. ISSN: 13616463. DOI: 10.1088/0022-3727/22/12/014.

[101] F. J. Humphreys. "Grain and subgrain characterisation by electron backscatter diffraction". In: *Journal of Materials Science* 36.16 (2001), pp. 3833–3854. ISSN: 00222461. DOI: 10.1023/A:1017973432592.

[102] C. K. Yan et al. "Dynamic recrystallization of titanium: Effect of pre-activated twinning at cryogenic temperature". In: *Acta Materialia* 154 (2018), pp. 311–324. ISSN: 13596454. DOI: 10.1016/j.actamat.2018.05.057.

[103] W. Pantleon. "Resolving the geometrically necessary dislocation content by conventional electron backscattering diffraction". In: *Scripta Materialia* 58.11 (2008), pp. 994–997. ISSN: 13596462. DOI: 10.1016/j.scriptamat.2008.01.050.

[104] O. Muránsky et al. "On the measurement of dislocations and dislocation substructures using EBSD and HRSD techniques". In: *Acta Materialia* 175 (2019), pp. 297–313. DOI: 10.1016/j.actamat.2019.05.036.

[105] F. Pedregosa et al. "Scikit-learn: Machine Learning in Python". In: *Journal of Machine Learning Research* 12.85 (2011), pp. 2825–2830. ISSN: 15529924. DOI: 10.1289/EHP4713.

[106] T. Wang et al. "Effects of strain rates on deformation twinning behavior in α-titanium". In: *Materials Characterization* 106 (2015), pp. 218–225. ISSN: 10445803. DOI: 10.1016/j.matchar.2015.05.016.

[107] M. S. Lee and T. S. Jun. "Mechanical properties and deformation modes of grade 1 commercially pure titanium at cryogenic temperature". In: *Journal of Physics: Conference Series* 2169.1 (2022), pp. 1–6. ISSN: 17426596. DOI: 10.1088/1742-6596/2169/1/012025.

[108] S. J. Lainé, K. M. Knowles, and D. Rugg. "Grain Boundary Interactions of Deformation Twins in CP Titanium After Room Temperature Ballistic Impact Testing". In: *Proceedings of the 13th World Conference on Titanium* (2016), pp. 1071–1076. DOI: 10.1002/9781119296126.ch182.

[109] J.W. Won et al. "Simultaneous Improvement in the Strength and Formability of Commercially Pure Titanium via Twinning-induced Crystallographic Texture Control". In: *Scientific Reports* 9.1 (2019), pp. 1–11. ISSN: 20452322. DOI: 10.1038/s41598-019-38652-1.

[110] R. Y. Zhang, M.R. Daymond, and R. A. Holt. "A finite element model of deformation twinning in zirconium". In: *Materials Science and Engineering A* 473.1-2 (2008), pp. 139–146. ISSN: 09215093. DOI: 10.1016/j.msea.2007.04.021.

[111] F. Siska et al. "Numerical analysis of twin thickening process in magnesium alloys". In: *Acta Materialia* 124 (2017), pp. 9–16. ISSN: 13596454. DOI: 10.1016/j.actamat.2016.10.068.

[112] M. J. Tan and X. J. Zhu. "Dynamic recrystallization in commercially pure titanium". In: *Journal of Achievements in Materials and Manufacturing Engineering* 18.1-2 (2006), pp. 183–186.

[113] G. I. Taylor. "Plastic strain in metals". In: *Journal of the Institute of Metals* 62 (1938), pp. 307–324.

[114] P. Luo et al. "A modified Hall-Petch relationship in ultrafine-grained titanium recycled from chips by equal channel angular pressing". In: *Scripta Materialia* 66.10 (2012), pp. 785–788. DOI: 10.1016/j.scriptamat.2012.02.008.

[115] M. A. Meyers and K. K. Chawla. *Mechanical Behavior of Materials*. 2nd ed. Cambridge University Press. ISBN: 9780521866750.

[116] G. Tsukamoto et al. "Effect of twinning deformation on work hardening in commercially pure titanium". In: *Materials Science and Engineering: A* 840.March (2022), p. 142907. ISSN: 09215093. DOI: 10.1016/j.msea.2022.142907.

[117] Y. Guo et al. "Growth of $\{11\bar{2}2\}$ twins in titanium: A combined experimental and modelling investigation of the local state of deformation". In: *Acta Materialia* 126 (2017), pp. 221–235. DOI: 10.1016/j.actamat.2016.12.066.

[118] Dassault Systèmes. "Abaqus 2016Abaqus/Cae User's Guide". In: (2016), p. 1144.

[119] R. S. Hartley, T. J. Cloete, and G. N. Nurick. "An experimental assessment of friction effects in the split Hopkinson pressure bar using the ring compression test". In: *International Journal of Impact Engineering* 34.10 (2007), pp. 1705–1728. DOI: 10.1016/j.ijimpeng.2006.09.003.

[120] A. Siegel, S. Laporte, and F. Sauter-Starace. "Johnson–cook parameter identification for commercially pure titanium at room temperature under quasi-static strain rates". In: *Materials* 14.14 (2021), pp. 1–13. DOI: 10.3390/ma14143887.

[121] E. D.H. Davies and S. C. Hunter. "The dynamic compression testing of solids by the method of the split Hopkinson pressure bar". In: *Journal of the Mechanics and Physics of Solids* 11.3 (1963), pp. 155–179. ISSN: 00225096. DOI: 10.1016/0022-5096(63)90050-4.

[122] D. Steinberg. *Equation of State and Strength Properties of Selected Materials*. Tech. rep. 1996.

[123] D. C. Murray et al. "Biometry of the silicone oil-filled eye: II". In: *Eye* 16.6 (2002), pp. 727–730. ISSN: 0950222X. DOI: 10.1038/sj.eye.6700176.

[124] A. Cafarelli et al. "Speed of sound in rubber-based materials for ultrasonic phantoms". In: *Journal of Ultrasound* 19.4 (2016), pp. 251–256. DOI: 10.1007/s40477-016-0204-7.

[125] L. Wang et al. "Direct measurement of critical resolved shear stress of prismatic and basal slip in polycrystalline Ti using high energy X-ray diffraction microscopy". In: *Acta Materialia* 132 (2017), pp. 598–610. DOI: 10.1016/j.actamat.2017.05.015.

[126] S. Hémery and P. Villechaise. "Investigation of Size Effects in Slip Strength of Titanium Alloys: α Nodule Size Dependence of the Critical Resolved Shear Stress". In: *Metallurgical and Materials Transactions A: Physical Metallurgy and Materials Science* 49.10 (Oct. 2018), pp. 4394–4397. DOI: 10.1007/s11661-018-4678-0.

[127] P. Baudoin, T. Hama, and H. Takuda. "Influence of critical resolved shear stress ratios on the response of a commercially pure titanium oligocrystal: Crystal plasticity simulations and experiment". In: *International Journal of Plasticity* 115.November 2018 (2019), pp. 111–131. DOI: 10.1016/j.ijplas.2018.11.013.

[128] D. Gloaguen et al. "Experimental and theoretical studies of intergranular strain in an alpha titanium alloy during plastic deformation". In: *Acta Materialia* 61.15 (2013), pp. 5779–5790. DOI: 10.1016/j.actamat.2013.06.022.

[129] K. E. K. Amouzou et al. "Micromechanical modeling of hardening mechanisms in commercially pure α-titanium in tensile condition". In: *International Journal of Plasticity* 80 (2016), pp. 222–240. DOI: 10.1016/j.ijplas.2015.09.008.

[130] E. Parzen. "On Estimation of a Probability Density Function and Mode". In: *The Annals of Mathematical Statistics* 33.3 (1962), pp. 1065–1076. ISSN: 2278-1811. DOI: 10.1214/aoms/1177704472.

[131] P. Virtanen et al. "SciPy 1.0: fundamental algorithms for scientific computing in Python". In: *Nature Methods* 17.3 (2020), pp. 261–272. ISSN: 15487105. DOI: 10.1038/s41592-019-0686-2. arXiv: 1907.10121.

[132] B.A. Turlach. "Bandwidth selection in kernel density estimation: A review". In: *Handbook of Systemic Autoimmune Diseases* (1999), pp. 1–33.

[133] D.M. Bashtannyk and R.J. Hyndman. "Bandwidth selection for kernel conditional density estimation". In: *Computational Statistics and Data Analysis* 36.3 (2001), pp. 279–298. ISSN: 01679473. DOI: 10.1016/S0167-9473(00)00046-3.

[134] D. Lemke et al. "Comparing adaptive and fixed bandwidth-based kernel density estimates in spatial cancer epidemiology". In: *International Journal of Health Geographics* 14.1 (2015), pp. 1–10. DOI: 10.1186/s12942-015-0005-9.

[135] H.-J. Bunge. *Texture Analysis in Material Science*. Butterworth & Co, 1969. ISBN: 978-0-408-10642-9. DOI: 10.1016/C2013-0-11769-2.

[136] L. Wang et al. "Twin nucleation by slip transfer across grain boundaries in commercial purity titanium". In: *Metallurgical and Materials Transactions A: Physical Metallurgy and Materials Science* 41.2 (2010), pp. 421–430. DOI: 10.1007/s11661-009-0097-6.

[137] K. Sofinowski et al. "In situ characterization of work hardening and spring-back in grade 2 α-titanium under tensile load". In: *Acta Materialia* 181 (Dec. 2019), pp. 87–98. ISSN: 13596454. DOI: 10.1016/j.actamat.2019.09.039.

[138] D. Li et al. "Enhanced strength in pure Ti via design of alternating coarse- and fine-grain layers". In: *Acta Materialia* 206 (2021), p. 116627. ISSN: 13596454. DOI: 10.1016/j.actamat.2021.116627.

[139] A.P. Dempster, N.M. Laird, and D.B. Rubin. "Maximum Likelihood from Incomplete Data via the EM Algorithm". In: *Journal of the Royal Statistical Society. Series B (Methodological)* 39.1 (1977), pp. 1–38. DOI: 10.1111/j.2517-6161.1977.tb01600.x.

[140] M. Battaini, E. V. Pereloma, and C. H.J. Davies. "Orientation effect on mechanical properties of commercially pure titanium at room temperature". In: *Metallurgical and Materials Transactions A: Physical Metallurgy and Materials Science* 38.2 (2007), pp. 276–285. ISSN: 10735623. DOI: 10.1007/s11661-006-9040-2.

[141] L. Carneiro et al. "Twinning characteristics in rolled AZ31B magnesium alloy under three stress states". In: *Materials Characterization* 175.January (2021), p. 111050. ISSN: 10445803. DOI: 10.1016/j.matchar.2021.111050.

[142] H. El Kadiri and A. L. Oppedal. "A crystal plasticity theory for latent hardening by glide twinning through dislocation transmutation and twin accommodation effects". In: *Journal of the Mechanics and Physics of Solids* 58.4 (2010), pp. 613–624. ISSN: 00225096. DOI: 10.1016/j.jmps.2009.12.004.

[143] A. Fitzner et al. "On the work hardening of titanium: new insights from nanoindentation". In: *Journal of Materials Science* 54.10 (2019), pp. 7961–7974. ISSN: 15734803. DOI: 10.1007/s10853-019-03431-w.

[144] S. I. Wright, M.M. Nowell, and D. P. Field. "A review of strain analysis using electron backscatter diffraction". In: *Microscopy and Microanalysis* 17.3 (2011), pp. 316–329. DOI: 10.1017/S1431927611000055.

[145] J. A. Muñoz et al. "Prediction of Generation of High- and Low-Angle Grain Boundaries (HAGB and LAGB) During Severe Plastic Deformation". In: *Metallurgical and Materials Transactions A: Physical Metallurgy and Materials Science* 51.9 (2020), pp. 4674–4684. ISSN: 10735623. DOI: 10.1007/s11661-020-05873-3.

[146] G. Zhou et al. “Annihilation Mechanism of Low-Angle Grain Boundary in Nanocrystalline Metals”. In: *Metals* (2022), pp. 1–10.

[147] J. W. Won et al. “Deformation anisotropy and associated mechanisms in rolling textured high purity titanium”. In: *Journal of Alloys and Compounds* 651 (2015), pp. 245–254. DOI: 10.1016/j.jallcom.2015.08.075.

[148] J. W. Won et al. “Anisotropic twinning and slip behaviors and their relative activities in rolled alpha-phase titanium”. In: *Materials Science and Engineering: A* 698.February (2017), pp. 54–62. ISSN: 09215093. DOI: 10.1016/j.msea.2017.05.042.

[149] T. Hama, A. Kobuki, and H. Takuda. “Crystal-plasticity finite-element analysis of anisotropic deformation behavior in a commercially pure titanium Grade 1 sheet”. In: *International Journal of Plasticity* 91 (2017), pp. 77–108. ISSN: 07496419. DOI: 10.1016/j.ijplas.2016.12.005.

[150] J. W. Won et al. “Anisotropy in twinning characteristics and texture evolution of rolling textured high purity alpha phase titanium”. In: *Journal of Alloys and Compounds* 683 (2016), pp. 92–99. DOI: 10.1016/j.jallcom.2016.05.029.

[151] P. Baudoin et al. “Crystal plasticity analysis of the deformation of a grade 2 CP-Ti oligocrystal”. In: *Journal of Physics: Conference Series* 1063.1 (Aug. 2018). DOI: 10.1088/1742-6596/1063/1/012048.

[152] M. Arul Kumar et al. “Numerical study of the stress state of a deformation twin in magnesium”. In: *Acta Materialia* 84 (2015), pp. 349–358. ISSN: 13596454. DOI: 10.1016/j.actamat.2014.10.048.

[153] H. Li et al. “Mechanical response of dislocation interaction with grain boundary in ultrafine-grained interstitial-free steel”. In: *Acta Materialia* 206 (2021), p. 116621. ISSN: 13596454. DOI: 10.1016/j.actamat.2021.116621.

[154] S. Chen and Q. Yu. “The role of low angle grain boundary in deformation of titanium and its size effect”. In: *Scripta Materialia* 163 (2019), pp. 148–151. ISSN: 13596462. DOI: 10.1016/j.scriptamat.2018.10.054.

[155] L. L. Li et al. “Distinct fatigue cracking modes of grain boundaries with coplanar slip systems”. In: *Acta Materialia* 120 (2016), pp. 120–129. ISSN: 13596454. DOI: 10.1016/j.actamat.2016.06.032.

[156] A. Avelin et al. “Use of combined physical and statistical models for online applications in the pulp and paper industry”. In: *Use of combined physical and statistical models for online applications in the pulp and paper industry* 15.5 (2009), pp. 425–434. DOI: 10.1080/13873950903375403.

[157] A. Agrawal and A. Choudhary. “Perspective: Materials informatics and big data: Realization of the ”fourth paradigm” of science in materials science”. In: *APL Materials* 4.5 (2016). DOI: 10.1063/1.4946894.

[158] Anindya Bhaduri, Ashwini Gupta, and Lori Graham-Brady. "Stress field prediction in fiber-reinforced composite materials using a deep learning approach". In: *Composites Part B: Engineering* 238.April (2022), p. 109879. ISSN: 13598368. DOI: 10.1016/j.compositesb.2022.109879. arXiv: 2111.05271.

[159] O. Yasniy et al. "Application of machine learning for modeling of 6061-T651 aluminum alloy stressstrain diagram". In: *Procedia Structural Integrity* 48 (2023), pp. 183–189. ISSN: 24523216. DOI: 10.1016/j.prostr.2023.07.146.

[160] J. Lizarazu et al. "Application of machine learning-based algorithms to predict the stress-strain curves of additively manufactured mild steel out of its microstructural characteristics". In: *Results in Engineering* 20.September (2023), p. 101587. ISSN: 25901230. DOI: 10.1016/j.rineng.2023.101587.

[161] S. Wold, K. Esbensen, and P. Geladi. "Principal Component Analysis". In: *Chemometrics and intelligent laboratory systems* 2.1-3 (1987), pp. 37–52. arXiv: arXiv:1011.1669v3.

[162] I.T. Jolliffe. *Principal Components Analysis*. 2nd ed. 2002. DOI: 10.1016/S0922-3487(97)80047-0.

[163] F. L. Gewers et al. "Principal component analysis: A natural approach to data exploration". In: *ACM Computing Surveys* 54.4 (2022). DOI: 10.1145/3447755.

[164] M. I. Latypov et al. "Application of chord length distributions and principal component analysis for quantification and representation of diverse polycrystalline microstructures". In: *Materials Characterization* 145.May (2018), pp. 671–685. ISSN: 10445803. DOI: 10.1016/j.matchar.2018.09.020.

[165] C. Xu, S. Gao, and M. Li. "A novel PCA-based microstructure descriptor for heterogeneous material design". In: *Computational Materials Science* 130 (2017), pp. 39–49. DOI: 10.1016/j.commatsci.2016.12.031.

[166] G. A. Sengodan. "Prediction of two-phase composite microstructure properties through deep learning of reduced dimensional structure-response data". In: *Composites Part B: Engineering* 225.September (2021), p. 109282. ISSN: 13598368. DOI: 10.1016/j.compositesb.2021.109282.

[167] C.E. Rasmussen and C.K. I. Williams. *Gaussian Processes for Machine Learning*. The MIT Press, 2006. ISBN: 026218253X.

[168] Q. Liu and D. Wu. "Machine learning and feature representation approaches to predict stress-strain curves of additively manufactured metamaterials with varying structure and process parameters". In: *Materials and Design* 241.January (2024), p. 112932. ISSN: 18734197. DOI: 10.1016/j.matdes.2024.112932.

[169] D. An, N. H. Kim, and J. H. Choi. "Practical options for selecting data-driven or physics-based prognostics algorithms with reviews". In: *Reliability Engineering and System Safety* 133 (2015), pp. 223–236. ISSN: 09518320. DOI: 10.1016/j.ress.2014.09.014.

[170] S. Myren and E. Lawrence. "A comparison of Gaussian processes and neural networks for computer model emulation and calibration". In: *Statistical Analysis and Data Mining* 14.6 (2021), pp. 606–623. ISSN: 19321872. DOI: 10.1002/sam.11507.

[171] J. Wang. "An Intuitive Tutorial to Gaussian Process Regression". In: *Computing in Science and Engineering* 25.4 (2023), pp. 4–11. ISSN: 1558366X. DOI: 10.1109/MCSE.2023.3342149. arXiv: 2009.10862.

[172] Y. Zhou and Z. Lu. "An enhanced Kriging surrogate modeling technique for high-dimensional problems". In: *Mechanical Systems and Signal Processing* 140 (2020), p. 106687. ISSN: 10961216. DOI: 10.1016/j.ymssp.2020.106687.

[173] A. Karolczuk, D. Skibicki, and Ł. Pejkowski. "Gaussian Process for Machine Learning-Based Fatigue Life Prediction Model under Multiaxial Stress–Strain Conditions". In: *Materials* 15.21 (2022). ISSN: 19961944. DOI: 10.3390/ma15217797.

[174] M. Minsky. "Steps Toward Artificial Intelligence". In: *Proceedings of the IRE* 49.1 (1961), pp. 8–30. ISSN: 00968390. DOI: 10.1109/JRPROC.1961.287775.

[175] S. Haykin. *Neural Networks: A Comprehensive Foundation*. Pearson, 1999. DOI: 10.1049/el:19990177.

[176] J. Schmidhuber. "Deep Learning in neural networks: An overview". In: *Neural Networks* 61 (2015), pp. 85–117. ISSN: 18792782. DOI: 10.1016/j.neunet.2014.09.003. arXiv: 1404.7828.

[177] Y. LeCun et al. "Gradient-based learning applied to document recognition". In: *Proceedings of the IEEE* 86.11 (1998), pp. 2278–2323. DOI: 10.1109/5.726791.

[178] S. Ruder. "An overview of gradient descent optimization algorithms". In: (2017), pp. 1–14. arXiv: 1609.04747.

[179] A. Paszke et al. "PyTorch: An imperative style, high-performance deep learning library". In: *Advances in Neural Information Processing Systems* 32.NeurIPS (2019). ISSN: 10495258. arXiv: 1912.01703.

[180] Z. Ghahramani. *A Tutorial on Gaussian Processes (or why I don't use SVMs)*. 2011.

[181] C. M. Bishop and N. M. Nasrabadi. *Pattern Recognition and Machine Learning*. Vol. 4. 1. Springer, 2006. ISBN: 9780387310732. DOI: 10.53759/7669/jmc202404020.

[182] D. K. Duvenaud. "Automatic Model Construction with Gaussian Processes". PhD thesis. University of Cambridge, 2014.

[183] S. Arlot and A. Celisse. "A survey of cross-validation procedures for model selection". In: *Statistics Surveys* 4 (2010), pp. 40–79. DOI: 10.1214/09-SS054. arXiv: 0907.4728.

[184] W.T. Stephenson and T. Broderick. "Approximate Cross-Validation in High Dimensions with Guarantees". In: *Proceedings of Machine Learning Research* 108 (2020), pp. 2424–2434. arXiv: 1905.13657.

[185] D. P. Kingma and J.L. Ba. "Adam: A method for stochastic optimization". In: *3rd International Conference on Learning Representations, ICLR 2015 - Conference Track Proceedings* (2015), pp. 1–15. arXiv: 1412.6980.

[186] F. D'Angelo et al. "Why Do We Need Weight Decay in Modern Deep Learning?" In: *Advances in Neural Information Processing Systems* 37.NeurIPS (2024). ISSN: 10495258. arXiv: 2310.04415.

[187] Jin Woong Lee et al. "A machine-learning-based alloy design platform that enables both forward and inverse predictions for thermo-mechanically controlled processed (TMCP) steel alloys". In: *Scientific Reports* 11.1 (2021), pp. 1–18. ISSN: 20452322. DOI: 10.1038/s41598-021-90237-z.

[188] J. Hensman, N. Fusi, and N.D. Lawrence. "Gaussian Processes for Big Data". In: *Uncertainty in Artificial Intelligence*. 2013. DOI: 10.48550/arXiv.1309.6835.

[189] J. Hensman, A. G. Matthews, and Z. Ghahramani. "Scalable variational Gaussian process classification". In: *Journal of Machine Learning Research* 38 (2015), pp. 351–360. ISSN: 15337928. arXiv: 1411.2005.

[190] K. Krauth et al. "AutoGP: Exploring the capabilities and limitations of Gaussian process models". In: *Uncertainty in Artificial Intelligence - Proceedings of the 33rd Conference, UAI 2017* (2017). arXiv: 1610.05392.

[191] G.M. Harshvardhan et al. "A comprehensive survey and analysis of generative models in machine learning". In: *Computer Science Review* 38 (2020), p. 100285. ISSN: 15740137. DOI: 10.1016/j.cosrev.2020.100285.

[192] H. Bhasin. "Introduction to Generative Models". In: *Hands-on Deep Learning* (2024), pp. 307–321. DOI: 10.1007/979-8-8688-1035-0_12. arXiv: arXiv:2103.00265v1.

[193] M. Nareklishvili, N. Polson, and V. Sokolov. "Generative Modeling: A Review". In: (2024), pp. 1–38. arXiv: 2501.05458.

[194] A. Kazerouni et al. "Diffusion models in medical imaging: A comprehensive survey". In: *Medical Image Analysis* 88.November 2022 (2023), p. 102846. DOI: 10.1016/j.media.2023.102846.

[195] Ji. Liu et al. "WGAN-based multi-structure segmentation of vertebral cross-section MRI using ResU-Net and clustered transformer". In: *Scientific Reports* 14.1 (2024), pp. 1–18. ISSN: 20452322. DOI: 10.1038/s41598-024-79244-y.

[196] D. Vemula et al. "CADD, AI and ML in drug discovery: A comprehensive review". In: *European Journal of Pharmaceutical Sciences* 181.August 2022 (2023), p. 106324. ISSN: 18790720. DOI: 10.1016/j.ejps.2022.106324.

[197] Dolores R. Serrano et al. "Artificial Intelligence (AI) Applications in Drug Discovery and Drug Delivery: Revolutionizing Personalized Medicine". In: *Pharmaceutics* 16.10 (2024). ISSN: 19994923. DOI: 10.3390/pharmaceutics16101328.

[198] Matan Sela et al. "GazeGAN - Unpaired Adversarial Image Generation for Gaze Estimation". In: (2017). arXiv: 1711.09767.

[199] G. B. Olson. "Designing a material world". In: *Science* 288.5468 (2000), pp. 993–998. DOI: 10.1126/science.288.5468.993.

[200] R. C. Reed, T. Tao, and N. Warnken. "Alloys-By-Design: Application to nickel-based single crystal superalloys". In: *Acta Materialia* 57.19 (2009), pp. 5898–5913. ISSN: 13596454. DOI: 10.1016/j.actamat.2009.08.018.

[201] A. R. Oganov et al. "Structure prediction drives materials discovery". In: *Nature Reviews Materials* 4.5 (2019), pp. 331–348. DOI: 10.1038/s41578-019-0101-8.

[202] Mouyang Cheng et al. "AI-driven materials design: a mini-review". In: (2025), pp. 1–18. arXiv: 2502.02905.

[203] Anindya Bhaduri et al. "An efficient optimization based microstructure reconstruction approach with multiple loss functions". In: *Computational Materials Science* 199.March (2021), p. 110709. ISSN: 09270256. DOI: 10.1016/j.commatsci.2021.110709. arXiv: 2102.02407.

[204] J. Sohl-Dickstein et al. "Deep unsupervised learning using nonequilibrium thermodynamics". In: *32nd International Conference on Machine Learning, ICML 2015* 3 (2015), pp. 2246–2255. arXiv: 1503.03585.

[205] J. Ho, A. Jain, and P. Abbeel. "Denoising diffusion probabilistic models". In: *Advances in Neural Information Processing Systems* 2020-Decem.NeurIPS 2020 (2020), pp. 1–25. arXiv: 2006.11239.

[206] R. Rombach et al. "High-Resolution Image Synthesis with Latent Diffusion Models". In: *Proceedings of the IEEE Computer Society Conference on Computer Vision and Pattern Recognition* 2022-June (2022), pp. 10674–10685. ISSN: 10636919. DOI: 10.1109/CVPR52688.2022.01042. arXiv: 2112.10752.

[207] A. Vaswani et al. "Attention Is All You Need". In: *NIPS'17: Proceedings of the 31st International Conference on Neural Information Processing Systems*. 2017, pp. 6000–6010. ISBN: 9798400701245. DOI: 10.48550/arXiv.1706.03762. arXiv: 2304.03103.

[208] P. Esser, R. Rombach, and B. Ommer. "Taming transformers for high-resolution image synthesis". In: *Proceedings of the IEEE Computer Society Conference on Computer Vision and Pattern Recognition* (2021), pp. 12868–12878. ISSN: 10636919. DOI: 10.1109/CVPR46437.2021.01268. arXiv: 2012.09841.

[209] A. Ramesh et al. "Zero-Shot Text-to-Image Generation". In: *Proceedings of Machine Learning Research* 139 (2021), pp. 8821–8831. ISSN: 26403498. arXiv: 2102.12092.

[210] I.J. Goodfellow et al. *Generative Adversarial Nets*. 2014. DOI: 10.48550/arXiv.1406.2661.

[211] I. Goodfellow et al. "Generative adversarial networks". In: *Communications of the ACM* 63.11 (2020), pp. 139–144. ISSN: 15577317. DOI: 10.1145/3422622.

[212] M. Krichen. "Generative Adversarial Networks". In: *2023 14th International Conference on Computing Communication and Networking Technologies, ICCCNT 2023* (2023), pp. 1–7. DOI: 10.1109/ICCCNT56998.2023.10306417.

[213] M. Arjovsky and L. Bottou. "Towards principled methods for training generative adversarial networks". In: *5th International Conference on Learning Representations, ICLR 2017 - Conference Track Proceedings* (2017), pp. 1–17. arXiv: 1701.04862.

[214] Y. Kossale, M. Airaj, and A. Darouichi. "Mode Collapse in Generative Adversarial Networks: An Overview". In: *8th International Conference on Optimization and Applications, ICOA 2022 - Proceedings* (2022), pp. 1–6. DOI: 10.1109/ICOA55659.2022.9934291.

[215] S. Arora et al. "Generalization and equilibrium in generative adversarial nets (GANs)". In: *34th International Conference on Machine Learning, ICML 2017* 1 (2017), pp. 322–349. arXiv: 1703.00573.

[216] H. Thanh-Tung and T. Tran. "On Catastrophic Forgetting and Mode Collapse in Generative Adversarial Networks". In: (2018). arXiv: 1807.04015.

[217] M. Arjovsky, S. Chintala, and L. Bottou. "Wasserstein GAN". In: (2017). arXiv: 1701.07875.

[218] I. Gulrajani et al. "Improved training of wasserstein GANs". In: *Advances in Neural Information Processing Systems* 2017-Decem (2017), pp. 5768–5778. ISSN: 10495258. arXiv: 1704.00028.

[219] Y. Rubner, C. Tomasi, and L. J. Guibas. "Metric for distributions with applications to image databases". In: *Proceedings of the IEEE International Conference on Computer Vision* (1998), pp. 59–66. DOI: 10.1109/iccv.1998.710701.

[220] S. Hochreiter and J. Schmidhuber. "Long Short-Term Memory". In: *Neural Computation* 9.8 (1997), pp. 1735–1780. ISSN: 08997667. DOI: 10.1162/neco.1997.9.8.1735.

[221] K. Cho et al. "On the properties of neural machine translation: Encoder–decoder approaches". In: *Proceedings of SSST 2014 - 8th Workshop on Syntax, Semantics and Structure in Statistical Translation* (2014), pp. 103–111. DOI: 10.3115/v1/w14-4012. arXiv: 1409.1259.

[222] Junyoung Chung et al. "Empirical Evaluation of Gated Recurrent Neural Networks on Sequence Modeling". In: (2014), pp. 1–9. arXiv: 1412.3555.

[223] S. Yang, X. Yu, and Y. Zhou. "LSTM and GRU Neural Network Performance Comparison Study: Taking Yelp Review Dataset as an Example". In: *Proceedings - 2020 International Workshop on Electronic Communication and Artificial Intelligence, IWECAI 2020* (2020), pp. 98–101. DOI: 10.1109/IWECAI50956.2020.00027.

[224] R. Cahuantzi, X. Chen, and S. Güttel. "A Comparison of LSTM and GRU Networks for Learning Symbolic Sequences". In: *Lecture Notes in Networks and Systems* 739 LNNS (2023), pp. 771–785. ISSN: 23673389. DOI: 10.1007/978-3-031-37963-5_53. arXiv: 2107.02248.

[225] M. Marek et al. "Small Batch Size Training for Language Models: When Vanilla SGD Works, and Why Gradient Accumulation Is Wasteful". In: 1 (2025), pp. 1–18. arXiv: 2507.07101.

[226] D. Saxena and J. Cao. "Generative Adversarial Networks (GANs): Challenges, Solutions, and Future Directions". In: (2020), pp. 1–42. DOI: 10.48550/arXiv.2005.00065. arXiv: 2005.00065.

[227] Y. T. Tang et al. "Alloys-by-design: Application to new superalloys for additive manufacturing". In: *Acta Materialia* 202 (2021), pp. 417–436. ISSN: 13596454. DOI: 10.1016/j.actamat.2020.09.023.